Implicit Time Spectral Method for time-periodic Incompressible flows

Sylvain Antheaume

UNIVERSITE DE GRENOBLE
INSTITUT POLYTECHNIQUE DE GRENOBLE

N^o ***attribué par la bibliothèque***
|_|_|_|_|_|_|_|_|_|_|_|

THESE

pour obtenir le grade de

DOCTEUR DE L'Université de Grenoble
délivré par l'Institut polytechnique de Grenoble

Spécialité « Mécanique des Fluides, Procédés, Énergétique »

préparée au ***L**aboratoire des **É**coulements **G**éophysiques et **I**ndustriels*
(LEGI, UMR 5519, CNRS-UJF-INPG)

dans le cadre de l' **École Doctorale « Ingénierie - Matériaux Mécanique Energétique Environnement Procédés Production »**

présentée et soutenue publiquement

par

Sylvain ANTHEAUME

le 4 novembre 2010

IMPLICIT TIME SPECTRAL METHOD FOR TIME-PERIODIC INCOMPRESSIBLE FLOWS

Directeur de thèse : Pr. C. CORRE

JURY

Dr. Pascal FERRAND	Directeur de Recherche du CNRS, Ecole Centrale de Lyon	Président
Pr. Herman DECONINCK	Professeur, Von Karman Institute, Belgium	Rapporteur
Dr. Michel VISONNEAU	Directeur de recherche du CNRS, Ecole Centrale de Nantes	Rapporteur
Pr. Christophe CORRE	Professeur, Grenoble INP	Directeur de thèse
Dr. Eric GONCALVES	Maître de Conférence, Grenoble INP	Examinateur

Remerciements

Au début de ma thèse, il y a une idée de Jean-Luc Achard :
"Sylvain, j'ai lu quelque part qu'on pouvait réduire les temps de calculs d'écoulements périodiques en temps en utilisant le principe de la décomposition en série de Fourier de la solution, tu voudrais pas voir ce que ça donne pour nos hydroliennes ?"
Sans trop savoir à ce moment dans quoi je m'embarquais, j'attaquais la lecture des publications de Gilles Carte, Jan Dusĕk and Philippe Fraunié sur le sujet dont les travaux précurseurs à la TSM ne sont, à mon avis, pas assez cités. Je tiens donc à remercier en premier lieu Jean-Luc pour cette ébauche de sujet et aussi Thierry Maître pour m'avoir mis le pied à l'étrier au début de la thèse.

Ensuite, comme à l'évidence, je n'étais pas suffisament armé pour affronter seul le sujet, Christophe est venu à mon secours. Je tiens ici à lui adresser mes profonds remerciements pour le suivi de cette thèse. Sa rigueur scientifique et son expertise en méthodes numériques ont été essentielles au cadrage et à la réussite du projet de thèse. En même temps, la liberté dont j'ai disposé pour explorer des pistes originales et la confiance qu'il m'a accordé pour mener à bien certains développements ont grandement participé à mon épanouissement personnel et à ma construction de scientifique.

Je souhaite également remercier Herman Deconinck et Michel Visonneau d'avoir accepté le rôle de rapporteur sur mon mémoire. Leur lecture attentive du mansucript et leurs remarques très pertinentes m'ont permis de prendre du recul et de mieux cadrer la place de mon travail dans le contexte plus général des méthodes numériques. Par ailleurs, ils ont proposé des pistes d'amélioration et ouvert des perspectives de travail très intéressantes qui, j'espère, sauront être exploitées par la communauté CFD.

Merci aussi à Eric Goncalvès d'avoir assisté à ma soutenance en tant qu'examinateur et à Pascal Ferrand d'avoir bien voulu présider le jury.

Autour du projet HARVEST gravitent de nombreux personnes qui contribuent à la bonne ambiance générale de travail. Ils ne sont plus seulement des collègues mais bien des amis. Plus généralement, j'ai eu le plaisir de rencontrer de nombreux doctorants avec qui j'ai souvent partagé plus qu'un repas au RU. Merci donc à Thomas pour ses passes décisives, Jéronimo pour avoir assisté à mes répétitions de soutenance, Jonathan avec qui mon pari tient toujours, Guilherme pour son assurage dynamique, Alexandre pour son assistance technique mac, Boris pour ses sites webs insolites, Sylvain T pour les paires dans les voies dures, Nicolas pour toutes les aventures sportives.

J'ai eu la chance pendant ma thèse, de partir pour 6 mois à Seattle, à l'Université de Washington (USA) où j'ai travaillé sur la problématique du sillage des hydroliennes. Ce séjour à été extrèmement enrichissant pour moi grâce notamment à Alberto Aliseda, Oscar Florès et Jim Riley avec qui j'ai travaillé sur place.

Je remercie la société EDF d'avoir cru dans ce projet en m'accompagnant financièrement pendant ces 3 ans.

C'est une maison blanche. Adossée à la colline. On y vient à pied (ou en poussant fort sur les pédales...) et j'y ai certainement vécu la meilleure expérience de vie collective possible. Merci à tous les (nombreux) colocs du 8 chemin du Coteau qui sont passé dans cette ruche toujours en pleine activité.

Je remercie mes parents de s'être déplacés pour ma soutenance et pour les bons produits régionaux dont ils nous ont fait profiter pendant le buffet.

Mon dernier remerciement s'adresse à Mélanie qui m'a patiemment soutenu pendant ces 3 ans. Merci d'avoir compris l'importance que cette thèse représentait pour moi et pour l'organisation du pot de soutenance qui restera un moment fort de cette journée.

Contents

List of Figures

Nomenclature

$\boldsymbol{A}, \boldsymbol{B}, \boldsymbol{J}$	=	flux Jacobian matrices
C_X, C_Y	=	force coefficients
C_p	=	pressure coefficient
c	=	airfoil chord
$\boldsymbol{F}$	=	physical flux vectors
$\boldsymbol{f}, \boldsymbol{g}$	=	cartesian coordinates of the physical flux vector
f^*	=	nondimensional frequency, fc/U_∞
H_0	=	heaving amplitude
$\mathcal{H}$	=	numerical flux
h	=	typical grid lenght
$\boldsymbol{K}$	=	artifical compressibility singular matrix
N	=	number of harmonics
$\mathbf{n}$	=	cell surface outward unit vector
p	=	pressure
$\boldsymbol{Q}^E$	=	Roe numerical dissipation matrix $\lvert\boldsymbol{J}^E\rvert$
Re	=	Reynolds number
$\mathcal{R}$	=	residual vector discretizing the flux balance
$\mathcal{R}^t$	=	full residual including unsteady terms
$\boldsymbol{r}$	=	vector extending from cell center to cell face center
$\boldsymbol{s}$	=	grid velocity vector
s_n	=	normal grid velocity
$\boldsymbol{T}, \boldsymbol{T}^{-1}$	=	matrix of right eigenvectors of $\boldsymbol{J}$ (columns), left eigenvectors of $\boldsymbol{J}$ (lines)
t, τ	=	physical and dual time
U	=	velocity magnitude
V_n, V_t	=	normal and tangential velocity
u, v	=	cartesian velocity components

$\boldsymbol{v}_p$	=	primitive variable vector
$\boldsymbol{w}$	=	conservative variable vector
$\boldsymbol{x}$	=	vector of grid location
x, y	=	cartesian coordinates
y_p	=	distance from the wall to the first adjacent cell centroid
α	=	incidence angle (chord, upwind velocity)
β	=	artificial compressibility parameter
Γ	=	face
Δ	=	increment
θ	=	angular position
θ_0	=	pitching amplitude
$\boldsymbol{\Lambda}$	=	diagonal matrix of the Jacobian $\boldsymbol{J}$
ν	=	dynamic viscosity
ρ	=	density
$\rho()$	=	spectral radii
Ω	=	cell surface
ω	=	angular velocity
∂_x, ∂_y	=	differential operator

Subscripts

i	=	cell index
k	=	face index
i, k	=	interface k of cell i
$o(i, k)$	=	cell sharing face $\Gamma_{i,k}$ with i
∞	=	freestream value
n	=	TSM n^{th} time instant
$\perp$	=	perpendicular direction

Superscripts

i	=	implicit stage
E, V	=	inviscid and viscous
L, R	=	left and right states
l	=	Jacobi iteration counter
m	=	dual time counter

n	=	physical time counter

Acronyms

AC	=	Artifical Compressibility
ALE	=	Arbitrary Lagrangian Eulerian
BDF	=	Backward Difference Formula
C	=	Compressible
CFL	=	Courant Friedrichs Lewy
DTS	=	Dual Time Step
GCL	=	Geometric Conservation Law
PJ	=	Point Jacobi
S	=	Steady
TSM	=	Time Spectral Method

Introduction

The general context of the present study is the HARVEST industrial/academic joint project devoted to the development of a cross flow water turbine technology allowing to harness the kinetic energy of rivers and oceans streams. The flow in such a turbine is complex and involves many unsteady phenomena (dynamic stall in particular) that need to be accurately captured in order to get an optimal design of the turbine. The current design strategy of the HARVEST cross flow water turbines relies on a dual experimental/numerical strategy; there is however a strong need to increase the use of computations in the design stage for obvious cost and time-to-market reduction reasons. Fast steady models have been previously developed [3] for studying HARVEST turbines both isolated and interacting within so-called farms; their scope is however limited to the estimate of turbine global wake effect and global efficiency. Recently, thanks to the major improvements in computer hardware as well as faster and more accurate algorithms made available in commercial flow solvers, refined unsteady computations of cross-flow water turbines have been made possible using a 3D Unsteady Reynolds-Averaged Navier-Stokes (URANS) approach [2] [78]. However, the computational time associated with such a 3D unsteady application remains so large that a parametric study of the turbine, though needed for an improved design of the machine, remains currently out of reach. Such an observation of excessive computational cost is not specific to the design of cross flow water turbines: it also holds more generally for the design of fluid devices involving *unsteady* flows over complex 3D geometries, such as helicopters rotors for instance, wind turbines, flapping-wing propulsion mechanisms as far as external aerodynamics is concerned but also internal flows within rotor-stator combinations in the context of turbomachinery applications. It is interesting to note the applications that have just been listed involve more specifically *time-periodic* flow fields, responding to a forcing function associated at the macroscopic level with the periodic motion of a body or at least of some body parts through the fluid. Another category of time-periodic problems involves flows with an unsteadiness that is not predetermined by a macroscopic forcing; for instance, the von Kármán wake flows behind bluff bodies falls into this category as well as the prediction of flutter and limit-cycle oscillations. When in operation, the HARVEST turbine yields periodic unsteady flows that

belong to one or the other category : some flow features, like the wake behind the rotational axis, are uncorrelated from the rotational frequency while some others, like the dynamic stall phenomenon, are correlated with the period of rotation and can be stable or unstable.

Usually, the study of these time-periodic flow configurations is treated in the same manner as non-periodic unsteady flows. The so-called dual-time approach represents a well-established way to compute general unsteady flows regardless of their periodicity, with typically second-order accuracy in physical time and the possibility to use large physical time-steps. In the dual-time approach the unsteady field at each step of the physical time marching procedure is obtained as a steady solution with respect to a dual-time step [60] [34]. This dual-time step (DTS) strategy can also be viewed as finding the solution of the steady (with respect to the dual time) governing equations of the flow augmented by a source term corresponding to the discretization of the physical time derivative using typically a second-order Backward Difference Formula (BDF). The numerical methods previously available for steady flows can be readily extended to handle unsteady flows by simply taking into account this source term. A major drawback of the BDF-DTS method for periodic flows is that it requires to compute, typically from an initial rest configuration, the whole transient of the flow before the periodic flow of interest becomes established.

This flaw of the conventional dual-time strategy motivated the development of numerical methods looking directly for the periodic solution of the flow. The time-periodicity of the flow field provides a strong constraint that should indeed be reflected in an efficient numerical method targeted for time-periodic configurations. Taking advantage of the development of the periodic flow solution into a Fourier series, Hall & al [31] introduced an efficient method dedicated to time periodic flows for turbomachinery applications. Following a similar line of thought, Gopinath and Jameson proposed in 2005 the Time Spectral Method (TSM) for external aerodynamics applications [27]. The TSM method transforms the original system of $(2 + d)$ unsteady equations describing the d-dimensional compressible flow field at each time moment into an extended set of $(2N + 1) \times (d + 2)$ equations corresponding to the flow solution at $(2N + 1)$ time moments in the flow period, selected so as to ensure spectral accuracy for the physical time-derivative.

The long-term objective of the present study is to improve the efficiency of the sea turbine numerical design process by replacing the current BDF computations of turbulent flows over HARVEST turbine configurations with a TSM approach. When the present PhD work was initiated, TSM had been already used for a wide range of applications (turbomachinery [21], rotorcraft [10]) but limited to compressible flows. Moreover, all the available studies were performed using structured grid solvers [27, 66, 76, 68]. Having

made the choice of unstructured grids to deal with the possibly complex geometries of a realistic turbine (involving blades, connecting arms between the blades and the rotation axis, hub) and since the targeted HARVEST application involves incompressible flows, the projected application of the TSM approach for a more efficient sea turbine design process required two major steps: the first one was to express and develop the TSM approach in the context of an existing unstructured grid solver for compressible flows (using conventional BDF-DTS time-integration); the second one was to adapt this strategy to an (initially not available) incompressible flow solver. Note this development work has been performed using research codes and not commercial flow solvers; though reasonably complex to perform in a conventional unsteady solver based on a BDF-DTS approach, the coding of the TSM strategy requires nonetheless significant modifications of the solver structure which make crucial the full access to the code source files. As will be explained in the first part of this report, an Arbitrary Lagrangian Eulerian (ALE) strategy was also implemented in the initially available flow solver to describe the motion of the unstructured computational grids. Once the ALE and TSM techniques implemented, validated and assessed in the context of compressible flows, it was decided to extend the approach to incompressible flows using the Artificial Compressibility (AC) method. Indeed, the AC system of conservation laws is formally very close to the compressible Navier-Stokes equations, which considerably simplifies the adaptation of the TSM approach to incompressible flows. The approach combining ALE with TSM is compared with the usual strategy combining ALE and BDF-DTS both from the viewpoint of accuracy and efficiency.
During the course of this PhD, a first attempt to extend the TSM strategy from compressible to incompressible flows has been performed in 2009 by Jameson [35] also using an Artificial Compressibility method but on structured grids. Note however that Jameson reported stability concerns when computing high-frequency pitching airfoils. Very recently (in 2010), an extension of the TSM approach to compressible flow computations on unstructured grids has been presented by Yang and Mavriplis in [77]. To the best of our knowledge, the periodic incompressible flow computations performed with the TSM approach and presented in this work are the first available results of this kind. These results have been presented in an article submitted to the AIAA Journal, reproduced in the appendix E of the present document.
Though the long-term objective of the study is to contribute to the more efficient numerical design of sea turbines, which involves at least 3D URANS computations, it was decided to limit the applications computed in the present work to less complex flows, namely 2D inviscid or viscous laminar flows over airfoils, in order to better assess the impact of the sole TSM strategy (without interference with turbulence modeling issues for instance). Moreover, the limited cost of the 2D configurations also allowed an in-depth assessment of the TSM approach proposed in the present work to speed up the integration of periodic low-speed flows.

Thesis Outline

The present document is divided into three main parts:

- the first part reviews the key numerical ingredients of the conventional unsteady compressible and incompressible flow solvers developed for unstructured grid computations. These baseline solvers include in particular a second-order dual-time strategy for time-integration as well as an ALE formulation allowing to take into account moving grid computations.
- The second part is mostly devoted to the design principles of the Time Spectral Method and includes a first application of the method to a time-dependent heat conduction model problem.
- The third part gathers the results obtained in this work using TSM for external flow applications and proposes a detailed assessment of TSM accuracy and efficiency analysis with respect to a conventional BDF-DTS approach.

The first part is divided into 2 chapters:

- Chapter 1 describes the compressible unsteady flow solver in which an ALE (Arbitrary Eulerian Lagrangian) formulation has been implemented to deal with moving mesh applications. The main numerical ingredients of the unstructured grid solver are briefly reviewed. Two well-established numerical fluxes (ROE and AUSM$^+$) are retained for space-discretization. The time discretization of the Navier-Stokes system of equations, including the ALE treatment and the implicit formulation, is detailed. This compressible solver is validated on inviscid and laminar viscous flows around a moving NACA0012 airfoil.
- Chapter 2 deals with the development of the Artificial Compressibility (AC) method. The required modifications of the ALE compressible solver, such as the adaptation of the Roe scheme to the AC model, are described. The choice of the AC numerical parameters is validated by performing some fixed grid applications: a steady computation of a NACA0015 profile at 4° of incidence and an unsteady computation of a NACA0015 profile at 16° of incidence. Next, the simulation of a pitching and heaving NACA0015 airfoil recently computed and analyzed by Kinsey and Dumas [41] is used to validate the full ALE-BDF-AC laminar solver (that is including the ALE formulation applied to the AC system and solved using BDF-DTS).

The second part is divided into three chapters:

- Chapter 3 is a brief review of the harmonic methods developed in the past 15 years to compute directly the time-periodic solutions of compressible and incompressible

flows. The selection of the TSM approach among this panel of methods is explained as well as the design principles of TSM.

- Chapter 4 describes the adaptation of the TSM to the various numerical treatments presented in the first part of the report, namely: the ALE treatment, the time implicit formulation and the derivation of TSM for the AC system. Some emphasis is put on the implicit TSM treatment since it plays a key role in the overall efficiency of the TSM approach. A methodology allowing to compare the computational costs associated with the TSM and BDF approaches is introduced.

- Chapter 5 is devoted to a first application of the TSM on the linear heat conduction equation. The simplicity of the problem is useful to better understand the TSM concepts and put into practice the implicit formulations presented in the previous chapter. A particular focus is made on the stability of these methods since the amplification factor can be analyzed analytically in that linear case.

The third part is divided into 2 chapters:

- Chapter 6 deals with the application of TSM for compressible flow applications on unstructured grids. The case of a fixed mesh is first treated with a rotating cylinder flow taken from [8]. The moving mesh application is the case of a pitching aerofoil previously computed in Chapter 1 with a conventional BDF-DTS approach. The TSM results obtained for both cases are analyzed and compared to the BDF-DTS reference data.

- Chapter 7 displays two incompressible flow test cases taken from the recent pitching and heaving airfoil study performed by Kinsey and Dumas [41]. Since these cases are distinct from the validation problem previously computed in Chapter 2, some reference BDF simulations of these cases are first performed. TSM computations are then carried out for an increasing number of harmonics N in order to determine the best trade-off between cost and accuracy (both increasing functions of N) and check wether TSM can outperform BDF.

Conclusions on the interest of the TSM approach for performing efficient unsteady flow computations are drawn in the last chapter of the report and future tasks to perform in order to achieve the application of TSM to the numerical design of sea turbines are detailed.

Part I

Unsteady Solver Presentation

Chapter 1

Compressible flow solver

This chapter describes the main features of the unstructured flow solver initially available to compute unsteady compressible flows in fixed grids. A first technical step carried out in the present work was to extend this solver to deal with moving grids in order to be able to treat unsteady problems of the oscillating airfoil type. This extension was performed using a well-established Arbitrary-Lagrangian-Eulerian formulation. The salient features of the solvers are reviewed to better understand how they will be impacted by the development of a TSM approach presented in the second part of the thesis report.

1.1 Governing equations

The Navier-Stokes equations are derived from basic principles of mass, momentum and energy conservation. In its most general form, a conservation law states that the rate of change of a quantity in a control volume must be equal to the net volume of the quantity transported through the control volume's boundaries plus the amount that is created/destroyed inside the control volume.
Let us consider an Arbitrary Lagrangian Eulerian (ALE) formulation where the control volume $\Omega_{(t)}$ (t being the physical time) can move independently from the flow motion and is not attached to the absolute frame of reference either (Fig. 1.1). In this ALE framework, $\Omega_{(t)} \subset \Re^2$ is bounded by a smooth closed surface $\partial\Omega_{(t)}$ of curvilinear abscissa γ which moves with a velocity $\boldsymbol{s}(\boldsymbol{x},t) = s_x(t)\ \boldsymbol{i} + s_y(t)\ \boldsymbol{j}$, where $\boldsymbol{x} = x\ \boldsymbol{i} + y\ \boldsymbol{j}$ denotes the Cartesian coordinates in the absolute frame of reference.
The two-dimensional Navier-Stokes equations for compressible unsteady flows, in the absence of body forces can be expressed in the following integral form:

$$\frac{\partial}{\partial t} \int\limits_{\Omega(t)} \boldsymbol{w}\ d\Omega(t) + \oint\limits_{\partial\Omega(t)} (\boldsymbol{F}^E - \boldsymbol{F}^V) \cdot \boldsymbol{n}\ d\gamma = 0 \tag{1.1}$$

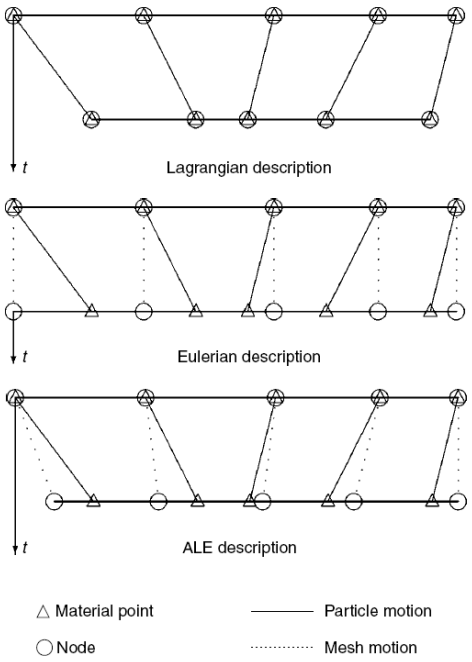

Figure 1.1: Lagrangian, Eulerian and ALE description from [19]

The non-dimensional unknown variable $\boldsymbol{w}$ is the vector of conserved absolute variables, representing the density, momentum and energy.

$$\boldsymbol{w} = \begin{bmatrix} \rho \\ \rho u \\ \rho v \\ \rho E \end{bmatrix}$$

The second term represents the transport of $\boldsymbol{w}$ across the control volume's boundary $\partial\Omega(t)$ where $\boldsymbol{n} = (n_x, n_y)$ is the outward unit normal vector. The convective flux vector $\boldsymbol{F}^E = (\boldsymbol{f}^E, \boldsymbol{g}^E)$ and viscous flux vector $\boldsymbol{F}^V = (\boldsymbol{f}^V, \boldsymbol{g}^V)$ are given by :

$$\boldsymbol{f}^E(\boldsymbol{w}) = \begin{pmatrix} \rho(u - s_x) \\ \rho u(u - s_x) + p \\ \rho v(u - s_x) \\ \rho E(u - s_x) + pu \end{pmatrix}, \qquad \boldsymbol{g}^E(\boldsymbol{w}) = \begin{pmatrix} \rho(v - s_y) \\ \rho u(v - s_y) \\ \rho v(v - s_y) + p \\ \rho E(v - s_y) + pv \end{pmatrix}$$

$$\boldsymbol{f}^V(\boldsymbol{w}) = \frac{1}{Re} \begin{pmatrix} 0 \\ \tau_{xx} \\ \tau_{xy} \\ u\tau_{xx} + v\tau_{xy} - q_x \end{pmatrix}, \qquad \boldsymbol{g}^V(\boldsymbol{w}) = \frac{1}{Re} \begin{pmatrix} 0 \\ \tau_{xy} \\ \tau_{yy} \\ u\tau_{xy} + v\tau_{yy} - q_y \end{pmatrix}$$

where p is the pressure, (u, v) the fluid velocity. $(u - s_x)$, $(v - s_y)$ are the components of the relative velocity of the fluid with respect to the surface velocity of the control volume to take into account the grid motion.
The non-dimensionalization is based upon a representative length scale L (typically the airfoil chord c for airfoil aerodynamic calculations), the free stream velocity $U_\infty = \sqrt{u_\infty^2 + v_\infty^2}$, the free stream density, ρ_∞ and the free stream dynamic viscosity, μ_∞. The pressure is normalized by $\rho_\infty U_\infty^2$ and the Reynolds number is $Re = \rho_\infty U_\infty L/\mu_\infty$.

The viscous flux includes the stress tensor $\overline{\overline{\tau}}$ modelized under Boussinesq assumptions

$$\tau_{xx} = \frac{2}{3}\mu(2\frac{\partial u}{\partial x} - \frac{\partial v}{\partial y}), \quad \tau_{yy} = \frac{2}{3}\mu(2\frac{\partial u}{\partial x} - \frac{\partial v}{\partial y}) \tag{1.2}$$

The heat flux vector q is given by the Fourier law [24] :

$$q_i = -\kappa\frac{\partial T}{\partial i}, \quad i = (x, y)$$

T is the temperature and μ the viscosity which depends on temperature and is given by the Sutherland equation. The coefficient of thermal conductivity κ is given by :

$$\kappa = C_P\frac{\mu}{Pr}$$

where Pr is the Prandtl number and C_P is the specific heat at constant pressure. Closure is provided, for an ideal gas, using the equation of state :

$$p = (\gamma - 1)\rho\left(E - \frac{u_i u_i}{2}\right) \tag{1.3}$$

wheres γ is the ratio of the heat capacity at constant pressure C_P to heat capacity at constant volume C_V (1.4 for air).

1.2 Spatial discretization

1.2.1 Finite Volume formulation on unstructured grids

The integral form of the equations is well adapted to a finite volume formulation, in which case the control volume $\Omega(t)$ represents a cell of the grid. A cell being made up of several faces, the fluxes through these cell faces are calculated to allow the transmission of information from one cell to another. Thus, the method is intrinsically conservative which makes it widely used in CFD.
The Finite Volume method can be applied on structured and unstructured meshes. On the one hand, a structured mesh has a regular connectivity of the grid cells. It is made of quadrangles in 2 dimensions and, thus can be stored into a 2 dimensional array with direct

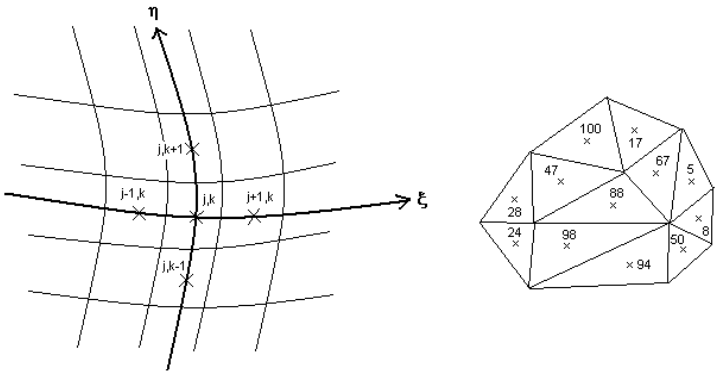

Figure 1.2: Location of cells in structured and unstructured meshes.

addressing. A cell located with indexes (j, k) will always have cells of indexes $(j \pm 1, k)$ and $(j, k \pm 1)$ for neighbors. It makes the computation of fluxes trough faces easier. It is also a method of choice for boundary layer problems because the connectivity regularity serves a particular direction. However, in the case of more complex geometries, one cannot use a single block for the whole geometry and the use of several structured blocks is required. This task is not trivial and can be time-consuming. Mesh refinement is also made more complicated since mesh lines propagate in the refined direction. Therefore, there are zones where mesh is excessively fine and the total cell counts can become prohibitive.
On the other hand, an unstructured mesh is well adapted to complex geometries and allows easy local refinement. It is typically made of triangles in 2D but can also be built from quadrangles or a combination of triangles and quadrangles (hybrid mesh). One of the drawback of an unstructured grid approach lies in the associated memory requirement. Indeed, one needs to know the location of all the neighboring cells for the computation of fluxes in a given cell. However, there is no implicit numbering relationships between cells unlike the case of structured grids. Hence, one needs to handle the mesh connectivity prior to any numerical simulation. It consists, minimally, in :

1. A list of nodes coordinates with their associated faces numbers and normal vector coordinates.

2. A list of cell centers coordinates and their associated cell numbers

3. A list of face numbers with the left and right cells numbers

When integrating the flux on a cell boundary, the contribution of the fluxes on the finite number of faces forming the cell volume are summed up so that :

$$\oint_{\partial\Omega} \boldsymbol{F}(\boldsymbol{w}).\boldsymbol{n}\ d\gamma = \sum_{p} \int_{N_P}^{N_{P+1}} \boldsymbol{F}(\boldsymbol{w}).\boldsymbol{n}\ d\gamma_p \tag{1.4}$$

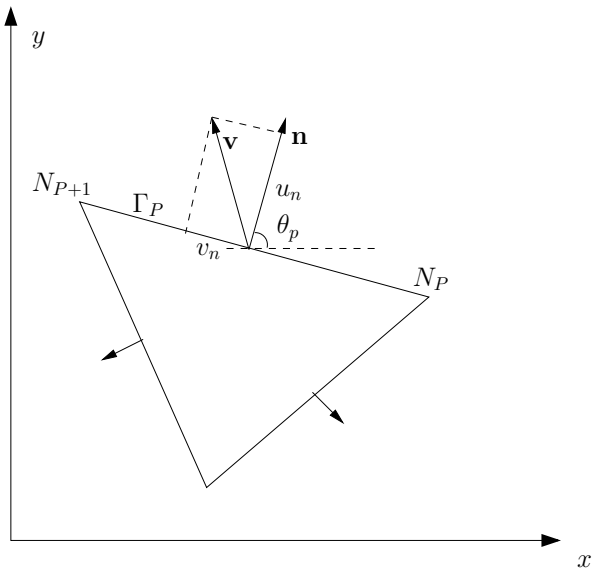

Figure 1.3: Unstructured grid cell.

Using the notations defined in Figure 1.3 and denoting $\boldsymbol{n} = (n_x, n_y) = (\cos(\theta_p), \sin(\theta_p))$, one can rewrite :

$$\int_{N_P}^{N_{P+1}} \boldsymbol{F}(\boldsymbol{w}).\boldsymbol{n}\ d\gamma_p = \int_{N_P}^{N_{P+1}} (\boldsymbol{f}(\boldsymbol{w})\cos(\theta_p) + \boldsymbol{g}(\boldsymbol{w})\sin(\theta_p))\ d\gamma_p \tag{1.5}$$

It can be easily shown that :

$$\boldsymbol{f}(\boldsymbol{w})\cos(\theta_p) + \boldsymbol{g}(\boldsymbol{w})\sin(\theta_p) = T_p^{-1}\boldsymbol{f}(T_p\boldsymbol{w}) = \boldsymbol{f}_n(T_p\boldsymbol{w}) \tag{1.6}$$

with T_p the rotation matrix

$$T_p = \begin{pmatrix} 1 & 0 & 0 & 0 \\ 0 & \cos(\theta_p) & \sin(\theta_p) & 0 \\ 0 & -\sin(\theta_p) & \cos(\theta_p) & 0 \\ 0 & 0 & 0 & 1 \end{pmatrix}$$

and T_p^{-1} its inverse

$$T_p^{-1} = \begin{pmatrix} 1 & 0 & 0 & 0 \\ 0 & \cos(\theta_p) & -\sin(\theta_p) & 0 \\ 0 & \sin(\theta_p) & \cos(\theta_p) & 0 \\ 0 & 0 & 0 & 1 \end{pmatrix}$$

In practise, a one dimensional convective flux $\boldsymbol{f}_n^E$ associated with the outward normal face direction $\boldsymbol{n}$ is used

$$\boldsymbol{F}^E(\boldsymbol{w}) \cdot \boldsymbol{n} = \boldsymbol{f}_n^E(\boldsymbol{w}_n) \tag{1.7}$$

where

$$\boldsymbol{f}_n^E = \begin{pmatrix} \rho(u_n - s_n) \\ \rho(u_n - s_n)u + pn_x \\ \rho(u_n - s_n)v + pn_y \\ \rho(u_n - s_n)E + pu_n \end{pmatrix} = \begin{pmatrix} \rho u_n \\ \rho u_n u + pn_x \\ \rho u_n v + pn_y \\ \rho u_n E + pu_n \end{pmatrix} - s_n \cdot \boldsymbol{w}, \quad \text{and} \quad \boldsymbol{w}_n = T_p \boldsymbol{w} = \begin{bmatrix} \rho \\ \rho u_n \\ \rho v_n \\ \rho E \end{bmatrix}$$

1.2.2 Numerical flux

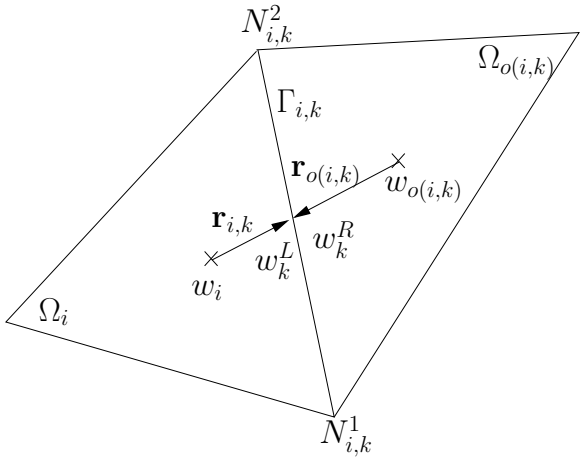

Figure 1.4: Notation definitions for numerical flux expression.

Applying Eq. (1.1) on a given cell Ω_i, introducing the average value $\overline{\boldsymbol{w}}$ of $\boldsymbol{w}$ over the cell and decomposing the flux balance as the sum of fluxes through each face $\Gamma_{i,k}$ of cell Ω_i leads to:

$$\frac{\partial}{\partial t}(\overline{\boldsymbol{w}_i}|\Omega_i|) + \sum_k \int_{\Gamma_{i,k}} (\boldsymbol{F}^E - \boldsymbol{F}^V) \cdot \boldsymbol{n} \; d\gamma \;=\; 0 \tag{1.8}$$

where $|\Omega_i|$ is the surface of the i-th grid cell Ω_i. The normal physical flux $(\boldsymbol{F}^E - \boldsymbol{F}^V) \cdot \boldsymbol{n}$ through the face $\Gamma_{i,k}$ of length $|\Gamma_{i,k}|$ is approximated by the numerical flux $\mathcal{H} = \mathcal{H}^E - \mathcal{H}^V$ computed at the center i,k of the face $\Gamma_{i,k}$:

$$\int_{\Gamma_{i,k}} (\boldsymbol{F}^E - \boldsymbol{F}^V) \cdot \boldsymbol{n} \; d\gamma \;= \left(\mathcal{H}^E_{i,k} - \mathcal{H}^V_{i,k}\right) |\Gamma_{i,k}| + O(h^p) \tag{1.9}$$

where h denotes a typical grid length. The space accuracy order p will depend on the choice of polynomial reconstruction used for the conservative variable inside each grid cell; a linear reconstruction will be systematically used in this work leading to second-order accuracy in space. For this reason and without loss of accuracy, the average state in cell i is replaced by the state at cell center, denoted $\boldsymbol{w}_i$ from now on.

Inviscid fluxes

Two well-established numerical inviscid fluxes have been used in this work : the ROE scheme [61] and the AUSM$^+$ scheme [45]. They are both briefly described in the context of their ALE formulation.

ROE flux The Roe approximate Riemann solver [61] approximates the inviscid physical flux using the following numerical flux formula $\mathcal{H}_{i,k}^E$:

$$\mathcal{H}_{i,k}^E = \frac{1}{2}(\boldsymbol{F}^E(\boldsymbol{w}_k^L)\cdot\boldsymbol{n}_{i,k} + \boldsymbol{F}^E(\boldsymbol{w}_k^R)\cdot\boldsymbol{n}_{i,k}) + \frac{1}{2}Q_{i,k}^E(\boldsymbol{w}_k^L - \boldsymbol{w}_k^R) \tag{1.10}$$

where $\boldsymbol{w}^{L/R}$ are the states, respectively, on the left and right side of the k^{th} interface $\Gamma_{i,k}$ of cell Ω_i, $\boldsymbol{Q}^E$ is the Roe numerical dissipation matrix given by

$$\boldsymbol{Q}^E = |\boldsymbol{A}^E n_x + \boldsymbol{B}^E n_y| = |\boldsymbol{J}_\perp^E|$$

where $\boldsymbol{n} = (n_x, n_y)$ and $\boldsymbol{A}^E$, $\boldsymbol{B}^E$ are the inviscid flux Jacobian matrices: $\boldsymbol{A}^E = d\boldsymbol{f}^E/d\boldsymbol{w}$, $\boldsymbol{B}^E = d\boldsymbol{g}^E/d\boldsymbol{w}$. The expressions of these Jacobian matrices are provided in Appendix A.1; the following expression is eventually obtained for the normal Jacobian matrix $\boldsymbol{J}_\perp^E$:

$$\boldsymbol{J}_\perp^E = \begin{pmatrix} V_n - s_n & \rho n_x & \rho n_y & 0 \\ 0 & V_n - s_n & 0 & n_x/\rho \\ 0 & 0 & V_n - s_n & n_y/\rho \\ 0 & \rho c^2 n_x & \rho c^2 n_y & V_n - s_n \end{pmatrix}$$

where $V_n = u\ n_x + v\ n_y$ and $s_n = s_x n_x + s_y n_y$ are respectively the flow normal velocity and the grid normal velocity.

This Jacobian matrix can be also expressed as $\boldsymbol{J}_\perp^E = \boldsymbol{T}\boldsymbol{\Lambda}^E\boldsymbol{T}^{-1}$ with $\boldsymbol{\Lambda}^E$ the diagonal matrix containing the real eigenvalues of the hyperbolic system (1.1). The Roe dissipation matrix is eventually computed as

$$\boldsymbol{Q}_{i,k}^E = \boldsymbol{T}_{i,k}|\boldsymbol{\Lambda}_{i,k}^E|T_{i,k}^{-1}$$

with the so-called "Roe average" state $\widetilde{\boldsymbol{w}}_{i,k}$ given by

$$
\begin{aligned}
a &= \sqrt{\frac{\rho^R}{\rho^L}} \\
\widetilde{\rho} &= a \cdot \rho^L \\
\widetilde{u} &= \frac{u^L + a u^R}{1+a} \\
\widetilde{v} &= \frac{v^L + a v^R}{1+a} \\
\widetilde{H} &= \frac{H^L + a H^R}{1+a} \\
\widetilde{c} &= \sqrt{\frac{\gamma - 1}{\widetilde{H} - 1/2\ (\widetilde{u}^2 + \widetilde{v}^2)}}
\end{aligned}
$$

and with the grid velocity s_n, computed at the face centroid. The Roe average is such that $(\boldsymbol{f}_n^E(\boldsymbol{w}_{nk}^L) - \boldsymbol{f}_n^E(\boldsymbol{w}_{nk}^R)) = \boldsymbol{J}_\perp^E(\widetilde{\boldsymbol{w}}_{i,k}) \cdot (\boldsymbol{w}_k^L - \boldsymbol{w}_k^R)$, which allows to ensure Rankine-Hugoniot relationships at the discrete level hence the correct representation of weak solutions.
Using the Roe-average property, Equation (1.10) can also be recast in the form :

$$
\mathcal{H}_{i,k}^E = \frac{1}{2}\left(\boldsymbol{f}_n^E(\boldsymbol{w}_{nk}^L) + \boldsymbol{f}_n(\boldsymbol{w}_{nk}^R)\right) + \frac{1}{2}\,\boldsymbol{T}_{i,k}|\mathrm{sgn}(\boldsymbol{\Lambda}_{i,k}^E)|\boldsymbol{T}_{i,k}^{-1}(\boldsymbol{f}_n^E(\boldsymbol{w}_{nk}^L) - \boldsymbol{f}_n^E(\boldsymbol{w}_{nk}^R)) \qquad (1.11)
$$

making clear the upwinding introduced by the Roe scheme. The numerical flux (1.11), when coupled with a linear representation of the variable w inside each cell (see below), offers an accurate and robust approximation of compressible flows for a large range of regimes. Note however the matrix numerical dissipation associated with the Roe scheme makes it rather expensive to compute, which is a known weakness of the method.

AUSM$^+$ Alternatively, Liou and Steffen [46] have proposed the Advection Upstream Splitting Method (AUSM) and its improved version AUSM$^+$ [45]. The potential advantage of this upwind scheme with respect to the Roe scheme is its simplicity, since it manipulates scalar quantity only when introducing numerical dissipation through upwinding. The drawback could be the use of several tuning parameters in the method but in practice these parameters have been given recommended values once for all. The ALE derivation of the AUSM$^+$ flux can be found in [17], [49]; its application to compute unsteady flows on moving meshes has also been successfully performed in [49] for instance.
The basic idea of Liou and Steffen [46] is to recognize convection and acoustic waves as

two distinct processes and consist in treating them separately:

$$\boldsymbol{f}_n^E = \boldsymbol{f}_n^c + \boldsymbol{f}_n^p, \tag{1.12}$$

where

$$\boldsymbol{f}_n^c = \begin{bmatrix} \rho(V_n - s_n) \\ \rho(V_n - s_n)u \\ \rho(V_n - s_n)v \\ \rho(V_n - s_n)H + ps_n \end{bmatrix}, \qquad \boldsymbol{f}_n^p = \begin{bmatrix} 0 \\ pn_x \\ pn_y \\ 0 \end{bmatrix}$$

One can rewrite

$$\boldsymbol{f}_n^c = M \cdot c \begin{bmatrix} \rho \\ \rho u \\ \rho v \\ \rho H \end{bmatrix}, \qquad \boldsymbol{f}_n^p = \begin{bmatrix} 0 \\ pn_x \\ pn_y \\ ps_n \end{bmatrix}$$

Compared to the classical formulation of AUSM for non-moving mesh, the Mach number M is based on the relative normal velocity $M = (V_n - s_n)/c$ and c is the speed of sound. Moreover, the additional term ps_n appearing in the energy equation can be splitted as a pure pressure term because the interface velocity has the same value on the left and on the right of the interface.
The numerical fluxes $\mathcal{H}_{i,k}^c$ and $\mathcal{H}_{i,k}^p$ that approximate the physical fluxes $\boldsymbol{f}_n^c$ and $\boldsymbol{f}_n^p$ at the k^{th} interface $\Gamma_{i,k}$ of cell Ω_i read

$$\mathcal{H}_{i,k}^c(\boldsymbol{w}_k^L, \boldsymbol{w}_k^R) = m_k \; c_k \; \Phi_k; \qquad \boldsymbol{\Phi}_k = \begin{bmatrix} \rho \\ \rho u \\ \rho v \\ \rho H \end{bmatrix} \tag{1.13}$$

$$\mathcal{H}_{i,k}^p(\boldsymbol{w}_k^L, \boldsymbol{w}_k^R) = p_k \begin{bmatrix} 0 \\ n_x \\ n_y \\ s_n \end{bmatrix} \tag{1.14}$$

Let us now specify how to express $m_k, c_k, \boldsymbol{\Phi}_k$ and p_k at the interface k.
The design of the numerical flux $\mathcal{H}_{i,k}^c$ is based on an upwind discretization according to the flow direction whereas the construction of $\mathcal{H}_{i,k}^p$ is obtained by upwind discretization following acoustic considerations.

Stage 1. Upwind discretization of the convective term $\boldsymbol{\Phi}_k$

$$\boldsymbol{\Phi}_k = \begin{cases} \boldsymbol{\Phi}^L & \text{if } m_k \geq 0 \\ \boldsymbol{\Phi}^R & \text{otherwise} \end{cases} \tag{1.15}$$

As a consequence, the convective flux reads

$$\mathcal{H}^c_{i,k}(\boldsymbol{w}^L_k, \boldsymbol{w}^R_k) = c_k \left[\frac{1}{2} m_k (\boldsymbol{\Phi}^L + \boldsymbol{\Phi}^R) - \frac{1}{2} |m_k| (\boldsymbol{\Phi}^R - \boldsymbol{\Phi}^L) \right] \tag{1.16}$$

Stage 2. Treatment of the characteristics m_k, p_k and c_k The second idea of the AUSM scheme is that an appropriate Mach number at the interface m_k should be made of a contribution $\mathcal{M}^+(M^L)$ associated to the wave coming from the left at wave speed $M+1$ and a contribution $\mathcal{M}^-(M^R)$ associated to the wave coming from the right at wave speed $M-1$. More precisely, we write

$$m_k = \mathcal{M}^+_{(4,\beta)}(M^L) + \mathcal{M}^-_{(4,\beta)}(M^R) \tag{1.17}$$

where $M^L = (V^L_n - s_n)/c_k$ et $M^R = (V^R_n - s_n)/c_k$.
Likewise, the pressure at the interface is written

$$p_k = \mathcal{P}^+_{(5,\alpha)}(M^L)\ p^L + \mathcal{P}^-_{(5,\alpha)}(M^R)\ p^R \tag{1.18}$$

where $\mathcal{P}^\pm$ are the split pressure functions associated respectively with the left and right waves
The numerical speed of sound at the interface c_k is computed by the simple average formula

$$c_k = \frac{1}{2}(c^L + c^R) \tag{1.19}$$

Stage 3. Construction of the split functions $\mathcal{M}^\pm_{(4,\beta)}$ and $\mathcal{P}^\pm_{(5,\alpha)}$ Velocity and pressure at the interface are polynomial function of $(M \pm 1)$ derived from Van Leer flux-vector splitting. The split Mach numbers are defined as :

$$\mathcal{M}^\pm_{(1)} = \frac{1}{2}(M \pm |M|) \tag{1.20}$$

$$\mathcal{M}^\pm_{(2)} = \begin{cases} \mathcal{M}^\pm_{(1)}(M) & \text{if } |M| \geq 1 \\ \pm\frac{1}{4}(M \pm 1)^2 & \text{otherwise} \end{cases} \tag{1.21}$$

$$\mathcal{M}^\pm_{(4,\beta)} = \begin{cases} \mathcal{M}^\pm_{(1)}(M) & \text{if } |M| \geq 1 \\ \mathcal{M}^\pm_{(2)}(M) \left[1 \mp 16\ \beta \mathcal{M}^\mp_{(2)}(M) \right] & \text{otherwise} \end{cases} \tag{1.22}$$

$$\mathcal{P}^\pm_{(5,\alpha)} = \begin{cases} \frac{1}{M}\mathcal{M}^\pm_{(1)}(M) & \text{if } |M| \geq 1 \\ \pm\mathcal{M}^\pm_{(2)}(M) \left[(2 \mp M) - 16\ \alpha M \mathcal{M}^\mp_{(2)}(M) \right] & \text{otherwise} \end{cases} \tag{1.23}$$

with $\alpha = 3/16$ and $\beta = 1/8$. In the present study, there will be no specific analysis of the influence of the numerical flux formula on the numerical solution, be it obtained by a

time-marching approach or the Time Spectral Method. The Roe scheme and the AUSM+ scheme will be indifferently used, keeping in mind the AUSM+ scheme implementation is slightly less expensive than the Roe scheme's one. Note also some comparisons with the commercial solver Fluent have been performed throughout this work and since this solver relies on these same numerical fluxes, it was found interesting to also implement both of them in the research code used in this thesis to allow code-to-code comparison with the same space discretization on the same grid.

High order extension If one uses the cell center values of the left (i) and right ($o(i,k)$) cells for the left and right state at interface $\Gamma_{i,k}$, the previous scheme are only first order accurate in space. This is why, a MUSCL variable reconstruction approach [5] [18] is used. The states at face centers i,k are linearly reconstructed from the cell center values in the cells i and $o(i,k)$ sharing the face $\Gamma_{i,k}$ and the cell gradients $\nabla \boldsymbol{w}$ in each of these cells

$$\begin{cases} \boldsymbol{w}_k^L = \boldsymbol{w}_i + \nabla \boldsymbol{w}_i \cdot \boldsymbol{r}_{i,k} \\ \boldsymbol{w}_k^R = \boldsymbol{w}_{o(i,k)} + \nabla \boldsymbol{w}_{o(i,k)} \cdot \boldsymbol{r}_{o(i,k)} \end{cases} \tag{1.24}$$

where $\boldsymbol{r}_{i,k}$ (resp. $\boldsymbol{r}_{o(i,k)}$) denotes the vector extending from the cell center i (resp. $o(i,k)$) to the center of the interface $\Gamma_{i,k}$. The gradient $\nabla \boldsymbol{w}_i$ is computed at each cell center i using a least-square formula applied on a fixed spatial support including the neighboring cells sharing at least a node with cell i [18].

Viscous flux

The viscous numerical flux $\mathcal{H}_{i,k}^V$ approximating the diffusive physical flux is obtained from the arithmetic average of the viscous fluxes computed at the vertices $N_{i,k}^1$,$N_{i,k}^2$ of face $\Gamma_{i,k}$ (see Fig. 1.4).

$$\mathcal{H}_{i,k}^V = \frac{1}{2}\left(\boldsymbol{F}^V(\boldsymbol{w}_{N_{i,k}^1}, \nabla \boldsymbol{w}_{N_{i,k}^1}) + \boldsymbol{F}^V(\boldsymbol{w}_{N_{i,k}^2}, \nabla \boldsymbol{w}_{N_{i,k}^2})\right) \cdot \boldsymbol{n}_{i,k} \tag{1.25}$$

The value of $\boldsymbol{w}$ at a grid node N is computed from a set of cell-centered values in the cells sharing this node and the value of $\nabla \boldsymbol{w}$ at N is obtained from a least-square formula applied using the same set of cell-centered values.

1.2.3 Conclusion on spatial discretization

Whatever the numerical flux retained, the space discretized integral form of the Navier Stokes equations will be eventually written:

$$\frac{\partial}{\partial t}(\boldsymbol{w}_i|\Omega_i|) + \sum_k (\mathcal{H}_{i,k}^E - \mathcal{H}_{i,k}^V)|\Gamma_{i,k}| = 0 \tag{1.26}$$

The numerical inviscid flux balance or residual will be denoted from now on :

$$\mathcal{R}_i^E(\boldsymbol{w}, \boldsymbol{x}, \boldsymbol{s}) = \frac{1}{|\Omega_i|} \sum_k \mathcal{H}_{i,k}^E \, |\Gamma_{i,k}| \tag{1.27}$$

where, in the context of the ALE formulation, the dependence of this flux balance on the mesh position $\boldsymbol{x}$ and velocity $\boldsymbol{s}$ has been made explicit. Similarly, the viscous flux balance or residual will be denoted:

$$\mathcal{R}_i^V(\boldsymbol{w}, \boldsymbol{x}) = \frac{1}{|\Omega_i|} \sum_k \mathcal{H}_{i,k}^V \, |\Gamma_{i,k}| \tag{1.28}$$

with an explicit dependence on the grid position $\boldsymbol{x}$. Since the present work will focus on rigid body motion for the grid, the cell surface $|\Omega_i|$ will stay constant over time and the semi-discrete form (1.26) of the ALE compressible system can also be expressed as

$$\frac{\partial \boldsymbol{w}_i}{\partial t} + \mathcal{R}_i^E(\boldsymbol{w}, \boldsymbol{x}, \boldsymbol{s}) = \mathcal{R}_i^V(\boldsymbol{w}, \boldsymbol{x}) \tag{1.29}$$

1.3 Time discretization

1.3.1 Time discretization including ALE treatment

Moving mesh strategy When dealing with moving airfoils in the ALE reference frame, two main approaches can be considered for taking into account the grid motion. The first approach is the rigid body technique in which all grid points have the same motion as the airfoil. The initial quality of the mesh is preserved but unsteady boundary conditions must be implemented that include the grid velocities. A drawback of this approach is that, for high frequency pitching movements, relative velocity of in cells away from the center of rotation may become very large leading to excessive numerical dissipation. The second approach deforms the inner cells of the grid to conform to the instantaneous position of the airfoil while the outer boundaries are kept fixed. Deformation can be performed using methods based on spring analogy, which involve either the solution of a large system of equations for the displacements of nodes [55, 6] and/or a local remeshing at each physical time step of the calculation [48, 32]. In all these methods, a geometric conservation law must also be satisfied to avoid volume discretization errors [42]. The Chimera technique is yet another alternative for dealing with moving bodies that makes use of independently meshed overlapping zones, typically a grid zone attached to the body and a grid zone for the background domain [7, 39]. While the deforming grid approach is required for aeroelastic studies or problems involving moving bodies within fixed multi-block geometries, it can be avoided for the simple heaving and pitching airfoils cases treated in this study. Consequently, a simple rigid body approach is retained with the mesh position $\boldsymbol{x}$ directly derived from the law of motion and the grid velocity $\boldsymbol{s}$ computed using the simple

analytical relationship

$$\boldsymbol{s}(t) = \boldsymbol{\Omega}(t) \wedge (\boldsymbol{x}(t) - \boldsymbol{x}_c(t)) + \boldsymbol{t} \tag{1.30}$$

where $\boldsymbol{\Omega}$ is the rotational velocity vector, $\boldsymbol{x}_c$ the center of rotation and $\boldsymbol{t}$ the translation velocity vector.

Geometric Conservation Law An important requirement on transient simulations in moving meshes is that they should satisfy the so-called geometric conservation law. This property requires that the equations should be able to predict exactly the behavior of a uniform flow in the moving grid. Mathematically, this requirement reads

$$\frac{\mathrm{d}}{\mathrm{d}t} \int\limits_{\Omega(t)} d\Omega - \oint\limits_{\partial\Omega(t)} \boldsymbol{s}.\boldsymbol{n} d\gamma = 0 \tag{1.31}$$

Equation (1.31) is known as the continuous Geometric Conservation Law (GCL). When this equation is integrated between the times t^n et t^{n+1}, the new numerical equation that must be verified is

$$\int\limits_{t^n}^{t^{n+1}} \frac{\mathrm{d}}{\mathrm{d}t} \int\limits_{\Omega(t)} d\Omega \; dt = \int\limits_{t^n}^{t^{n+1}} \oint\limits_{\partial\Omega(t)} \boldsymbol{s}.\boldsymbol{n} d\gamma \; dt \tag{1.32}$$

This new equation (1.32), known as the discrete GCL states that the change in area of cell i between the times t^n and t^{n+1} must be equal to the area swept by the faces animated by a velocity $\boldsymbol{s}$ during the time step $\Delta t = t^{n+1} - t^n$.

The left hand side of equation (1.32) reduces to zero in the case of a rigid body motion of the grid. To evaluate the right hand side, we make use of the Stokes's theorem to write

$$\oint\limits_{\partial\Omega(t)} \boldsymbol{s}.\boldsymbol{n} d\gamma = \int\limits_{\Omega(t)} \nabla \cdot \boldsymbol{s} \; d\Omega$$

and since $\nabla \cdot \boldsymbol{s} = \mathrm{div}(\boldsymbol{s}) = 0$ given the analytic expression of the grid velocity (Eq. 1.30), the GCL is automatically satisfied for a rigid-body motion of the grid.

Time scheme Using a second-order backward difference formula (BDF) for the physical time-derivative in (2.5) yields:

$$\boldsymbol{K} \frac{\left(\frac{3}{2}\boldsymbol{w}_i^{n+1} - 2\boldsymbol{w}_i^n + \frac{1}{2}\boldsymbol{w}_i^{n-1}\right)}{\Delta t} + \mathcal{R}_i^E\left(\boldsymbol{w}^{n+1}, \boldsymbol{x}^{n+1}, \boldsymbol{s}^{n+1}\right) = \mathcal{R}_i^V\left(\boldsymbol{w}^{n+1}, \boldsymbol{x}^{n+1}\right) \tag{1.33}$$

which leads to second-order accuracy in physical time over fixed grids as long as the residuals are computed at time-level $n+1$.

1.3.2 Pseudo time marching technique

An unsteady solution of equation (1.33) is found using the dual time stepping method to overcome the lack of numerical efficiency of the global time stepping approach. For each physical time step, a solution for the unknown $\boldsymbol{w}_i^{n+1}$ is sought as a steady solution with respect to the dual time τ.

$$\frac{\partial}{\partial \tau_i}(\boldsymbol{w}_i^{n+1}) + \frac{\left(\frac{3}{2}\boldsymbol{w}_i^{n+1} - 2\boldsymbol{w}_i^{n} + \frac{1}{2}\boldsymbol{w}_i^{n-1}\right)}{\Delta t} + \mathcal{R}_i\left(\boldsymbol{w}^{n+1}\right) = 0 \tag{1.34}$$

with the full residual $\mathcal{R}$ defined by $\mathcal{R}_i\left(\boldsymbol{w}^{n+1}\right) = \mathcal{R}_i^E\left(\boldsymbol{w}^{n+1}\right) - \mathcal{R}_i^V\left(\boldsymbol{w}^{n+1}\right)$, where the dependence on the grid position and velocity has been omitted for the sake of clarity.
We use a first order approximation for the dual-time derivative (which will vanish at steady state anyway) . The Euler explicit formulation in dual time of equation (1.34) reads:

$$\frac{\boldsymbol{w}_i^{n,m+1} - \boldsymbol{w}_i^{n,m}}{\Delta \tau_i^{n,m}} + \frac{\left(\frac{3}{2}\boldsymbol{w}_i^{n,m} - 2\boldsymbol{w}_i^{n} + \frac{1}{2}\boldsymbol{w}_i^{n-1}\right)}{\Delta t} + \mathcal{R}_i(\boldsymbol{w}^{n,m}) = 0 \tag{1.35}$$

where $\boldsymbol{w}^{n,m}$ is the fictitious state at the m^{th} subiteration on τ performed between the n^{th} and $(n+1)^{th}$ physical time-levels. The initial fictitious state at each physical time-level is chosen as $\boldsymbol{w}^{n,0} = \boldsymbol{w}^n$ and the new physical state is defined as $\boldsymbol{w}^{n+1} = \boldsymbol{w}^{n,m_{max}}$ with m_{max} the number of sub-iterations on τ needed to achieve steady-state convergence of (1.35).

1.3.3 Stability

In the case of unsteady simulation, the physical time step Δt is usually restricted by the desired accuracy. Moreover, the explicit scheme of equation (1.35) is submitted to a restrictive CFL condition on the time step $\Delta\tau$. Indeed, if we consider the following steady-state discretized equation :

$$\frac{\boldsymbol{w}_i^{m+1} - \boldsymbol{w}_i^{m}}{\Delta \tau_i^{m}} + \mathcal{R}_i(\boldsymbol{w}^{m}) = 0 \tag{1.36}$$

$\mathcal{R}_i$ is linearized and leads to the following approximation :

$$\boldsymbol{w}_i^{m+1} \approx \left(\boldsymbol{I_d} - \boldsymbol{J}_i^m \, \frac{\Delta \tau_i^m}{|\Omega_i|}\right) \boldsymbol{w}_i^m \tag{1.37}$$

where $\boldsymbol{J}_i^m$ is the Jacobian of the spatial operator $\mathcal{R}_i$ at iteration m. A sufficient condition for the stability of this approximate explicit scheme can be expressed as:

$$\frac{||\lambda_i^m||\Delta \tau_i^m}{|\Omega_i|} \leq 1 \tag{1.38}$$

where $||\lambda_i^m||$ is the spectral radius of $\boldsymbol{J}_i^m$.
Therefore, we define the pseudo time step as:

$$\Delta\tau_i^m = \mathrm{CFL}\frac{|\Omega_i|}{||\lambda_i^m||} \tag{1.39}$$

where the CFL (Courant-Friedrichs-Lewy) number is a numerical parameter that is set by the user. For instance, the convective pseudo time step reads:

$$\Delta\tau_i^m = \mathrm{CFL}\frac{|\Omega_i|}{\max(U_i^m - S_i + c, U_i^m - S_i - c)} \tag{1.40}$$

in agreement with the expression of the convective Jacobian eigenvalues (see Eq. (A.6)). U_i and S_i are the values of respectively the velocity magnitude and grid velocity magnitude at the center of the cell i.
Equation (1.38) imposes a restrictive condition on the CFL. In practice, a viscous pseudo time step is also computed, based on the viscous Jacobian spectral radius and select the minimum of both the convective and viscous pseudo time steps.

1.4 Implicit method

In order to get free of the CFL limitation of the explicit scheme, an implicit dual-time integration is used, which results in the following scheme :

$$\frac{\Delta\boldsymbol{w}_i^{n,m}}{\Delta\tau_i^{n,m}} = -\mathcal{R}_i\left(\boldsymbol{w}^{n,m+1}\right) - \frac{\left(\frac{3}{2}\boldsymbol{w}_i^{n,m+1} - 2\boldsymbol{w}_i^n + \frac{1}{2}\boldsymbol{w}_i^{n-1}\right)}{\Delta t} = -\mathcal{R}_i^t\left(\boldsymbol{w}^{n,m+1}\right) \tag{1.41}$$

with $\boldsymbol{w}^{n,m+1} = \boldsymbol{w}^{n,m} + \Delta\boldsymbol{w}^{n,m}$. Since the solution accuracy in physical time and space does not depend on the dual-time increment $\Delta\boldsymbol{w}^{n,m}$ which goes to zero at steady-state on τ, the full residual $\mathcal{R}_i^t\left(\boldsymbol{w}^{n,m+1}\right)$ can be expanded as :

$$\mathcal{R}_i^t\left(\boldsymbol{w}^{n,m+1}\right) = \mathcal{R}_i^t\left(\boldsymbol{w}^{n,m}\right) + \frac{3}{2}\frac{\Delta\boldsymbol{w}_i^{n,m}}{\Delta t} + \frac{1}{|\Omega_i|}\sum_k \left(\Delta\mathcal{H}_{i,k}^{(i)}\right)^{n,m} |\Gamma_{i,k}| \tag{1.42}$$

where $(\Delta\mathcal{H}_{i,k}^{(i)})^{n,m} = \mathcal{H}^{(i)^{n,m+1}} - \mathcal{H}^{(i)^{n,m}}$ and $\mathcal{H}^{(i)} = \mathcal{H}^{E(i)} - \mathcal{H}^{V(i)}$ denotes the numerical flux formula retained in the implicit stage.

1.4.1 Matrix Free Implicit treatment

A way to reduce unit cost and memory requirement is to develop implicit treatments that do not rely on full flux Jacobian matrices usually introduced when linearizing the explicit stage. Since the implicit stage vanishes at steady-state this implicit numerical flux formula does not impact the overall accuracy. However, the simplifications that can be introduced

in the implicit stage linearization are likely to induce a loss of intrinsic efficiency which will have to be balanced through a lower unit cost, so as to preserve the global efficiency [47] [48].

Simplified inviscid implicit stage Following [36], [47], [48] the inviscid numerical flux $\mathcal{H}^{E(i)}$ appearing in the implicit stage is simply computed using the first-order Rusanov numerical flux:

$$\mathcal{H}_{i,k}^{E(i)} = \frac{1}{2}(\boldsymbol{F}_i^E \cdot \boldsymbol{n}_{i,k} + \boldsymbol{F}_{o(i,k)}^E \cdot \boldsymbol{n}_{i,k}) + \frac{1}{2}\rho(\boldsymbol{J}_\perp^E)_{i,k}(\boldsymbol{w}_i - \boldsymbol{w}_{o(i,k)}) \tag{1.43}$$

where $\rho(\boldsymbol{J}_\perp^E)_{i,k}$ is the spectral radius of the inviscid Jacobian matrix $\boldsymbol{J}_\perp^E$ computed at the center of face $\Gamma_{i,k}$
The linearization of the time increment of this implicit numerical flux leads to the following approximation

$$(\Delta\mathcal{H}^{E(i)})_{i,k}^{n,m} = \frac{1}{2}((\Delta\boldsymbol{F}_i^E)^{n,m} \cdot \boldsymbol{n}_{i,k} + (\Delta\boldsymbol{F}_{o(i,k)}^E)^{n,m} \cdot \boldsymbol{n}_{i,k}) + \frac{1}{2}\rho(\boldsymbol{J}_\perp^E)_{i,k}^{n,m}(\Delta\boldsymbol{w}_i^{n,m} - \Delta\boldsymbol{w}_{o(i,k)}^{n,m}) \tag{1.44}$$

The resulting contribution of the implicit inviscid numerical flux balance eventually reads

$$\sum_k (\Delta\mathcal{H}^{E(i)})_{i,k}^{n,m} = \frac{1}{2}\left[\sum_k (\Delta\boldsymbol{F}_{o(i,k)}^E)^{n,m} \cdot \boldsymbol{n}_{i,k} + \sum_k \rho(\boldsymbol{J}_\perp^E)_{i,k}^{n,m}(\Delta\boldsymbol{w}_i^{n,m} - \Delta\boldsymbol{w}_{o(i,k)}^{n,m})\right] |\Gamma_{i,k}| \tag{1.45}$$

since

$$\sum_k (\Delta\boldsymbol{F}_i^E)^{n,m} \cdot \boldsymbol{n}_{i,k})|\Gamma_{i,k}| = (\Delta\boldsymbol{F}_i^E)^{n,m} \cdot \sum_k \boldsymbol{n}_{i,k}|\Gamma_{i,k}| = 0$$

Simplified viscous implicit stage The time-increment of the physical viscous flux normal to a face can be linearized as follows:

$$\begin{aligned}\Delta(\boldsymbol{F}^V) \cdot \boldsymbol{n} = {} & \Delta(\boldsymbol{f}^V(\boldsymbol{w}, \nabla\boldsymbol{w}))n_x + \Delta(\boldsymbol{g}^V(\boldsymbol{w}, \nabla\boldsymbol{w}))n_y \\ & + [(\boldsymbol{A}_0^V)\Delta\boldsymbol{w} + (\boldsymbol{A}_1^V)\Delta\boldsymbol{w}_x + (\boldsymbol{A}_2^V)\Delta\boldsymbol{w}_y]n_x \\ & + [(\boldsymbol{B}_0^V)\Delta\boldsymbol{w} + (\boldsymbol{B}_1^V)\Delta\boldsymbol{w}_x + (\boldsymbol{B}_2^V)\Delta\boldsymbol{w}_y]n_y\end{aligned}$$

where the viscous Jacobian matrices have been introduced: $\boldsymbol{A}_0^V = \dfrac{\partial \boldsymbol{f}^V}{\partial \boldsymbol{w}}$, $\boldsymbol{A}_1^V = \dfrac{\partial \boldsymbol{f}^V}{\partial \boldsymbol{w}_x}$, $\boldsymbol{A}_2^V = \dfrac{\partial \boldsymbol{f}^V}{\partial \boldsymbol{w}_y}$ and similarly $\boldsymbol{B}_0^V = \dfrac{\partial \boldsymbol{g}^V}{\partial \boldsymbol{w}}$, $\boldsymbol{B}_1^V = \dfrac{\partial \boldsymbol{g}^V}{\partial \boldsymbol{w}_x}$, $\boldsymbol{B}_2^V = \dfrac{\partial \boldsymbol{g}^V}{\partial \boldsymbol{w}_y}$.

The partial derivatives $\boldsymbol{w}_x$, $\boldsymbol{w}_y$ with respect to the x and y space-directions are related to the partial derivatives $\boldsymbol{w}_\perp$, $\boldsymbol{w}_\parallel$ with respect to the (local) normal and tangential directions relative to a face by the equalities $\boldsymbol{w}_x = \boldsymbol{w}_\perp n_x - \boldsymbol{w}_\parallel n_y$ and $\boldsymbol{w}_y = \boldsymbol{w}_\perp n_y + \boldsymbol{w}_\parallel n_x$. Inserting these relationships into the above flux linearization yields:

$$\Delta(F^V)\cdot\boldsymbol{n} = (\boldsymbol{J}_0^V)\cdot\Delta\boldsymbol{w} + (\boldsymbol{J}_\perp^V)\cdot\Delta\boldsymbol{w}_\perp + (\boldsymbol{J}_\parallel^V)\cdot\Delta\boldsymbol{w}_\parallel$$

where $\boldsymbol{J}_0^V = [\boldsymbol{A}_0^V n_x + \boldsymbol{B}_0^V n_y]$, $\boldsymbol{J}_\perp^V = [\boldsymbol{A}_1^V n_x^2 + \boldsymbol{B}_2^V n_y^2 + (\boldsymbol{A}_2^V + \boldsymbol{B}_1^V) n_x n_y]$ and $\boldsymbol{J}_\parallel = [\boldsymbol{A}_2^V n_x^2 - \boldsymbol{B}_1^V n_y^2 + (\boldsymbol{B}_2^V - \boldsymbol{A}_1^V) n_x n_y]$.
This highly expensive linearization is drastically simplified by retaining only the contributions involving a positive definite matrix coefficient, namely:

$$\Delta(\boldsymbol{F}^V)\cdot\boldsymbol{n} \approx (\boldsymbol{J}_\perp^V)\cdot\Delta\boldsymbol{w}_\perp$$

with $\boldsymbol{J}_\perp^V = [\boldsymbol{A}_1^V n_x^2 + \boldsymbol{B}_2^V n_y^2]$.
Furthermore, since $\boldsymbol{J}_\perp^V$ is a positive definite matrix it can be replaced by its spectral radius $\rho(\boldsymbol{J}_\perp^V)$ without compromising the linear stability of the implicit stage.

The normal derivative of $\boldsymbol{w}$ with respect to a face $\Gamma_{i,k}$ is computed with a simple 2-point formula using the difference between the variable in the i-cell and its k^{th} neighbor, divided by the sum of the distances between the involved cell centers and the interface

$$\Delta(\boldsymbol{w}_\perp)_{i,k} = \frac{\Delta\boldsymbol{w}_{o(i,k)} - \Delta\boldsymbol{w}_i}{||\boldsymbol{r}_{i,k}|| + ||\boldsymbol{r}_{o(i,k)}||}$$

Eventually, the resulting contribution of the implicit numerical viscous flux to the numerical flux balance is:

$$\sum_k \left(\Delta\mathcal{H}_{i,k}^{V(i)}\right)^{n,m} |\Gamma_{i,k}| = \sum_k \widetilde{\rho(\boldsymbol{J}_\perp^V)}_{i,k}^{n,m} (\Delta\boldsymbol{w}_{o(i,k)}^{n,m} - \Delta\boldsymbol{w}_i^{n,m})\ |\Gamma_{i,k}| \tag{1.46}$$

with $\widetilde{\rho(\boldsymbol{J}_\perp^V)}_{i,k} = \rho(\boldsymbol{J}_\perp^V)_{i,k} / \left(||\boldsymbol{r}_{i,k}|| + ||\boldsymbol{r}_{o(i,k)}||\right)$.

Simplified full implicit stage Inserting the expressions (1.45) and (1.46) of the implicit numerical fluxes into the expansion of the residual (1.42) and rearranging (1.41) yields the following implicit solution for the ALE-C system (1.33) :

$$D_i^{n,m}\Delta\boldsymbol{w}_i^{n,m} + \frac{1}{2|\Omega_i|}\sum_k \left(\Delta\boldsymbol{F}_{o(i,k)}^E\right)^{n,m}\cdot\boldsymbol{n}_{i,k}\ |\Gamma_{i,k}| - \sum_k C_{i,k}^{n,m}\Delta\boldsymbol{w}_{o(i,k)}^{n,m} = -\mathcal{R}_i^t(\boldsymbol{w}^{n,m}) \tag{1.47}$$

with the scalar coefficients $D_i^{n,m}$, $C_{i,k}^{n,m}$ defined by:

$$D_i^{n,m} = \left(\frac{1}{\Delta\tau_i^{n,m}} + \frac{3}{2\Delta t} + \sum_k C_{i,k}^{n,m} \right) \quad , \quad C_{i,k}^{n,m} = \frac{1}{|\Omega_i|} \left(\frac{1}{2}\rho(\boldsymbol{J}_\perp^E) + \widetilde{\rho(\boldsymbol{J}_\perp^V)} \right)_{i,k}^{n,m} |\Gamma_{i,k}| \tag{1.48}$$

Point-Jacobi resolution Equation (1.47) can be solved at an extremely low cost per iteration using a simple point-Jacobi relaxation method. Denoting l the iteration counter associated with this method when (1.47) is iteratively solved to obtain $\boldsymbol{w}^{n,m+1}$ from the known $\boldsymbol{w}^{n,m}$ and introducing $\Delta\phi^{(l)} = \phi^{(l)} - \phi^{n,m}$, the PJ-BDF-ALE-C procedure reads :

$$\begin{aligned}
&\Delta\boldsymbol{w}_i^{(0)} = 0 \\
&\begin{cases} l = 0,\ l_{max} - 1 \\ \Delta\boldsymbol{w}_i^{(l+1)} = (D_i^{n,m})^{-1} \left(-\mathcal{R}_i^t(\boldsymbol{w}^{n,m}, x^n, s^n) - \dfrac{1}{2|\Omega_i|} \displaystyle\sum_k \left(\Delta F_{o(i,k)}^E\right)^{(l)} \cdot \boldsymbol{n}_{i,k}\ |\Gamma_{i,k}| + \sum_k C_{i,k}^{n,m} \Delta\boldsymbol{w}_{o(i,k)}^{(l)} \right) \end{cases} \\
&\boldsymbol{w}_i^{n,m+1} = \boldsymbol{w}_i^{n,m} + \Delta\boldsymbol{w}_i^{(l_{max})}
\end{aligned} \tag{1.49}$$

Let us recall that, with the BDF approach, the physical time-step included in the full residual $\mathcal{R}^t$ is computed using the three-level formula (**??**); within the ALE framework, the grid is kept fixed during the sub-iterative process on dual-time which means the expressions of $\mathcal{R}^E(\boldsymbol{w}^{n,m}, \boldsymbol{x}^n, \boldsymbol{s}^n)$ and $\mathcal{R}^V(\boldsymbol{w}^{n,m}, \boldsymbol{x}^n)$ given in formula (1.33) are retained when the counter m varies to obtain $\boldsymbol{w}^{n+1}$ from $\boldsymbol{w}^n$.

1.5 Boundary conditions

1.5.1 Far field

When computing external flow around a body, the far field boundary of the flow domain will be set systematically far enough from the object. The physical state on the far field boundary face is computed with the one dimensionnal Riemann invariants associated with the direction normal to the boundary [33]. We assume that the flow is uniform at the far field boundaries. The system of characteristic equations (c.f Appendix C) then reduces to :

$$L^{-1}\delta\boldsymbol{v}_p = 0 \tag{1.50}$$

or explicitely

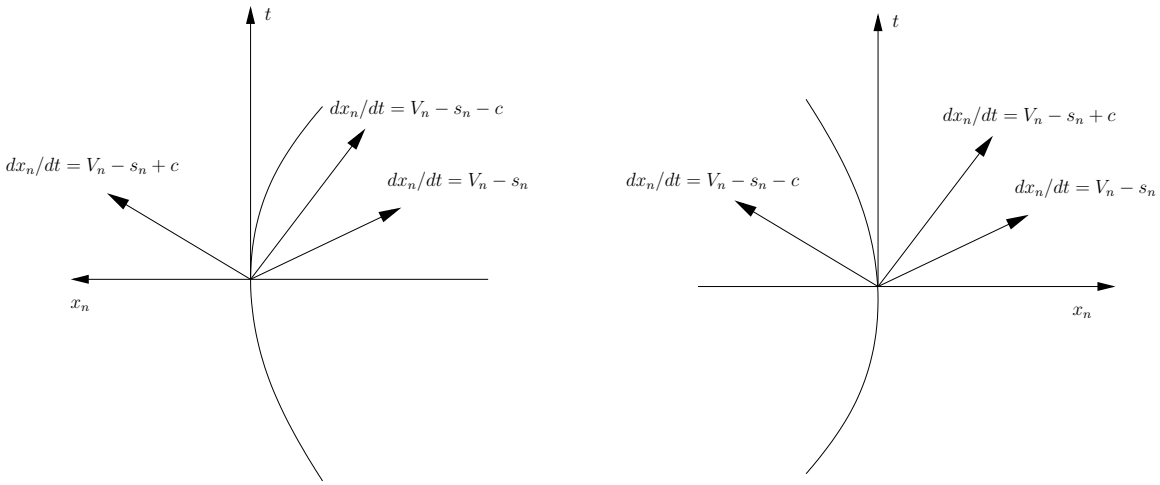

(a) Subsonic inlet boundary

(b) Subsonic outlet boundary

Figure 1.5: Riemann Far-field boundary conditions

$$\delta\rho - \frac{\delta p}{c^2} = 0 \quad \text{along} \quad \frac{dx_n}{dt} = V_n - s_n \tag{1.51}$$

$$\delta V_t = 0 \quad \text{along} \quad \frac{dx_n}{dt} = V_n - s_n \tag{1.52}$$

$$\delta V_n + \frac{\delta p}{\rho c} = 0 \quad \text{along} \quad \frac{dx_n}{dt} = V_n - s_n + c \tag{1.53}$$

$$\delta V_n - \frac{\delta p}{\rho c} = 0 \quad \text{along} \quad \frac{dx_n}{dt} = V_n - s_n - c \tag{1.54}$$

The first equation and second equation of (1.51) describes respectively the constancy of entropy and tangential velocity along the streamline $\frac{dx_n}{dt} = V_n - s_n$.
The last two Riemann invariants associated to the acoustic waves can be integrated which leads to the conservation of $R_n^+ = V_n + \frac{2c}{\gamma - 1}$ along the path $\frac{dx_n}{dt} = V_n - s_n + c$ and $R_n^- = V_n - \frac{2c}{\gamma - 1}$ along the path $\frac{dx_n}{dt} = V_n - s_n - c$

In the present study, the normal vectors are systematically oriented towards the exterior of the domain at the boundary. We use the subscript B to indicate boundary variables, the subscript i for the interior points and ∞ for the freestream values. The system of Riemann invariants at the boundary is specified according to the sign of the characteristics (Fig. 1.5) and is solved for the boundary variables. At the subsonic inlet, we have:

$$\frac{p_B}{\rho_B \gamma} = \frac{p_\infty}{\rho_\infty \gamma} \qquad \text{since} \quad V_n - s_n < 0 \tag{1.55}$$

$$V_{tB} = V_{t\infty} \qquad \text{since} \quad V_n - s_n < 0 \tag{1.56}$$

$$R^+_{nB} = V_{nB} + \frac{2c_B}{\gamma - 1} = V_{ni} + \frac{2c_i}{\gamma - 1} \qquad \text{since} \quad V_n - s_n + c > 0 \tag{1.57}$$

$$R^-_{nB} = V_{nB} - \frac{2c_B}{\gamma - 1} = V_{n\infty} - \frac{2c_\infty}{\gamma - 1} \qquad \text{since} \quad V_n - s_n - c < 0 \tag{1.58}$$

and at the subsonic outlet, we have:

$$\frac{p_B}{\rho_B \gamma} = \frac{p_i}{\rho_i \gamma} \qquad \text{since} \quad V_n - s_n > 0 \tag{1.59}$$

$$V_{tB} = V_{ti} \qquad \text{since} \quad V_n - s_n > 0 \tag{1.60}$$

$$R^+_{nB} = V_{nB} + \frac{2c_B}{\gamma - 1} = V_{ni} + \frac{2c_i}{\gamma - 1} \qquad \text{since} \quad V_n - s_n + c > 0 \tag{1.61}$$

$$R^-_{nB} = V_{nB} - \frac{2c_B}{\gamma - 1} = V_{n\infty} - \frac{2c_\infty}{\gamma - 1} \qquad \text{since} \quad V_n - s_n - c < 0 \tag{1.62}$$

The flux on the boundary face is then computed using the physical flux formula with the computed physical state. The far-field boundary treatment for viscous flows is the same as for the inviscid flows.

1.5.2 Wall

At a solid wall boundary, the normal velocity is zero since no mass or other convective flux can penetrate the solid body. For moving grid application this condition reads $V_n - s_n = 0$. The pressure is estimated using the solution polynomial in the cell adjacent to the wall face under consideration. The inviscid flux at the solid wall boundary is then:

$$\boldsymbol{f}^E_{n,wall} = \begin{pmatrix} 0 \\ pn_x \\ pn_y \\ ps_n \end{pmatrix} \tag{1.63}$$

If no other flux is specified, this boundary treatment leads to a slip condition. For viscous flow applications, a zero velocity tangential velocity boundary condition is also enforced. The velocity at the wall nodes is made equal to the grid velocity $\boldsymbol{v}_{wall} = \boldsymbol{s}$ and the viscous flux is calculated like for the interior cells.

1.6 Code Validation

In this section, we will present an inviscid and viscous calculation of a moving NACA0012 profile since our focus is on the assessment of the ALE treatment newly implemented in the existing compressible solver. The validation methodology is based on the comparison of the PJ-BDF-ALE-C solver, FLUENT®solver and some reference results from the literature. We try to use as much as possible the same numerical parameters for both our research code and FLUENT®. The grid is identical and moves in the same rigid body fashion. The spatial schemes (ROE, AUSM$^+$) described in section 1.2.2 are available in FLUENT®. Likewise, second order implicit time accurate scheme and density based solver are selected. The time step size depends on the case of study and will be specified for each case. A sufficient number of subiterations are calculated to ensure a residual drop of 4 orders of magnitude at each physical time step (typically 40).

1.6.1 Inviscid case oscillating NACA0012 CT1

The PJ-BDF-ALE-C inviscid validation test case is a pitching NACA-0012 aerofoil selected form the AGARD database [44]. A periodic motion of the aerofoil is defined by the instantaneous angle of attack

$$\alpha(t) = \alpha_m + \alpha_0 \sin(\omega t) \tag{1.64}$$

The freestream Mach number is $M_\infty = 0.6$, the mean incidence $\alpha_m = 2.89°$, the amplitude $\alpha_0 = 2.41°$, the reduced frequency $k = 0.0808$ and the pitching is about the quarter chord ($x_p/c = 0.25$). k is related to the pulsation ω and the frequency f by:

$$k = \frac{\pi f c}{U_\infty} = \frac{\omega c}{2U_\infty}$$

This CT1 case is actually turbulent since the Reynolds number is $Re = 4.8 \times 10^6$. However, since no turbulence model has been yet implemented in the code, the inviscid computations are compared with reference [17], in which both inviscid and turbulent computations are carried out. Other turbulent simulations can be found in [4, 76].
The aerofoil can be moved using a rigid body mesh motion or a deforming grid approach.

- In the first case, all grid points have the same motion as the airfoil. Therefore the initial grid quality is preserved. This is the method chosen in the PJ-BDF-ALE-C and FLUENT®solvers.

- In the second case , a layer of outer grid points is kept rigid while the inner cells are deforming. The main drawback is that a remeshing algorithms must be used at each outer time step. The geometric conservation law must also account for the the change of cell volume to avoid discretization errors. This is the method chosen by Darracq [17].

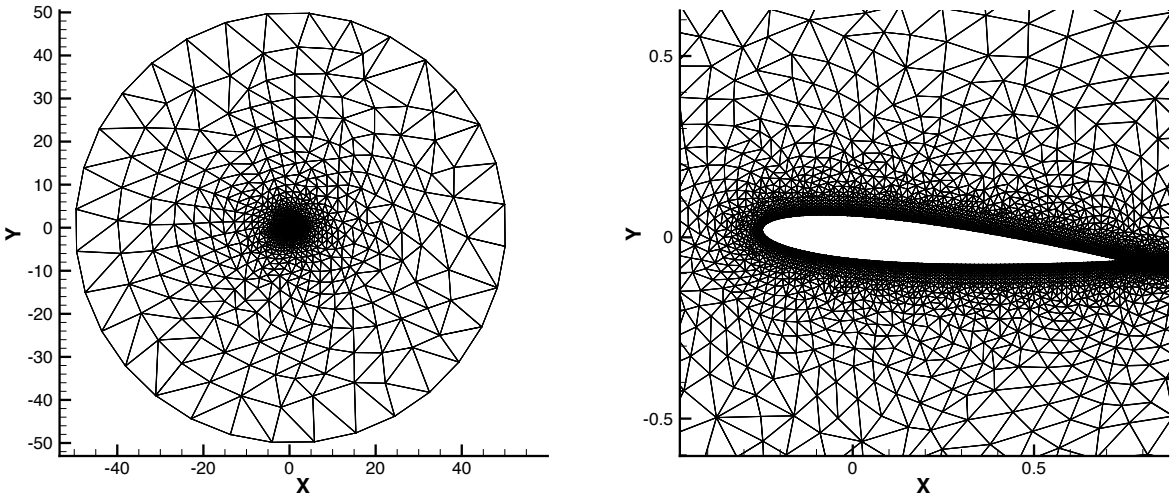

(a) (b)

Figure 1.7: Inviscid CT1. (a): global view of the computational grid. (b): close-up on the airfoil region.

Figure 1.6 illustrate the two moving mesh approaches on a 192×48 C-mesh

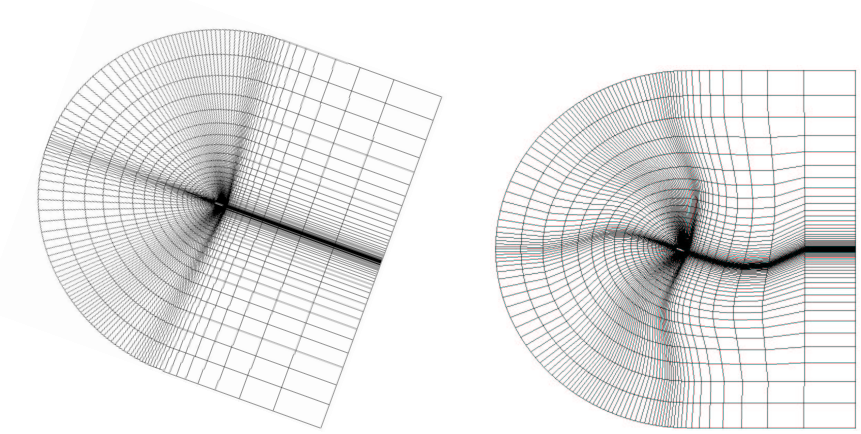

Figure 1.6: Rigid body mesh motion (left) and deforming mesh (right) approaches from [17]

The grid is a O type mesh of 8822 cells displayed in Figure 1.7. The far field boundaries are located 50 chords away from the profile.
The AUSM$^+$ scheme is used in all simulations and a time discretization of 256 time-steps per period is chosen. The PJ-BDF-ALE-C computations make use of $l_{max} = 16$ for the implicit PJ solver and CFL $= 10^6$ for computing the dual time.
To fulfill the similarity conditions between calculations, the Mach numbers must be kept equal. Since the FLUENT®code is dimensional, the choice of keeping the same grid

dimensions and adjusting the upstream velocity U_∞ is made. The resulting parameters are described in Table 1.1.

			Solvers	
			PJ-BDF-ALE-C	FLUENT®
Parameters	Chord	c [m]	1	1
	Upstream velocity	U_∞ [m.s $^{-1}$]	1	208.2
	Pulsation	ω [rad.s^{-1}]	0.1616	33.64
	Time step	Δt [s]	0.15	7 $\times 10^{-4}$
	Period	T [s]	38.88	0.186
	Number of time steps per cycle	$N_{\Delta t}$	260	265

Table 1.1: Inviscid CT1. Solvers parameters

Aerodynamic coefficients

Comparisons between the 3 codes are represented in figure 1.8 for the lift coefficient C_L and pitching moment C_m around the quarter chord for the 5^{th} cycle. The lift and pitching moment coefficients are defined by

$$C_L = \frac{F_L}{\frac{1}{2}\rho c U_\infty^2}, \qquad C_m = \frac{M}{\frac{1}{2}\rho c U_\infty^2} \tag{1.65}$$

where F_L and M are respectively the force exerted on the airfoil in the direction perpendicular to the flow and M the pitching moment.

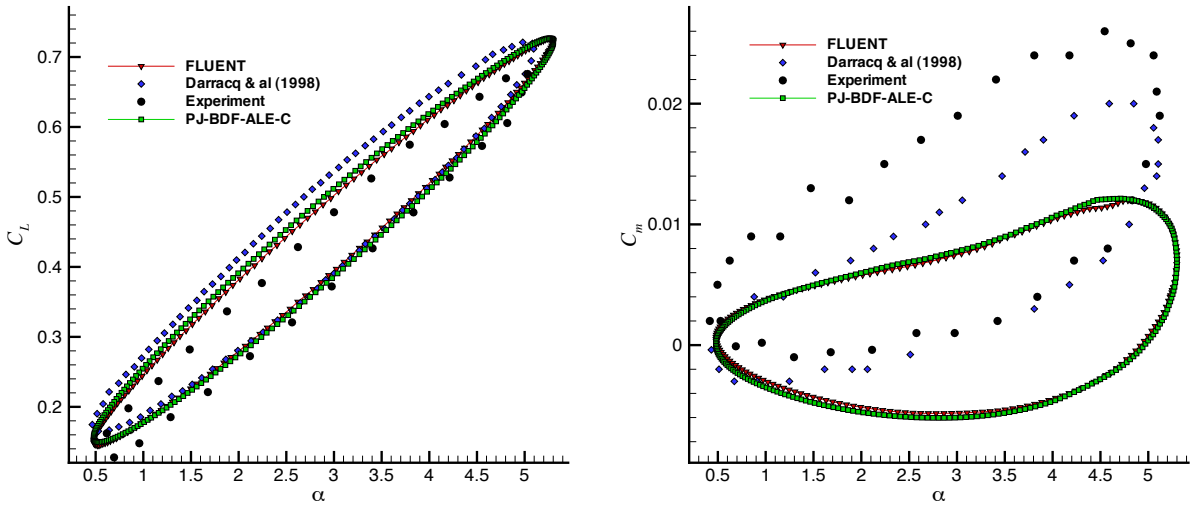

(a) (b)

Figure 1.8: Inviscid CT1. (a): Lift coefficient. (b): Pitching moment coefficient

There is a very good agreement on the prediction of the lift and moment coefficient evolution between the PJ-BDF-ALE-C and the FLUENT®codes. However, one can observe substantial differences with the results of Darracq [17], in particular on the moment coefficient which is a rather sensitive quantity. These discrepancies can be explained by mesh considerations since the mesh moving technique is different and also because the mesh itself is different, with results which are not necessarily grid-converged. The observed differences with experiment are of course expected since the computations are all inviscid ones. The agreement between the developed solver and the commercial code demonstrates the proper implementation of the ALE formulation in our code.

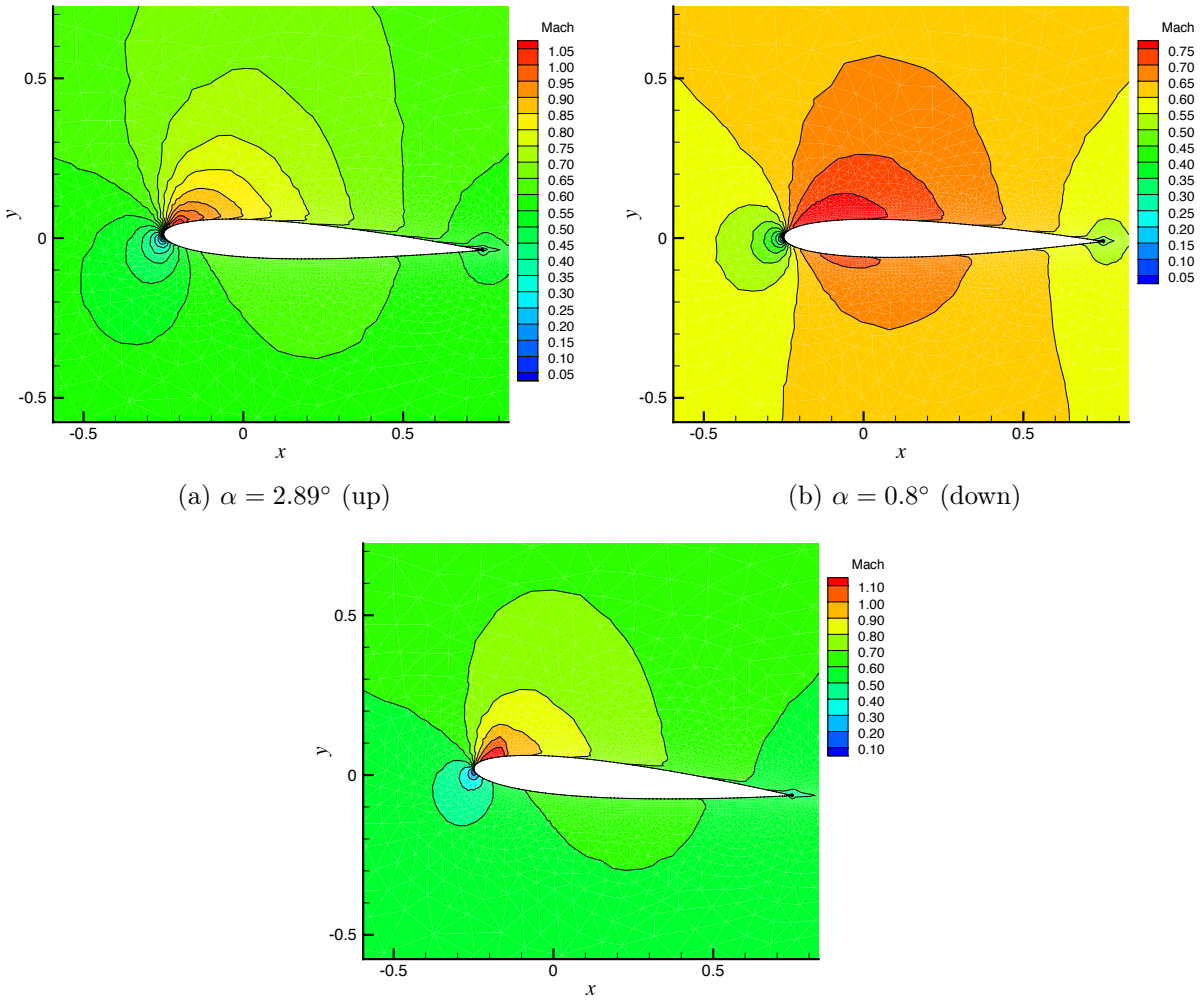

(a) $\alpha = 2.89°$ (up)

(b) $\alpha = 0.8°$ (down)

(c) $\alpha = 4.98°$ (down)

Figure 1.9: Inviscid CT1. Contours of Mach levels. The terms (up) and (down) indicate an increasing or decreasing incidence angle respectively

1.6.2 Viscous case -plunging NACA0012

The viscous moving mesh application involves a plunging airfoil. This kind of motion is interesting because, traditionally, lift and thrust are produced by steady flow devices like in commercial aircrafts. In contrast, insects and birds create the same forces from unsteady aerodynamics by flapping and hovering their wings. This flapping flight is a fine example of optimum motion of aerodynamic surfaces that simultaneously develop the necessary thrust for forward motion and sustained lift to remain airborne. These studies have been gaining a lot of interest due to their potential application to the design of innovative unmanned aircraft vehicles (UAVs).
In this viscous compressible study, we consider an NACA0012 airfoil animated by a plunging motion defined by :

$$y(t) = H_0 \cos(\omega t) \tag{1.66}$$

Flows around plunging airfoils can be classified according to their Strouhal numbers

$$S_t = \frac{\omega H_0 c}{U_\infty} = 2hk \tag{1.67}$$

The case of study is characterized by a low Strouhal number $S_t = 0.288$, an amplitude of plunging motion $h = 0.08$ and a reduced frequency $k = 1.8$. The freestream Mach number is $M_\infty = 0.2$ and the Reynolds number is $Re = 1850$. For this low Reynolds number, the flow can be assumed to be laminar.
Like in the previous section, results of the PJ-BDF-AE-C solver are compared with the results of FLUENT®and the results of Allaneau [1]. In the latest reference, simulations were done on a structured C-type mesh counting 4096×512 cells; the mesh is subject to rigid body motion and moves with the airfoil.
For the FLUENT®and PJ-BDF-ALE-C computations, the grid presented in the previous section (see Fig. 1.7) and the ROE spatial scheme are used. The time discretization is of 72 time-steps per period. The PJ-BDF-ALE-C computations make use of $l_{max} = 16$ for the implicit PJ solver and CFL $= 10^6$ for computing the dual time.
In the case of viscous compressible flow computations, three adimensional numbers - Mach, Reynolds and Prandtl numbers - must be adjusted to match the values used in the non-dimensional research solver (respectively 0.2, 1850 and 0.72). The FLUENT®freestream velocity is calculated from the Mach number and the speed of sound

$$U_\infty = M_\infty \sqrt{\gamma \frac{p_\infty}{\rho_\infty}} = 0.2 \times \sqrt{1.4 \times \frac{101325}{1.176}} = 69.43 \text{ m.s}^{-1}$$

.
To keep the Reynolds number, the first solution is to modify the dynamic viscosity. In that case the thermal diffusivity α must be changed to keep the Prandtl number $Pr = \frac{\mu}{\rho\alpha}$.

			Solvers	
			PJ-BDF-ALE-C	FLUENT®
Parameters	Chord	c [m]	1	4.05E^{-4}
	Upstream velocity	U_∞ [m.s^{-1}]	1	69.4
	Pulsation	ω [rad.s^{-1}]	3.6	6.15E^{6}
	Amplitude	H_0 [m]	0.08	3.24E^{-5}
	Time step	Δt [s]	0.024	1.41E^{-7}
	Period	T [s]	1.74	1.1E^{-5}
	Number of time step per period	$N_{\Delta t}$	72	72

Table 1.2: Viscous plunging NACA0012. Solvers parameters

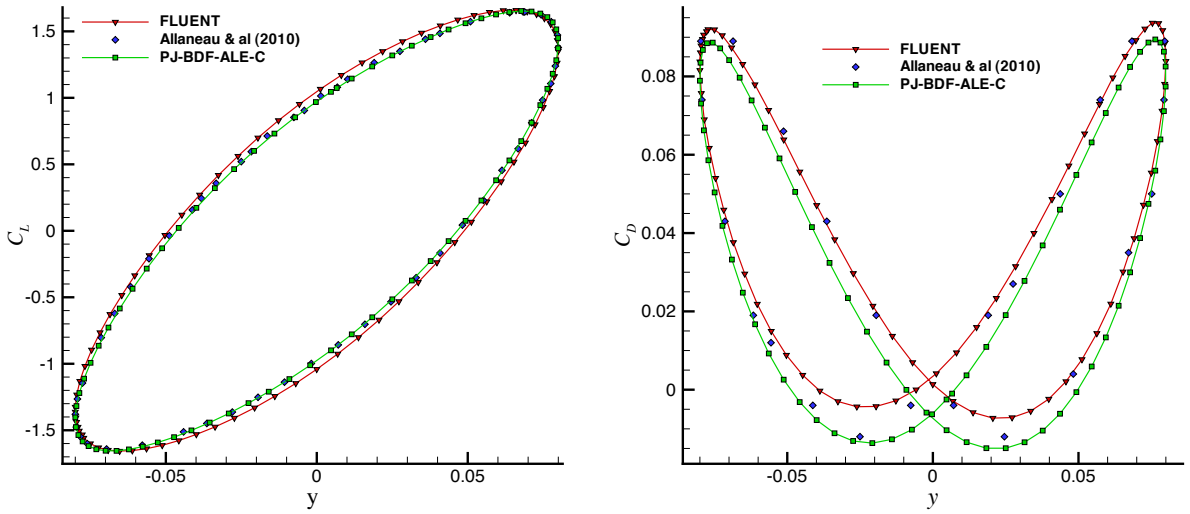

(a) (b)

Figure 1.10: Viscous plunging NACA0012. (a): Lift coefficient. (b): Drag coefficient

The second solution, which is prefered here, is to modify the mesh dimension in which case the Prandlt number is not affected. From the Reynolds number we have

$$c = \frac{\mu Re}{\rho U_\infty} = \frac{1.78 \times 10^{-5} \times 1850}{1.176 \times 69.43} \approx 4.05 \times 10^{-4}$$

All the resulting parameters are summarized in table 1.2

Lift and drag coefficients are represented in polar form, as a function of the vertical coordinate y in figure 1.10. The agreement with both FLUENT®and reference [1] results is satisfactory. This set of parameters (plunging amplitude and frequency) corresponds to a case where the fluid exerts drag on the airfoil in the flow direction since C_D is positive. Fig. 1.11 shows the pattern developed by the flow for three positions in the cycle. The time-accurate compressible flow solver has been successfully extended to moving grid

computations. Before proceeding to analyze in the second part of this report how the efficiency of this solver can be improved by making use of a Time-Spectral-Method, it is first extended in the next chapter to deal with incompressible flows on moving grids.

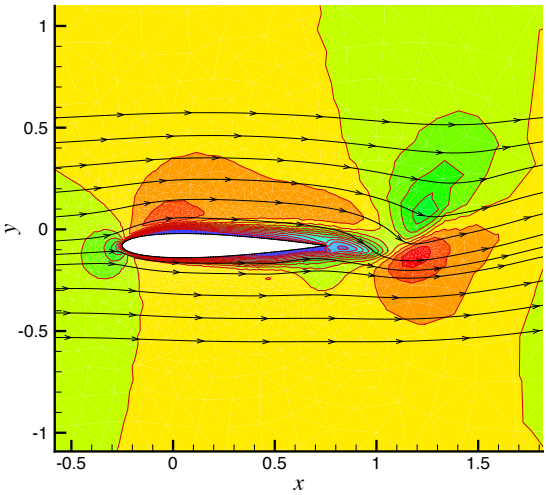

(a) $y = -0.08$

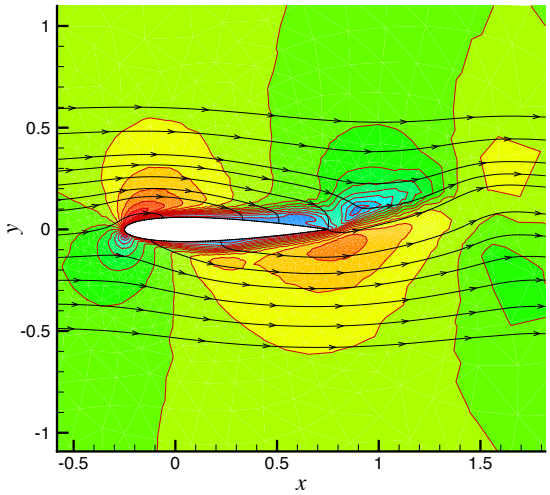

(b) $y = -0.00298$

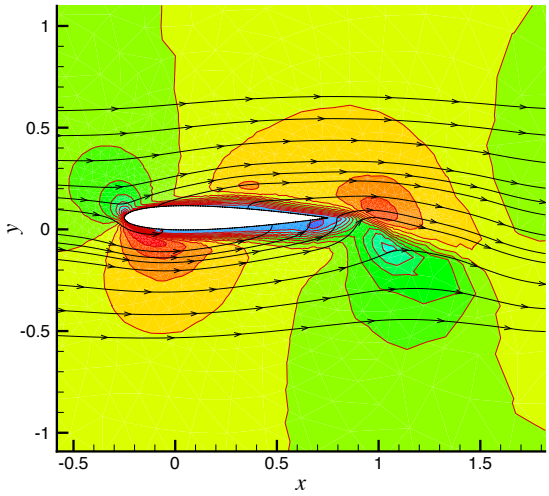

(c) $y = 0.0567$

Figure 1.11: Viscous plunging NACA0012. Contours of Mach numbers levels and velocity streamlines

Chapter 2

Incompressible flow solver

2.1 Artificial Compressibility Method

When dealing with incompressible viscous flow problems, it is customary to rely on a pressure-correction formulation to solve the incompressible Navier-Stokes equations and deal with the typical decoupling of the continuity and momentum equations. The salient features of such a formulation are a staggered-grid formulation (even though co-located incompressible solvers have also been developed over the past years) and the need of an efficient Poisson solver for the derived pressure equation. This equation is used for calculating the pressure field, given a velocity field that satisfies the incompressibility condition both inside the computational domain as well as at the boundaries.
Since no incompressible flow solver on general unstructured grid was available at the start of the thesis to be used as a development platform for implementing the TSM idea, it was decided to develop from scratch such an incompressible solver, taking advantage of the available compressible solver presented in the previous chapter. It was therefore natural to rely on the artificial compressibility (AC) approach initially proposed by Chorin [14]. The main idea of Chorin's method consisted in adding an artificial pressure term to the continuity equation. This pseudo term changes the mathematical character of the continuity equation from elliptic to hyperbolic by introducing the artificial compressibility and allows the system of equations to be solved with a variety of time-marching schemes developed for compressible flow solvers. The AC strategy has therefore been favored in this work to take full advantage of the efficient implicit methods previously developed for solving hyperbolic problems and rather easy to adapt to the AC system as briefly described in this chapter.

2.2 Governing equations

2.2.1 Steady equation

The original form of the Artificial Compressibility method was developed for steady-state problems. Let us recall the original AC method provides a steady solution of the 1D Euler equations by finding the steady-state of the following hyperbolic system of conservation laws with respect to the dual or fictitious time τ:

$$\frac{\partial}{\partial \tau} \underbrace{\begin{pmatrix} p \\ u \end{pmatrix}}_{=\boldsymbol{w}} + \frac{\partial}{\partial x} \underbrace{\begin{pmatrix} \beta u \\ u^2 + p \end{pmatrix}}_{=\boldsymbol{f}(\boldsymbol{w};\beta)} = 0 \tag{2.1}$$

with x the space variable p, u the pressure and velocity, β the constant artificial compressibility parameter. At steady-state on τ, the solution $u(x)$ of (2.1) satisfies the zero-divergence condition while both fields $u(x)$ and $p(x)$ satisfy the steady (with respect to τ) momentum equation.
The square root of the artificial compressibility parameter β represents a speed of artificial pressure wave and affects the overall convergence rate. If β gets higher, then the artificial pressure wave travels faster. However, for an extremely fast wave speed (ideally, the wave speed goes to the infinity in an incompressible media), a large disparity in eigenvalues is introduced. This degrades the overall convergence and stability. The value of β affects as well as the accuracy of the physical solution through the numerical dissipation of the space discretization. Hence an optimal β (wave speed) has to be found for a given problem. This is the goal of section 2.5.1. However, as long as the steady-state on τ is correctly achieved, the AC system remains consistent with the incompressible flow equations whatever the value of β.

2.2.2 Unsteady equation

The AC method was extended to time accurate formulations first by Peyret [59]. A time-accurate solution of the 1D Euler equations is now found as the steady solution respect to the dual time τ:

$$\frac{\partial}{\partial \tau} \begin{pmatrix} p \\ u \end{pmatrix} + \underbrace{\begin{pmatrix} 0 & 0 \\ 0 & 1 \end{pmatrix}}_{=\boldsymbol{K}} \cdot \frac{\partial}{\partial t} \begin{pmatrix} p \\ u \end{pmatrix} + \frac{\partial}{\partial x} \boldsymbol{f}(\boldsymbol{w};\beta) = 0 \tag{2.2}$$

with t the physical time. The singular matrix $\boldsymbol{K}$ is introduced to remove the contribution of a physical time derivative for the pressure variable which must not appear in the continuity equation. At steady-state on τ, the solution $u(x,t)$ of Eq. (2.2) satisfies the zero-divergence condition while both fields $u(x,t)$ and $p(x,t)$ satisfy the unsteady (with respect to t)

momentum equation. Rewriting Eq. (2.2) in the compact form of a 1D hyperbolic system with a source term

$$\frac{\partial \boldsymbol{w}}{\partial \tau} + \frac{\partial}{\partial x}\boldsymbol{f}(\boldsymbol{w};\beta) = \boldsymbol{S} = -\boldsymbol{K}\frac{\partial \boldsymbol{w}}{\partial t}$$

makes clear the AC system can be efficiently driven to an accurate steady-solution by making use of tools initially developed in the context of compressible flow solutions: second-order upwind discretization for the flux derivative, second-order BDF discretization for the physical time-derivative and first-order implicit stage for fast convergence on the dual-time.

Let us now turn to the AC system extended to the case of 2D incompressible viscous flows computed on moving grids. Let $\Omega(t) \subset \Re^2$ be an arbitrary control volume bounded by a smooth closed surface $\partial\Omega(t)$ which moves independently from the flow with a velocity $\boldsymbol{s}(\boldsymbol{x},t) = s_x(t)\,\boldsymbol{i} + s_y(t)\,\boldsymbol{j}$, where $\boldsymbol{x} = x\,\boldsymbol{i} + y\,\boldsymbol{j}$ denotes the vector of Cartesian coordinates in the absolute frame of reference.
In the Arbitrary Lagrangian Eulerian (ALE) framework, the 2D Navier-Stokes equations for incompressible unsteady flows, modified to account for the AC method, can be expressed in the following integral form

$$\frac{\partial}{\partial \tau}\int_{\Omega(t)} \boldsymbol{w}\; d\Omega(t) \;+\; \boldsymbol{K}\frac{\partial}{\partial t}\int_{\Omega(t)} \boldsymbol{w}\; d\Omega \;+\; \int_{\partial\Omega(t)} (\boldsymbol{F}^E - \boldsymbol{F}^V)\cdot \boldsymbol{n}\; d\gamma \;=\; 0\;, \tag{2.3}$$

where $\boldsymbol{n}$ is the outward unit normal vector and γ the curvilinear abscissa of $\partial\Omega$. The vector of variables $\boldsymbol{w}$, the singular matrix $\boldsymbol{K}$, the inviscid fluxes $\boldsymbol{F}^E = (\boldsymbol{f}^E, \boldsymbol{g}^E)$ and the viscous fluxes $\boldsymbol{F}^V = (\boldsymbol{f}^V, \boldsymbol{g}^V)$ are defined by:

$$\boldsymbol{w} = \begin{pmatrix} p \\ u \\ v \end{pmatrix}, \quad \boldsymbol{K} = \begin{pmatrix} 0 & 0 & 0 \\ 0 & 1 & 0 \\ 0 & 0 & 1 \end{pmatrix}, \quad \boldsymbol{f}^E(\boldsymbol{w}) = \begin{pmatrix} \beta(u - s_x) \\ u(u - s_x) + p \\ v(u - s_x) \end{pmatrix}, \quad \boldsymbol{g}^E(\boldsymbol{w}) = \begin{pmatrix} \beta(v - s_y) \\ u(v - s_y) \\ v(v - s_y) + p \end{pmatrix}$$

$$\boldsymbol{f}^V(\frac{\partial \boldsymbol{w}}{\partial x}, \frac{\partial \boldsymbol{w}}{\partial y}) = \frac{1}{Re}\begin{pmatrix} 0 \\ 2\dfrac{\partial u}{\partial x} \\ \dfrac{\partial u}{\partial y} + \dfrac{\partial v}{\partial x} \end{pmatrix}, \quad \boldsymbol{g}^V(\frac{\partial \boldsymbol{w}}{\partial x}, \frac{\partial \boldsymbol{w}}{\partial y}) = \frac{1}{Re}\begin{pmatrix} 0 \\ \dfrac{\partial u}{\partial y} + \dfrac{\partial v}{\partial x} \\ 2\dfrac{\partial v}{\partial y} \end{pmatrix}$$

The pressure p and the components (u, v) of the fluid velocity in the absolute frame of reference are normalized respectively by $\rho_\infty U_\infty^2$ and U_∞, with ρ_∞ and U_∞ the freestream density and velocity magnitude. The Reynolds number is $Re = \rho_\infty U_\infty L/\mu_\infty$ with L a typical length scale.

Note that, because of the geometric conservation law (section 1.3.1), it is possible to write the inviscid flux continuity equation component without including the grid velocity.

2.3 Numerical discretization of the AC system

In this section, the notations of Chapter 1 are adopted unless stated differently.

2.3.1 Spatial discretization

The Roe approximate Riemann solver initially developed to solve the compressible Euler equations [61] is adapted to the hyperbolic ALE-AC system (Eq. 2.3) and combined with a MUSCL variable reconstruction approach (presented in Sec. 1.2.2) in order to derive the inviscid numerical flux formula $\mathcal{H}_{i,k}^E$:

$$\mathcal{H}_{i,k}^E = \frac{1}{2}(\boldsymbol{F}^E(\boldsymbol{w}_k^L)\cdot\boldsymbol{n}_{i,k} + \boldsymbol{F}^E(\boldsymbol{w}_k^R)\cdot\boldsymbol{n}_{i,k}) + \frac{1}{2}\boldsymbol{Q}_{i,k}^E(\boldsymbol{w}_k^L - \boldsymbol{w}_k^R) \tag{2.4}$$

where $\boldsymbol{w}^{L/R}$ are the reconstructed states, respectively, on the left and right side of the k^{th} interface $\Gamma_{i,k}$ of cell Ω_i and $\boldsymbol{Q}^E = |\boldsymbol{A}^E n_x + \boldsymbol{B}^E n_y| = |\boldsymbol{J}_\perp^E|$ is the Roe numerical dissipation matrix. The expressions of the inviscid Jacobian matrices for the AC system $\boldsymbol{A}^E = d\boldsymbol{f}^E/d\boldsymbol{w}, \boldsymbol{B}^E = d\boldsymbol{g}^E/d\boldsymbol{w}$ are detailed in Appendix B.1.
An immediate calculation for system (2.3) yields:

$$\boldsymbol{J}_\perp^E = \begin{pmatrix} 0 & \beta n_x & \beta n_y \\ n_x & V_n - s_n + u\ n_x & u\ n_y \\ n_y & v\ n_x & V_n - s_n + v\ n_y \end{pmatrix}$$

This Jacobian matrix can be also expressed as $\boldsymbol{J}_\perp^E = \boldsymbol{T}|\boldsymbol{\Lambda}^E|\boldsymbol{T}^{-1}$ with $\boldsymbol{\Lambda}^E$ the diagonal matrix containing the real eigenvalues of the hyperbolic system (2.3). The Roe dissipation matrix is eventually computed as

$$\boldsymbol{Q}_{i,k}^E = \boldsymbol{T}_{i,k}|\boldsymbol{\Lambda}_{i,k}^E|\boldsymbol{T}_{i,k}^{-1}$$

with the state $\boldsymbol{w}_{i,k}$ taken as the arithmetic average of $\boldsymbol{w}_{i,k}^L$, $\boldsymbol{w}_{i,k}^R$ following the references [62, 70, 38]. Indeed it is demonstrated in Appendix B.3 that this average state satisfies the ROE properties [61].
The viscous fluxes are approximated using a linearly exact extension of the diamond method of Noh [58], not detailed here. Let us point out the steady-state of (2.3) depends on the AC parameter β through the numerical dissipation matrix $\boldsymbol{Q}^E$.

2.3.2 Implicit method

The semi-discrete form of the ALE-AC system is given by:

$$\frac{\partial \boldsymbol{w}_i}{\partial \tau_i} + \boldsymbol{K}\frac{\partial \boldsymbol{w}_i}{\partial t} + \mathcal{R}_i^E(\boldsymbol{w}, \boldsymbol{x}, \boldsymbol{s}) = \mathcal{R}_i^V(\boldsymbol{w}, \boldsymbol{x}) \tag{2.5}$$

Equation (2.5) differs from the dual-time marching compressible equation by the singular matrix $\boldsymbol{K}$ which multiplies the physical time derivative term. Consequently, it is clear that, from a numerical point of view, the time-implicit resolution of Eq. (2.5) does not need major modification of the compressible solver.

The numerical method described in the context of the unsteady compressible solver are recycled. The physical time-derivative is discretized with a second-order BDF scheme with a choice of grid positions and velocities for integrating $\mathcal{R}_i^E(\boldsymbol{w}, \boldsymbol{x}, \boldsymbol{s})$ and $\mathcal{R}_i^V(\boldsymbol{w}, \boldsymbol{x})$ described in Sec. 1.3.
A first-order implicit dual-time integration is used so that the AC equivalent of Equation (1.41) is

$$\frac{\Delta \boldsymbol{w}_i^{n,m}}{\Delta \tau_i^{n,m}} = -\mathcal{R}_i\left(\boldsymbol{w}^{n,m+1}\right) - \boldsymbol{K}\frac{\left(\frac{3}{2}\boldsymbol{w}_i^{n,m+1} - 2\boldsymbol{w}_i^n + \frac{1}{2}\boldsymbol{w}_i^{n-1}\right)}{\Delta t} = -\mathcal{R}_i^t\left(\boldsymbol{w}^{n,m+1}\right) \tag{2.6}$$

with $\boldsymbol{w}^{n,m+1} = \boldsymbol{w}^{n,m} + \Delta \boldsymbol{w}^{n,m}$ and the full residual $\mathcal{R}_i^t\left(\boldsymbol{w}^{n,m+1}\right)$ is expanded as

$$\mathcal{R}_i^t\left(\boldsymbol{w}^{n,m+1}\right) = \mathcal{R}_i^t\left(\boldsymbol{w}^{n,m}\right) + \boldsymbol{K}\frac{3}{2}\frac{\Delta \boldsymbol{w}_i^{n,m}}{\Delta t} + \frac{1}{|\Omega_i|}\sum_k \left(\Delta \mathcal{H}_{i,k}^{(i)}\right)^{n,m} |\Gamma_{i,k}| \tag{2.7}$$

where $(\Delta \mathcal{H}_{i,k}^{(i)})^{n,m} = {\mathcal{H}^{(i)}}^{n,m+1} - {\mathcal{H}^{(i)}}^{n,m}$ and $\mathcal{H}^{(i)} = \mathcal{H}^{E(i)} - \mathcal{H}^{V(i)}$ denotes the numerical flux formula retained in the implicit stage.
Like in section 1.4.1, $\mathcal{H}^{E(i)}$ appearing in the implicit stage is simply computed using the first-order Rusanov numerical flux:

$$\mathcal{H}_{i,k}^{E(i)} = \frac{1}{2}(\boldsymbol{F}_i^E \cdot \boldsymbol{n}_{i,k} + \boldsymbol{F}_{o(i,k)}^E \cdot \boldsymbol{n}_{i,k}) + \frac{1}{2}\rho(\boldsymbol{J}_\perp^E)_{i,k}(\boldsymbol{w}_i - \boldsymbol{w}_{o(i,k)}) \tag{2.8}$$

where $\rho(\boldsymbol{J}_\perp^E)_{i,k}$ is the spectral radius of the inviscid Jacobian matrix $\boldsymbol{J}_\perp^E$ computed at the center of face $\Gamma_{i,k}$.
The implicit numerical viscous flux takes the following simplified form :

$$\mathcal{H}_{i,k}^{V(i)} = \frac{\rho(\boldsymbol{J}_\perp^V)_{i,k}}{||\boldsymbol{r}_{i,k}|| + ||\boldsymbol{r}_{o(i,k)}||}(\boldsymbol{w}_{o(i,k)} - \boldsymbol{w}_i) = \widetilde{\rho(\boldsymbol{J}_\perp^V)}_{i,k}(\boldsymbol{w}_{o(i,k)} - \boldsymbol{w}_i) \tag{2.9}$$

where $\rho(\boldsymbol{J}_\perp^V)_{i,k}$ is the spectral radius of the viscous Jacobian matrix.
The expressions of the inviscid and viscous Jacobian matrices leading to the spectral radii for the AC system are given in Appendix B.

Inserting the expressions (2.8) (2.9) of the implicit numerical fluxes into the expansion of the residual (2.7) and rearranging (2.6) yields the following implicit solution for the ALE-AC system (1.33):

$$\boldsymbol{D}_i^{n,m}\Delta\boldsymbol{w}_i^{n,m} + \frac{1}{2|\Omega_i|}\sum_k \left(\Delta\boldsymbol{F}^E_{o(i,k)}\right)^{n,m}\cdot\boldsymbol{n}_{i,k}\,|\Gamma_{i,k}| - \sum_k C_{i,k}^{n,m}\Delta\boldsymbol{w}_{o(i,k)}^{n,m} = -\mathcal{R}_i^t(\boldsymbol{w}^{n,m}) \tag{2.10}$$

where the coefficients $\boldsymbol{D}_i^{n,m}$, $C_{i,k}^{n,m}$ are now defined by:

$$\boldsymbol{D}_i^{n,m} = \left(\frac{\boldsymbol{I}}{\Delta\tau_i^{n,m}} + \frac{3}{2}\frac{\boldsymbol{K}}{\Delta t} + \sum_k C_{i,k}^{n,m}\boldsymbol{I}\right) \quad , \quad C_{i,k}^{n,m} = \frac{1}{|\Omega_i|}\left(\frac{1}{2}\rho(\boldsymbol{J}^E_\perp) + \widetilde{\rho(\boldsymbol{J}^V_\perp)}\right)_{i,k}^{n,m}|\Gamma_{i,k}| \tag{2.11}$$

The implicit stage is still matrix-free with a scalar diagonal coefficient D for $\Delta p_i^{n,m}$ deprived from the $\frac{3}{2\Delta t}$ contribution in the mass conservation equation and including this term in the momentum conservation equations which involve $\Delta u_i^{n,m}$ and $\Delta v_i^{n,m}$. Equation (2.10) is solved with the same point-Jacobi relaxation procedure presented in Section 1.4.1.

In the next sections, the different versions of the code will be refered to as PJ-S-AC for the steady solver, PJ-BDF-AC for the unsteady solver on fixed mesh and PJ-BDF-ALE-AC for the unsteady solver on moving meshes.

2.4 Boundary conditions

2.4.1 Far field

The far field boundary conditions are deduced from the system of compatibility equations (Appendix C).

$$\delta h_1 = \left(-2cV_t\delta p + A(c+\frac{s_n}{2})\delta V_t + B(c-\frac{s_n}{2})\delta V_t - (A-B)V_t\delta V_n\right) = 0 \quad \text{along } \frac{dx_n}{dt} = V_n - s_n \tag{2.12}$$

$$\delta h_2 = \left(-(c+\frac{s_n}{2})\delta p + B\delta V_n\right) = 0 \quad \text{along } \frac{dx_n}{dt} = V_n - \frac{s_n}{2} - c \tag{2.13}$$

$$\delta h_3 = \left((c-\frac{s_n}{2})\delta p + A\delta V_n\right) = 0 \quad \text{along } \frac{dx_n}{dt} = V_n - \frac{s_n}{2} + c \tag{2.14}$$

Introducing the quantity $\phi = p + \frac{1}{2}V_n^2$, one obtains

$$\begin{aligned} V_t\delta\phi - s_n\delta V_n - (c - \frac{s_n}{2})(c + \frac{s_n}{2})\delta V_t = 0 \\ (c + \frac{s_n}{2})\delta\phi - (c + \frac{s_n}{2})^2\delta V_n = 0 \\ (c - \frac{s_n}{2})\delta\phi + (c - \frac{s_n}{2})^2\delta V_n = 0 \end{aligned} \tag{2.15}$$

Unlike the boundary condition for the compressible system of Euler equations, it is not possible to integrate the Riemann variables. Hence, system (2.15) is linearized using the interior values for the coefficients. The characteristics variables are discretized in an upwind fashion depending on the sign of the characteristics.

At the subsonic inlet

There are two ingoing characteristics corresponding to eigenvalues $\lambda_1 = V_n - s_n$ and $\lambda_2 = V_n - s_n/2 - c$ and one outgoing characteristic $\lambda_3 = V_n - s_n/2 + c$, thus the discretized system of boundary conditions system is

$$\begin{aligned} V_{ti}(\phi_B - \phi_\infty) - s_n(V_{nB} - V_{n\infty}) - (c_i - \frac{s_n}{2})(c_i + \frac{s_n}{2})(V_{tB} - V_{t\infty}) = 0 \\ (\phi_B - \phi_\infty) - (c_i - \frac{s_n}{2})(V_{nB} - V_{n\infty}) = 0 \\ (\phi_B - \phi_i) + (c_i + \frac{s_n}{2})(V_{nB} - V_{ni}) = 0 \end{aligned} \tag{2.16}$$

and the solution of system (2.16) for the boundary variables is:

$$\begin{aligned} V_{nB} &= \frac{(c_i - \frac{s_n}{2})V_{n\infty} + (c_i + \frac{s_n}{2})V_{ni}}{2c_i} + \frac{\phi_i - \phi_\infty}{2c_i} \\ p_B &= \frac{(c_i + \frac{s_n}{2})\phi_\infty + (c_i - \frac{s_n}{2})\phi_i}{2c_i} + \frac{(c_i + \frac{s_n}{2})(c_i - \frac{s_n}{2})(V_{ni} - V_{n\infty})}{2c_i} - \frac{1}{2}V_{nc}^2 \\ V_{tB} &= V_{t\infty} + \frac{V_{ti}(\phi_c - \phi_\infty) - s_n(V_{nc} - V_{n\infty})}{(c_i + \frac{s_n}{2})(c_i - \frac{s_n}{2})} \end{aligned} \tag{2.17}$$

At the subsonic outlet

There are two outgoing characteristics $\lambda_1 = V_n - s_n$ and $\lambda_3 = V_n - \frac{s_n}{2} + c$ and one ingoing chacracteristic $\lambda_2 = V_n - \frac{s_n}{2} - c$, thus the discretized system of boundary conditions is:

$$
\begin{aligned}
V_{ti}(\phi_B - \phi_i) - s_n(V_{nB} - V_{ni}) - (c_i - \frac{s_n}{2})(c_i + \frac{s_n}{2})(V_{tB} - V_{ti}) = 0 \\
(\phi_B - \phi_\infty) - (c_i + \frac{s_n}{2})(V_{nB} - V_{n\infty}) = 0 \\
(\phi_B - \phi_i) + (c_i - \frac{s_n}{2})(V_{nB} - V_{ni}) = 0
\end{aligned}
\tag{2.18}
$$

and the solution of system (2.18) for the boundary variables is:

$$
\begin{aligned}
V_{nB} &= \frac{(c_i - \frac{s_n}{2})V_{n\infty} + (c_i + \frac{s_n}{2})V_{ni}}{2c_i} + \frac{\phi_i - \phi_\infty}{2c_i} \\
p_B &= \frac{(c_i + \frac{s_n}{2})\phi_\infty + (c_i - \frac{s_n}{2})\phi_i}{2c_i} + \frac{(c_i + \frac{s_n}{2})(c_i - \frac{s_n}{2})(V_{ni} - V_{n\infty})}{2c_i} - \frac{1}{2}V_{nc}^2 \\
V_{tB} &= V_{ti} + \frac{V_{ti}(\phi_c - \phi_i) - s_n(V_{nc} - V_{ni})}{(c_i + \frac{s_n}{2})(c_i - \frac{s_n}{2})}
\end{aligned}
\tag{2.19}
$$

2.4.2 Wall

At a solid wall boundary, the normal velocity is zero since no mass or other convective flux can penetrate the solid body. For moving grid application this condition reads $u_n - s_n = 0$. The pressure is extrapolated from the interior ghosts cells to the boundary. The inviscid flux at the solid wall boundary is then:

$$
\boldsymbol{f}_{n,wall}^{E} = \begin{pmatrix} 0 \\ pn_x \\ pn_y \end{pmatrix} \tag{2.20}
$$

2.5 Code Validation

This section presents a validation of the newly developed unsteady incompressible code. First, the solver is used on a stationary mesh for the computation of steady and unsteady flows over a NACA0015 airfoil corresponding respectively to the angles of attack $\alpha = 4°$ and $\alpha = 16°$. Then, the solver is validated for moving mesh applications with a pitching and heaving NACA0015 airfoil recently studied by Kinsey and Dumas [41].

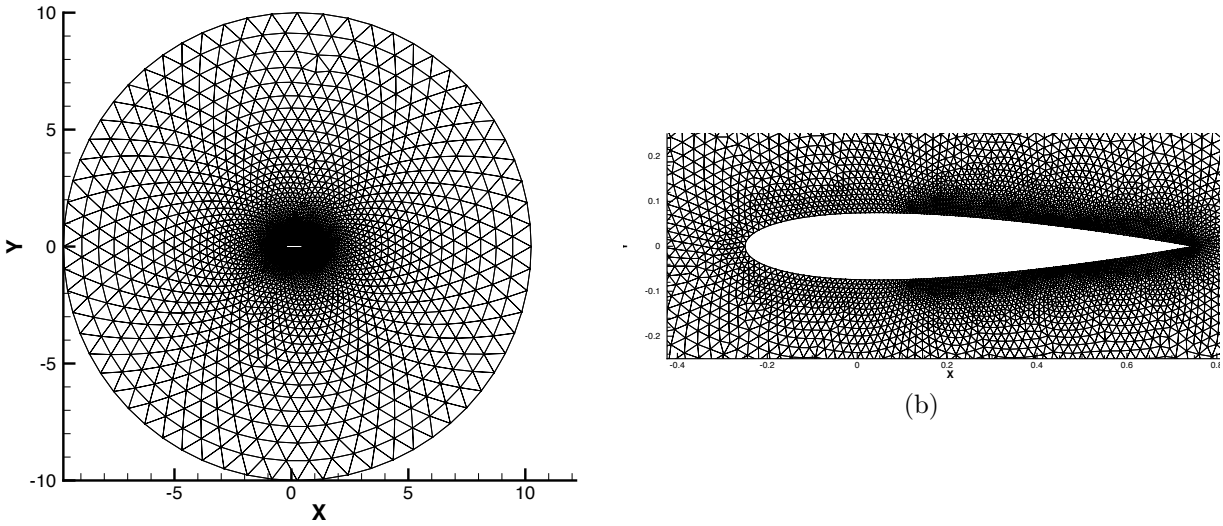

(a)

(b)

Figure 2.1: Static NACA0015. (a): global view of the computational grid. (b): close-up on the airfoil region.

2.5.1 Fixed mesh simulations

Common numericals parameters

All the computations make use of $l_{max} = 16$ for the implicit PJ solver and CFL $= 10^6$ for computing the dual time. The unstructured mesh counts 14000 cells and is represented in Fig. 2.1. The far field boundary is located 10 chords away from the airfoil.

Steady simulation

The test case is a NACA 0015 airfoil at 4° of incidence and $Re = 1000$. The results are compared with reference [23] in which the author uses an incompressible viscous flow solver based on a vorticity stream fonction formulation. We also compare the PJ-S-AC solver with the commercial software FLUENT®which uses a SIMPLE algorithm for pressure and velocity coupling. The numerical flux used for the AC computation is the ROE scheme adapted to the artificial compressibility method as presented in section 2.3. We test different values of the artificial compressibility parameter β in order to determine the optimal choice with regards to the convergence speed and solver precision.

In the case of incompressible viscous flow, the only adimentional number which matters is the Reynolds number. Hence, the grid does not need to be resized for the FLUENT®simulations and the upstream velocity is simply calculated from the chord and Reynolds number (see table 2.2 for the numerical values).

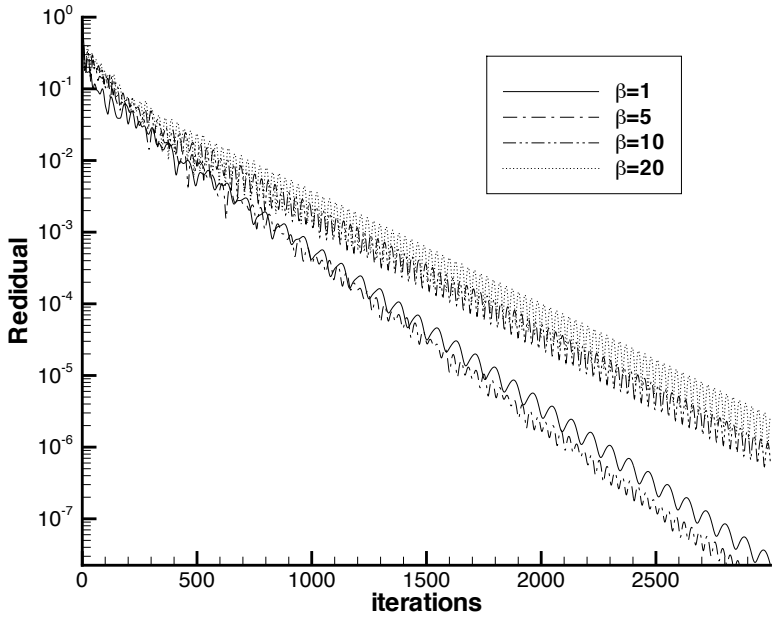

Figure 2.2: Static NACA0015. Convergence histories for different values of β, PJ-S-AC solver, incidence $\alpha = 4°$,$Re = 1000$.

Residuals Figure 2.2 shows that the best convergence rate is obtained for a parameter $\beta = 5$. For this value, approximately 2000 iterations are needed to achieved a drop residual of 4 orders. This value of the AC parameter will be systematically used from now on.

Velocity contours The velocity streamlines represented in figure 2.3 show a recirculation zone at the extrados in the trailing edge region.

Solvers	PJ-S-AC				FLUENT®	Fang [23]
Incompressible method	β=1	β=5	β=10	β=20	SIMPLE	$\omega - \Psi - \Gamma$
C_L	0.1418	0.1429	0.1432	0.1436	0.156	0.148
C_D	0.1340	0.1342	0.1343	0.1344	0.1249	0.129

Table 2.1: Global aerodynamic coefficients resuts, steady NACA0015, incidence $\alpha = 4°$, $Re = 1000$, incompressible flow.

Aerodynamic coefficients Concerning the accuracy, the comparison of the PJ-S-AC, FLUENT codes and reference [23] is presented in table 2.1. We can see the slight dependence of the results with β (through the matrix dissipation). The global coefficients C_L and C_D are in good agreement with the results of purely incompressible solvers. For $\beta = 5$, the difference is of 8% and 3% for C_L with FLUENT®and Fang [23] respectively and 7% and 4% for C_D. From now on, we will retain the value $\beta = 5$ in all the AC simulations.

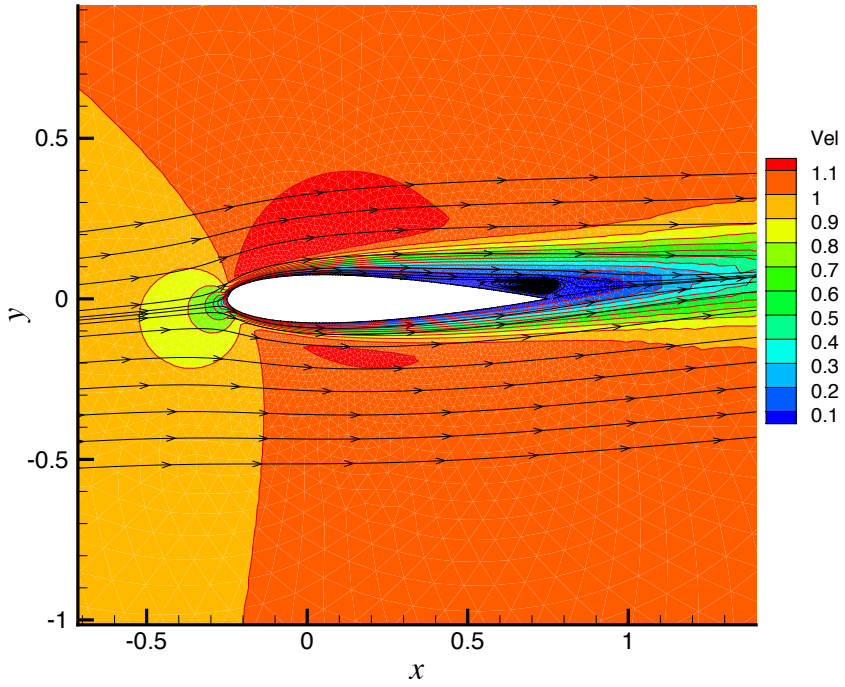

Figure 2.3: Static NACA0015. Contours of velocity magnitude and velocity streamlines, PJ-S-AC solver $\beta = 5$, $\alpha = 4°$, Re=1000.

Unsteady simulations

The test case is a NACA0015 airfoil at 16° of incidence and $Re = 1000$. For these conditions, the flow becomes unsteady and periodic. Again, we compare the results of PJ-BDF-AC solver with the reference [23] and a FLUENT®computation. We use 100 sub-iterations in dual time to achieve a residual drop of 3 orders of magnitude. Like for the steady case, the grid dimension is identical in both solvers and the upstream velocity is adapted in FLUENT®to match the Reynolds number. The time step is $\Delta t = 0.05$ in the PJ-BDF-AC solver and leads to approximately 30 discretization points per cycle of the periodic unsteady phenomenon.

			Solvers	
			PJ-BDF-AC	FLUENT®
Parameters	Chord	c [m]	1	1
	Upstream velocity	U_∞ [m.s $^{-1}$]	1	0.0145
	Time step	Δt [s]	0.05	3.441

Table 2.2: Static NACA0015. Code parameters for unsteady incompressible NACA0015 computations, $\alpha = 16°$, $Re = 1000$.

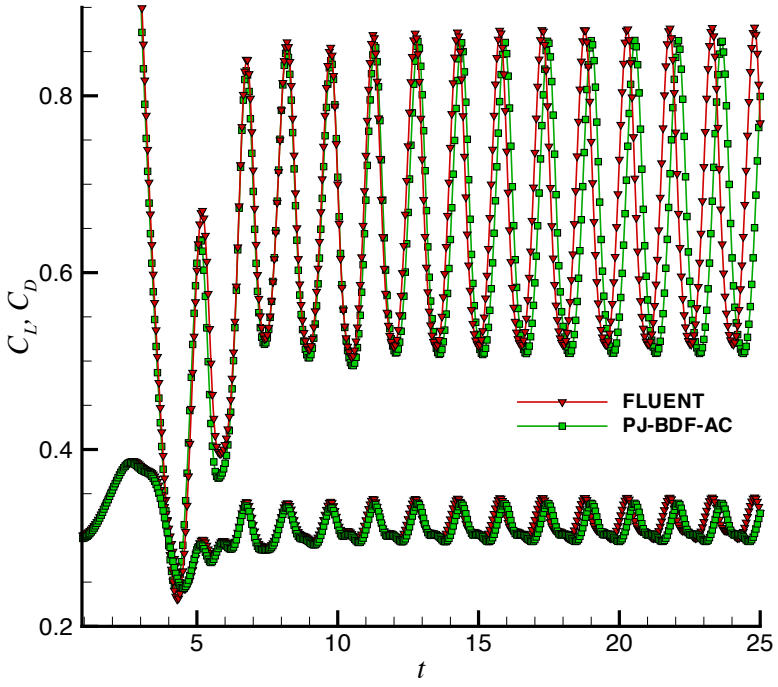

Figure 2.4: Static NACA0015. Aerodynamic coefficients, C_L and C_D as a function of time, PJ-BDF-AC solver,$\alpha = 16°$, $Re = 1000$.

Aerodynamic coefficients Figure 2.4 represents the time history of the Lift and Drag coefficient. Note that the time is made adimensional in FLUENT®by dividing the physical time by the characteristic time $t_c = c/U_\infty$.

Results are summarized in table 2.3. Generally, there is a good agreement between PJ-BDF-AC and FLUENT®. Errors on the amplitude and average values of the aerodynamic coefficients are below 1.5%.

		Solvers		
		PJ-BDF-AC	FLUENT	Fang [23]
Results	Average C_L	0.684	0.694	0.669
	C_L amplitude	0.352	0.352	0.31
	Average C_D	0.317	0.322	0.304
	C_D amplitude	0.043	0.045	0.047
	Period T [s]	1.54	1.52	1.6

Table 2.3: Static NACA0015, $\alpha = 16°$, $Re = 1000$. Comparison of global aerodynamic coefficients computed using various incompressible solvers.

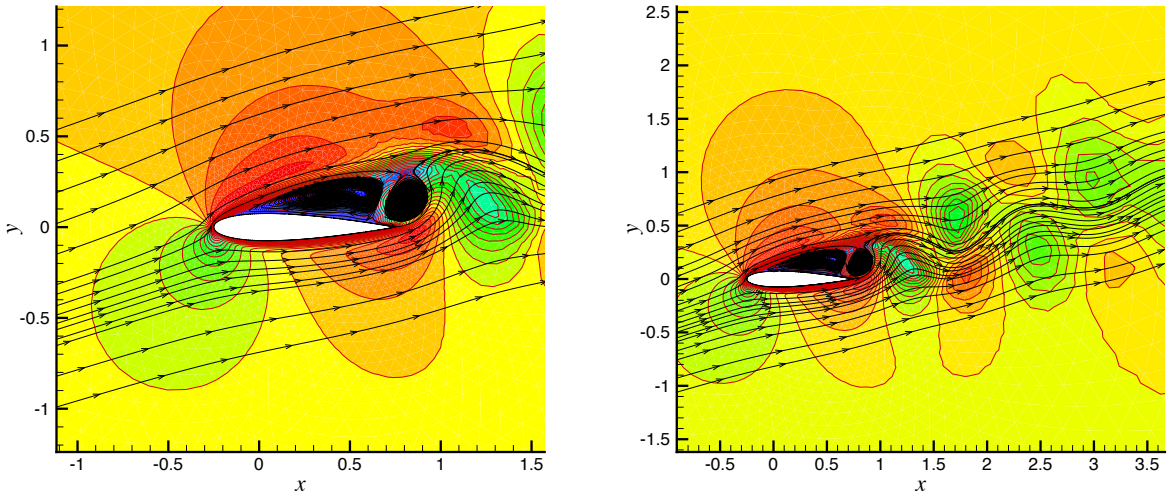

(a) (b)

Figure 2.5: Static NACA0015. Contours of velocity magnitude and velocity streamlines à $t = 20$, $C_L = 0.55$ and $C_D = 0.296$, PJ-BDF-AC solver,$\alpha = 16°$, $Re = 1000$.

Contours Figure 2.5 illustrates the unsteady vortex shedding that appears at the airfoil extrados. Figure 2.6 shows that the far-field treatment is correct even if the far-field boundaries are relatively close.

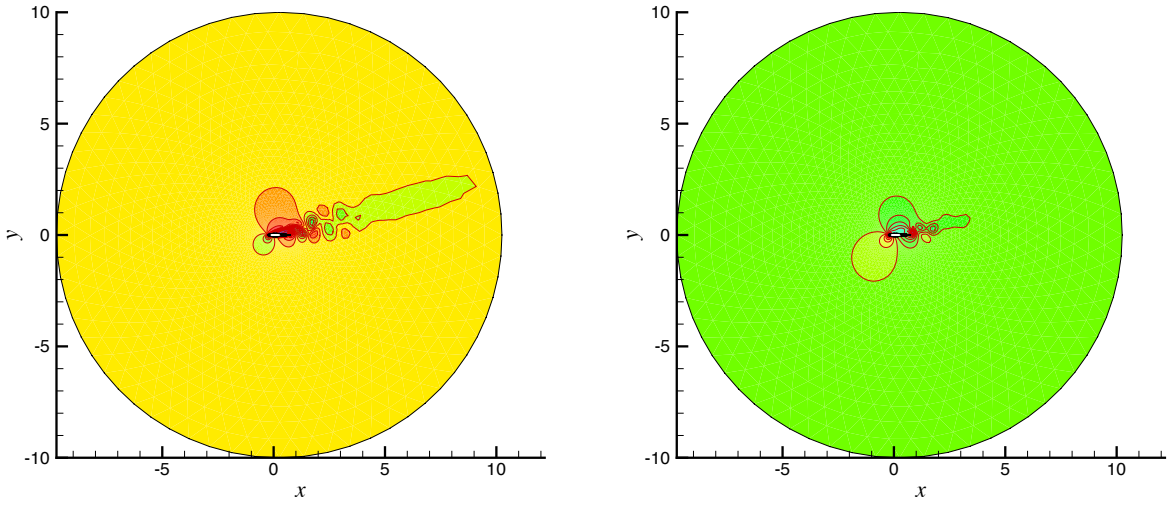

(a) Velocity contours (b) Pressure contours

Figure 2.6: Static NACA 0015. Far field boundary treatment, PJ-BDF-AC solver, $\alpha = 16°$, $Re = 1000$.

2.5.2 Moving mesh simulation

The unsteady incompressible solver is used to compute incompressible unsteady laminar flows over moving airfoils. An interesting application is motivated by the following observation : a wing that is simultaneously heaving and pitching can extract energy from an incoming flow. Several tidal turbine concept are based on this power extraction principle [71]. Kinsey and Dumas [41] recently studied the theoretical performance of such a system by performing a parametric study of a pitching and heaving airfoil.
The airfoil flow computations presented in [41] were carried out using a conventional pressure-based solver implemented in the commercial solver FLUENT®on very fine grids and with a very small time-step to ensure time and grid convergence and allow a fine analysis of the flowfield. These computations will therefore be retained as first reference data and the ability of the proposed PJ-BDF-ALE-AC to provide similar results will be established in the present section.

Test-cases description

The geometry under study is a NACA0015 airfoil submitted to a pitching motion around an axis located at one-third of the airfoil chord $x_p/c = 1/3$ and/or a heaving motion. These prescribed motions are defined by the following laws of evolution for the pitching angle $\theta(t)$, and the vertical position $y(t)$

$$\begin{cases} \theta(t) = \theta_0 \sin(\omega t) \\ y(t) = H_0 \sin(\omega t + \frac{\pi}{2}) \end{cases} \tag{2.21}$$

where θ_0 and H_0 are respectively the pitching and heaving amplitudes, ω is the angular velocity. The reduced frequency f^* is defined as $f^* = \dfrac{fc}{U_\infty}$, where U_∞ is the freestream velocity. The Reynolds number based on the freestream conditions and the airfoil chord is equal to $Re = 1100$ hence the flow is assumed laminar.
Depending on the pitching/heaving amplitude and frequency, the airfoil can either be in the power extraction or in the propulsion regime. Kinsey & al found that the highest efficiency is achieved for $\theta_0 = 76.33°$, $H_0 = 1$ and $f^* = 0.14$. This test case (which will be denoted by HE for Highest Efficiency from now on) is also the more detailed in the publication [41]. It is thus used as the validation test case for our PJ-BDF-ALE-AC solver. Two other cases will be presented in the last chapter of this report, dedicated to TSM incompressible flow applications.

Numerical parameters

The computational mesh displayed in Fig. 2.9 was generated so as to be similar to the grid used in [41] since both the proposed PJ-BDF-ALE-AC solver and the commercial solver used by Kinsey and Dumas are second-order methods on unstructured triangular grids.

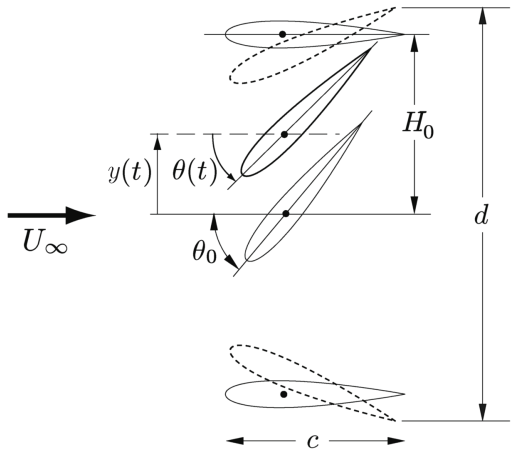

Figure 2.7: Pitching and heaving motion parameters from [41]

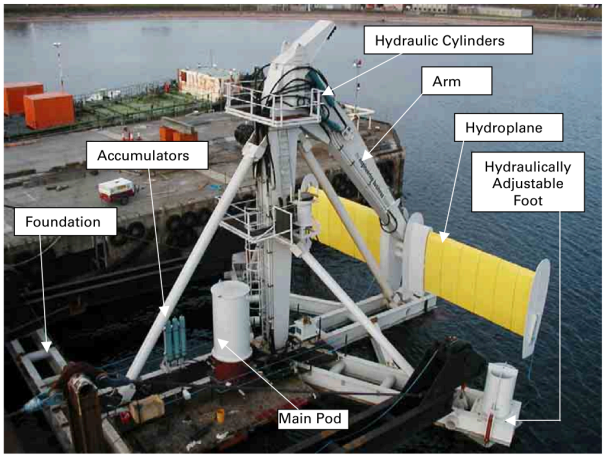

Figure 2.8: Stingray tidal turbine device [71]

Parameters	Pulsation	ω [rad.s^{-1}]	0.8796
	Heaving amplitude	H_0 [m]	1
	Pitching amplitude	θ_0 [°]	76.33
	Time step	Δt [s]	0.0137
	Period	T [s]	7.142
	Number of time step per period	$N_{\Delta t}$	520

Table 2.4: HE test case. Solver parameters

This mesh is different than the mesh presented in figure 2.1. It is finer and the far field boundary is located at 50 chords. It counts 32000 cells, with 360 points set on the airfoil and a near body resolution tailored to satisfy the criterion $y_p^2 \frac{U_\infty}{\nu_\infty \Delta} \sim 1$, where y_p is the distance from the wall to the first adjacent cell centroid and Δ is the minimal edge length on the airfoil. The enforcement of this criterion combines a low cell-Reynolds number and a moderate cell aspect-ratio near the airfoil surface to ensure solution accuracy. The AC parameter β is constant and equal to 5 according to section 2.5.

520 physical time steps per period or cycle are used with 100 dual time iterations performed at each physical time step, 16 iterations of the PJ method and a CFL of 10^6 for computing the dual time to achieve a residual drop of 3 orders of magnitude. The computation is started with a uniform pressure and velocity flow field. 4 cycles must be computed before flow periodicity is fully achieved. A variation of the mean aerodynamic coefficient inferior to 0.2% between two consecutive cycles is the criterion typically used to ensure a fully periodic flow is obtained. All the PJ-BDF-ALE-AC results displayed hereafter correspond to the 5^{th} cycle for HE and will be labelled BDF from now on.

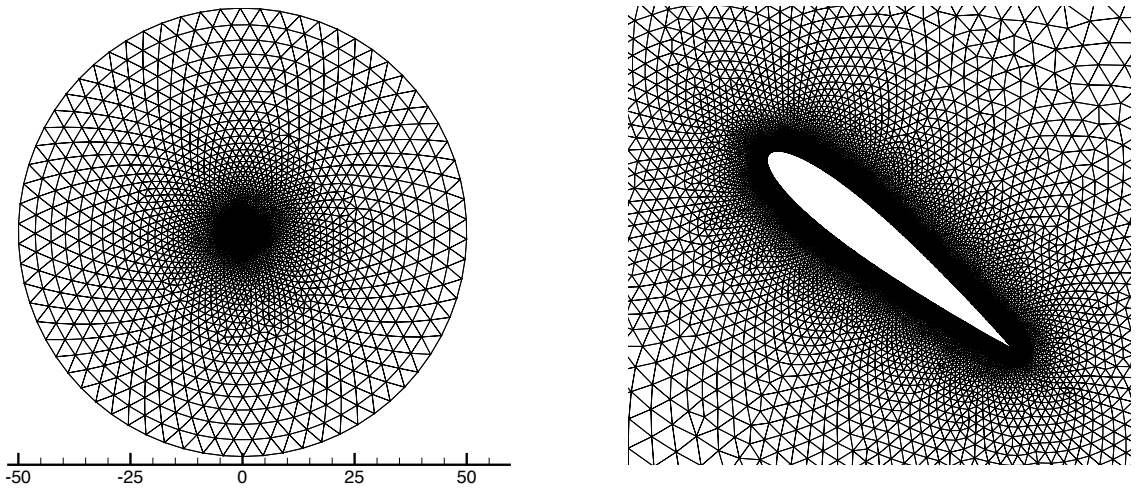

(a) (b)

Figure 2.9: Moving NACA0015. (a): global view of the computational grid. (b): close-up on the airfoil region.

Results

The comparison with the reference results [41] is performed on the force coefficients, more precisely on the C_Y coefficient and C_X coefficient. Figure 2.10 presents the computed C_X and C_Y coefficients over the normalized time period; note only 1 out of 8 physical time-steps are plotted for the present BDF computations.
The agreement between [41] and the present BDF results is globally very good.
In figure 2.11a, the pressure coefficient $C_p = \dfrac{p - p_\infty}{1/2\rho U_\infty^2}$ around the airfoil is plotted at two time instances in the period. At $t/T = 0$, we observe a noticeable difference between the PJ-BDF-ALE-AC results and the Kinsey results for the medium configuration (16000 cells and 2000 time steps per cycle) and the fine configuration (72000 cells and 4000 time steps per cycle). First, it is interesting to see that there is still a slight dependence of mesh and time step refinement between the medium and fine computations. A further mesh refinement targeted on the trailing edge region should probably improve the comparison. Besides, the range of C_p values extends from -1.5 to 1, which is relatively low compared to the C_p at $t/T = 0.25$, leading to visible errors. If we look at the corresponding pressure field at $t/T = 0$ in figure 2.12, the physics of the flow is respected with a trailing edge vortex shedding clearly visible in the wake. The PJ-BDF-ALE-AC pressure coefficient at $t/T = 0.25$ shows very good agreement with the finest Kinsey configuration (see Fig. 2.11b). In conclusion, an unsteady incompressible flow solver on unstructured grid is now available and ready to be possibly improved, as far as efficiency is concerned, by using a Time Spectral Method instead of the conventional BDF time-marching approach. The design principles of such a TSM strategy are investigated in the second part of this report.

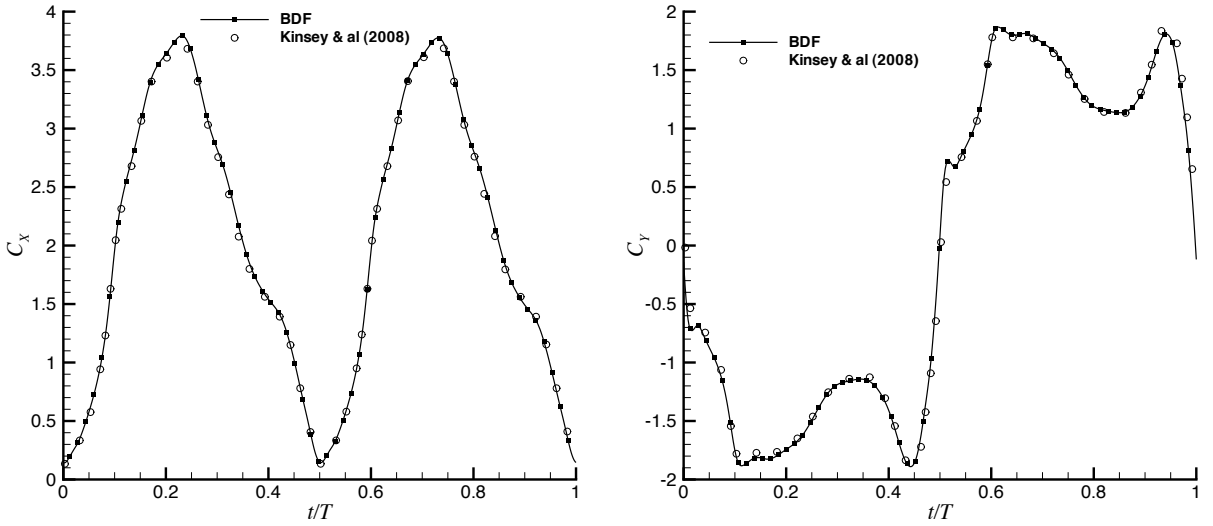

(a) (b)

Figure 2.10: HE test case. (a): C_X evolution computed computed in [41] and using the present BDF method. (b): C_Y evolution computed in [41] and using the present BDF method.

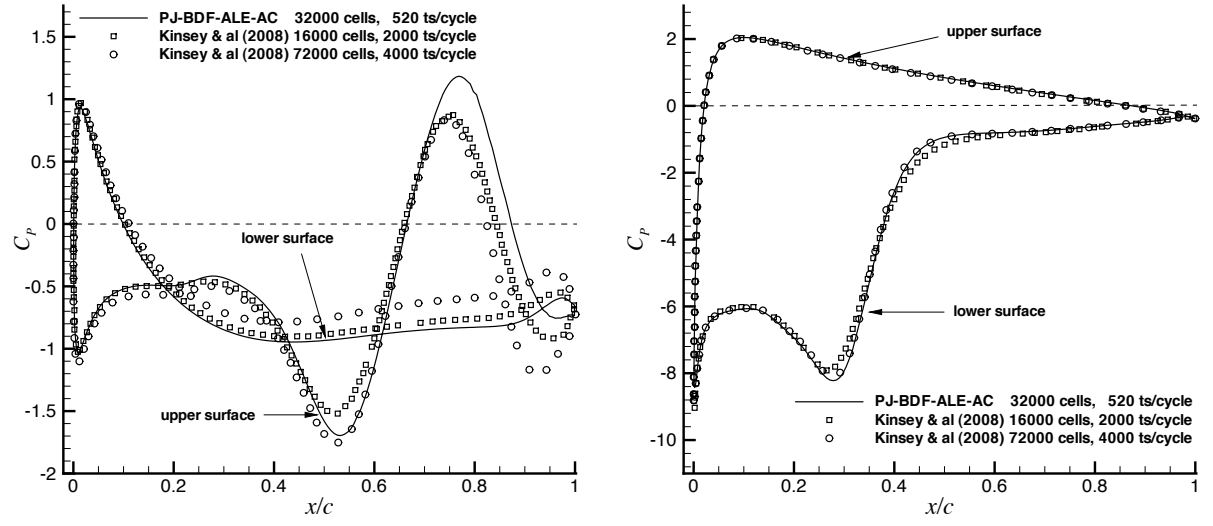

(a) $t/T = 0$ (b) $t/T = 0.25$

Figure 2.11: HE test case. Pressure coefficient distribution from leading edge to trailing edge.

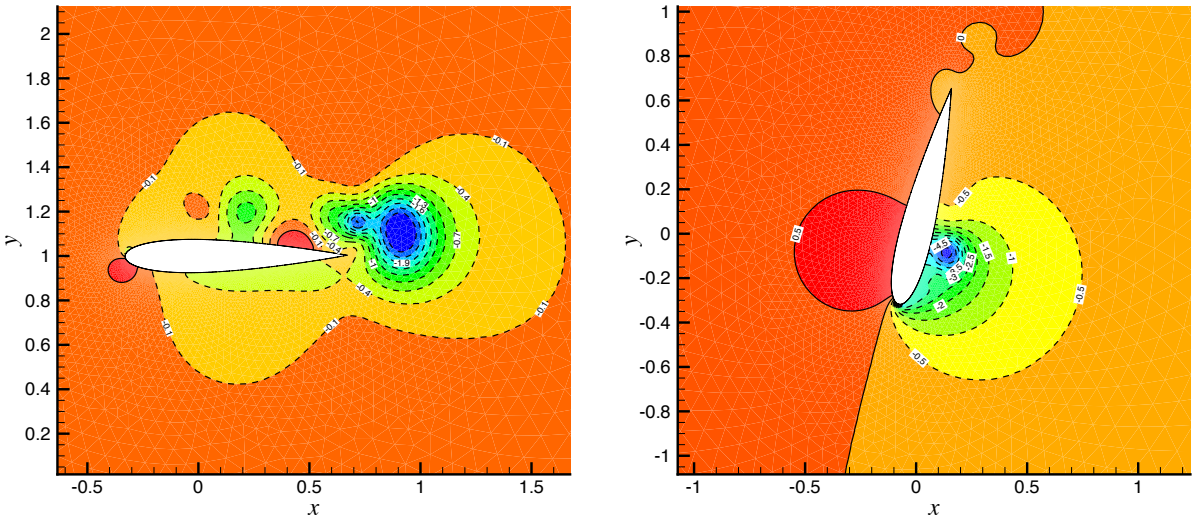

(a) $t/T = 0$ (b) $t/T = 0.25$

Figure 2.12: HE test case. Contours of pressure (dashed for negative, solid for positive).

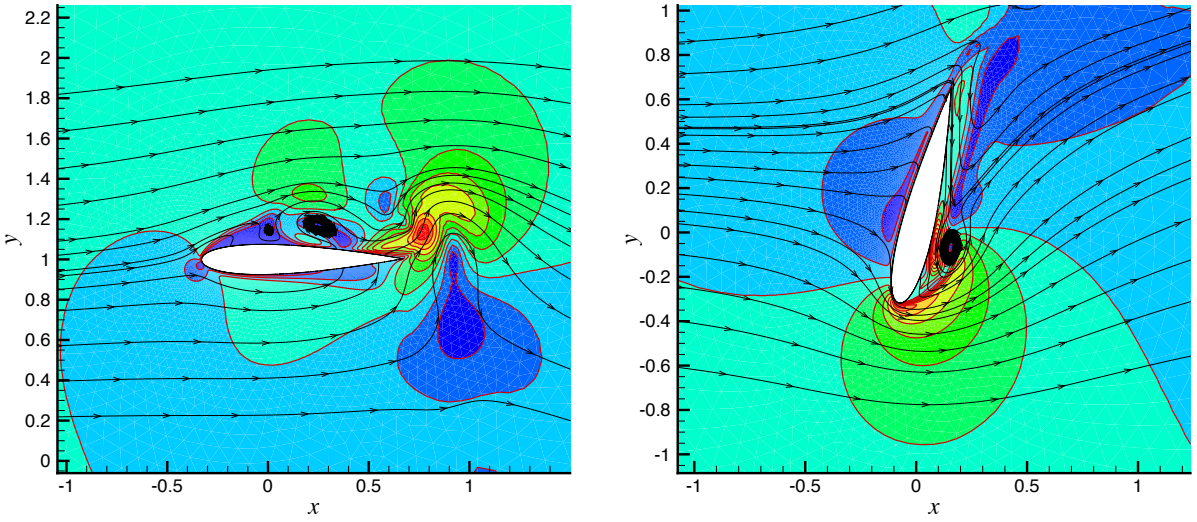

(a) $t/T = 0$ (b) $t/T = 0.25$

Figure 2.13: HE test case. Contours of velocity magnitude and velocity streamlines.

Part II

Time Spectral Method Principles

Chapter 3

A brief review of harmonic methods

Harmonic methods take advantage of the time periodicity of a problem to decompose its solution into several harmonic contributions and thus simplify a full unsteady problem into a set of coupled steady problems. The Time Spectral Method briefly discussed in the introduction belongs to this class of methods. A short overview of harmonics methods is proposed in this chapter before proceeding to describe with more details the TSM approach specifically used and analyzed in the present work.

Harmonic methods have been used for a long time in the structural analysis domain (see for instance [43]) and in electronics [25]. To the best of our knowledge, spectral time discretization methods have been first introduced first in Computational Fluid Dynamics (CFD) in 1995 by Carte, Dusěk and Fraunié [11, 12] for incompressible wake flow simulations. Later on, in 2001, these methods have also been investigated for internal compressible flow computations in turbomachinery by Chen [13] and McMullen [53]. In these studies, a periodic solution is sought via the Fourier coefficients in the frequency domain. In 2002, Hall & al [31] are the first to suggest another approach, namely the Harmonic Balance Technique (HBT), by casting the frequency domain equations back into the time domain. In 2005, Gopinath and Jameson [27] itemize the matrix formulation of Hall & al [31] to provide an expression of the time spectral operator for every time instant, which they call the "Time Spectral Method" or TSM. The present chapter offers a brief review of the harmonic methods following their chronological order of appearance. Thus, the frequency domain methods are first presented and the successive ideas leading to the TSM are explained next.

3.1 Frequency domain methods

3.1.1 Single harmonic methods

The single harmonic methods consider the solution of a time-periodic flow as the sum of a basic state and the contribution of a fundamental frequency. A complete review of these methods can be found in [65]. In the so-called linearized Euler method [29, 73], the basic state is a steady flow $\overline{\overline{\boldsymbol{w}}}$ and the instantaneous flow solution is expressed as:

$$\boldsymbol{w} = \overline{\overline{\boldsymbol{w}}} + \widetilde{w}, \quad \widetilde{w} = \widehat{\boldsymbol{w}}\ e^{\underline{i}\omega t} \tag{3.1}$$

with $\underline{i}$ the imaginary complex number and ω the fundamental pulsation. The assumed solution Eq. (3.1) is substituted into the Euler equations and the resulting system is truncated at first order, leading to an equation for the steady part and another one to compute the complex amplitude of the harmonics in the frequency domain, called the linearized Euler equation.
In the Non Linear Harmonic Method of Ning and He [57], the vector of conserved variables is decomposed as the sum of a time-averaged contribution and a single harmonic perturbation:

$$\boldsymbol{w} = \overline{\boldsymbol{w}} + \widetilde{w}, \quad \widetilde{w} = \widehat{\boldsymbol{w}}\ e^{\underline{i}\omega t} \tag{3.2}$$

Starting from the compressible Navier-Stokes equations, Ning and Heb derive a new system of conservation laws, with a standard continuity equation for the time-averaged contribution but with momentum equations containing additional terms, introduced by the non-linearities of the Navier-Stokes system, similar to the turbulent Reynolds stress tensor components associated with RANS modeling. These terms appearing in the time-averaged fluxes must be modeled. A term such as $\overline{\widetilde{u}\widetilde{v}}$ for instance is computed by taking advantage of the fact $\widetilde{u}$ and $\widetilde{v}$ vary in a harmonic manner, so that the time average $\overline{\widetilde{u}\widetilde{v}}$ over a period can be expressed as:

$$\overline{\widetilde{u}\widetilde{v}} = \frac{1}{2}|\widehat{u}||\widehat{v}|\cos\Phi_{uv} \tag{3.3}$$

where Φ_{uv} is the phase difference between $\widetilde{u}$ and $\widetilde{v}$ and the amplitudes of the unsteady perturbations $\widehat{u}$, $\widehat{v}$ are obtained from the linearized Euler equation.

3.1.2 Multi-harmonic methods

Incompressible flows

The first application of a multi-harmonic method in the domain of fluid mechanics must be granted, according to our analysis of the available literature, to Carte & al [11], where the simulation of a laminar incompressible after-body wake was considered. Let us briefly explain the key principles of the approach proposed in [11], which could have been the approach retained in this work to reduce the computational cost of the targeted incom-

pressible flow problems. The Navier-Stokes equations for incompressible viscous flows in velocity-pressure formulation read:

$$\begin{aligned} &\frac{\partial \boldsymbol{v}}{\partial t} + \boldsymbol{v}\nabla\boldsymbol{v} - \nu\nabla^2\boldsymbol{v} + \nabla p = 0 \\ &\nabla.\boldsymbol{v} = 0 \end{aligned} \tag{3.4}$$

where $\boldsymbol{v}$ denotes the velocity and p is the pressure. If the flow is assumed periodic in time, any of the flow variable can be expressed as a Fourier series:

$$\boldsymbol{v} = \sum_{k=-\infty}^{k=+\infty} \widehat{\boldsymbol{c}}_k(\boldsymbol{x}) e^{ik\omega t} \tag{3.5}$$

$$p = \sum_{k=-\infty}^{k=+\infty} \widehat{d}_k(\boldsymbol{x}) e^{ik\omega t} \tag{3.6}$$

where $\omega = 2\pi/T$ and with T the period. The complex Fourier coefficients $\widehat{\boldsymbol{c}_k}(\boldsymbol{x})$ and $\widehat{d_k}(\boldsymbol{x})$ are no longer time-dependent of course; moreover velocity and pressure being real variables, the conditions $\widehat{\boldsymbol{c}_k} = \overline{\widehat{\boldsymbol{c}_{-k}}}$ and $\widehat{d_k} = \overline{\widehat{d_{-k}}}$ must be fulfilled, where the overbar denotes the complex conjugate.

The time derivative of the velocity is then given by:

$$\frac{\partial \boldsymbol{v}}{\partial t} = \sum_{k=-\infty}^{k=+\infty} \underline{i}k\omega\widehat{\boldsymbol{c}}_k(\boldsymbol{x}) e^{ik\omega t} \tag{3.7}$$

The variable decompositions (Eq. (3.5) and (3.7)) are next introduced in system (3.4) and the orthogonality of the Fourier series is exploited to derive an equivalent momentum equation in the Fourier space:

$$(\underline{i}k\omega - \nu\nabla^2)\widehat{\boldsymbol{c}}_k + \sum_{n=-\infty}^{n=+\infty} (\widehat{\boldsymbol{c}}_n \cdot \nabla)\widehat{\boldsymbol{c}}_{k-n} + \nabla\widehat{d}_k = 0, \quad \forall\ k \in \mathbb{Z} \tag{3.8}$$

with the Fourier components $\boldsymbol{c_k}$ satisfying the continuity equation:

$$\nabla \cdot \widehat{\boldsymbol{c}}_k = 0, \quad \forall\ k \in \mathbb{Z} \tag{3.9}$$

Note that, because of the non-linearity of the momentum equation, the individual equations for each mode are not independent: the equation for the k^{th} wave-number also depends on the values of all the other modes $n \neq k$.

Only a finite number of modes k are computed in practice: $-N \leq k \leq N$ where N is the highest number of harmonics retained. The method becomes attractive if a satisfactory solution accuracy can be achieved with a not too large truncated number of harmonics. Indeed, the flow solution is obtained after solving simultaneously in the frequency domain a system of $2N+1$ steady equations of the type (3.8)-(3.9). This set of equation differs from the original Navier-Stokes system in the time domain (3.4) by the formulation of the non-linear term in equation (3.8) and the complex nature of the Fourier coefficients $\boldsymbol{c}_k$ and d_k; however the very structure of the individual equations (3.8) and (3.9) remains similar to the original Navier-Stokes system so that the modification of the initially available Navier-Stokes solver into a multi-harmonics solver can be performed for a moderate effort of development.
In the original formulation proposed in [11, 12], the variables are not necessarily periodic in time. Transient behaviors, and not only periodic oscillations, can also be accounted for by adding an additional degree of freedom to the variables $\boldsymbol{v}$ and p. For the sake of simplicity, this additional degree will not be considered in the next paragraph, limited to periodic problems.

Numerical implementation The discrete solution method for (3.8) and (3.9) adopted in [11, 12] is based on a modification of an implicit finite volume time-marching solution of the Navier-Stokes equations initially developed by Braza and co-workers [37, 9]. A pseudo-time derivative on τ is introduced to drive the system to a steady state:

$$\left.\begin{aligned} \frac{\widehat{\boldsymbol{c}}_k^{m+1} - \widehat{\boldsymbol{c}}_k^{m}}{\Delta\tau} + \underline{i}k\omega\widehat{\boldsymbol{c}}_k^{m+1} + \sum_{n=-N}^{n=+N} (\widehat{\boldsymbol{c}}_n^{m} \cdot \nabla)\widehat{\boldsymbol{c}}_{k-n}^{m+1} - \nu\nabla^2\widehat{\boldsymbol{c}}_k^{m+1} + \nabla\widehat{d}_k^{m} = 0 \\ \nabla \cdot \widehat{\boldsymbol{c}}_k^{m+1} = 0 \end{aligned}\right\} \quad \forall\, k \in [-N:N] \tag{3.10}$$

The usual projection procedure for coupling velocity and pressure in incompressible flow solvers is then adapted to solve system (3.10) using the following steps:

$$\frac{\widehat{\boldsymbol{c}}_k^{*} - \widehat{\boldsymbol{c}}_k^{m}}{\Delta\tau} + \underline{i}k\omega\widehat{\boldsymbol{c}}_k^{*} + \sum_{n=-N}^{n=+N} (\widehat{\boldsymbol{c}}_n^{m} \cdot \nabla)\widehat{\boldsymbol{c}}_{k-n}^{*} - \nu\nabla^2\widehat{\boldsymbol{c}}_k^{*} + \nabla\widehat{d}_k^{m} = 0 \tag{3.11}$$

$$\nabla^2\Phi_k = \nabla.\widehat{\boldsymbol{c}}_k^{*} \tag{3.12}$$

$$\widehat{\boldsymbol{c}}_k^{m+1} = \widehat{\boldsymbol{c}}_k^{*} - \nabla^2\Phi_k \tag{3.13}$$

$$\widehat{d}_k^{m+1} = \widehat{d}_k^{m} + \frac{\Phi_k}{\Delta\tau} \tag{3.14}$$

Eq. (3.11)-(3.14) are discretized in space using a second-order finite volume method and solved by an Alternate Direction Implicit algorithm well suited at the time for the struc-

tured grid computations performed by the authors. The parameter $\Delta\tau$ appearing in Eq. (3.11) is chosen so as to optimize the performance of the ADI algorithm. For each dual time step, one ADI sweep in both space directions (2D problems are considered) is carried out in Eq. (3.11) and Eq. (3.12) is solved by several iterations of an ADI Poisson solver to obtain the new divergence-free approximation of the velocity by Eq. (3.13). The pressure correction at level $m+1$ is given by Eq. (3.14). Note the solution strategy and the associated solvers are directly adapted from the initial Navier-Stokes solver in the time domain, which greatly simplifies the development cost of the method.

Another more recent contribution involving a frequency domain harmonic technique for incompressible flow can be found in the work of Welch & al [74]. In this study, a multi harmonic approach is applied to the stream function and vorticity transport formulation of the 2-D incompressible Navier-Stokes equations and used to efficiently obtain the time-periodic flow field associated with synthetic jets in quiescent flows and cross-flows.

Compressible flows

Hall & al in [30], then Chen & al [13] and McMullen [53] have been pioneering the use of harmonic methods in the frequency domain for the compressible Navier-Stokes equations. In order to explain the main design principles of their approach, let us start from the semi-discrete form (1.29) of the compressible Navier-Stokes equations introduced in Chapter 1:

$$\frac{\partial \boldsymbol{w}}{\partial t} + \mathcal{R}(\boldsymbol{w}) = 0 \tag{3.15}$$

where the residual operator $\mathcal{R}$ contains the spatial discretization of the convective and diffusive fluxes (see Eq. (1.27) and (1.28)).
Assuming again the time periodicity of $\boldsymbol{w}$ and therefore of $\mathcal{R}(\boldsymbol{w})$, with a pulsation ω, the Fourier transform of equation (3.15) reads :

$$\sum_{k=-\infty}^{k=+\infty} \left(\underline{i} k\omega |\Omega| \widehat{\boldsymbol{w}}_k + \widehat{\mathcal{R}}_k \right) e^{\underline{i} k\omega t} = 0 \tag{3.16}$$

As seen in the previous section, an equation for each mode can be deduced from equation (3.16), leading to:

$$\underline{i} k\omega \widehat{\boldsymbol{w}}_k + \widehat{\mathcal{R}}_k = 0, \quad \text{for } k \in [-N, N] \tag{3.17}$$

where only a limited number N of modes has been taken into account. The non-linearity of $\mathcal{R}$ implies:

$$\widehat{\mathcal{R}}_k(\boldsymbol{w}) \neq \mathcal{R}(\widehat{\boldsymbol{w}}_k) \tag{3.18}$$

The coefficients $\widehat{\mathcal{R}}_k$ can be computed from $\widehat{\boldsymbol{w}}_k$ but, unlike the nonlinear term in the incompressible momentum equation (see 3.8), the expression of the nonlinear operator for the compressible equations involves the product of u, v and ρ which must be individually developped as Fourier series. This results in complex series of convolution that becomes massively time consuming [30].
The alternative proposed by Hall & al in [30] is to compute $\widehat{\mathcal{R}}_k$ from the residual in the time domain $R(\boldsymbol{w})$, taking advantage of the Fast Fourier Transform (FFT) computational efficiency. The strategy is described in Figure 3.1: the vector $\boldsymbol{w}(t)$ is calculated from the Fourier coefficients $\widehat{\boldsymbol{w}}_k$ using an inverse FFT at evenly distributed intervals over the time period; at each of these time instances, the steady operator $\mathcal{R}(\boldsymbol{w}(t))$ can then be computed; next, a FFT is used to transform the spatial operator back into the frequency domain where $\widehat{\mathcal{R}}_k$ is known for all wavenumbers. The unsteady residual $\widehat{\mathcal{I}}_k = \underline{i}\ k\omega\widehat{\boldsymbol{w}}_k + \widehat{\mathcal{R}}_k$ is obtained by adding $\widehat{\mathcal{R}}_k$ to the spectral representation of the temporal derivative $\underline{i}k\omega\widehat{\boldsymbol{w}}_k$.

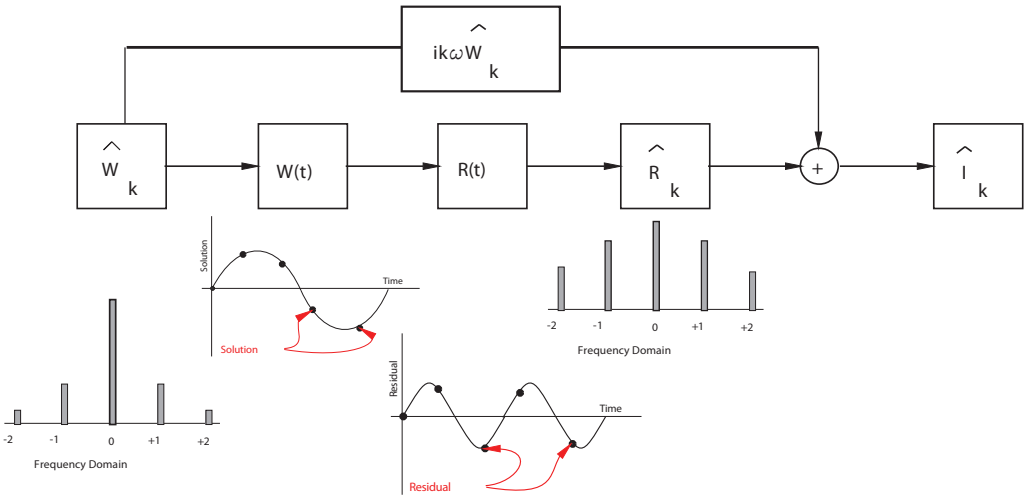

Figure 3.1: Simplified dataflow diagram of the time advancement scheme illustrating the pseudo spectral approach used in calculating the non-linear spatial operator from [52].

A first-order pseudo time derivative is eventually introduced in [30] to integrate equation (3.17) and yields:

$$\frac{\partial\widehat{\boldsymbol{w}}_k}{\partial\tau_k} + \underline{i}k\omega\widehat{\boldsymbol{w}}_k + \widehat{\mathcal{R}}_k = 0 \tag{3.19}$$

This method is named Non-Linear Frequency Domain (NLFD) since it takes into account the full non linearity of the operator $\mathcal{R}$ and solves the equations in the frequency domain. In [54], Mc Mullen & al test the NLFD on a laminar flow over a cylinder with an imposed Strouhal number and a turbulent pitching airfoil. It is demonstrated that, despite of

the cost of the FFT, the NLFD reduces the overall computational cost with respect to a conventional dual time step approach, as described in section 1.3.2.

3.2 Time domain methods

Frequency domain methods proved to be efficient and accurate for computing periodic flows and it is possible to rely on some key ingredients of an existing Time Domain solver to facilitate the development of the Frequency Domain solver (see for instance in the previous section the detailed description of the strategy proposed by [11, 12] which recycles the pressure correction strategy and Poisson solver from the time domain to the frequency domain). However, for compressible flow, an additional procedure must be implemented to compute the residual vector in the frequency domain. Besides, since most of the programming langages only deal with real numbers, the resolution of complex equation in the frequency domain comes down to the resolution of two equations. For the reasons mentionned above, it might be desirable to work in the time domain for an even more straightforward implementation of an harmonic method. Following this line of idea, Hall & al [31] suggested a strategy, called "Harmonic Balance Technique" (HBT), that cast the modal equations back into the time domain. HBT was further elaborated in 2005 by Gopinath and Jameson [27], who provided an explicit expression of the time spectral operator and christened the approach "Time Spectral Method" or TSM.

3.2.1 Time Spectral Method

The Nyquist-Shannon theorem [64] states that $2N+1$ time instances evenly distributed in the time period of a signal allow to compute at best the N^{th} harmonic of the fundamental frequency (the first harmonic being the fundamental frequency itself). Therefore, considering the Fourier series decomposition of $\boldsymbol{w}$ truncated to the N^{th} harmonic

$$\boldsymbol{w} = \sum_{k=-N}^{N} \widehat{\boldsymbol{w}}_k(x) e^{\underline{i}k\omega t} \tag{3.20}$$

the k^{th} Fourier coefficient $\widehat{\boldsymbol{w}}_k$ $(-N \leq k \leq N)$ can be accurately computed using the forward discrete Fourier transform over $2N+1$ time instances evenly distributed over the time period.
The analytic expression of this discrete Direct Fourier Transform (DFT) is given by :

$$\widehat{\boldsymbol{w}}_k(x) = \frac{1}{2N+1} \sum_{n=0}^{2N} \boldsymbol{w}_n e^{-\underline{i}k\omega n\Delta t} \tag{3.21}$$

with $\boldsymbol{w}_n \equiv \boldsymbol{w}(n\Delta t)$ and $\Delta t = T/(2N+1)$.

The main idea of the time domain spectral methods is to look for these solutions $\boldsymbol{w}_n$ in order to retrieve the solution at any time t in the period using (3.20).
Conversely the discrete Inverse Fourier Transform (IFT) allows to retrieve $\boldsymbol{w}_n$ using the harmonics :

$$\boldsymbol{w}_n = \sum_{k=-N}^{N} \widehat{\boldsymbol{w}}_k e^{\underline{i}k\omega n\Delta t} \tag{3.22}$$

These relations can be written in matrix form :

$$\widehat{\boldsymbol{w}}^* = \mathcal{E}\boldsymbol{w}^* \quad \text{and} \quad \boldsymbol{w}^* = \mathcal{E}^{-1}\widehat{\boldsymbol{w}}^* \tag{3.23}$$

where

$$\widehat{\boldsymbol{w}}^* = (\widehat{\boldsymbol{w}}_{-N}, \widehat{\boldsymbol{w}}_{1-N}, \cdots, \widehat{\boldsymbol{w}}_N), \quad \boldsymbol{w}^* = (\boldsymbol{w}_0, \boldsymbol{w}_1, \cdots, \boldsymbol{w}_{2N}) \tag{3.24}$$

The matrices of the DFT and IFT are given by :

$$\mathcal{E}_{k,n} = \frac{1}{2N+1}\exp(-2\underline{i}\pi k\frac{n}{2N+1}), \quad \mathcal{E}^{-1}_{k,n} = \exp(2\underline{i}\pi k\frac{n}{2N+1}) \tag{3.25}$$

The periodic solution of (3.15) is searched as the solution of the following problem:

$$\frac{\partial}{\partial t}(\boldsymbol{w}^*) + \mathcal{R}(\boldsymbol{w}^*) = 0 \tag{3.26}$$

Applying the DFT to (3.26) leads to $2N+1$ equations (one for each wavenumber) in the frequency domain similar to (3.17) and written here in matrix form:

$$\mathcal{D}\mathcal{E}\boldsymbol{w}^* + \widehat{\mathcal{R}}(\boldsymbol{w}^*) = 0 \tag{3.27}$$

where $\mathcal{D}$ is a diagonal matrix with elements defined by

$$\mathcal{D}_{kk} = \underline{i}k\omega \tag{3.28}$$

The application of the IFT to $\widehat{\mathcal{R}}^* = \widehat{\mathcal{R}}(\widehat{\boldsymbol{w}}^*)$ leads to the original expression $\mathcal{R}$ because the DFT is bijective. Besides, the IFT of the term $\mathcal{D}\mathcal{E}\boldsymbol{w}^*$ becomes a source term that coupling all the time instants :

$$\underbrace{\mathcal{E}^{-1}\mathcal{D}\mathcal{E}\boldsymbol{w}^*}_{D_t(\boldsymbol{w}^*)} + \mathcal{R}(\boldsymbol{w}^*) = 0 \tag{3.29}$$

Let us denote D_t the spectral operator approximating the physical time derivative $\dfrac{\partial}{\partial t}$ of equation (3.26)

$$D_t(\boldsymbol{w}^*) = \mathcal{E}^{-1}\mathcal{D}\mathcal{E}\boldsymbol{w}^* \approx \frac{\partial \boldsymbol{w}^*}{\partial t} \tag{3.30}$$

Gopinath and Jameson [27] have provided a detailed expression of this matrix spectral operator for each instant n:

$$D_t(\boldsymbol{w}_n) = \sum_{j=1}^{2N+1} d_{n,j}\boldsymbol{w}_{j-1} \tag{3.31}$$

with

$$d_{n,j} = \begin{cases} \frac{\pi}{T}(-1)^{n-j}\csc\left(\frac{\pi\ (n-j)}{2N+1}\right) & \text{if } n \neq j \\ 0 & \text{if } n = j \end{cases} \tag{3.32}$$

Performing the change of variable $p = j - i$, the expression of D_t simplifies into :

$$D_t(\boldsymbol{w}_n) = \sum_{p=-N}^{N} d_p\boldsymbol{w}_{n+p} \tag{3.33}$$

with

$$d_p = \begin{cases} \frac{\pi}{T}(-1)^{(p+1)}\csc\left(\frac{\pi p}{2N+1}\right) & \text{if } p \neq 0 \\ 0 & \text{if } p = 0 \end{cases} \tag{3.34}$$

Note the subscript $n + p$ of $\boldsymbol{w}$ in (3.33) actually refers to the remainder of the euclidian division of $n + p$ by $2N + 1$. Moreover, $d_{-p} = -d_p$ and $d_p = d_{p-N}$, so that the coefficients d_p need to be computed for $p \in [0; N]$ only.

Using (3.33) to approximate the physical time derivative at t_n, system (3.15) written at $t = t_n$ becomes:

$$D_t(\boldsymbol{w}_n) + \mathcal{R}(\boldsymbol{w}_n) = 0 \tag{3.35}$$

Since the spectral time-derivative depends on the whole set of solutions w_{n+p} with p ranging from $-N$ to N, system (3.35) must be written for each time instance in the period:

$$D_t(\boldsymbol{w}_n) + \mathcal{R}(\boldsymbol{w}_n) = 0, \quad 0 \leq n < 2N + 1 \tag{3.36}$$

with the residual vector $\mathcal{R}$ a non-linear function of $\boldsymbol{w}_n$. The non-linear system of equations (3.36) is iteratively solved through a dual time-marching strategy, that is looking for the steady-state with respect to τ of the following system

$$\frac{\partial \boldsymbol{w}_n}{\partial \tau} = -\mathcal{R}_n^t(\boldsymbol{w}), \quad 0 \leq n < 2N + 1 \tag{3.37}$$

where the total residual is defined as $\mathcal{R}_n^t(\boldsymbol{w}) = D_t(\boldsymbol{w}_n) + \mathcal{R}(\boldsymbol{w}_n)$ for the TSM approach.

The operator D_t is a spectral time discretization scheme centered on the time instant n.

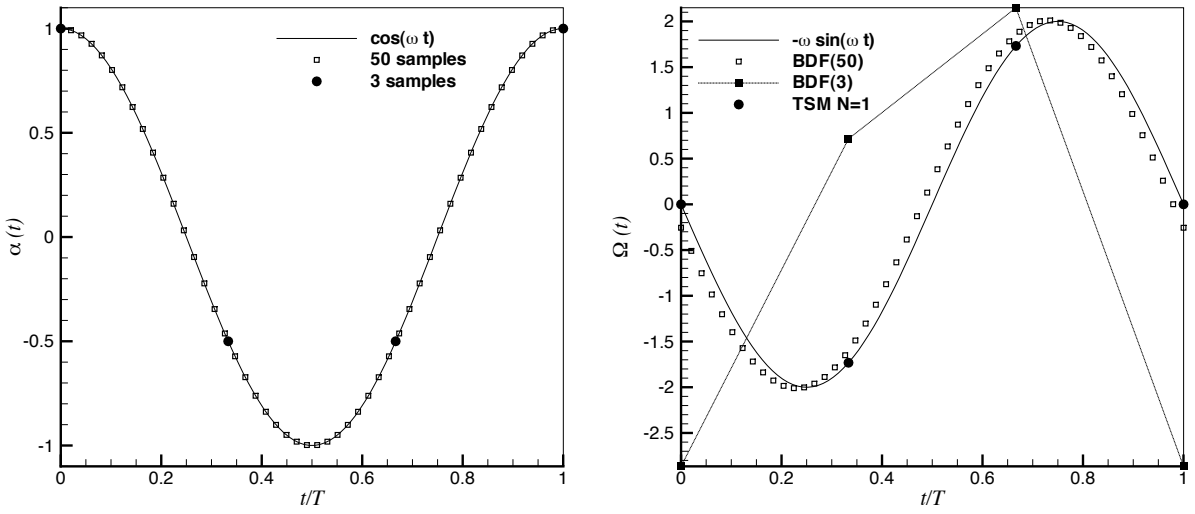

(a) cosine function

(b) derivative

Figure 3.2: Time derivative of the cosine function with the TSM and BDF approaches.

The accuracy of this spectral operator can be illustrated on the cosine function $f(t) = \cos(\omega t)$ (with $\omega = 2$). In figure 3.2a, f is sampled with 3 and 50 points. The 2nd order BDF scheme described by formula (**??**) is applied on the 50 points to estimate the derivative $f'(t) = -\omega \sin(\omega t)$; the periodicity condition is used to apply the 3-point scheme at the boundary points. The computed discrete derivative, denoted BDF(50), is displayed in figure 3.2b and shows a reasonable agreement with the exact derivative, despite a slight phase difference which goes to zero when the number of discretization points is increased. Meanwhile, the same BDF scheme applied with 3 discretization points only yields an approximate derivative, BDF(3), which is far from the exact solution. When the TSM scheme is applied with these same 3 discretization points evenly distributed on the period, an excellent approximation of the time derivative is obtained.

Odd-even decoupling

Equation (3.33) can be written as a matrix vector product:

$$D_t(\boldsymbol{w}_n) = D\boldsymbol{w}^* \tag{3.38}$$

where the matrix D^{odd} is given by :

$$D^{odd} = \begin{pmatrix} 0 & d_1^{odd} & \cdots & d_N^{odd} & -d_N^{odd} & \cdots & -d_1^{odd} \\ -d_1^{odd} & 0 & d_1^{odd} & d_2^{odd} & \cdots & \cdots & -d_2^{odd} \\ \vdots & \vdots & \vdots & \vdots & \vdots & \vdots & \vdots \\ d_1^{odd} & d_2^{odd} & \cdots & \cdots & -d_2^{odd} & -d_1^{odd} & 0 \end{pmatrix} \tag{3.39}$$

and the d_p^{odd} coefficients are given by (3.34). An even number of instants $2N$ could also be used. In that case, (3.33) and (3.34) become:

$$D_t(\boldsymbol{w}_n) = \sum_{p=-N}^{N-1} d_p^{even} \boldsymbol{w}_{n+p} \tag{3.40}$$

with

$$d_p^{even} = \begin{cases} \frac{\pi}{T}(-1)^{(p+1)} \cot\left(\frac{\pi p}{2N}\right) & : p \neq 0 \\ 0 & : p = 0 \end{cases} \tag{3.41}$$

and the matrix D^{even} is

$$D^{even} = \begin{pmatrix} 0 & d_1^{even} & \cdots & d_{N-1}^{even} & 0 & -d_N^{even} & \cdots & -d_1^{even} \\ -d_1^{even} & 0 & d_1^{even} & d_2^{even} & \cdots & 0 & \cdots & -d_2^{even} \\ \vdots & \vdots & \vdots & \vdots & \vdots & \vdots & \vdots & \vdots \\ d_1^{even} & d_2^{even} & \cdots & 0 & \cdots & -d_2^{even} & -d_1^{even} & 0 \end{pmatrix} \tag{3.42}$$

It is clear that every row of D^{even} contains two zeros, while the rows of D^{odd} have only one zero. As a consequence, D^{odd} has only one zero eigenvalue corresponding to eigenvector $e_1 = (1, 1, \Delta \cdots, 1)^T$. Eigenvector e_1 corresponds itself to a zero time derivative for a constant solution (all w_n are identical), a property of a consistent scheme. D^{even} has two zero eigenvalues with eigenvectors e_1 and $e_2 = (1, 0, 1, 0, \cdots, 1, 0)^T$. Eigenvector e_2 which results in a discrete zero time-derivative too corresponds to an odd-even decoupled solution, *i.e.* this mode is not damped by D^{even} and the scheme might become unstable. It was found in practice that, for cases of pitching airfoils and wings where the time derivative is relatively small, both D^{even} and D^{odd} are stable. However for problems where the time derivative becomes large, *e.g.* high rotational speed turbomachinery problems, the odd-even decoupling introduces instabilities, which lead to the failure of the algorithm using an even number of time intervals. Consequently, only an odd number of time intervals will be used from now on.

3.2.2 Pseudo-time marching and TSM strategies

The TSM strategy applied to solve a time-periodic flow governed by (3.15)

$$\frac{\partial \boldsymbol{w}}{\partial t} + \mathcal{R}(\boldsymbol{w}) = 0$$

transforms the original equation (3.15) into a set of coupled steady equations (3.36)

$$D_t(\boldsymbol{w}_n) + \mathcal{R}(\boldsymbol{w}_n) = 0, \quad 0 \leq n < 2N+1$$

or, using the vector notation (3.24)

$$D_t(\boldsymbol{w}^*) + \mathcal{R}(\boldsymbol{w}^*) = 0.$$

In the remainder of this report, the notation $\boldsymbol{w}_n$ will be favored because it makes more explicit the discretization index n in the time domain. When describing fully discrete TSM strategies, the index i, n for the solution vector w will refer to the grid cell space-location i and time-location n within the period. Moreover, since the non-linear system of equations (3.36) is solved using a sub-iterative process (3.37) the quantity w_n^m is introduced to denote the flow solution at (physical) time-instance n and sub-iteration m (the space discretization is not considered here for the sake of simplicity); similarly, $(\boldsymbol{w}^*)^m$ would denote the set of flow solutions at all the time-instances spanned over the period, computed at the m^{th} level of the sub-iterative process converging to a steady-state with respect to τ. Assuming for instance a simple Euler explicit approximation for the dual-time derivative in (3.37) leads to:

$$\frac{(\boldsymbol{w}^*)^{m+1} - (\boldsymbol{w}^*)^m}{\Delta\tau} = -D_t((\boldsymbol{w}^*)^m) - \mathcal{R}((\boldsymbol{w}^*)^m) \tag{3.43}$$

Fig. 3.3 illustrates the convergence process for (3.43). The targeted (unknown) solution of (3.36) - or equivalently steady solution of (3.43) - is plotted over a period as a solid line; the initial state $(\boldsymbol{w}^*)^0$ is typically defined using the free-stream value associated with each TSM instant, represented by points on the figure 3.3(a). After several sub-iterations on m using (3.43), the flow solution $(\boldsymbol{w}^*)^m$ takes for instance the intermediate values depicted in Fig.3.3(b). When full steady convergence is achieved on 3.43 after m_{max} sub-iterations, the TSM states provide an accurate representation $(\boldsymbol{w}^*)^{m_{max}}$ of the periodic solution instances $\boldsymbol{w}^*$. For a given number of modes N (fixed by accuracy considerations), the efficiency of the TSM strategy is therefore directly related to the number of sub-iterations m_{max} needed to achieve a steady-state on τ and to the computational time spent to evolve from $(\boldsymbol{w}^*)^m$ to $(\boldsymbol{w}^*)^{m+1}$. The choice of an optimal dual-time marching strategy (explicit / implicit) will be discussed in the next chapter. It is worth noticing that some computational time might be saved by first computing the $2N+1$ steady uncoupled equations as the initial guess of the solution [76].

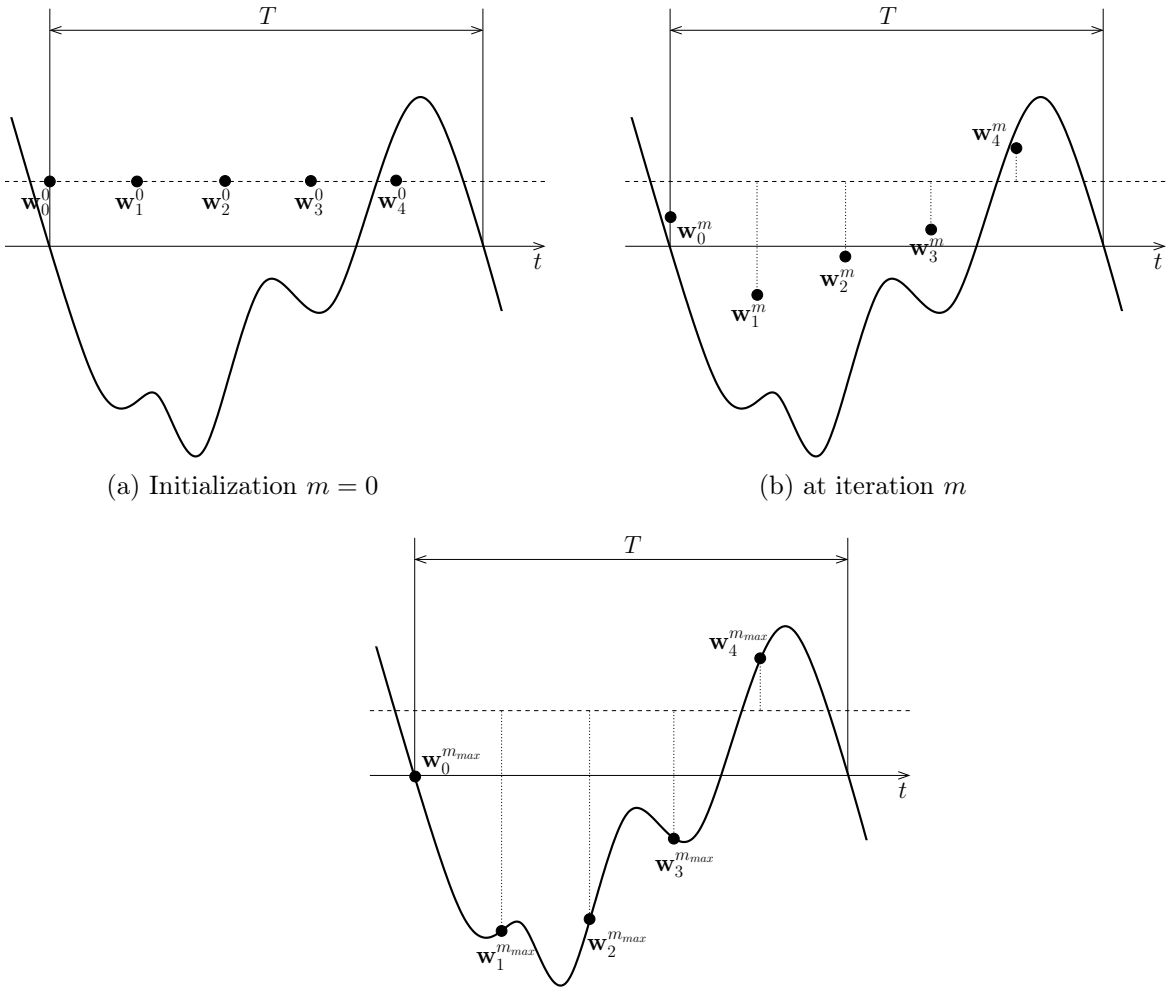

(a) Initialization $m = 0$

(b) at iteration m

(c) Final converged solution $m = m_{max}$

Figure 3.3: TSM dual time-marching convergence principle

3.3 Selected method

The Time Spectral Method has been retained in this work because it can be implemented within an existing time-accurate solver with a moderate amount of effort. Indeed, the available code at the beginning of this Ph.D was a compressible unstructured grid solver. Thus, the TSM has been first tested in this code to deal with compressible applications which are the topic of Chapter 6.2.3.

Once the TSM has been validated for these compressible cases, the Artificial Compressibility (AC) strategy has been favored to deal with incompressible applications because of the ease of coding starting from the original compressible code (see Chap. 2). The implementation of the implicit TSM for compressible and incompressible flows will be presented in the next Chapter 4 and TSM incompressible results are gathered in Chapter 7.

Had the reference code been a pressure-based incompressible solver, the strategy would certainly have been different. Indeed, we could imagine to apply the TSM to the incompressible system of Navier-Stokes. System (3.4) would be transformed into:

$$\left.\begin{array}{l} D_t(\boldsymbol{v}_n) + \boldsymbol{v}_n \nabla \boldsymbol{v}_n - \nu \nabla^2 \boldsymbol{v}_n + \nabla p_n = 0 \\ \nabla . \boldsymbol{v}_n = 0 \end{array}\right\} \quad 0 \leq n < 2N+1 \tag{3.44}$$

And the time domain discretized system equivalent to (3.10) is

$$\left.\begin{array}{l} \dfrac{\boldsymbol{v}_n^{m+1} - \boldsymbol{v}_n^m}{\Delta\tau} + D_t(\boldsymbol{v}_n^{m(+1)}) + \boldsymbol{v}_n^m \nabla \boldsymbol{v}_n^{m+1} - \nu \nabla^2 \boldsymbol{v}_n^{m+1} + \nabla p_n^m = 0 \\ \nabla . \boldsymbol{v}_n^{m+1} = 0 \end{array}\right\} \quad 0 \leq n < 2N+1 \tag{3.45}$$

Again, the TSM time instants are coupled trough the TSM source term which can be treated explicitely or implicitely. The individual equations, modified with this additional source term, can be solved with the incompressible solver [37, 9] presented in Sec. 3.1.2 for the frequency domain harmonic method for instance.

This method has not been further investigated but could be worth developing in order to be compared with its frequency domain counterpart (See section 3.1.2).

Moreover, in the literature, we find that the harmonic methods have been extended to much more complex situations where the frequency is not known a-priori [28, 67], the number of harmonics is adapted in each grid cell to fit the harmonic content [50], when the TSM time sampling is not uniform [56], when there are multiple excitation fundamental frequencies [21, 20]. A short review of these methods is present in reference [65].

An attempt to carry out the Gradient Based Variable Time Period (GBVTP) [28] to deal with self-induced periodic behavior in the laminar wake of a cylinder is presented in Appendix D.

However, in the remainder of the report, we will limit the range of applications to periodic-flows with a single fundamental excitation frequency and only the "basic" TSM will be used.

Chapter 4

Implicit Time Spectral Method

As explained in the previous chapter, the efficiency of the Time Spectral Method depends for a great part on the numerical strategy used to drive the coupled equations (3.37) to a steady-state on the dual or fictitious time τ. It will be first recalled that the explicit dual-time integration of the TSM system displays severe stability limits when the number of harmonics N increases and/or the frequency is high. This is why several authors [66, 76, 68] in the recent past have put forward implicit solution strategies that allow the use of both large CFL numbers ensuring faster convergence to a steady-state and a high number of harmonics N that might be needed to accurately describe complex unsteady flows. However, the TSM implicit formulation introduces off-diagonal terms in the implicit matrix, which can make the linear system hard to solve with simple relaxation techniques such as Point Jacobi or Gauss-Seidel. A simple fix will be presented, that allows to successfully extend to the TSM formulation an original matrix free implicit formulation initially developed for BDF-DTS computations.

4.1 Explicit TSM for compressible flows

4.1.1 Combining TSM and ALE

Recalling on one hand the description of the ALE formulation provided in 1 and on the other hand the TSM system (3.37) introduced in the previous Chapter, it is possible to write a generalization of the TSM approach within an ALE framework :

$$\frac{\partial \boldsymbol{w}_n}{\partial \tau} = -\mathcal{R}_n^t(\boldsymbol{w}, \boldsymbol{x}_n, \boldsymbol{s}_n), \quad 0 \leq n < 2N+1 \tag{4.1}$$

where the total residual is defined as $\mathcal{R}_n^t(\boldsymbol{w}) = D_t(\boldsymbol{w}_n) + \mathcal{R}(\boldsymbol{w}_n, \boldsymbol{x}_n, \boldsymbol{s}_n)$ for the TSM approach. In the present study, the $2N+1$ grid positions $\boldsymbol{x}_n$ and velocities $\boldsymbol{s}_n$ are *a priori* known from the prescribed grid motion. For each instant n, the grid is moved to its expected position and the grid velocity $\boldsymbol{s}_n$ needed for the computation of the ALE

convective fluxes is analytically computed using Eq. (1.30) at time instance t_n.
Note this simplified implementation is made possible because the mesh remains rigid during the motion in the application test-cases treated in this work. However, when the mesh is deforming in the general case, the task of determining the grid velocity is not trivial. Indeed, as seen in section 1.3.1, the grid velocity for general moving mesh application is calculated using a linear combination of the surrounding mesh position corresponding to physical time steps t^{n-1}, t^n, t^{n+1}. If the same method is used for TSM computations, it can lead to non-negligible errors, especially if a small number of harmonics is considered, *i.e.* if the mesh positions are significantly spaced out. Sicot & al [65] propose to use the mesh positions at the TSM instants and the spectral time derivative to compute the deforming grid velocity. Such as strategy is well justified by the spectral accuracy of the time derivative operator which was exemplified in Figure 3.2b. Another well-known issue when dealing with dynamically deforming grids is the implementation of a Geometric Conservation Law (see Sec. 1.3.1). A GCL for the TSM in the context of unstructured grids has been recently presented by Yang and Mavriplis [77].
As previously described in Section 3.2.2 for a fixed grid, a simple first-order Euler explicit discretization of the dual-time derivative appearing in (4.1), yields the following iterative formula for the TSM time-marching process to a dual-time steady-state:

$$\frac{\Delta \boldsymbol{w}_n^m}{\Delta \tau_n^m} = -\mathcal{R}_n^t(\boldsymbol{w}^m, \boldsymbol{x}_n, \boldsymbol{s}_n), \quad 0 \leq n < 2N+1 \tag{4.2}$$

where $\Delta \boldsymbol{w}_n^m = \boldsymbol{w}_n^{m+1} - \boldsymbol{w}_n^m$ and $\Delta \tau_i^m$ is the local (dual) time-step in cell i of the grid associated to the time instance t_n within the period.

4.1.2 Stability Analysis

Van der Weide & al [72] have proposed a stability analysis for the pseudo time step $\Delta\tau$ when used in the TSM approach (4.2), which leads to a new stability condition (depending on the problem frequency and the number of modes N) with respect to the usual stability condition (1.39) recalled in Chapter 1.
In the frequency domain, an explicit formulation of (4.2) for wave-number k with a local pseudo-time step $\Delta\tau_k$ reads :

$$\frac{\widehat{\boldsymbol{w}}_{i,k}^{m+1} - \widehat{\boldsymbol{w}}_{i,k}^m}{\Delta \tau_{i,k}^m} + \underline{i} k\omega \widehat{\boldsymbol{w}}_{i,k}^m + \widehat{\mathcal{R}}_{i,k}^m = 0 \tag{4.3}$$

Following the linearization strategy of the spatial operator described in section 1.3.3, (4.3) can also be recast in the form:

$$\widehat{\boldsymbol{w}}_{i,k}^{m+1} \approx \left(\boldsymbol{I_d} - \widehat{\boldsymbol{J}}_{i,k}^m \frac{\Delta \tau_{i,k}^m}{h_i} - \Delta \tau_{i,k}^m \underline{i} k\omega\right) \widehat{\boldsymbol{w}}_{i,k}^m \tag{4.4}$$

where $\widehat{\boldsymbol{J}}_{i,k}^m$ is the Jacobian matrix of the frequency residual vector $\widehat{\mathcal{R}}_{i,k}^m$. As first established in [72], the pseudo time step in the frequency domain $\Delta\tau_{i,k}^m$ ensuring the stability of (4.4) can be estimated as :

$$\Delta\tau_{i,k}^m = \mathrm{CFL}\frac{h_i}{||\lambda||_{i,k}^m + k\omega h_i} \tag{4.5}$$

with h_i a characteristic length of the cell i in the computational grid, $||\lambda||_{i,k}^m$ the spectral radius of the frequency Jacobian matrix $\widehat{\boldsymbol{J}}_{i,k}^m$ and the CFL number such that $CFL \leq 1$.

An additional term based on the wave number is added to the denominator of (4.5) compared to the standard steady definition of equation (1.39). The maximal pseudo-time step given by (4.5) is associated with a solution in the frequency domain. To estimate a maximal pseudo-time step in the time domain, a first strategy is to consider the inverse Fourier transform of equation (4.3) for all the wavenumbers $-N \leq k \leq N$:

$$\mathcal{E}^{-1}\left(\frac{\Delta\widehat{\boldsymbol{w}}_i^{*,m}}{\Delta\tau_i^{*,m}} + \underline{i}k\omega\widehat{\boldsymbol{w}}_i^{*,m} + \widehat{\mathcal{R}}_i^{*,m}\right) = 0 \tag{4.6}$$

or

$$\mathcal{E}^{-1}\left(\frac{\Delta\widehat{\boldsymbol{w}}_i^{*,m}}{\Delta\tau_i^{*,m}}\right) + D_t(\boldsymbol{w}_i^{*,m}) + \mathcal{R}(\boldsymbol{w}_i^{*,m}) = 0 \tag{4.7}$$

Such an inverse Fourier transform operation, with different time steps $\Delta\tau_{i,k}^*$ in the frequency domain, yields a matrix time-step in the time domain coupling all the time levels t_n. The proper estimate of the local time-step would then require to invert this matrix in each cell and at every pseudo time iteration, making this approach rather costly.

Alternatively, a time-step in the frequency domain corresponding to the highest mode, *i.e.* the most restrictive of all wavenumbers, can be used; the local pseudo-time no longer depends on the wave number and is given by:

$$\Delta\tau_i^m = \mathrm{CFL}\frac{h_i}{||\lambda||_{i,N}^m + N\omega\ h_i} \tag{4.8}$$

On transforming back into the time domain, the time-step $\Delta\tau_i^m$ retains the form (4.8) since it is independent of the wave-number. Note this choice of time-step is likely to become restrictive when the number of harmonics increases and/or the frequency of the periodic phenomenon is high. However such a simplified choice considerably reduces the computational cost required by the multiple matrix inversions associated with the IFT of the wave-number dependent choice Eq. (4.5)

Actually, for programming reasons, a slightly different definition was adopted, which takes into account the difference of spectral radius for the time instances t_n:

$$\Delta\tau_i^m = \mathrm{CFL}\frac{h_i}{||\lambda||_{i,n}^m + \omega N h_i} \tag{4.9}$$

However, the use of large CFL makes no difference between the two definitions.

4.2 Implicit Time Spectral Method

Using an Euler implicit dual-time strategy for integrating (4.1) in each grid cell i at each time instance t_n allows the use of large dual-time steps, hence fast convergence to a steady-state independently of ω or N, but the following implicit non-linear TSM-ALE problem must be solved:

$$\frac{\Delta \boldsymbol{w}_n^m}{\Delta\tau_n^m} = -\mathcal{R}_n^t(\boldsymbol{w}^{m+1}, \boldsymbol{x}_n, \boldsymbol{s}_n), \quad 0 \leq n < 2N+1 \tag{4.10}$$

From now on and for the sake of simplicity, the dependence of the spatial residual vector on the grid position $\boldsymbol{x}_n$ and mesh velocity $\boldsymbol{s}_n$ will no longer appear. How these terms are computed in the present work has been explained in the previous Section.

4.2.1 Semi-implicit approach

The most straightforward implicitation of the TSM scheme computes the spatial residual vector at the new time level but leaves the computation of the time spectral derivative at the known time level, leading to the following equation:

$$\frac{\Delta \boldsymbol{w}_n^m}{\Delta\tau_n^m} = -D_t(\boldsymbol{w}_n^m) - \mathcal{R}(\boldsymbol{w}_n^{m+1}), \quad 0 \leq n < 2N+1 \tag{4.11}$$

The residual vector at iteration $m+1$ is next linearized around the state at iteration m:

$$\mathcal{R}(\boldsymbol{w}_n^{m+1}) \approx \mathcal{R}(\boldsymbol{w}_n^m) + \boldsymbol{J}_n\ \Delta \boldsymbol{w}_n^m + \mathcal{O}(\Delta \boldsymbol{w}_n^2) \tag{4.12}$$

where $\boldsymbol{J}_n$ is the Jacobian matrix $\boldsymbol{J}_n = \dfrac{\partial \mathcal{R}_n(\boldsymbol{w})}{\partial \boldsymbol{w}}$. The final formulation of the semi-implicit method reads:

$$\left(\frac{\boldsymbol{I_d}}{\Delta\tau_n^m} + \boldsymbol{J}_n\right)\Delta \boldsymbol{w}_n^m = -\mathcal{R}_n^t(\boldsymbol{w}^m), \quad 0 \leq n < 2N+1 \tag{4.13}$$

This method is very simple to implement since it introduces no formal modification of the implicit stage with respect to the one used for DTS-BDF in Chapter 1. The $2N+1$ steady states at time instances t_n are coupled through the explicit stages only. Previous authors [66, 76] report stability problems quickly arise with this semi-implicit formulation; therefore it will not be further investigated in this work.

4.2.2 Full implicitation

To improve the stability, the source term of the TSM is treated implicitly, that is computed at the new time level $m+1$, which yields:

$$\frac{\Delta \boldsymbol{w}_n^m}{\Delta \tau_n^m} = -D_t(\boldsymbol{w}_n^{m+1}) - \mathcal{R}(\boldsymbol{w}_n^{m+1}), \quad 0 \leq n < 2N+1 \tag{4.14}$$

The linearity of the D_t operator allows to write

$$D_t(\boldsymbol{w}_n^{m+1}) = D_t(\boldsymbol{w}_n^m) + D_t(\Delta \boldsymbol{w}_n^m) \tag{4.15}$$

so that the full implicitation of the TSM eventually reads:

$$\left(\frac{1}{\Delta \tau_n^m} + \boldsymbol{J}_n\right)\Delta \boldsymbol{w}_n^m + D_t(\Delta \boldsymbol{w}_n^m) = -\mathcal{R}_n^t(\boldsymbol{w}^m), \quad 0 \leq n < 2N+1 \tag{4.16}$$

Since $d_0 = 0$ in the spectral time derivative operator, the diagonal terms of the implicit TSM matrix are not modified compared to the steady state solver implicit matrix but new off-diagonal terms are introduced. The TSM fully implicit formulation (4.16) can be written in matrix form:

$$\boldsymbol{A}^{*,m}\Delta \boldsymbol{w}^{*,m} = -\mathcal{R}^t\left(\boldsymbol{w}^{*,m}\right) \tag{4.17}$$

with

$$\boldsymbol{A}^* = \begin{pmatrix} \frac{\boldsymbol{I_d}}{\Delta \tau_0} + \boldsymbol{J}_0 & d_1\boldsymbol{I_d} & \cdots & d_N\boldsymbol{I_d} & d_{-N}\boldsymbol{I_d} & \cdots & d_{-1}\boldsymbol{I_d} \\ d_{-1}\boldsymbol{I_d} & \ddots & \ddots & \vdots & \ddots & \ddots & \vdots \\ \vdots & \ddots & \ddots & d_1\boldsymbol{I_d} & \ddots & \ddots & \vdots \\ d_{-N}\boldsymbol{I_d} & \cdots & d_{-1}\boldsymbol{I_d} & \frac{\boldsymbol{I_d}}{\Delta \tau_N} + \boldsymbol{J}_N & d_1\boldsymbol{I_d} & \cdots & d_N\boldsymbol{I_d} \\ \vdots & \ddots & \ddots & d_1\boldsymbol{I_d} & \ddots & \ddots & \vdots \\ \vdots & \ddots & \ddots & \vdots & \ddots & \ddots & d_1\boldsymbol{I_d} \\ d_1\boldsymbol{I_d} & \cdots & d_N\boldsymbol{I_d} & d_{-N}\boldsymbol{I_d} & \cdots & d_{-1}\boldsymbol{I_d} & \frac{\boldsymbol{I_d}}{\Delta \tau_{2N}} + \boldsymbol{J}_{2N} \end{pmatrix} \tag{4.18}$$

4.2.3 Review of the implicit TSM solvers

All the existing contributions on the implicit formulation of the TSM strategy [66, 76, 68] start from an implicit scheme of the form (4.17). These contributions differ by the solution method applied manifold.

The goal of this section is not to present the numerous existing implicit linear solvers (see [15] for instance) but to focus on the solutions adopted by previous researchers to deal with the specificities of the new matrix $\boldsymbol{A}^*$ associated with TSM implicit treatment.
The main problem arising with the full implicit TSM formulation is the emergence of off-diagonal terms introduced by the D_t operator applied on the increments $\Delta \boldsymbol{w}$. These off-

diagonal terms and the zero-contribution of D_t to the diagonal coefficients of the implicit TSM matrix lead to a loss of diagonal dominance for the matrix $\boldsymbol{A}^*$ which can compromise the performance of some linear solvers.
In the context of turbomachinery simulations on structured grids, Sicot & al [66] solved the system (4.17) with a block Jacobi method. The implicit coupling term $D_t(\Delta \boldsymbol{w}_n^m)$ were thus moved to the right hand side of the implicit scheme leaving a diagonally dominant left-hand-side matrix; an over-relaxation strategy was used at each Jacobi iteration to speed up the convergence of the method.

Su & al [68] also noticed that the fully-implicit TSM can leads to a loss of diagonal dominance for the matrix $\boldsymbol{A}^*$ associated with the implicit scheme. Therefore, they use the GMRES solver of Saad and Schultz [63] to solve Eq. (4.17).
Woodgate & al [76] also noticed this problem and eventually solved the linear system using a Krylov subspace method with BILU factorization and no fill-in (*i.e.* the sparsity pattern of the factorization is the same as the coefficient matrix).

Let us point out the contributions [66], [68] and [76], published in 2008 and 2009, were all devoted to structured grid computations. Recently, in June-July 2010, Z. Yang and D. Mavriplis [77] have presented results obtained on unstructured meshes using the TSM method for periodic and quasi-periodic unsteady computations. The main contribution of their work is the extension of TSM to deal with flows including a slow transient in addition to strong periodic behavior. It can be noted however a fully implicit treatment is also used in their work, relying on a block Jacobi method which combines, on unstructured grids, multigrid and line-implicit agglomeration techniques D. Mavriplis is well known for [51].

4.2.4 Matrix-free implicit solution with Jacobi iteration

In the present work, the matrix-free implicit treatment described in Chapter 1 for the BDF approach (see Sec. 1.4.1) is adapted to deal with the TSM implicit stage. The TSM residual at dual time-level $m+1$ can be approximated as follows :

$$\mathcal{R}_{i,n}^t\left(\boldsymbol{w}^{m+1}\right) = \mathcal{R}_{i,n}^t\left(\boldsymbol{w}^m\right) + D_t(\Delta \boldsymbol{w}_{i,n}^m) + \frac{1}{|\Omega_i|}\sum_k \left(\Delta \mathcal{H}_{(i,k),n}^{(i)}\right)^m \; |\Gamma_{i,k}| \tag{4.19}$$

where the balance of the flux increment is computed using the formulae (1.45) and (1.46) previously introduced when deriving the BDF implicit stage but now applied with the variable increment $\Delta \boldsymbol{w}_{i,n}^m$ instead of $\Delta \boldsymbol{w}_i^{n,m}$. It is important to point out $\Delta \boldsymbol{w}_{i,n}^m$ used in the TSM strategy denotes the conservative variable increment at point i,n in the space and time domain, with a time domain spectral discretization applied on a single flow period; the exponent m refers to the time-marching index to the dual steady-state. In contrast, $\Delta \boldsymbol{w}_i^{n,m}$ used in the BDF-DTS strategy denotes the conservative variable increment at point i in the space domain with an exponent n,m referring to the m^{th} sub-iteration of

the time-marching process on the pseudo-time τ performed at each physical-time level n. Expanding the flux increment balance and the spectral approximation of the physical time derivative with (3.33) and (3.34) leads to the following implicit relationship, where the terms depending on $\Delta \boldsymbol{w}_{i,n}^m$ have been gathered in the LHS:

$$\begin{aligned}\left(\frac{1}{\Delta\tau_i^m}+\sum_k C_{(i,k),n}^m\right)\Delta\boldsymbol{w}_{i,n}^m \;=\; & -\mathcal{R}_{i,n}^t(\boldsymbol{w}^m)-\frac{1}{2|\,\Omega_{i,n}|}\sum_k\left(\Delta\boldsymbol{F}_{o(i,k),n}^E\right)^m\cdot\boldsymbol{n}_{(i,k),n}\;|\Gamma_{(i,k),n}| \\ & +\sum_k C_{(i,k),n}^m\Delta\boldsymbol{w}_{(o(i,k)),n}^m-\sum_{p=-N}^{N}d_p\Delta\boldsymbol{w}_{i,n+p}^m\end{aligned} \tag{4.20}$$

with the scalar coefficients $C_{(i,k),n}^m$ defined by (notation for spectral raddi are unchanged with respect to Chapter 1):

$$C_{(i,k)n}^m=\frac{1}{|\Omega_{i,n}|}\left(\frac{1}{2}\rho(\boldsymbol{J}_\perp^E)+\widetilde{\rho(\boldsymbol{J}_\perp^V)}\right)_{(i,k),n}^m|\Gamma_{(i,k),n}| \tag{4.21}$$

Since (4.20) is formally very close to (1.47), it makes sense to straightforwardly apply the point-Jacobi relaxation procedure described by (1.49) in Chapter 1 to the resolution of (4.20). However, doing so, stability problems quickly appear because of the loss of diagonal dominance for $\boldsymbol{A}^*$ translated to the presence of the term $\displaystyle\sum_{p=-N}^{N}d_p\Delta\boldsymbol{w}_{i,n+p}^m$ in the RHS of (4.20). A simple fix is adopted in this work: the LHS diagonal coefficient $D_{i,n}^m$ of $\Delta\boldsymbol{w}_{i,n}^m$ is modified to include the contribution $\displaystyle\sum_{p=-N}^{p=N}|d_p|$, which is sufficient to ensure the diagonal dominance of the implicit stage with only a limited impact on its efficiency. System (4.20) is then iteratively solved using a simple PJ relaxation technique, yielding the following PJ-TSM-ALE system:

$$\begin{aligned}&\Delta\boldsymbol{w}_{i,n}^{(0)}=0\\ &\begin{cases}l=0,\;l_{max}-1\\ \Delta\boldsymbol{w}_{i,n}^{(l+1)}=\left(D_{i,n}^m\right)^{-1}\\ \left(-\mathcal{R}_{i,n}^t(\boldsymbol{w}^m)-\dfrac{1}{2|\,\Omega_{i,n}|}\displaystyle\sum_k\left(\Delta\boldsymbol{F}_{o(i,k),n}^E\right)^{(l)}\cdot\boldsymbol{n}_{(i,k),n}\;|\Gamma_{(i,k),n}|+\sum_k C_{(i,k),n}^m\Delta\boldsymbol{w}_{(o(i,k)),n}^{(l)}-\displaystyle\sum_{p=-N}^{N}d_p\Delta\boldsymbol{w}_{i,n+p}^{(l)}\right)\end{cases}\\ &\boldsymbol{w}_{i,n}^{m+1}=\boldsymbol{w}_{i,n}^m+\Delta\boldsymbol{w}_{i,n}^{(l_{max})}\end{aligned} \tag{4.22}$$

with the modified diagonal coefficient $D_{i,n}^m=\dfrac{1}{\Delta\tau_i^m}+\displaystyle\sum_k C_{(i,k),n}^m+\sum_{p=-N}^{N}|d_p|$.

4.3 Adaptation of TSM to artificial compressibility

To the best of our knowledge, the only previous application of TSM to the AC system for incompressible laminar periodic flow has been performed by Jameson [35], but with a limited success since stability concerns were encountered for high frequency and/or large number of harmonics.
The space-discretized ALE-AC system at time instance t_n reads

$$\frac{\partial \boldsymbol{w}_n}{\partial \tau} + \boldsymbol{K}\frac{\partial \boldsymbol{w}_n}{\partial t} + \mathcal{R}(\boldsymbol{w}_n, \boldsymbol{x}_n, \boldsymbol{s}_n) = 0 \tag{4.23}$$

where

$$\boldsymbol{K} = \begin{pmatrix} 0 & 0 & 0 \\ 0 & 1 & 0 \\ 0 & 0 & 1 \end{pmatrix}$$

If the physical time operator is replaced by the Time Spectral operator coupling all the time instants, the TSM-ALE-AC system reads

$$\frac{\partial \boldsymbol{w}_n}{\partial \tau} + \boldsymbol{K} D_t(\boldsymbol{w}_n) + \mathcal{R}(\boldsymbol{w}_n, \boldsymbol{x}_n, \boldsymbol{s}_n) = 0, \quad 0 \leq n < 2N+1 \tag{4.24}$$

The derivation of a fully implicit treatment for the TSM-ALE-AC system (4.24) is highly similar to the derivation of the fully implicit treatment for the ALE-AC system with BDF time-integration (2.5) described in Section 2.3.2. The design of this implicit scheme faces the same loss of diagonal dominance issue than the one met in the compressible case, at least for the momentum equation since there is no physical time-derivative hence no TSM term coupling the pressure variables p_n in the continuity equation. The need to distinguish between the continuity and momentum equations is easily taken into account using the singular matrix $\boldsymbol{K}$ previously introduced in Chapter 2.
Eventually, the implicit expression equivalent to (4.20), but for the TSM-ALE-AC system is:

$$\begin{aligned}\left(\frac{1}{\Delta\tau_i^m} + \sum_k C^m_{(i,k),n}\right)\Delta \boldsymbol{w}^m_{i,n} \;=\; & -\mathcal{R}^t_{i,n}(\boldsymbol{w}^m) - \frac{1}{2|\ \Omega_{i,n}|}\sum_k \left(\Delta \boldsymbol{F}^E_{o(i,k),n}\right)^m \cdot \boldsymbol{n}_{(i,k),n}\ |\Gamma_{(i,k),n}| \\ & + \sum_k C^m_{(i,k),n}\Delta \boldsymbol{w}^m_{(o(i,k)),n} - \boldsymbol{K}\sum_{p=-N}^{N} d_p \Delta \boldsymbol{w}^m_{i,n+p}\end{aligned} \tag{4.25}$$

with the appropriate AC definitions for the primitive variable, fluxes and residuals given in Chapter 2. For instance, the scalar coefficients $C^m_{(i,k),n}$ still defined by equation (4.21) involve spectral radii that correspond to the AC Jacobian matrices.
Equation (4.25) is solved with the iterative PJ procedure just described in the previous section for the compressible system yielding to the PJ-TSM-ALE-AC solver. Again, since

there is no TSM coupling term for the pressure variables p_n, there is no need to modify the diagonal coefficient for the continuity equation so that

$$D_{i,n}^m = \frac{1}{\Delta\tau_i^m} + \sum_k C_{(i,k),n}^m + \boldsymbol{K} \sum_{p=-N}^{N} |d_p|$$

4.4 Assesment of TSM against BDF

Before proceeding to the application of the TSM approach to a model heat conduction problem in the next chapter and to some external flow applications in the part III of this thesis report, let us introduce the tools and indicators that will be used to quantify the perform of TSM and assess the interest of the approach as an alternative to BDF-DTS when computing time-periodic problems.

4.4.1 Convergence of the TSM approach

With the TSM approach, the full unsteady residual of the BDF method $\mathcal{R}^t(\boldsymbol{w}^{n,m+1})$ is replaced by a full steady residual $\mathcal{R}^t(\boldsymbol{w}_n^{m+1})$. Both BDF and TSM benefit from the use of large CFL numbers hence large $\Delta\tau$ made possible by the implicit dual-time formulation. The main difference between these approaches is that BDF has to be converged to a dual steady-state at each physical time-iteration of a time-marching process performed on the space domain while TSM has to be converged only once to a dual steady-state but on an extended physical time and space domain. Expressed in yet another way, BDF requires to solve many times linear systems of moderate size (equal to the number of cells in the space grid multiplied by the number of conservative variables) while TSM requires to solve once a large linear system (the size of which is the size of the BDF linear systems multiplied by the number of time instances in the period). The other difference is the nature of the source term introduced by the physical-time approximation (using BDF or TSM) which strongly impacts the convergence rate to the dual steady-state.

The convergence of (4.22) to a steady-state is monitored by plotting the pressure residual defined as the root mean square of the residual operator $\mathcal{R}^t(\boldsymbol{w})$ first component, computed in all the grid cells and averaged by the number of time instances over the period:

$$res_{av}^m = \frac{1}{2N+1} \sum_{n=0}^{2N} \sqrt{\frac{1}{N_{cell}} \sum_{i=1}^{N_{cell}} \frac{\Delta p_{i,n}^{m\,2}}{\Delta\tau_i^{m2}}} \tag{4.26}$$

This quantity is normalized by its value at the first iteration to facilitate the comparison between calculations performed with different values for the number of harmonics N.

4.4.2 Accuracy

As seen in Chapter 1 and Chapter 2 when applying the BDF compressible and incompressible flow solver, the accuracy of a BDF computation for a quantity of interest, denoted C for the sake of argument, strongly depends on the fact the fully periodic regime is indeed reached. This condition is satisfied in practice by computing for instance the difference of the C time-average between two consecutive cycles and imposing this difference to drop below 2% to stop the unsteady computation. When applying TSM, the convergence to the (dual) steady-state is the sole condition to satisfy in order to obtain the estimate of the periodic solution. Note however the TSM solution for C is obtained for a reduced number of time instances $(2N + 1)$ in the period - typically N does not exceed 16 and can be as low as 2 or 4 -. Meanwhile the BDF solution for C is usually computed with a number of time-steps per cycle that can be equal to several hundreds and will not go below 50. In practice, the TSM solution for C is reconstructed over the cycle using (3.21) and (3.20) and then visually compared, on some graphical representations, to the BDF solution to allow at least a qualitative comparison. This type of comparison has been generally retained in the previously published works on TSM [27, 66] and will be also performed in the present contribution. A more quantitative error analysis can be performed by computing the RMS error between BDF and TSM computations after proper reconstruction of the TSM solution. This type of analysis will be presented in section 7.2.2 for the incompressible TSM applications. What is important to keep in mind at this stage is that the objective regarding TSM accuracy is to find the minimal number of modes N allowing to achieve at least a qualitative agreement with either a reference analytical solution (see next chapter) or a reference DTS solution (see next part).

4.4.3 CPU cost and memory requirement

The global computational cost of the usual BDF approach can be expressed as:

$$\mathcal{C}_{BDF} = N_{\Delta t} \times N_{cycles} \times m_{max}^{BDF} \times l_{max} \times N_{cells} \times c_u^{BDF}$$

where $N_{\Delta t}$ is the number of physical time-steps used to describe a flow period or cycle, N_{cycles} is the number of cycles to be computed before a periodic solution is actually reached, m_{max}^{BDF} is the number of dual sub-iterations used at each physical time-step to reach the dual steady-state (a residual drop of 3 orders is retained as the criterion) , l_{max} is the number of iterations used with the PJ relaxation method, N_{cells} is the grid size and c_u^{BDF} is the unit cost (per point and per iteration) of the TSM method.

Meanwhile, the global computational cost of the newly proposed TSM approach is expressed as:

$$\mathcal{C}_{TSM(N)} = (2N + 1) \times m_{max}^{TSM(N)} \times l_{max} \times N_{cells} \times c_u^{TSM}(N)$$

where $(2N+1)$ is the number of time-instances retained to describe the flow period, m_{max}^{TSM} is the number of iterations on the dual time needed to drive the TSM system to a steady-state (it is estimated for a convergence criterion of $res_{av} = 10^{-4}$) , l_{max} is the number of iterations used with the PJ relaxation method, N_{cells} is the grid size and $c_u^{TSM(N)}$ is the unit cost (per point and per iteration) of this TSM method.

Since l_{max} is the same for BDF and TSM, the cost ratio between TSM(N) and BDF used with the same computational grid reads:

$$\eta = \frac{\mathcal{C}_{TSM(N)}}{\mathcal{C}_{BDF}} = \underbrace{\frac{(2N+1)}{N_{\Delta t} \times N_{cycles}} \times \frac{m_{max}^{TSM(N)}}{m_{max}^{BDF}}}_{\Phi_1} \times \underbrace{\frac{c_u^{TSM(N)}}{c_u^{BDF}}}_{\Phi_2} \tag{4.27}$$

where the contribution Φ_1 depends on the flow problem while the contribution Φ_2, ratio of the unit costs associated with the TSM(N) and BDF methods, depends only on the numerical implementation of these methods into the computer code in use.

The unit cost ratio between the TSM approach and the BDF, $\Phi_2(N)$ method should display a weak dependency only on the number N of harmonics, on one hand through the extra terms introduced by the spectral time approximation and on the other hand through the extra-cost that might be induced by the memory access associated with the large-scale TSM systems which couple $2N+1$ systems of conservation laws. Ideally, with no memory issues, one would expect $\Phi_2(N)$ to remain close to unity whatever the value of N.

In practice, to assess the ratio $\Phi_2(N)$, TSM simulations are run on the computational machine for an increasing number of harmonics. The TSM times are averaged over 100 dual time iterations. Results are presented in figure 4.1 and eventually $\Phi_2(N)$ is numerically estimated as a linear function of N (which remains however implementation-dependent but, this is a key point, not problem-dependent) :

$$\Phi_2(N) \approx 0.8208 + 0.0925 \times N \tag{4.28}$$

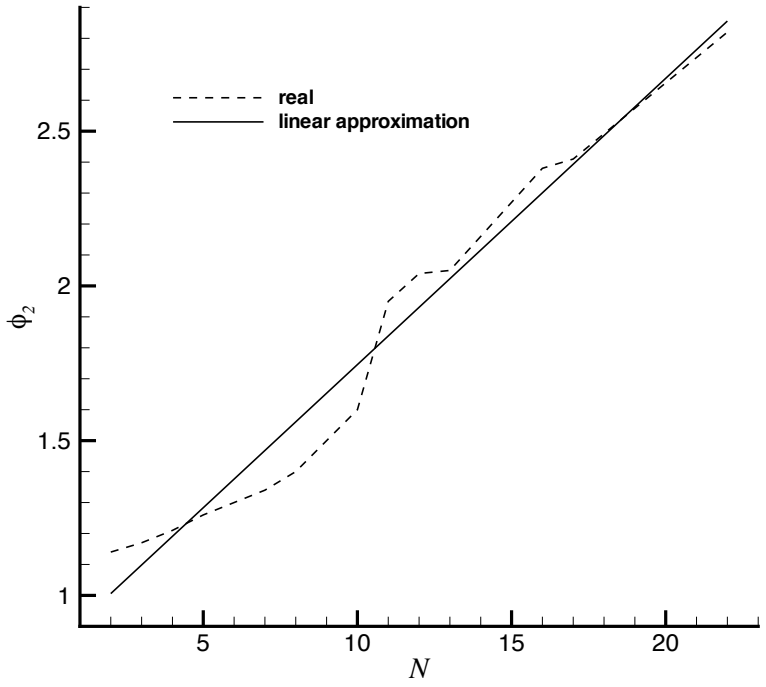

Figure 4.1: Evolution of the unit cost ratio of TSM over BDF methods as a function of N.

Formula (4.27) for the TSM efficiency (cost reduction factor with respect to BDF) will be next used as follows : in a first step the accuracy analysis will allow to define what is the value of N needed to ensure a TSM accuracy comparable with the BDF accuracy; in a second step, formula (4.27) will be applied to quantify the (possibly) net gain offered by TSM. Note again that $\eta = \Phi_1(N) \times \Phi_2(N)$ with a "universal" or intrinsic form for $\Phi_2(N)$ given by (4.28) but a value Φ_1 that depends on the type of problem to be solved. The next chapters will allow to identify typical values for Φ_1.

Chapter 5

Heat conduction benchmark problem

The TSM approach described in the previous chapters will be applied to compressible and incompressible time-periodic flows in chapter 6 and 7. For these external flow applications, the BDF results will be considered as reference solutions. Before proceeding to such a BDF / TSM comparison, it was thought interesting to analyze the TSM approach on a simpler test problem, namely an unsteady linear conduction problem, where an analytical solution is available and the reduced computational time allows for an in-depth analysis of various implicit strategies for instance. This chapter can also be considered as a modest tribute to Jean Baptiste Joseph Fourier (21 March 1768 - 16 May 1830), French mathematician and physicist who performed his experiments on the propagation of heat in Grenoble and presented in 1822 his work on heat flow in "Théorie analytique de la chaleur" [24]. The method of decomposition into the "not-yet" called Fourier series enabled him to find analytical solution to the heat conduction problem. Did he imagine that his idea would be used years later to reduce the computational cost of CFD time periodic problems ?

5.1 Description of the periodic heat-conduction problem

5.1.1 Problem set-up

Let us consider a one-dimensional unsteady conduction problem in a wall. At the initial time, the temperature is supposed uniform inside the wall, equal to T_0. At the left boundary of the wall, located at $x = 0$, the temperature is prescribed and varies periodically with respect to time with a pulsation ω and an amplitude αT_0 around the T_0 value. At the right boundary, located at $x = L$, the temperature is set to the constant value T_0. The thermal diffusivity of the wall material a is supposed to be constant. The evolution of the temperature distribution inside the wall is governed by the following set of equations :

- Heat equation

$$\frac{\partial T}{\partial t} = a\frac{\partial^2 T}{\partial x^2} \tag{5.1}$$

- Boundary conditions :

$$T(0,t) = T_0(1 + \alpha\cos(\omega t))$$
$$T(L,t) = T_0$$

- Initial condition

$$T(x,0) = T_0 \quad \forall x \in]0:L]$$

Given the left boundary condition, the initial condition is discontinuous since $T(0,0) = T_0(1+\alpha)$ while the initial temperature is equal to T_0 everywhere else. Introducing the normalized or non-dimensional variable $\theta(x,t) = \dfrac{T(x,t) - T_0}{\alpha T_0}$, the problem can also be expressed as :

- Heat equation:

$$\frac{\partial \theta}{\partial t} = a\frac{\partial^2 \theta}{\partial x^2} \tag{5.2}$$

- Boundary conditions:

$$\theta(0,t) = \cos(\omega t)$$
$$\theta(L,t) = 0$$

- Initial condition:

$$\theta(x,0) = 0 \quad \forall x \in]0:L]$$

Note again the initial distribution is discontinuous since $\theta(x,0) = 0$ everywhere but at $x = 0$ where $\theta(0,0) = 1$.

5.1.2 Exact periodic solution

After a transient regime, an established periodic flow is reached with a time-periodic solution that can be searched under the following form :

$$\theta_s(x,t) = \overline{\theta_s}(x)\exp(\underline{i}\omega t) \tag{5.3}$$

where $\underline{i}$ is the standard imaginary unit. Inserting the above expression in (5.2) yields the ordinary differential equation:

$$i\omega\overline{\theta_s} = a\frac{d^2\overline{\theta_s}}{dx^2} \tag{5.4}$$

The solution of (5.4) reads :

$$\overline{\theta_s}(x) = A\exp(-\sqrt{\frac{\omega}{2a}}x)\exp(-\underline{i}\sqrt{\frac{\omega}{2a}}x) + B\exp(\sqrt{\frac{\omega}{2a}}x)\exp(\underline{i}\sqrt{\frac{\omega}{2a}}x) \tag{5.5}$$

$\overline{\theta_s}$ is a wave solution of spatial period or wavelength $\lambda = \dfrac{2\pi}{\sqrt{\omega/(2a)}}$.
The constants A and B in (5.5) are determined by application of the boundary conditions. The left boundary condition $\overline{\theta_s}(0,t) = 1$ implies $A = 1$ while, assuming L is large with respect to $\sqrt{2a/\omega}$, the right boundary condition $\overline{\theta_s}(L,t) = 0$ yields $B \approx 0$. The periodic solution takes eventually the form:

$$\theta_s(x,t) = \exp(-\sqrt{\frac{\omega}{2a}}x)\cos(\omega t - \sqrt{\frac{\omega}{2a}}x) \tag{5.6}$$

This solution of period $T = 2\pi/\omega$ displays a phase difference $\sqrt{\frac{\omega}{2a}}x$ with respect to the imposed temperature at $x = 0$. For a given pulsation, the amplitude of the oscillations inside the wall is controlled by the position x and the thermal diffusivity a. This amplitude decreases when moving away from the left boundary where the periodic signal is applied; likewise, a weak diffusivity will damp the oscillations close to this source of perturbation.

5.1.3 Full unsteady solution

The full unsteady solution of the heat conduction problem, including the transient, can be found using Fourier series. Let us define a function $\Phi(x,t)$ as :

$$\Phi(x,t) = \theta(x,t) - \theta_s(x,t) \tag{5.7}$$

This function still satisfies the heat equation (5.2) with boundary conditions now given by :

$$\Phi(0,t) = 0$$
$$\Phi(L,t) = 0$$

and the initial condition:

$$\Phi(x,0) = \theta(x,0) - \theta_s(x,0) = -\exp(-\sqrt{\frac{\omega}{2a}}x)\cos(-\sqrt{\frac{\omega}{2a}}x)$$

The function Φ is found as a decomposition into sinus series on the space interval $[0:L]$, with the b_n coefficients depending on time :

$$\Phi(x,t) = \sum_{n=1}^{\infty} b_n(t) \sin(\frac{n\pi x}{L}) \tag{5.8}$$

Differentiating twice Φ with respect to the variable x yields:

$$\frac{\partial^2 \Phi(x,t)}{\partial x^2} = \sum_{n=1}^{\infty} -(\frac{n\pi}{L})^2 b_n(t) \sin(\frac{n\pi x}{L}) \tag{5.9}$$

so that after insertion in the heat equation the following ordinary differential equation is found for $b_n(t)$:

$$b_n'(t) = a(-\frac{n\pi}{L})^2 b_n(t) \tag{5.10}$$

This ODE is immediately solved to yield:

$$b_n(t) = B_n \exp(-n^2(\frac{\pi^2 a}{L^2})t) \tag{5.11}$$

so that the function $\Phi(x,t)$ can be eventually expressed as:

$$\Phi(x,t) = \sum_{n=1}^{\infty} B_n \exp(-n^2(\frac{\pi^2 a}{L^2})t) \sin(\frac{n\pi x}{L}) \tag{5.12}$$

The B_n coefficients are obtained from the initial condition

$$\Phi(x,0) = \sum_{n=1}^{\infty} B_n \sin(\frac{n\pi x}{L}) \tag{5.13}$$

These coefficients are nothing else but the sinus series coefficients of the initial solution, computed as:

$$B_n = \frac{2}{L}\int_0^L \Phi(x,0)dx = \frac{2}{L}\int_0^L -\exp(-\sqrt{\frac{\omega}{2a}}x)\cos(-\sqrt{\frac{\omega}{2a}}x)\sin(\frac{n\pi x}{L})dx \tag{5.14}$$

This integral formula is numerically estimated.
One can observe on solution (5.12) a typical diffusion time $L^2/(\pi^2 a)$. When time increases, the exponential term in (5.12) goes to zero and one retrieves the established time periodic solution. The highest harmonics disappear the most quickly and the smallest the thermal diffusivity, the longest the transient period. The now available exact solution of the unsteady heat conduction problem under consideration will be useful to assess the accuracy of the numerical methods that will be next applied to obtain discrete approximate solutions of the problem. Note however that, because of the initial discontinuity at $x = 0$, the exact solution in this neighborhood is accurately computed only when a large number of harmonics is used in (5.12).

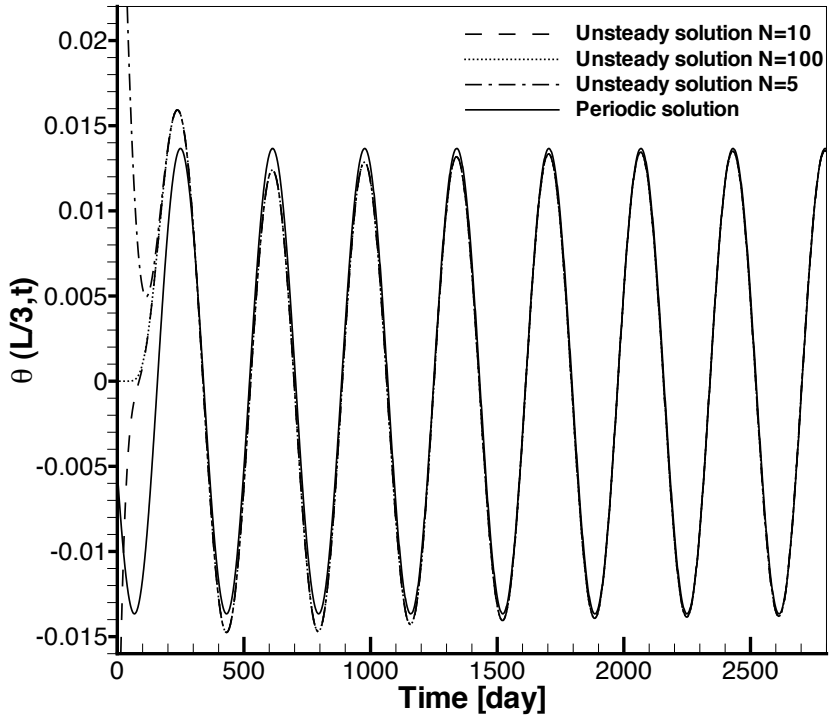

Figure 5.1: Evolution of the temperature at location $x = L/3$. Comparison of analytical solutions.

5.1.4 Analytical results

The solutions derived in the previous sections are computed for numerical values corresponding to the seasonal variation of temperature inside the earth crust : the period of the prescribed temperature at $x = 0$ is a one-year period $T = 3.1536 \times 10^7$s which leads to a pulsation $\omega = 2\pi/T = 2 \times 10^{-7}\text{s}^{-1}$ and the amplitude of the temperature oscillation is fixed by $\alpha = 2$. The earth crust is supposed to be $L = 30$m deep and its thermal diffusivity is taken as $a = 0.5 \times 10^{-6}\text{m}^2\text{s}^{-1}$. Analytical solutions are plotted in Figure (5.1) at the location $x = L/3 = 10$m. For this particular depth, the time periodic solution $\theta_s(L/3, t)$ and the full unsteady solution $\theta(L/3, t) = \theta_s(L/3, t) - \Phi(L/3, t)$ are computed for an overall span of time approximately equal to 8 years (2920 days) in order to ensure time periodicity is fully reached.

It can be observed in Figure 5.1 that a large number of harmonics N is needed to correctly capture the discontinuity of the initial solution. Moreover, the full unsteady solution catches up with the periodic solution after a time span of approximately 8 years.

5.2 Unsteady numerical modeling

The numerical method described in this section should be as much as possible representative of the BDF approach. However, because of the linearity of the simple heat conduction problem under study, it was not deemed necessary to use a BDF-DTS approach to ensure second-order accuracy in time and an even simpler second-order accurate Crank-Nicholson scheme was retained. Note the comparison between a conventional time-marching and the TSM approach remains fair since in that case the cost of the conventional time-marching strategy is even further reduced.

The heat equation (5.1) is approximated at second-order in time and space using the Crank-Nicholson implicit scheme which reads :

$$T_i^{n+1} - T_i^n = \lambda \frac{\Delta t}{\Delta x^2} a(T_{i+1}^{n+1} - 2T_i^{n+1} + T_{i-1}^{n+1}) + (1-\lambda)\frac{\Delta t}{\Delta x^2} a(T_{i+1}^n - 2T_i^n + T_{i-1}^n) \quad (5.15)$$

with $\lambda = 1/2$. Choosing $\lambda = 0$ yields the first-order in time Euler explicit scheme while $\lambda = 1$ corresponds to the first-order in time but unconditionally stable Euler implicit scheme. With $\lambda = 1/2$ second-order accuracy in time and unconditional stability are ensured. The Crank-Nicholson implicit scheme can also be recast in Δ-form as :

$$-\lambda \frac{a\Delta t}{\Delta x^2}\Delta T_{i-1}^n + (1 + 2\lambda \frac{a\Delta t}{\Delta x^2})\Delta T_i^n - \lambda \frac{a\Delta t}{\Delta x^2}\Delta T_{i+1}^n = \Delta T_i^{exp} \quad (5.16)$$

with the explicit stage given by :

$$\Delta T_i^{exp} = \frac{\Delta t}{\Delta x^2} a \left(T_{i+1}^n - 2T_i^n + T_{i-1}^n\right)$$

Scheme (5.16) is applied at all the interior points of the computational domain, *i.e.* for i ranging from $i = 2$ to $i = i_{max} - 1$ if the computational domain is discretized with a uniform grid counting $i_{max} = 101$ points. The Dirichlet boundary condition at the left boundary $x = 0$ ($i = 1$) is of course time-dependent, given by $T(0,t) = T_0(1 + \alpha cos(\omega t))$ or rather $\theta(0,t) = cost(\omega t)$ since the heat conduction problem is numerically solved using the non-dimensional variable θ rather than the dimensional temperature T.

5.3 Time Spectral Method

5.3.1 Time spectral discretization

Let us recall once again the basic concept of the Time Spectral Method is to replace the time derivative appearing in the governing equation(s) with a new time spectral operator that couples several time instants evenly distributed over the time-period of the periodic

problem. In the present case, the time spectral formulation of the heat equation reads :

$$D_t(T_n) = a\,\frac{\partial^2 T_n}{\partial x^2}, \quad 0 \leq n < 2N+1 \tag{5.17}$$

where T_n is the temperature at time $t_n = \frac{n}{2N+1}P$ with N the maximum number of harmonics considered and P the period (symbol P is exceptionally used here instead of T to avoid any confusion with the temperature variable T). Eq. (5.17) represents a system of $2N+1$ coupled steady equations. Note the left Dirichlet boundary condition at point $i = 1$ is transformed into :

$$T_{1,n} = T_0(1 + \alpha\cos(\omega\ t_n)), \quad \forall\ n \in [0 : 2N] \tag{5.18}$$

5.3.2 Direct solution

Applying to (5.17) the second-order centered discretization previously used with the Crank-Nicholson scheme yields :

$$D_t(T_{i,n}) = \frac{a}{\Delta x^2}(T_{i+1,n} - 2\ T_{i,n} + T_{i-1,n}) \tag{5.19}$$

or, in matrix form :

$$\boldsymbol{A}^*\ \boldsymbol{T}^* = \boldsymbol{B} \tag{5.20}$$

where the LHS matrix, the vector of unknowns and the RHS vector are given by :

$$\boldsymbol{A}^* = \begin{pmatrix} \boldsymbol{R} & d_1\boldsymbol{I_d} & \cdots & d_N\boldsymbol{I_d} & d_{-N}\boldsymbol{I_d} & \cdots & d_{-1}\boldsymbol{I_d} \\ d_{-1}\boldsymbol{I_d} & \ddots & \ddots & \vdots & \ddots & \ddots & \vdots \\ \vdots & \ddots & \ddots & d_1\boldsymbol{I_d} & \ddots & \ddots & \vdots \\ d_{-N}\boldsymbol{I_d} & \cdots & d_{-1}\boldsymbol{I_d} & \boldsymbol{R} & d_1\boldsymbol{I_d} & \cdots & d_N\boldsymbol{I_d} \\ \vdots & \ddots & \ddots & d_1\boldsymbol{I_d} & \ddots & \ddots & \vdots \\ \vdots & \ddots & \ddots & \vdots & \ddots & \ddots & d_1\boldsymbol{I_d} \\ d_1\boldsymbol{I_d} & \cdots & d_N\boldsymbol{I_d} & d_{-N}\boldsymbol{I_d} & \cdots & d_{-1}\boldsymbol{I_d} & \boldsymbol{R} \end{pmatrix},\ \boldsymbol{T}^* = \begin{pmatrix} T_{1,0} \\ \vdots \\ T_{i_{max},0} \\ \vdots \\ \vdots \\ T_{1,2N} \\ \vdots \\ T_{i_{max},2N} \end{pmatrix}$$

$$\boldsymbol{B} = \begin{pmatrix} T_{1,0} \\ 0 \\ \vdots \\ 0 \\ T_0 \\ \vdots \\ \\ \vdots \\ T_{1,2N} \\ 0 \\ \vdots \\ 0 \\ T_0 \end{pmatrix} \quad \text{with} \quad \boldsymbol{R} = \begin{pmatrix} 1 & 0 & \cdots & \cdots & \cdots & \cdots & 0 \\ -\frac{a}{\Delta x^2} & 2\ \frac{a}{\Delta x^2} & -\frac{a}{\Delta x^2} & 0 & \ddots & \ddots & \vdots \\ 0 & \ddots & \ddots & \ddots & \ddots & \ddots & \vdots \\ \vdots & 0 & -\frac{a}{\Delta x^2} & 2\ \frac{a}{\Delta x^2} & -\frac{a}{\Delta x^2} & 0 & \vdots \\ \vdots & \ddots & \ddots & \ddots & \ddots & \ddots & \vdots \\ \vdots & \ddots & \ddots & \ddots & -\frac{a}{\Delta x^2} & 2\ \frac{a}{\Delta x^2} & -\frac{a}{\Delta x^2} \\ 0 & \cdots & \cdots & \cdots & 0 & 0 & 1 \end{pmatrix} \tag{5.21}$$

The matrix $\boldsymbol{A}^*$ is a square matrix of size $(2N+1) \times i_{max}$ while the $\boldsymbol{R}$ tridiagonal matrix of size i_{max} directly results from the space discretization operator. The non-zero coefficients of the RHS vector $\boldsymbol{B}$ in equation (5.20) correspond to the boundary conditions. Owing to the linearity of the governing equation, (5.20) is a linear system that can be directly solved using the Lower Upper (LU) decomposition of matrix $\boldsymbol{A}^*$. The dual-time sub-iterative process to solve the TSM scheme in the general non-linear case is actually not needed for the very particular case of the linear heat equation considered here. Nonetheless, since our goal when solving this model problem is to take advantage of the problem simplicity to investigate various solution strategies, the dual-time marching to solve (5.19) will be next considered.

5.3.3 Dual-time marching strategy

In the case of compressible and incompressible periodic flow problems that will be treated in the last part of this thesis report, the governing TSM systems equivalent to (5.19) will be non-linear so that their solutions will be sought as steady states of an iterative procedure on a pseudo-time. Let us mimic the various dual-time strategies at hand when solving the simple linear equation (5.19).

Explicit TSM scheme

The application of the explicit TSM scheme (Sec. 4.4.1) to the heat equation yields :

$$\Delta T^m_{i,n} = \frac{\Delta\tau\ a}{\Delta x^2}(T^m_{i+1,n} - 2\ T^m_{i,n} + T^m_{i-1,n}) - \Delta\tau\ D_t(T_{i,n})^m \tag{5.22}$$

Following the methodology presented in Sec. 4.1.2, the stability of (5.22) can be analyzed by first writing the scheme in the frequency domain :

$$\widehat{T}_{i,k}^{m+1} = \widehat{T}_{i,k}^{m} + \frac{\Delta\tau\ a}{\Delta x^2}\left(\widehat{T}_{i+1,k}^{m} - 2\ \widehat{T}_{i,k}^{m} + \widehat{T}_{i-1,k}^{m}\right) - \Delta\tau\ \underline{i}k\omega\widehat{T}_{i,k}^{m} \tag{5.23}$$

where $\underline{i}$ is the imaginary unit. The Von-Neumann stability analysis technique is then used to find a stability criterion for equation (5.23). The vector $\widehat{T}_k$ is decomposed into spatial Fourier modes

$$\widehat{T}_{i,k} = \sum_{k'} \widehat{\widehat{T}_k} e^{\underline{i}k'x_i}$$

Since

$$\widehat{T}_{i+1,k}^{m} - 2\ \widehat{T}_{i,k}^{m} + \widehat{T}_{i-1,k}^{m} = 2(\cos(\eta) - 1)\ \widehat{T}_{i,k} = -4\ \sin^2(\frac{\eta}{2})\ \widehat{T}_{i,k} \tag{5.24}$$

with the wavenumber $\eta = k'\Delta x$, the relationship (5.23) can be rewritten as follows :

$$\widehat{T}_{i,k}^{m+1} = \left(1 - \Delta\tau\dot{a}\sin^2(\frac{\eta}{2}) - \Delta\tau\ \underline{i}k\omega\right)\widehat{T}_{i,k}^{m} \tag{5.25}$$

where $\dot{a} = \dfrac{4a}{\Delta x^2}$. The stability condition can be written:

$$\left|1 - \Delta\tau\ \dot{a}\sin^2(\frac{\eta}{2}) - \Delta\tau\underline{i}k\omega\right| \leq 1$$

or, after rearranging :

$$\Delta\tau \leq \frac{2\ \dot{a}\sin^2(\frac{\eta}{2})}{\left(\dot{a}\sin^2(\frac{\eta}{2})\right)^2 + (k\omega)^2}$$

A large number of harmonics N and/or a high frequency will limit the maximum allowable time step. It is found numerically that the right hand side of equation (5.26) is minimum for the highest harmonic $k = N$ and the maximum spatial Fourier mode $\eta_{max} = \pi$. The most restrictive stability condition is thus given by :

$$\Delta\tau \leq \frac{1}{\dfrac{\dot{a}}{2} + \dfrac{(N\omega)^2}{2\dot{a}}} \tag{5.26}$$

By analogy with the definition of the dual time step adopted for TSM in the case of a convective problem in Section 4.1.2, the time-step $\Delta\tau$ used for the present heat equation problem is computed as :

$$\Delta\tau = \mathrm{CFL}\ \frac{1}{\dfrac{\dot{a}}{2} + N\omega} \tag{5.27}$$

which allows to recover a usual expression $\Delta\tau = \mathrm{CFL}\ \dfrac{\Delta x^2}{2a}$ for a purely diffusive problem

without TSM. Note using the notation CFL in this case is somehow abusive since the CFL number refers to the stability condition for a convective problem. It should be understood that the CFL symbol is used here (though improperly) to denote the safety factor used to compute the time-step with respect to a chosen characteristic or reference time-step of the problem. Inserting (5.27) into (5.26) yields a stability condition expressed on the CFL number :

$$\mathrm{CFL} \leq \frac{1+\beta\, N}{1+\left(\frac{1}{2}\beta N\right)^2} \tag{5.28}$$

where $\beta = \frac{1}{2}\dfrac{\omega \Delta x^2}{a}$. With the choice of numerical values for a, ω and Δx previously given ($a = 0.5 \times 10^{-6}\, m^2\, s^{-1}$, $\omega = 2 \times 10^{-7}\, s^{-1}$, $\Delta x = L/100 = 0.3\, m$), it is immediate to compute $\beta = 0.018$. With $N = 1$, the stability condition (5.28) for the TSM explicit scheme yields a maximal allowable CFL to be used in (5.27) equal to $\mathrm{CFL}_{max} = 1.0179$. Numerical computations, not reproduced here for the sake of compactness and because our focus is on implicit TSM strategies, allowed to check that any larger value for the CFL resulted indeed in an unstable scheme.

Semi-implicit TSM scheme

When deriving the semi-implicit TSM scheme, the space discretization is treated implicitly whereas the TSM term remains treated explicitly:

$$\Delta T_{i,n}^m = \frac{\Delta\tau\ a}{\Delta x^2}\left(T_{i+1,n}^{m+1} - 2\ T_{i,n}^{m+1} + T_{i-1,n}^{m+1}\right) - \Delta\tau\ D_t(T_{i,n})^m \tag{5.29}$$

or in Δ-form :

$$-\frac{\Delta\tau\ a}{\Delta x^2}\Delta T_{i-1,n}^m + \left(1 + \frac{\Delta\tau\ 2a}{\Delta x^2}\right)\Delta T_{i,n}^m - \frac{\Delta\tau\ a}{\Delta x^2}\Delta T_{i+1,n}^m = \Delta T_{i,n}^{exp} \tag{5.30}$$

where the explicit increment is given by (5.22). There is no implicit coupling between equations for $n = 0, 2N$, with the TSM term present in the explicit stage only. Equation (5.30) can also be recast in the following matrix form:

$$\boldsymbol{R}\ \Delta \boldsymbol{T}_n^m = \Delta \boldsymbol{T}_n^{(exp)} \tag{5.31}$$

with

$$\boldsymbol{R} = \begin{pmatrix} 1 & 0 & \cdots & \cdots & \cdots & \cdots & 0 \\ -\frac{a\Delta\tau}{\Delta x^2} & 1+2\,\frac{a\Delta\tau}{\Delta x^2} & -\frac{a\Delta\tau}{\Delta x^2} & 0 & \ddots & \ddots & \vdots \\ 0 & \ddots & \ddots & \ddots & \ddots & \ddots & \vdots \\ \vdots & 0 & -\frac{a\Delta\tau}{\Delta x^2} & 1+2\,\frac{a\Delta\tau}{\Delta x^2} & -\frac{a\Delta\tau}{\Delta x^2} & 0 & \vdots \\ \vdots & \ddots & \ddots & \ddots & \ddots & \ddots & \vdots \\ \vdots & \ddots & \ddots & \ddots & -\frac{a\Delta\tau}{\Delta x^2} & 1+2\,\frac{a\Delta\tau}{\Delta x^2} & -\frac{a\Delta\tau}{\Delta x^2} \\ 0 & \cdots & \cdots & \cdots & 0 & -1 & 1 \end{pmatrix}, \quad \Delta\boldsymbol{T}_n^{(exp)} = \begin{pmatrix} 0 \\ \Delta T_{2,n}^{(exp)} \\ \vdots \\ \vdots \\ \vdots \\ \vdots \\ \Delta T_{i_{max}-1,n}^{(exp)} \\ 0 \end{pmatrix}$$

For each pseudo time iteration, the explicit stage is first computed and (5.31) is solved next using a tridiagonal matrix algorithm (TDMA)

The Von-Neumann stability analysis technique is applied to transform (5.30) into the frequency domain :

$$H\Delta\widehat{\widehat{T_k}} = -K\widehat{\widehat{T_k}}$$

with

$$\begin{aligned} H &= 1 + \Delta\tau\ \dot{a}\sin^2(\tfrac{\eta}{2}) \\ K &= \Delta\tau\ \dot{a}\sin^2(\tfrac{\eta}{2}) + \Delta\tau\underline{i}k\omega \end{aligned}$$

so that

$$\widehat{\widehat{T_k}}^{m+1} = \frac{H-K}{H}\widehat{\widehat{T_k}}^m = G\widehat{\widehat{T_k}}^m$$

The amplification factor G can be expressed as :

$$G = \frac{1-\Delta\tau\underline{i}k\omega}{1+\Delta\tau\ \dot{a}\sin^2(\frac{\eta}{2})}$$

and the stability condition $|G| \leq 1$ yields :

$$\Delta\tau \leq \frac{2\dot{a}\sin^2(\frac{\eta}{2})}{(k\omega)^2 - (\dot{a}\sin^2(\frac{\eta}{2}))^2} \tag{5.32}$$

The most restrictive condition is obtained for the minimal spatial Fourier mode $\eta_{min} = \frac{\pi}{L}\Delta x$ and the highest harmonic $k = N$. With $N = 1$ and the CFL definition of (5.27), the corresponding maximum allowable CFL for the semi-implicit TSM scheme is $\text{CFL}_{max} = 3.10$. The stability of the semi-implicit TSM formulation is slightly better than with the previous explicit scheme but for a greater cost per iteration (since a linear system solution

is needed at each iteration) which makes this semi-implicit scheme rather unattractive.

Fully implicit TSM

The fully implicit form of the TSM (Eq. (4.16)) applied to the conduction equation reads :

$$\Delta T_{i,n}^{m} = \frac{\Delta\tau\ a}{\Delta x^2}\left(T_{i+1,n}^{m+1} - 2\ T_{i,n}^{m+1} + T_{i-1,n}^{m+1}\right) - \Delta\tau\ D_t(T_{i,n})^{m+1} \tag{5.33}$$

or, in equivalent Δ-form :

$$-\frac{\Delta\tau\ a}{\Delta x^2}\Delta T_{i-1,n}^{m} + \left(1 + \frac{\Delta\tau\ 2a}{\Delta x^2}\right)\Delta T_{i,n}^{m} - \frac{\Delta\tau\ a}{\Delta x^2}\Delta T_{i+1,n}^{m} + \Delta\tau\ D_t(\Delta T_{i,n}^{m}) = \Delta T_{i,n}^{exp} \tag{5.34}$$

Equation (5.34) exhibits a TSM term in the implicit stage that couples all the time instants. Scheme (5.34) can also be recast in matrix form:

$$\boldsymbol{A}^{*}\Delta\boldsymbol{T}^{*,m} = \Delta\boldsymbol{T}^{*,(exp)} \tag{5.35}$$

where

$$\boldsymbol{A}^{*} = \begin{pmatrix} \boldsymbol{R} & d_1\boldsymbol{I_d} & \cdots & d_N\boldsymbol{I_d} & d_{-N}\boldsymbol{I_d} & \cdots & d_{-1}\boldsymbol{I_d} \\ d_{-1}\boldsymbol{I_d} & \ddots & \ddots & \vdots & \ddots & \ddots & \vdots \\ \vdots & \ddots & \ddots & d_1\boldsymbol{I_d} & \ddots & \ddots & \vdots \\ d_{-N}\boldsymbol{I_d} & \cdots & d_{-1}\boldsymbol{I_d} & \boldsymbol{R} & d_1\boldsymbol{I_d} & \cdots & d_N\boldsymbol{I_d} \\ \vdots & \ddots & \ddots & d_1\boldsymbol{I_d} & \ddots & \ddots & \vdots \\ \vdots & \ddots & \ddots & \vdots & \ddots & \ddots & d_1\boldsymbol{I_d} \\ d_1\boldsymbol{I_d} & \cdots & d_N\boldsymbol{I_d} & d_{-N}\boldsymbol{I_d} & \cdots & d_{-1}\boldsymbol{I_d} & \boldsymbol{R} \end{pmatrix},\ \Delta\boldsymbol{T}_n^{*,(exp)} = \begin{pmatrix} 0 \\ \Delta T_{2,1}^{(exp)} \\ \vdots \\ \Delta T_{i_{max}-1,1}^{(exp)} \\ 0 \\ \vdots \\ \Delta T_{2,n}^{(exp)} \\ \vdots \\ \Delta T_{i_{max}-1,n}^{(exp)} \\ 0 \end{pmatrix}$$

and the matrix $\boldsymbol{R}$ associated with the space discretization is identical to the one defined in Eq. (5.21).

The stability of this fully implicit approach is analyzed through the amplification factor G following the same procedure as the one described for the semi-implicit scheme. The Fourier symbols H and K respectively associated with the implicit and explicit stage read :

$$\begin{aligned} H &= 1 + \Delta\tau\ \dot{a}\sin^2(\tfrac{\eta}{2}) + \Delta\tau\underline{i}k\omega \\ K &= \Delta\tau\ \dot{a}\sin^2(\tfrac{\eta}{2}) + \Delta\tau\underline{i}k\omega \end{aligned} \tag{5.36}$$

yielding an amplification factor $G = (H - K)/H$ such that :

$$|G|^2 = \frac{1}{(1 + \Delta\tau\ \dot{a}\sin^2(\frac{\eta}{2}))^2 + (\Delta\tau k\omega)^2} \tag{5.37}$$

Obviously, $|G| \leq 1$ for all modes k which proves the purely implicit TSM solution is unconditionally stable.

Solution methods

The unconditional stability of the fully implicit TSM scheme (5.34) is ensured provided the system (5.35) is exactly solved. Such an exact solution can be performed with a LU decomposition of the matrix $\boldsymbol{A}^*$ - as previously mentioned in section 5.3.2 for the direction solution method, without pseudo-time marching. Let us emphasize once again the direct solution without time-marching is not an option in the general non-linear case. The exact solution of the fully implicit TSM scheme has to be performed at each pseudo-time iteration, which would make it costly to use. Therefore, equation (5.34) or system (5.35) is preferably solved using an iterative technique, such as the Point Jacobi solution method already described in the first part of this thesis report for the conventional unsteady compressible and incompressible flow solvers and also detailed in the section 4.2.4 of the previous chapter for the fully implicit TSM scheme. Let us recall the idea is to get rid of the implicit coupling of the $2N + 1$ equations by relaxing the TSM term. Thus, the original system is simplified into a set $2N + 1$ independent equations similar to Eq. (5.30) but with a different right hand side including the contribution of the spectral operator. In the case of the unsteady heat equation considered in this chapter, the point Jacobi iterative procedure can be written:

$$\begin{aligned}
&\Delta T_{i,n}^{(0)} = 0 \\
&\begin{cases} l = 0,\ l_{max} - 1 \\ n = 0,\ 2N \\ -\dfrac{\Delta\tau\ a}{\Delta x^2}\Delta T_{i-1,n}^{l+1} + \left(1 + \dfrac{\Delta\tau\ 2a}{\Delta x^2}\right)\Delta T_{i,n}^{l+1} - \dfrac{\Delta\tau\ a}{\Delta x^2}\Delta T_{i+1,n}^{l+1} = \Delta T_{i,n}^{exp} - \Delta\tau\ D_t(\Delta T_{i,n}^{l}) \end{cases} \\
&T_{i,n}^{m+1} = T_{i,n}^{m} + \Delta T_{i,n}^{l_{max}}
\end{aligned} \tag{5.38}$$

Under matrix form, this same Jacobi iteration reads:

$$\boldsymbol{R}\Delta\boldsymbol{T}_n^{l+1} = \Delta\boldsymbol{T}_n^{(exp)} - \Delta\tau\ \boldsymbol{D}\Delta\boldsymbol{T}^{*,l} \tag{5.39}$$

with

$$\boldsymbol{D} = \begin{pmatrix} 0 & d_1 & \cdots & d_N & d_{-N} & \cdots & d_{-1} \\ d_{-1} & \ddots & \ddots & \vdots & \ddots & \ddots & \vdots \\ \vdots & \ddots & \ddots & d_1 & \ddots & \ddots & \vdots \\ d_{-N} & \cdots & d_{-1} & 0 & d_1 & \cdots & d_N \\ \vdots & \ddots & \ddots & d_1 & \ddots & \ddots & \vdots \\ \vdots & \ddots & \ddots & \vdots & \ddots & \ddots & d_1 \\ d_1 & \cdots & d_N & d_{-N} & \cdots & d_{-1} & 0 \end{pmatrix}, \ \boldsymbol{T}^* = \begin{pmatrix} T_i^0 \\ T_i^1 \\ \vdots \\ \vdots \\ \vdots \\ \vdots \\ T_i^{2N} \end{pmatrix} \tag{5.40}$$

Since the fully implicit TSM scheme is now iteratively solved, the stability of the Point Jacobi TSM scheme (5.38) must be specifically assessed through a Von Neumann analysis. After Fourier transform, the Point Jacobi formula (5.38) is expressed as follows in the frequency domain :

$$H_\alpha \Delta\widehat{\widehat{T}}_k^{l+1} = -K\widehat{\widehat{T}}_k - (H - H_\alpha)\Delta\widehat{\widehat{T}}_k^{l} \tag{5.41}$$

where the Fourier symbols H and K are those associated with the exactly solved fully implicit TSM scheme, given by (5.36), while H_α is the Fourier symbol associated with the Point Jacobi implicit stage :

$$H_\alpha = 1 + \Delta\tau \ \dot{a} \sin^2(\frac{\eta}{2})$$

As demonstrated in [16, 40] the amplification factor G corresponding to the iterative method (5.41) can be written:

$$\begin{cases} G = G* + V^l(1 - G*) \\ V = 1 - H/H_\alpha \end{cases} \tag{5.42}$$

where $G*$ is the amplification factor associated with the exactly solved fully implicit TSM scheme, given by (5.37). This interesting formula (5.42) shows two levels of efficiency are involved in the Point Jacobi implicit scheme:

1. At a first level, the efficiency depends on the target amplification factor, $G*$. The Point Jacobi iterative solver is indeed only a way to converge to the solution of the exact fully implicit TSM scheme (5.34) or (5.35). In the present case, the efficiency offered by the amplification factor $G*$ associated with (5.34) and the Fourier symbols H, K given by (5.36) is ideal since the implicit stage corresponds to a full implicitation of the explicit stage. In the case of compressible and incompressible flows, the matrix-free implicit stage offers a more reduced intrinsic efficiency but balanced by its low computational cost.

2. At a second level, the iterative method aims to achieve as fast as possible the convergence of G towards $G*$, *i.e.* with the lowest possible number of Jacobi iterations.

This convergence speed depends on the V factor, function of H and H_α only. Since $|G - G*| = |V|^l|1 - G*|$, the most efficient iterative method is obtained when V is the closest to zero (ideally $V = 0$ for $H_\alpha = H$ but there is no relaxation in that case and the exact solution is recovered).

V can be computed exactly for the Point Jacobi applied to the fully implicit TSM solution of the unsteady heat conduction problem :

$$V = -\frac{\Delta\tau \underline{i} k\omega}{1 + \Delta\tau\ \dot{a}\sin^2(\frac{\eta}{2})} \tag{5.43}$$

It is again clear from (5.43) that a large number of harmonics and/or a high frequency is detrimental to the convergence of the point Jacobi iterative method.

For a given couple of parameters (N, ω), two cases can occur (remembering the target amplification factor $G*$ is such that $|G*| \leq 1$ for any value of the CFL number):

1. $|V| \leq 1$, then $|G| \leq 1,\ \forall\ l,\ \forall$ CFL and the relaxation method is unconditionally stable

2. $|V| \geq 1$ above a given CFL number CFL_{max}, then $\exists\ l_{stable} \in \Re$ so that $|G| \leq 1$ for $l \leq l_{stable}$ and for a CFL number below CFL_{max} while $|G| \geq 1$ for $l \geq l_{stable}$

With V given by (5.43), $|V|$ is maximum for $\sin^2(\frac{\eta}{2}) = 0$ and for $k = N$ so that a sufficient condition for ensuring $|V| \leq 1$ reads :

$$|\Delta\tau \underline{i} N\omega| \leq 1$$

which is easily transformed into :

$$\text{CFL} \leq \frac{\dot{a}/2 + N\omega}{N\omega} \tag{5.44}$$

For $N = 1$ and the specific heat conduction problem under study, the stability condition (5.44) yields a maximum allowable CFL number for the Point Jacobi solution of the fully implicit TSM scheme equal to $\text{CFL}_{max} = 56.55$.
In the following figures, the convergence of the TSM methods is assesed with respect to the TSM average temperature residual given by:

$$res^m_{av} = \frac{1}{2N+1}\sum_{n=0}^{2N}\sqrt{\frac{1}{N_{cell}}\sum_{i=1}^{N_{cell}}\frac{\Delta T^{m\,2}_{i,n}}{\Delta\tau^{m\,2}_{i,n}}} \tag{5.45}$$

Figure 5.2 shows the convergence histories of the fully implicit TSM method solved with a Point Jacobi technique and $l_{max} = 2$. the TSM residual is defined as: It can be checked

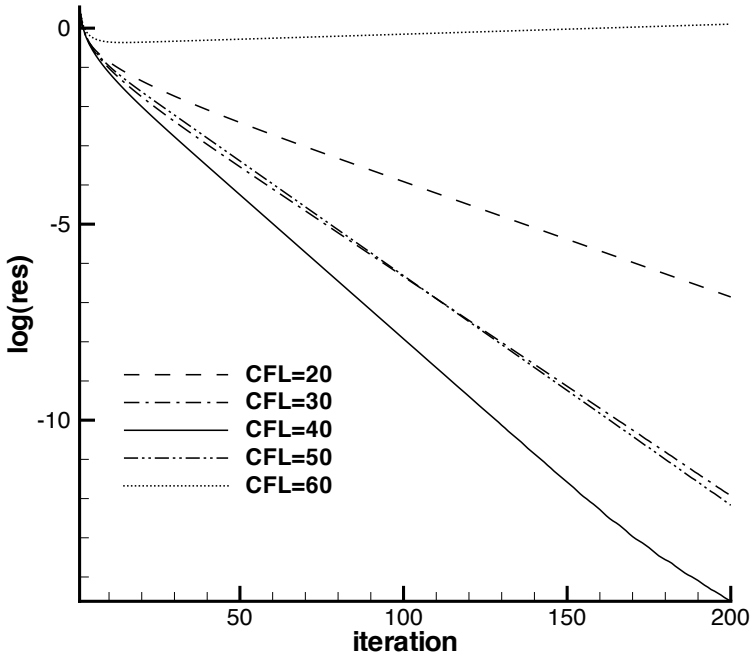

Figure 5.2: Convergence histories for the full implicit TSM method, PJ method of resolution, $N = 1$, $l_{max} = 2$.

that, in accordance with the previously developed theory, CFL ≥ 56 leads to an unstable scheme.

Note the best convergence result is obtained for CFL $= 40$, a lower value than the maximum allowable CFL. This occurrence of an optimal value for the CFL number which is not necessarily the maximum stable value results from the very behavior of G for the Point Jacobi approach but has not been further analyzed from a theoretical viewpoint.

The PJ method should make use of a minimal number of Jacobi iterations to efficiently move the TSM solution from the m^{th} to the $m + 1^{th}$ pseudo time iteration. In order to determine this optimal l_{max} number, several simulations were performed with $l_{max} = 2, 4, 8$ for a fixed CFL number retained equal to the optimal value CFL $= 40$ previously observed. Figure 5.3a shows that some efficiency relatively to the number of pseudo time iterations can be obtained by using $l_{max} = 4$ instead of $l_{max} = 2$. Meanwhile, the further increase of the number of Jacobi iterations from $l_{max} = 4$ to $l_{max} = 8$ does not show significant improvement. However, this result must be counterbalanced by the total number of iteration involved in the solution process. Indeed, if the global number of iterations is considered, that is the product of the pseudo time iterations by the Jacobi iterations, it can be observed on Fig. (5.3b) that using $l_{max} = 2$ represents actually the most efficient strategy.

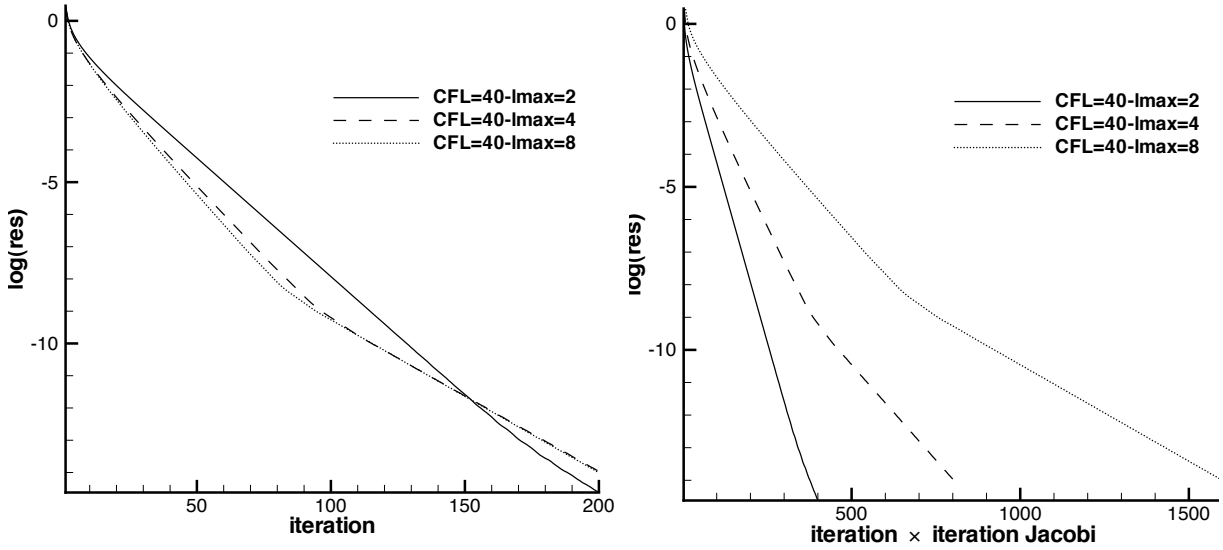

(a) (b)

Figure 5.3: Convergence histories for the full implicit TSM method and an increasing number of PJ iterations, $N = 1$, CFL = 40.

Correction of diagonal dominance

The conditional stability of the fully implicit TSM scheme when solved by the PJ method is an undesirable property. This means indeed that when computing next compressible and incompressible unsteady flows one would probably need to perform several preliminary computations in order to select a CFL number yielding stable computations. This is clearly not convenient with respect for instance to the existing practice with the matrix-free implicit PJ solver associated with the BDF method and described in Chapter 1, which can be safely used with systematic very large values for the CFL number. Following the idea already developed in the previous chapter, the stability of the PJ solver applied to the fully implicit TSM scheme is improved by adding a diagonal contribution to the implicit stage in order to preserve the diagonal dominance of the implicit stage matrix $\boldsymbol{A}^*$. The baseline fully implicit TSM scheme (5.34) is thus modified into :

$$-\frac{\Delta\tau\ a}{\Delta x^2}\Delta T^m_{i-1,n}+\left(1+\boldsymbol{\Delta\tau}\sum_{\boldsymbol{m=-N}}^{\boldsymbol{N}}|\boldsymbol{d_m}|+\frac{\Delta\tau\ 2a}{\Delta x^2}\right)\Delta T^m_{i,n}-\frac{\Delta\tau\ a}{\Delta x^2}\Delta T^m_{i+1,n}+\Delta\tau\ D_t(\Delta T^m_{i,n})=\Delta T^{exp}_{i,n} \tag{5.46}$$

where the new contribution to the coefficient of $\Delta T^m_{i,n}$ appears in bold characters. Naturally, this added contribution to the implicit stage tends to make the solver intrinsically less efficient since the implicit stage is no longer the exact full implicitation of the explicit stage. However, as will be now demonstrated for the heat conduction problem under study, this slight modification is sufficient to ensure the unconditional stability of the PJ method applied to (5.46).

Retaining the notations previously introduced, the Fourier symbol H for the modified TSM scheme reads :

$$H = 1 + \Delta\tau\ \dot{a}\sin^2(\frac{\eta}{2}) + \Delta\tau \sum_{m=-N}^{N} |d_m| + \Delta\tau \underline{i} k\omega \tag{5.47}$$

thereof the amplification factor of the exactly solved (5.46) is given by :

$$G* = \frac{1 + \Delta\tau \sum_{m=-N}^{N} |d_m|}{1 + \Delta\tau\ \dot{a}\sin^2(\frac{\eta}{2}) + \Delta\tau \underline{i} k\omega} \tag{5.48}$$

Note this new amplification factor $G*$ is greater than the one without diagonal correction given by (5.37). However, the key advantage of the proposed correction is that when the Point Jacobi method is applied to solve (5.46) :

$$\begin{aligned}
&\Delta T_{i,n}^{(0)} = 0 \\
&\begin{cases}
l = 0,\ l_{max} - 1 \\
n = 0,\ 2N \\
-\dfrac{\Delta\tau\ a}{\Delta x^2}\Delta T_{i-1,n}^{l+1} + \left(1 + \Delta\tau \displaystyle\sum_{m=-N}^{N} |d_m| + \dfrac{\Delta\tau\ 2a}{\Delta x^2}\right)\Delta T_{i,n}^{l+1} - \dfrac{\Delta\tau\ a}{\Delta x^2}\Delta T_{i+1,n}^{l+1} = \Delta T_{i,n}^{exp} - \Delta\tau\ D_t(\Delta T_{i,n}^{l})
\end{cases} \\
&T_{i,n}^{m+1} = T_{i,n}^{m} + \Delta T_{i,n}^{l_{max}}
\end{aligned} \tag{5.49}$$

the Fourier symbol V associated with PJ is now given by :

$$V = -\frac{\Delta\tau \underline{i} k\omega}{1 + \Delta\tau\ \dot{a}\sin^2(\frac{\eta}{2}) + \Delta\tau \sum_{m=-N}^{N} |d_m|} \tag{5.50}$$

Since $|V| < 1$ whatever the value of the CFL number and since $|G*| < 1$ this means the modified Point Jacobi fully implicit TSM scheme is unconditionally stable.

In Fig. 5.4 are plotted the convergence histories of the full implicit method with an exact LU solver and the PJ solver with and without diagonal correction. It is obvious that the exact solver is the most efficient in terms of iterations; a residual of 10^{-6} is reached after 5 iterations. However, the computational cost of the method at each iteration becomes prohibitive when the size of the system increases and therefore the method will be no longer used in the flow applications treated in the last part of the report. The diagonal correction associated with the PJ method leads as expected to an unconditionally stable method. The best efficiency is obtained for a CFL = 1000 and a number of Jacobi iterations $l_{max} = 2$. For this choice of parameters a convergence of the residual to $res = 10^{-6}$ is obtained after 80 iterations. When compared to the best PJ solver without correction,

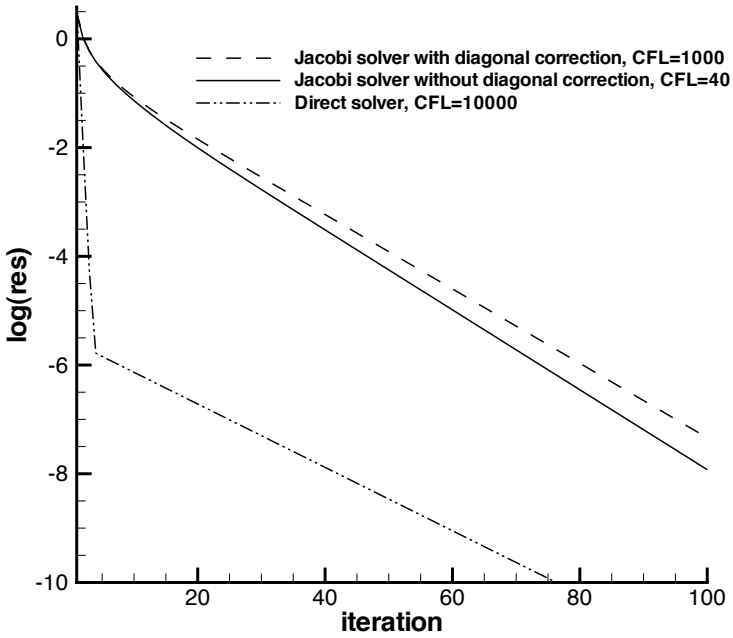

Figure 5.4: Comparison of convergence histories of implicit methods of resolution, $N = 1$.

one can see that the corrected PJ solver is slightly less efficient. However, this method is retained as the reference solution strategy for the remainder of this work because it is stable and yields an efficiency only weakly sensitive to the choice of the CFL number beyond CFL = 1000 - this value will be systematically retained from now on, avoiding any preliminary attempt.

5.4 Results

Various TSM algorithms (explicit, semi-implicit, fully implicit with and without diagonal correction) have been presented and analyzed in the previous Section. The fully implicit TSM with diagonal correction and solved using Point Jacobi has been selected as the reference TSM algorithm. This method will be used in the present section to compute the model heat conduction problem whose parameters are summarized in Table 5.1. Emphasis will be put on the accuracy of the TSM results with respect to the analytical solutions as well as the numerical solution computed using the unsteady Crank-Nicholson solver. Further comments will be made on the relation between the frequency spectrum of the input signal (here the left boundary unsteady condition) and the number of harmonics required by the TSM method to ensure a sufficient accuracy; the efficiency of the TSM approach will also be compared with the unsteady Crank-Nicholson solver.

Lenght L [m]	Thermal diffusivity a [$m^2.s^{-1}$]	Amplitude α	Pulsation ω [$rad.s^{-1}$]	Period T [s]
30	0.5×10^{-6}	2	2×10^{-7}	3.1536×10^{7}

Table 5.1: Parameters of the heat conduction problem

5.4.1 Single harmonic input

The unsteady boundary condition applied at $x = 0$ is supposed purely sinusoidal (see (5.1) or (5.2)). The periodic analytical solution of (5.6) can be decomposed into a Fourier series:

$$\theta(x,t) = \sum_{k=-1}^{k=+1} \widehat{\theta}_k(x) e^{ik\omega t} \tag{5.51}$$

where

$$\begin{cases} \widehat{\theta_0} = 0 \\ \widehat{\theta_{-1}} = \overline{\widehat{\theta_1}} = \exp(-\sqrt{\frac{\omega}{2a}}x)\exp(i\sqrt{\frac{\omega}{2a}}x) \end{cases} \tag{5.52}$$

Thus, the final periodic solution is entirely described by a single harmonic so that, consistently, the TSM method is applied with the minimal number of modes $N = 1$.
Figure 5.5a displays the computed evolution of the normalized temperature at the location $x/L = 3$. The numerical solutions are :

- on one hand the Crank-Nicholson solution computed using CFL = 1. This small value of the CFL number bas been retained in order to ensure a good accuracy of the time-accurate solution. Since for the unsteady solver $\Delta t = \text{CFL}\ \Delta x^2/a$, the choice CFL = 1 yields $\Delta t = 90000\,s \approx 25\,h$. Such a physical time-step corresponds to a time-discretization of 350 steps per period.

- on the other hand, the fully implicit TSM scheme with diagonal correction and PJ solution is applied with a single TSM mode, $N = 1$. The typical convergence to a steady state is plotted in Fig.5.4 : about 60 iterations on the dual or pseudo-time are needed in order to reach a steady-state (with a residual typically reduced by 5 orders of magnitude).

The analytical solution displayed in Fig.5.5a is the analytical periodic solution (5.6). For the sake of clarity and because it is already available in Fig.5.1, the full analytical solution including the transient behavior defined by (5.12) and (5.14) has not been plotted in Fig.5.5a. From Fig.5.1 and 5.5a it can be observed the Crank-Nicholson (CN) approach yields an approximate solution very close to the full analytical solution. Meanwhile, the TSM solution does not allow of course to reproduce the transient behavior since targeted at the computation of the periodic solution. The agreement between the TSM solution and

the analytical periodic solution plotted in Fig.5.5a is excellent. The unsteady CN solver and the full exact solution reach an established periodic behavior after approximately 7 periods. After 7 cycles, the match is perfect - at least at the plot scale - between the analytical solution, the unsteady CN solution and the TSM solution with $N = 1$. The solutions can also be analyzed by plotting the temperature distributions along x at selected time instances. Figure 5.5b displays the analytical (periodic) temperature distribution and the TSM distribution along the depth of the crust for the 3 time instants computed by the TSM approach (hence the TSM solutions T_0^*, T_1^* and T_2^* are directly compared with the exact distributions at t_0, t_1 and t_2). The agreement between both sets of distributions is excellent, demonstrating the accuracy of the TSM approach with $N = 1$ for the present test-problem.

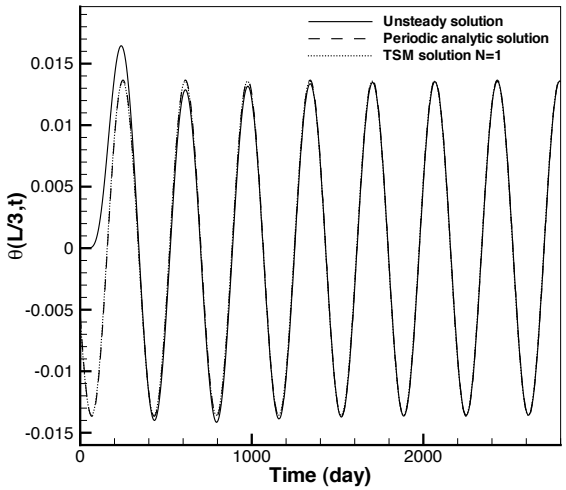

(a) $\theta(L/3, t)$ as a function of time

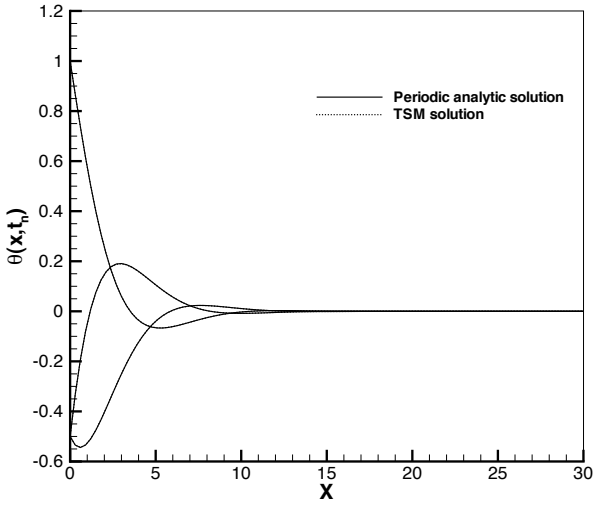

(b) $\theta(x, t_n)$ for $0 \leq n < 3$ as a function of space

Figure 5.5: Conduction equation. Comparison of unsteady analytical, unsteady numerical and TSM solutions.

5.4.2 Double harmonic input

The simple unsteady heat equation model problem allows to further investigate the influence of the choice of N on the TSM solution accuracy. Let us consider indeed a modified left boundary condition, with a time-varying prescribed temperature given by the following law :

$$T(0, t) = T_0(1 + \alpha(\cos(\omega t) + \cos(2\omega t))) \tag{5.53}$$

Because of the linearity of the conduction equation, the final periodic solution is the sum of the the solution for the 2 frequencies introduced in the Dirichlet boundary condition, corresponding to ω and 2ω:

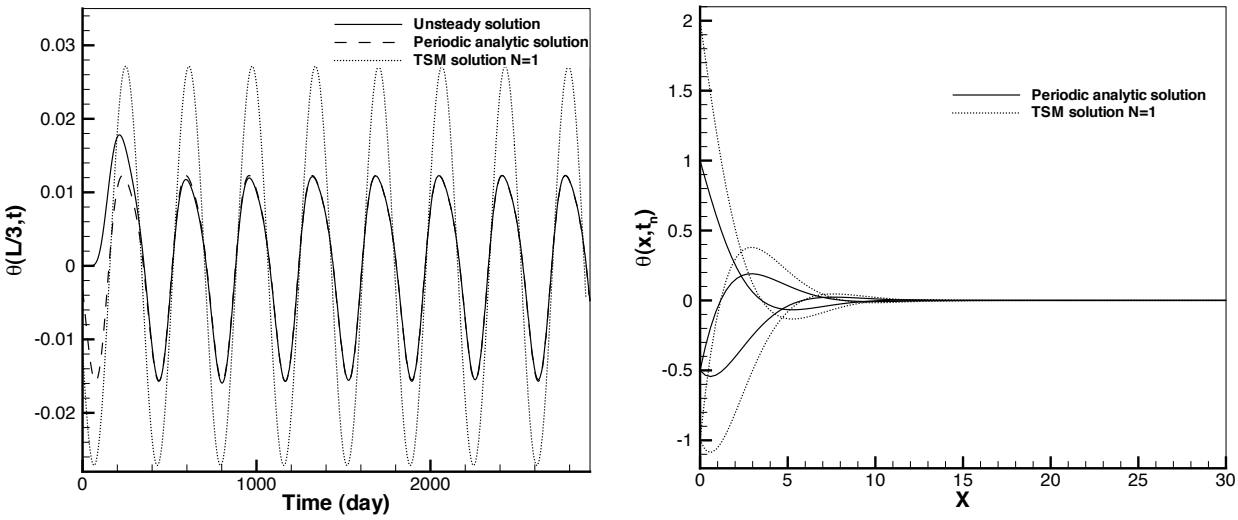

(a) $\theta(L/3, t)$ as a function of time

(b) $\theta(x, t_n)$ for $0 \leq n < 3$ as a function of space

Figure 5.6: Conduction equation. Double harmonic excitation, TSM solution with $N = 1$.

$$\theta_s(x,t) = \exp(-\sqrt{\frac{\omega}{2a}}x)\cos(\omega t - \sqrt{\frac{\omega}{2a}}x) + \exp(-\sqrt{\frac{2\omega}{2a}}x)cos(2\omega t - \sqrt{\frac{2\omega}{2a}}x) \qquad (5.54)$$

The solution of the new problem involving the modified boundary condition (5.53) but with all other physical parameters left unchanged is computed using the CN scheme with the same Δt as in the previous case of a single-harmonic problem and the TSM scheme with $N = 1$. The convergence to a steady-state of the TSM approach is achieved in a way similar to the previously computed single-harmonic test-case. But, as far as accuracy is concerned, the picture is now quite different since, as can be checked in Fig.5.6, using a single harmonic with TSM yields a numerical periodic solution which remains far from the exact periodic solution. Meanwhile, the unsteady CN solver coincides with this exact periodic solution after a short transient. It is also worth noticing that the TSM solution obtained for the heat conduction problem with a double harmonic input signal using TSM with $N = 1$ is different from the solution previously obtained using TSM with $N = 1$ for the heat conduction problem with a single harmonic input. Both TSM problems differ indeed through the left boundary values associated with the coupled steady solutions at time t_0, t_1, t_2 over the period. These three time-instances are displayed in Fig.5.7a and the points on the double harmonic left boundary condition correspond to the three fixed temperature values used in the TSM system. When solving the previous problem with a single harmonic left boundary condition, the fixed temperature values used at $x = 0$ in the TSM system correspond to different values, taken at the same time-instances since $N = 1$ with the same period but along the dotted curve associated with the single harmonic boundary condition. The spurious computation of the temperature time-derivative using

a spectral difference formula with $N = 1$ when the input signal contains a double harmonic is clearly visible in Fig.5.7b.
As soon as $N = 2$ is used with the TSM approach, the time derivative is correctly computed (Fig. 5.8b) and the exact periodic solution is very well approximated using TSM (Fig. 5.9).

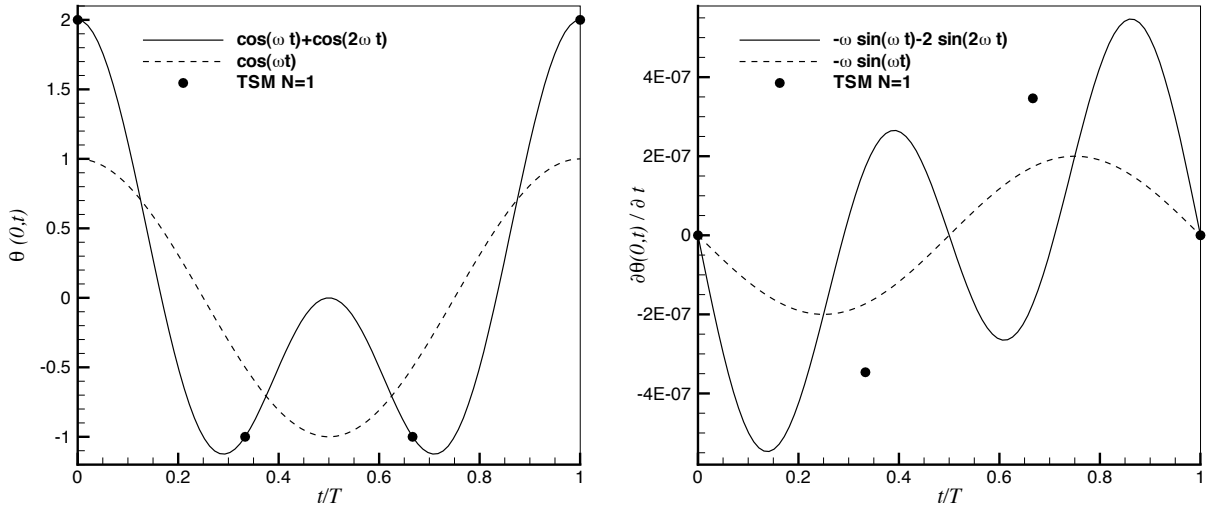

(a) (b)

Figure 5.7: Time Spectral derivative of the double harmonic input signal with $N = 1$.

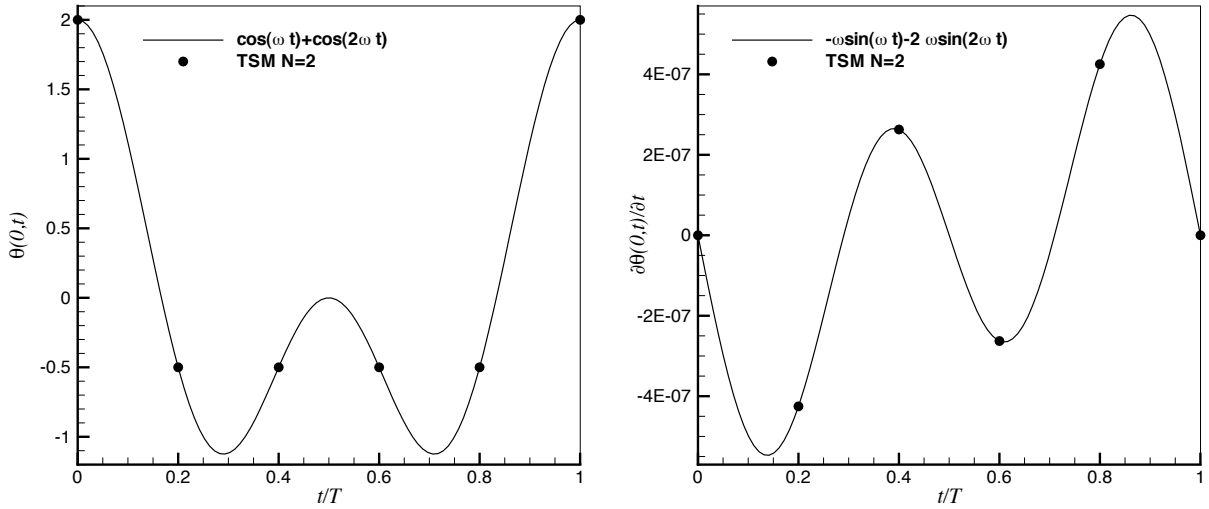

(a) (b)

Figure 5.8: Time Spectral derivative of the double harmonic input signal with $N = 2$

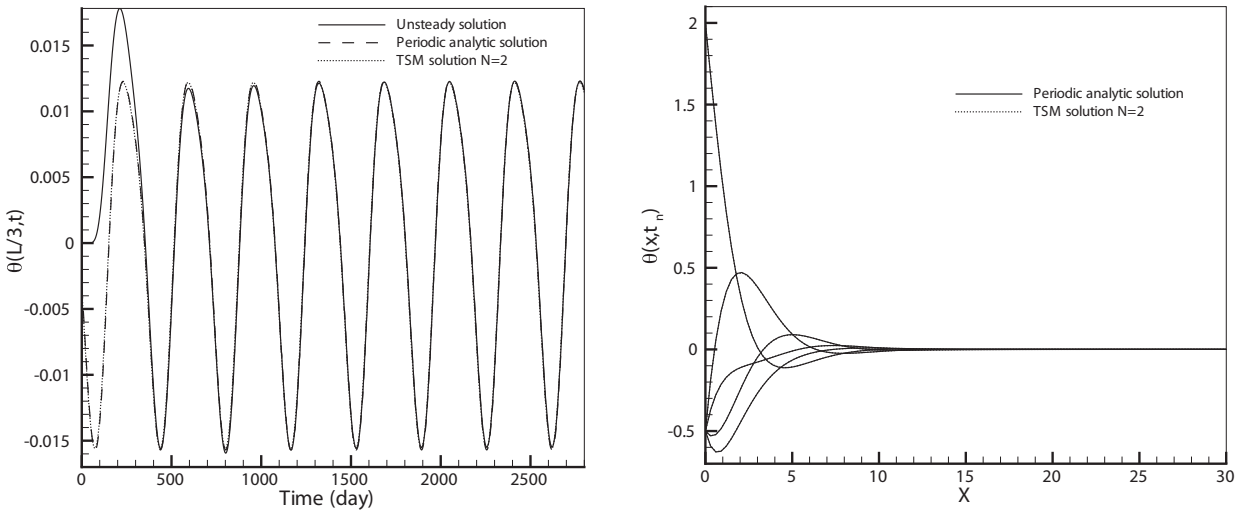

(a) $\theta(L/3, t)$ as a function of time

(b) $\theta(x, t_n)$ for $0 \leq n < 5$ as a function of space

Figure 5.9: Conduction equation. Double harmonic excitation, TSM solution with $N = 2$.

The additional contribution of puslation 2ω is not clearly visible in Fig. 5.9 because the term $\exp(-\sqrt{\frac{2\omega}{2a}}x)\cos(2\omega t - \sqrt{\frac{2\omega}{2a}}x)$ of the periodic solution (Eq. (5.54)) disappears closer to the boundary. If the solution is plotted at the location $x = L/20$ (see Fig.5.10), the contributions of both boundary modes are now clearly identified.It can also be observed the periodic state is reached faster when getting closer to the left boundary since the influence of this boundary is more immediate.

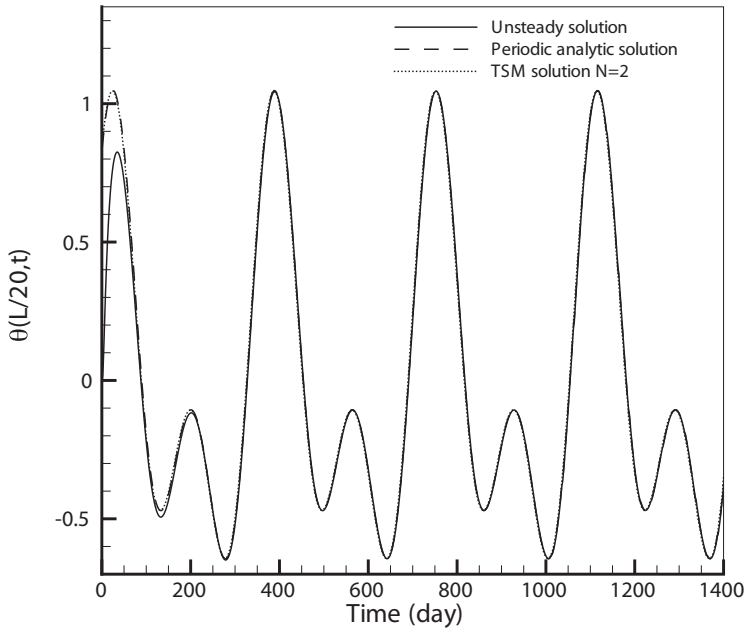

Figure 5.10: Normalized temperature $\theta(x, t)$ as a function of time at location $x = L/20$

5.4.3 TSM efficiency

As previously mentioned, the reference method retained for the unsteady calculation is the Crank-Nicholson scheme with CFL = 1, corresponding to a time-discretization counting $N_{\Delta t} = 350$ steps per period. Typically, $N_{cycles} = 7$ periods are necessary to reach the periodic state using the CN scheme. The method for evaluating the computational efficiency of the TSM which has been presented in Section 4.4.3 is not readily applicable to the present case since the conduction equation solver differs from the flow solver on two main points : i) the unsteady method, also denoted λ-scheme with $\lambda = 1/2$ for Crank-Nicholson, does not use a pseudo-time approach, ii) the unit cost ratio $\Phi_2(N)$ between TSM and the CN or λ-scheme is not given by (4.28). The way to evaluate the global cost ratio between TSM and the unsteady scheme still follows the same principles and yields :

$$\eta = \frac{\mathcal{C}_{TSM(N)}}{\mathcal{C}_\lambda} = \underbrace{\frac{(2N+1)}{N_{\Delta t} \times N_{cycles}} \times m_{max}^{TSM(N)}}_{\Phi_1} \times \underbrace{\frac{c_u^{TSM(N)}}{c_u^\lambda}}_{\Phi_2} \tag{5.55}$$

The cost per iteration of the λ-scheme is numerically computed using an average cost over 100 iterations and is estimated to be $\mathcal{C}_u^\lambda = 0.053$ s. The same method is applied to evaluate the unit cost of the TSM and leads to $c_u^{TSM(1)} = 0.07$ and $c_u^{TSM(2)} = 0.084$. Moreover, from Fig. 5.4, the number of dual iterations to achieve steady state with TSM is approximately $m_{max}^{TSM(N)} = 60$. As a consequence, $\eta(1) \approx 0.097$ and $\eta(2) \approx 0.194$ which demonstrates the efficiency of the TSM (cost reduction by a factor between 10 for the single-harmonic input case and 5 for the double-harmonic input case.

5.5 Lessons taught by the heat equation model problem

The simplicity of the unsteady heat equation has made possible to combine *a priori* analysis, in particular Von Neumann stability analysis, and actual TSM computations in order to identify the best strategy that should be followed when applying the TSM approach. It was concluded the Point Jacobi solution of the fully implicit TSM scheme with a diagonal correction designed to preserve the TSM system diagonal dominance offered a good level of both robustness and efficiency.Naturally, for the simple model problem considered in this chapter, better solutions are available, such as the direct solution (without any dual-time marching) of the TSM system using once for all a LU solver. The corrected PJ-TSM solver defined by (5.46) is however of particular interest because its design principles are those followed to derive the implicit TSM solver for compressible flows, denoted PJ-TSM-ALE and summarized in formula (4.22) of Chapter 4, as well its version for incompressible flows (4.25). The good properties of the PJ-TSM solver with diagonal correction reported in this Chapter are therefore a positive signal for the use of (4.22) in Chapter 6 and of (4.25) in Chapter 7. Treating an unsteady scalar heat conduction problem with TSM was

also enlightening as far as the practical implementation of the TSM approach within an existing time-accurate solver is concerned. This point does not explicitly appear in the report since details on the algorithmic developments are kept minimal but it was worth mentioning.
Let us keep in mind there is a number of limitations to the lessons drawn from this model problem analysis. Specific solution methods can be proposed for the linear systems associated with the TSM discretization of the $1D$ heat conduction problem (based in particular on the well-known efficient tridiagonal solver known as the Thomas algorithm) which cannot be extended to the general unstructured grids considered in the last part of this work. Because of the linearity of the spatial operator, the frequency spectrum of the excitation law and the field response are identical for the heat conduction problem. This makes easy to guess how many harmonics are needed with TSM to get the correct periodic solution. With a non-linear spatial operator, such as the one associated with the compressible or incompressible Navier-Stokes equations, the relationship between the harmonic content of the excitation and the number of TSM modes is much more complex and no longer *a priori* known. Last, the global efficiency gain reported in this chapter asks of course for a confirmation on more realistic applications. The last part of the thesis report is devoted to such an assessment of the TSM approach developed in this work for compressible and incompressible two-dimensional flow problems.

Part III

External Flows Applications

Chapter 6

Compressible flows

In this chapter, the TSM is applied to two compressible flows cases and compared in terms of accuracy and time-efficiency to a BDF approach following the methodology presented in Section 4.4. The first case involves a rotating cylinder studied by Bergmann [8] on a fixed grid whereas the second case is a moving grid application consisting of the pitching aerofoil already studied in section 1.6.1 with a conventional BDF-DTS approach. These simulations are representative of the ability of the TSM to deal with inviscid and laminar time-periodic compressible flows. Similar compressible flow applications have already been treated by Gopinath & al [27, 26] and Woodgate and Badcock [76]. The originality of the present study lies in the implicit formulation described in Chapter 4 which allows the use a large number of harmonics compared to references [27, 26] and in the use of unstructured grids compared to [27, 26, 76].

6.1 Rotating Cylinder

6.1.1 Test case description

The case of study consists in a cylinder animated of a periodic rotation around its axis. The fluid is considered compressible and viscous. The wake dynamics of a cylinder is characterized by its Reynolds number [75, 79].

$$Re = \frac{U_\infty D}{\nu}$$

where U_∞ is the velocity far upstream of the cylinder, D the diameter and ν the dynamic viscosity.

The Reynolds number $Re = 200$ corresponds to the upper limit of the laminar wake [79]. The wake flows becoming tridimensional for $Re \simeq 190$ [75], it is not legitimate to expect a realistic description of the cylinder wake dynamics using just a bidimensional approach. However, it is commonly accepted that bidimensional effects still play a major role beyond

$Re = 190$ which justifies the approach [8]. In his PhD thesis, Bergmann considers two cases: in the first one, the cylinder is rotated with a harmonic law of the form:

$$\lambda(t) = \frac{V_t(t)}{U_\infty} = \frac{R\dot{\theta}}{U_\infty} = A\sin(2\pi S_{tf} t) \tag{6.1}$$

where $V_t(t)$ is the tangential velocity of the cylinder, A and S_{tf} are respectively the amplitude and the forcing Strouhal.
In the second case, the cylinder is fixed. A natural instability breaks out in the near wake and a Von Kármán vortex shedding occurs downstream of the cylinder. Both phenomena are characterized by a shedding frequency, related to the Strouhal non-dimensional number by :

$$S_t = \frac{fD}{U_\infty} \tag{6.2}$$

where f is the shedding frequency. When the cylinder is rotated with an harmonic law, the shedding frequency is equal to the rotational frequency. In that case, the notation S_{tf} is used to point out a forcing Strouhal. When the cylinder is motionless, the shedding frequency is natural and only depends on the flow regime via the Reynolds number.
The main objective of rotating the cylinder is to obtain a drag reduction using this active control strategy. Bergmann [8] found that the couple of parameters ($A = 2.2, S_{tf} = 0.53$) leads to the best results as far as drag reduction is concerned. In his work, the incompressible Navier-Stokes equations are solved using a projection method of prediction-correction type for the pressure variable [37].
Figures 6.1 represent the temporal evolution of the drag and lift coefficients respectively for the driven/rotating and still cylinder; let us recall these coefficients are defined as :

$$C_D = \frac{F_D}{\frac{1}{2}\rho D U_\infty^2}, \quad C_L = \frac{F_L}{\frac{1}{2}\rho D U_\infty^2} \tag{6.3}$$

where F_D and F_L are respectively the force exerted on the cylinder in the direction of the flow and perpendicular to the flow direction. It can be observed in Fig.6.1 the drag and lift response adopts the forcing frequency of the Strouhal number S_{tf}. The reduction on the drag coefficient resulting from the harmonic rotation is about 25%. The average value of C_D goes down from 1.4 to 1.04 while the amplitude of the lift coefficient oscillations is also reduced by 75 % (from 1.38 to 0.34).

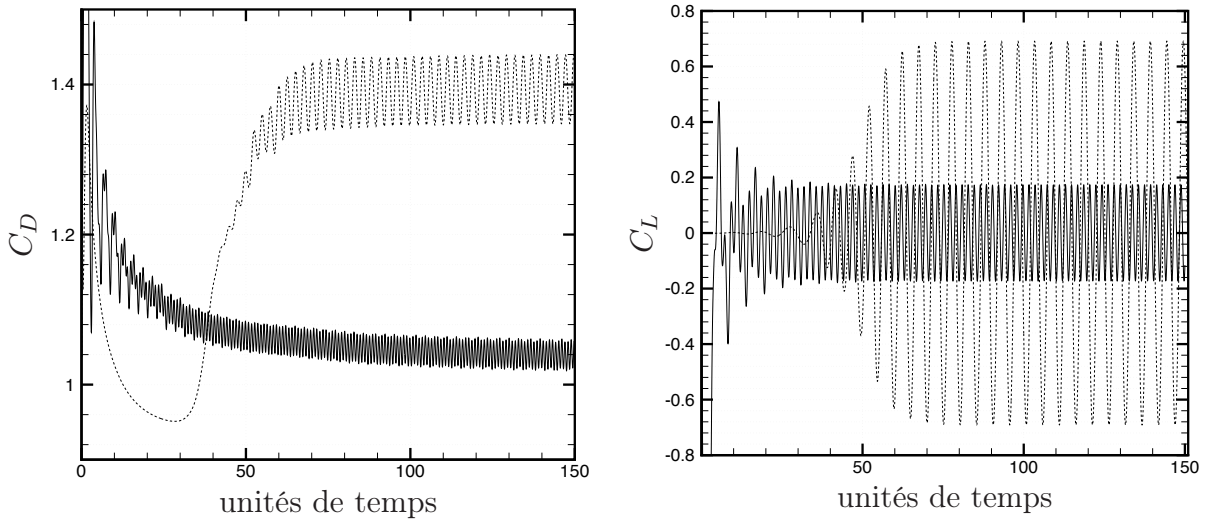

(a) (b)

Figure 6.1: (a) Drag coefficient C_D. (b) Lift coefficient C_L. Fixed cylinder (solid line), rotating cylinder (dotted line) from [8].

In the next sections, the results of the PJ-BDF-C solver are first compared with the reference [8] for the rotating cylinder case. Then, TSM calculations are performed and compared to the BDF approach. An attempt to apply the TSM to the particular case of the non-rotating cylinder where the frequency of oscillations is unknown is presented in Appendix D.

6.1.2 Numerical parameters

To drive the cylinder into rotation, the mesh is kept fixed and the tangential velocity is specified at the cylinder wall boundary where a no-slip viscous boundary condition is imposed.

The TSM and BDF versions of the compressible flow solver (PJ-BDF-C and PJ-TSM-C) are used with an upstream Mach number equal to $M_\infty = 0.2$ (minimal recommended value for the non-preconditioned compressible flow solver at hand to avoid low-Mach number issues) and compared with Bergman results obtained with an incompressible flow solver. The AUSM$^+$ numerical scheme is used for spatial discretization, CFL $= 10^6$ for computing the dual time step $\Delta\tau_{i,n}^m$ with (4.8) and $l_{max} = 16$ for the implicit stage point Jacobi resolution in both the TSM and BDF approaches.

The mesh, displayed in figure 6.2 counts 24000 cells. It is of O-grid type with boundaries located 20 D away from the cylinder center in order to be able to use the Riemann invariants for expressing the boundary conditions.

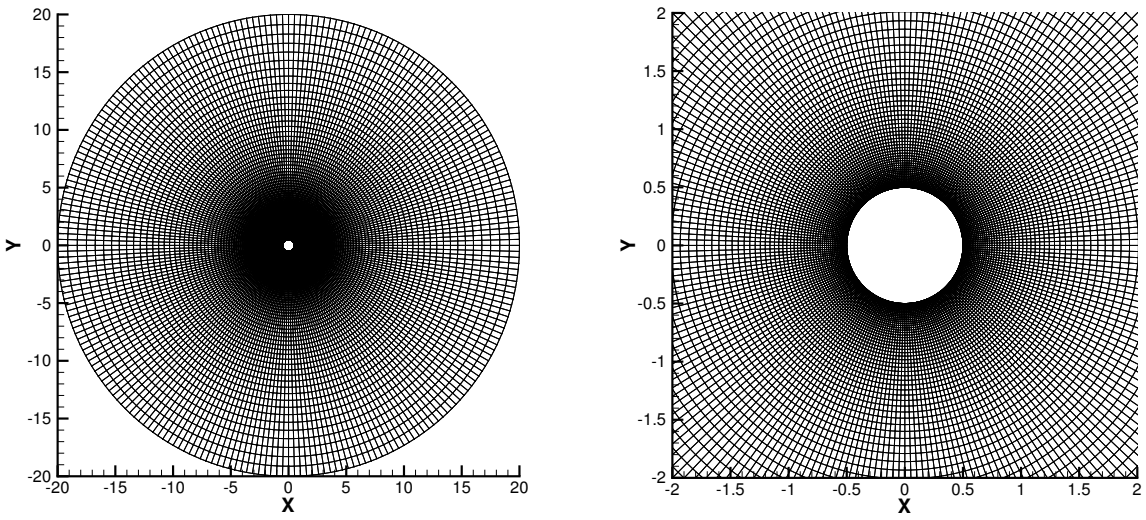

(a) (b)

Figure 6.2: Rotating cylinder. (a): Global view of the computational grid. (b): Close-up on the cylinder region.

6.1.3 BDF simulation

The flow period computed with (6.2) for $S_{tf} = 0.53$ is equal to $T \approx 1.886$ s. The time step is $\Delta t = 4 \times 10^{-2}$,, corresponding approximately to $N_{\Delta t} = 50$ time steps per cycle.

Reference	C_L	C_D
PJ-BDF-C	$\pm$ 0.41	1.00 $\pm$ 0.0325
Bergmann [8]	$\pm$ 0.36	1.04 $\pm$ 0.025

Table 6.1: Rotating cylinder. Global aerodynamic coefficients, BDF results, A=2.2, $S_{tf} = 0.53$, $Re = 200$, $M = 0.2$

The time-evolution of the global aerodynamic coefficients is plotted in Fig.6.3 for the BDF-DTS computation. The associated key values are summarized in table 6.1; they are in good agreement with reference [8]. The differences are likely due to the difference of physical modeling between the compressible and incompressible assumptions. The transient stage before the periodic state is quite long, as observed in Fig.6.3, with around 50 periods needed for the C_L to achieve an established periodic evolution and 100 periods for C_D. The lift coefficient oscillates at the forcing frequency whereas the drag coefficient oscillates twice as fast. This behavior is easily understood since there is a drag axis symmetry of the problem for two opposite tangential velocity values.

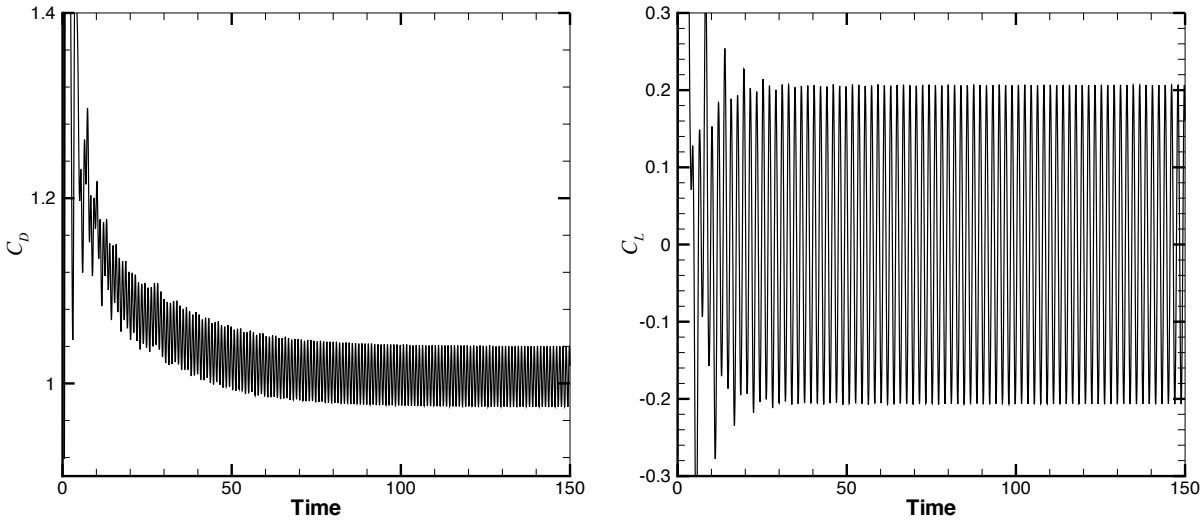

(a) (b)

Figure 6.3: Rotating cylinder with'$M = 0.2$, $Re = 200$, $A = 2.2$, $S_{tf} = 0.53$. Computed evolution of C_D (a) and C_L (b) using BDF-DTS.

6.1.4 Fourier Analysis

The global coefficients can be analyzed using a Fourier series development to get a first idea of the spectrum content of the solution and therefore of the number of time instants needed for the following TSM computations. Consider a periodic function f; if f is real, it can be decomposed using real coefficients so that

$$f(t) = a_0(f) + \sum_{n=1}^{+\infty} \left(a_n(f) \cdot \cos(n\omega t) + b_n(f) \cdot \sin(n\omega t)\right) \tag{6.4}$$

with $\omega = 2\pi/T$ and T the period. The real Fourier coefficients read

$$\begin{cases} a_0(f) = \frac{1}{T} \int_0^T f(t)dt \\ b_0(f) = 0 \end{cases} \tag{6.5}$$

and for any natural number $n > 0$

$$\begin{cases} a_n(f) = \frac{2}{T} \int_0^T f(t) \cos(n\omega t)dt \\ b_n(f) = \frac{2}{T} \int_0^T f(t) \sin(n\omega t)dt \end{cases} \tag{6.6}$$

The n^{th} harmonic is written as the function

$$x \mapsto a_n(f)\cos(n\omega x) + b_n(f)\sin(n\omega x) = \chi_n \cos\left(nx\frac{2\pi}{T} + \phi_n\right), \tag{6.7}$$

where $\chi_n^2 = a_n(f)^2 + b_n(f)^2$ and if $\chi_n \neq 0$, $\cos(\phi_n) = a_n/\chi_n$ and $\sin(\phi_n) = -b_n/\chi_n$. The amplitude of the n^{th} harmonic function is then

$$|\chi_n| = \sqrt{a_n(f)^2 + b_n(f)^2} \tag{6.8}$$

The output of this Fourier analysis applied to the global aerodynamic coefficients is presented in figure 6.4.

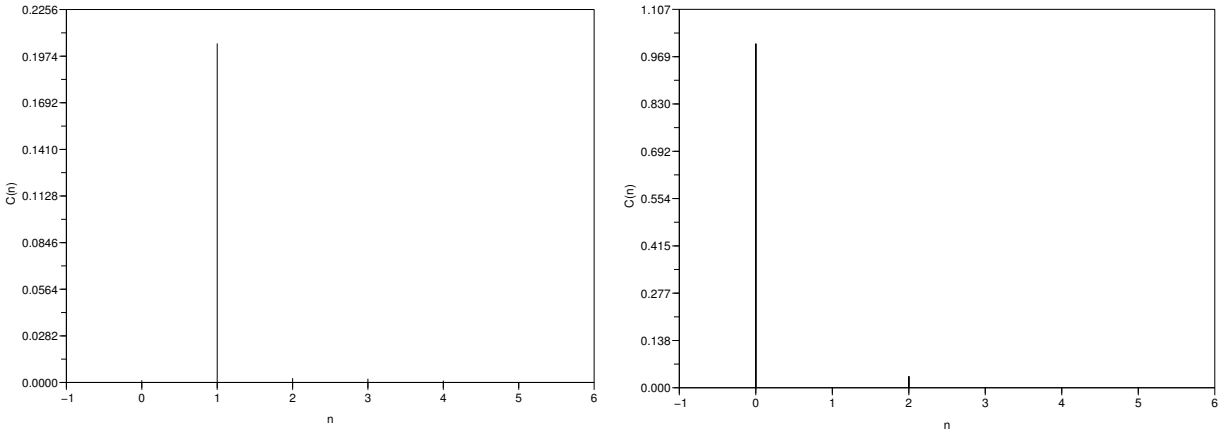

(a) C_L (b) C_D

Figure 6.4: Rotating cylinder. Spectrum of the BDF solution.

One can check that the average value of C_L is zero since the amplitude of harmonic 0 is $|\chi_0| = 0$ whereas the amplitude of the first harmonic is $|\chi_1| = \simeq 0.205$. The amplitudes of the higher modes are negligible but it will be seen later on that they play a significant role in the accuracy of the TSM computations. The average value of C_D is given by $|\chi_0| = 1.00$. The fact that the function oscillates twice as fast as the lift function is visible on the spectrum since the amplitude of the first harmonic is zero and the amplitude of harmonic 2 is $|\chi_2| \simeq 0.065$.

6.1.5 TSM simulation

Number of time instants

The harmonic content of the lift and drag coefficients led us to use only two harmonics for the TSM computations. This is equivalent (see previous section) to using $2N+1$ time instants evenly distributed over the period, that is - with $N = 2$ - looking for 5 steady

solutions which correspond to the five time instants t_n, $\quad 0 \leq n < 5$. The five flow fields are initialized with the freestream values and these problems only differ by the boundary condition written at the cylinder. Indeed, at each time instant corresponds a different tangential velocity:

$$V_t(t_n) = 2.2 \cdot \sin(2\pi \frac{n}{5}) \tag{6.9}$$

Figure 6.5 displays the position of the TSM time instants on the tangential velocity curve.

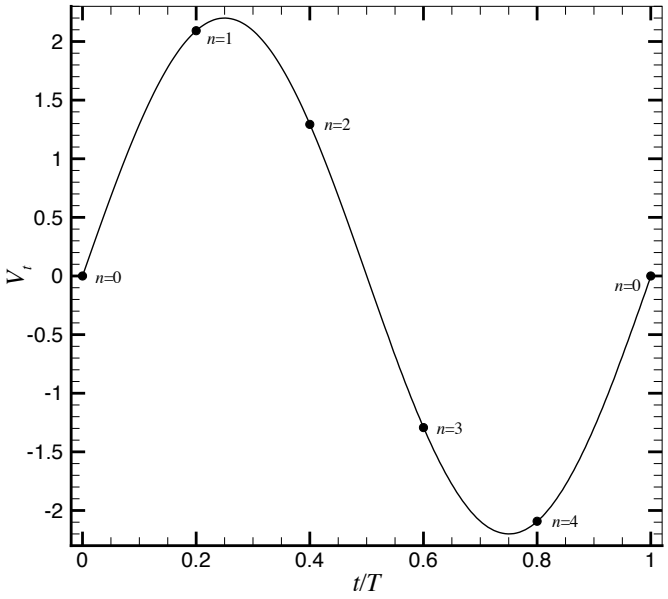

Figure 6.5: Rotating cylinder. Location of the TSM time instants on V_t, A=2.2, $S_{tf} = 0.53$.

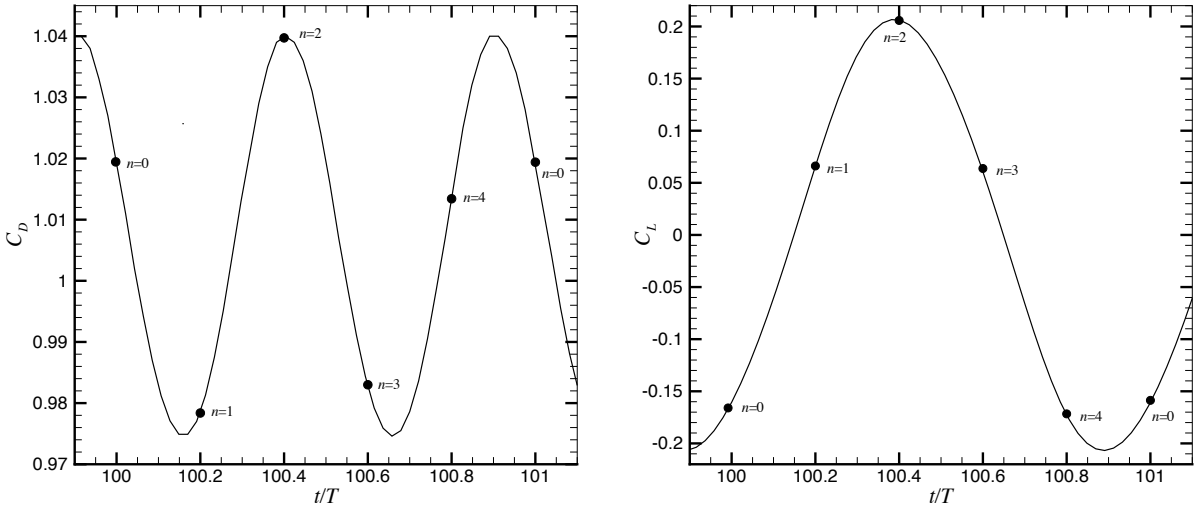

(a) C_D (b) C_L

Figure 6.6: Rotating cylinder. Location of the expected TSM solutions, A=2.2, $S_{tf} = 0.53$, $Re = 200$, $M = 0.2$.

TSM index n	0	1	2	3	4
C_L BDF	-0.1606	0.0657	0.2060	0.0606	-0.1723
C_L TSM	-0.1540	0.0521	0.1953	0.0562	-0.1723
C_D BDF	1.0191	0.9787	1.0398	0.9829	1.0134
C_D TSM	1.015	0.9735	1.042	0.9765	1.019

Table 6.2: Comparison of TSM and BDF results for $N = 2$, A=2.2, $S_{tf} = 0.53$, $Re = 200$, $M = 0.2$.

Figure 6.6 displays the projection of the TSM time instants on the BDF lift and drag curves : the points in this figure represent the expected steady solution of the TSM equations.

Global aerodynamic coefficients

A first TSM calculation is carried out with $N = 2$. Table 6.2 compares the results of the TSM with the previous BDF calculation at the TSM time instances. Note that the BDF results are obtained by linear interpolation using the nearby BDF discretization points. It shows a difference of 7% at worst for the C_L coefficient and $n = 2$ and under 0.03% at best for C_L and $n = 4$. Therefore, the TSM results show a correct trend with $N = 2$ but cannot be considered as accurate as the reference BDF results. This is why the number of harmonics considered in the TSM computation is increased. Moreover, a different representation of the TSM results is also used to allow a better comparison with the BDF method (see section 4.4.2) : the aerodynamic coefficients are reconstructed using the computed TSM values and formulae (3.21) and (3.20) for every BDF time discretization points in the period . Figure 6.7 displays these reconstructed lift and drag coefficients against the BDF results for the 100^{th} period. The increase in the number of modes significantly improves the TSM accuracy. For $N = 4$, the TSM and BDF lift coefficient curves are almost superimposed whereas there is still a little discrepancy for the drag coefficient. For $N = 8$, no improvement on the TSM solution is observed. The reason lies in the fact there is still some transient effects in the BDF solution which is not yet perfectly periodic in time, even for the 100^{th} period.

Convergence

The convergence history of the TSM approach plotted in figure 6.8 for an increasing number of modes shows that the convergence rate is weakly sensitive to the number of modes. It is worth mentioning that the method actually diverges for $N = 1$ and that, if the diagonal correction on the TSM fully implicit treatment is not applied, the method fails to converge for $N > 2$.

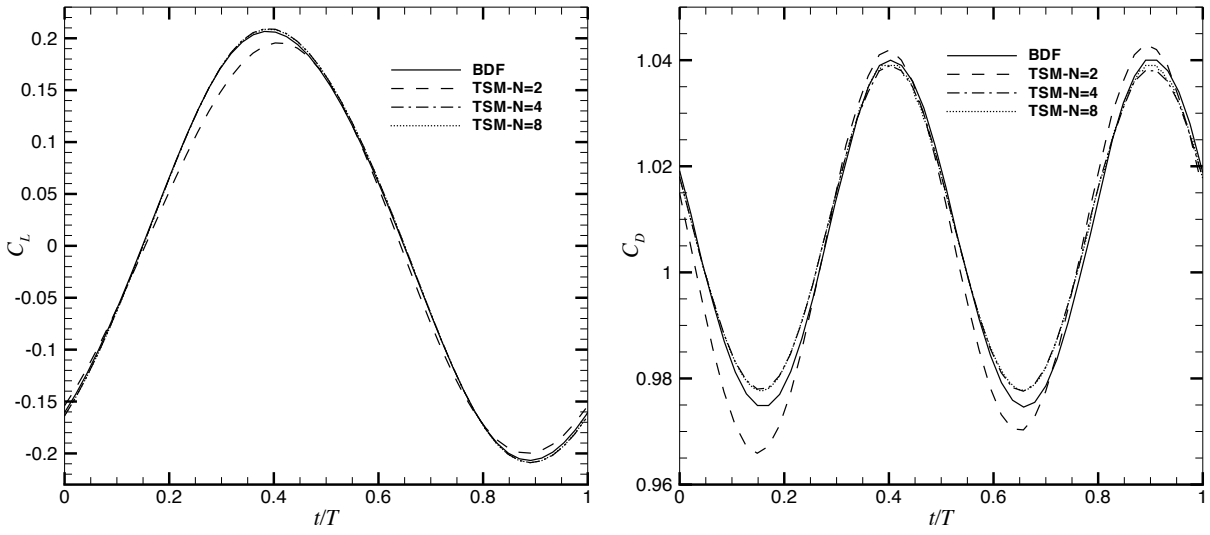

Figure 6.7: Rotating cylinder. Comparison of the C_L (a) and C_D (b) coefficients computed using BDF and TSM with an increasing number of harmonics

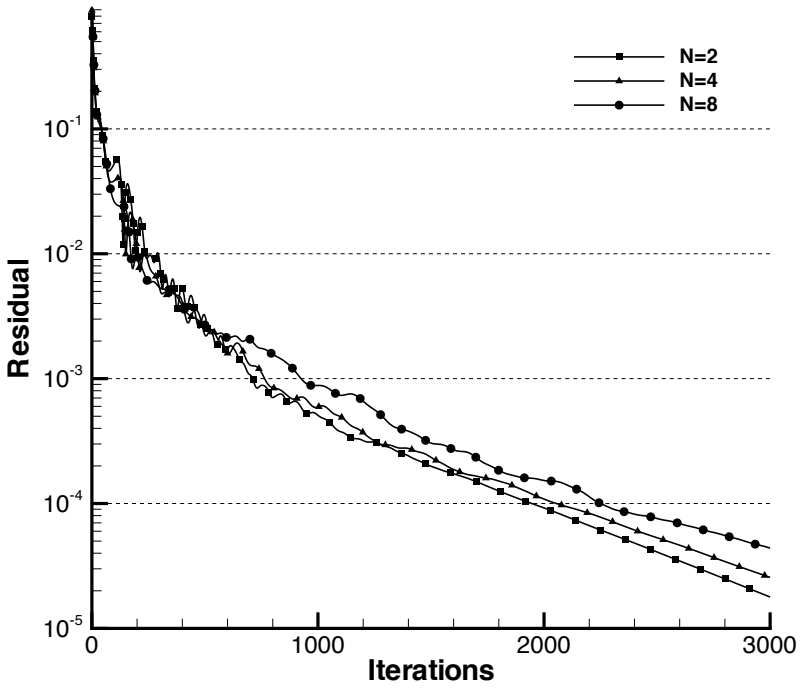

Figure 6.8: Convergence history for the PJ-TSM method, N ranging from 2 to 8.

Wall pressure distributions and pressure fields

Figure 6.9 shows the wall pressure coefficients computed with the TSM and BDF approaches. Five time instants corresponding to $N = 2$ are represented. The TSM results for $N = 2$ have been directly plotted whereas the TSM values for $N > 2$ have been reconstructed for these specific time instances. Consistently with the previous observations made on the global aerodynamic coefficients, a good agreement is observed between the TSM and BDF solutions for $N \geq 4$. The pressure fields corresponding to the same time instances and computed using TSM with $N = 8$ are displayed in Fig. 6.10 : the BDF and TSM contours are almost superimposed.

Efficiency of the TSM approach

The methodology presented in section 4.4.3 to analyze the global efficiency gain offered by the TSM approach with respect to the conventional BDF strategy is now applied on this cylinder flow problem to compute the flow-dependent factor Φ_1 appearing in formula (4.27). All the parameters needed for the computation of Φ_1 are summarized in table 6.3. The typical number $m_{max}^{TSM(N)}$ of iterations on the pseudo-time τ needed to achieve a steady state for the TSM computations is estimated for a convergence criterium of $res_{av} = 10^{-4}$. This number is roughly $m_{max}^{TSM(N)} = 2000$ whatever the value of N (see Fig.6.8). The global

Method	m_{max}	$N_{\Delta t}$	N_{cycle}
BDF	60	50	100
TSM	2000		

Table 6.3: Rotating cylinder. Parameters retained for the calculation of the contribution Φ_1 to the cost ratio η (4.27).

cost ratio for TSM and BDF strategies is then given by:

$$\eta = \Phi_1(N) \times \Phi_2(N) = (0.0066 \times (2N + 1)) \times \Phi_2(N) \tag{6.10}$$

with the problem-independent linear approximation of Φ_2 expressed as (4.28). As explained in 4.4.3, the ideal Φ_2 factor in the above formula would be roughly equal to 1.

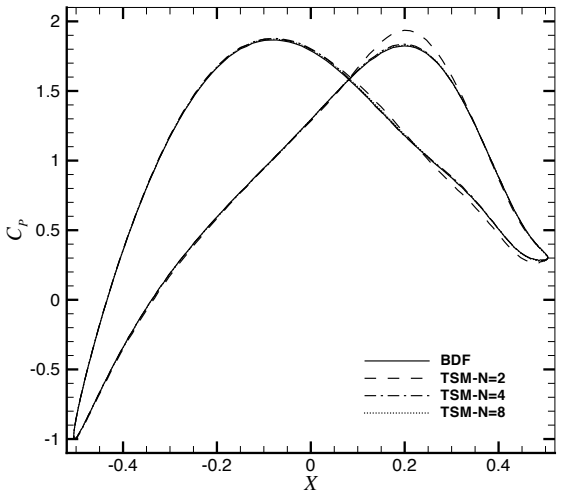

(a) $t/T = 0$

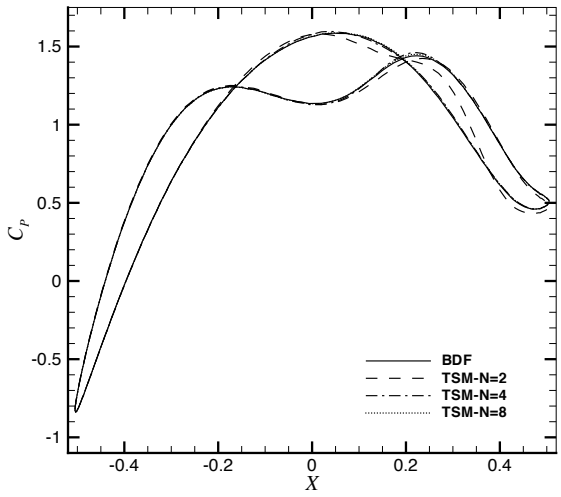

(b) $t/T = 0.2$

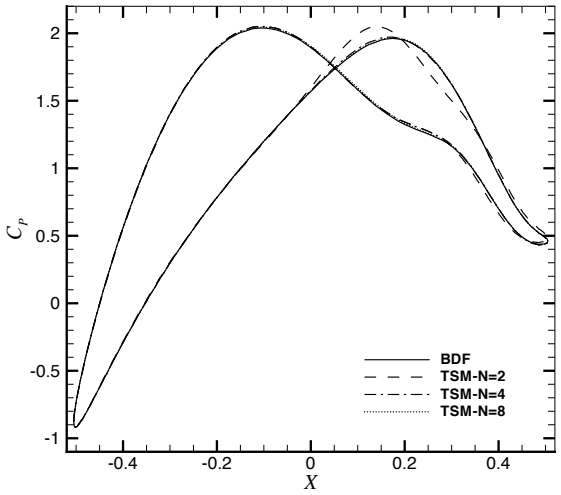

(c) $t/T = 0.4$

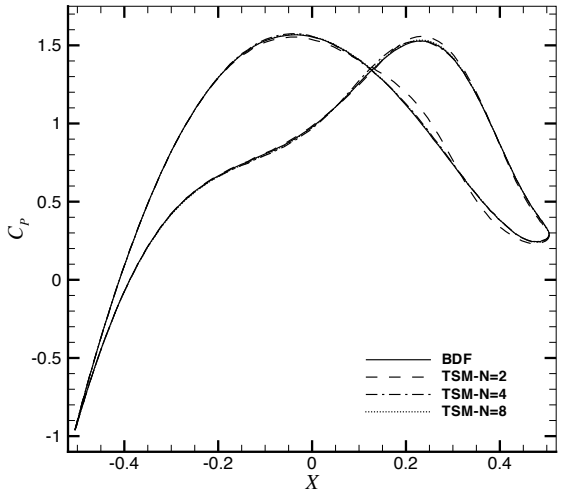

(d) $t/T = 0.6$

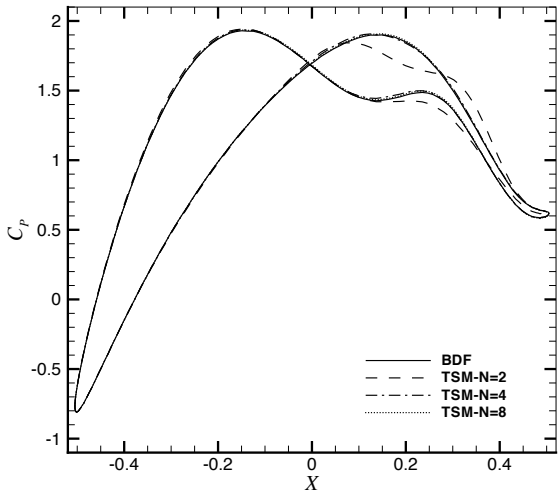

(e) $t/T = 0.8$

Figure 6.9: Rotating cylinder. Wall pressure coefficient for an increasing number of harmonics. Comparison with the reference BDF simulation.

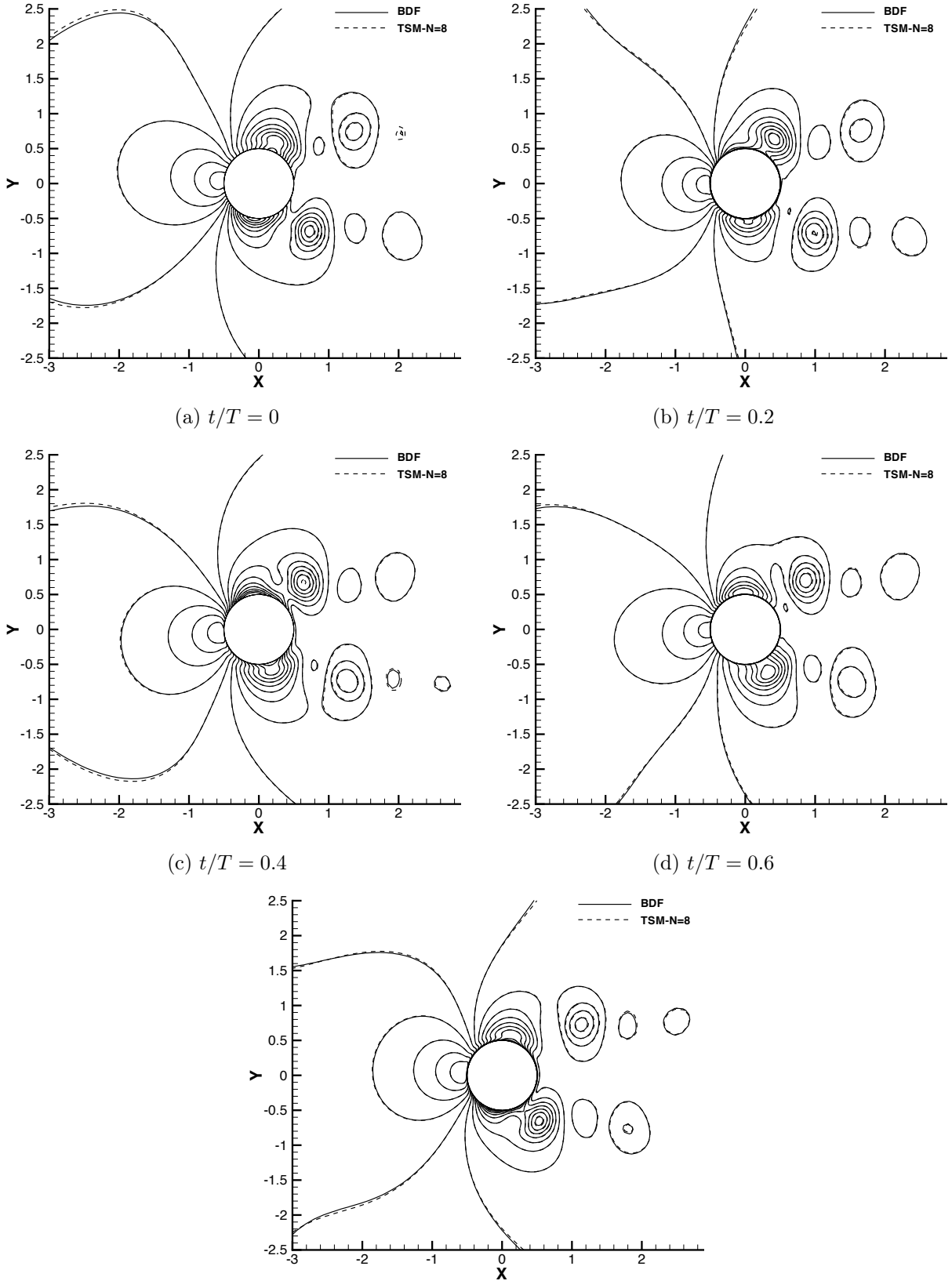

(a) $t/T = 0$

(b) $t/T = 0.2$

(c) $t/T = 0.4$

(d) $t/T = 0.6$

(e) $t/T = 0.8$

Figure 6.10: Rotating cylinder. Pressure contours for $N = 8$. Comparison with the reference BDF simulation.

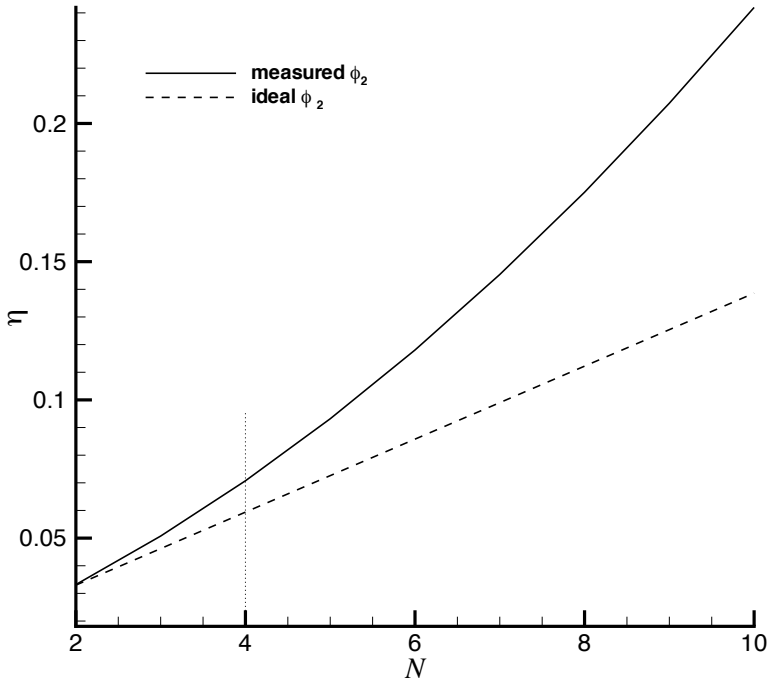

Figure 6.11: Evolution of the global cost ratio between TSM and BDF with an increasing number of harmonics.

Fig 6.11 displays the evolution of the global cost ratio η computed with the measured unit cost ratio $\Phi_2(N)$ given by (4.28), in which case η vary quadratically with N, or with an ideal unit cost ratio roughly equal to 1, in which case the variation of η remains linear with respect to N. This latter case provides an upper limit for the number of harmonics N that might be used by the TSM approach before its computational cost exceeds that of the BDF approach ($\eta > 1$). In the particular case of rotating cylinder under study though, the cost of the TSM stays well below the limit $\eta = 1$. For $N = 4$, when "engineering accuracy" is achieved according to the previous analysis of the TSM and BDF computations, $\eta \approx 0.07$ which speaks up for the TSM. The reason for this very low cost of the TSM with respect to BDF - with a reduction factor about 14 - is essentially to be found in the large number of flow cycles necessary to reach the periodic steady state ($N_{cycles} = 100$) when the BDF approach is used.

6.2 Pitching aerofoil

The TSM approach is now applied to the pitching airfoil test-case already computed with the BDF approach in 1.6.1. While the previous test-problem was computed on a fixed grid,

the present one makes full use of the moving grid features provided by the compressible TSM-ALE solver presented in section 4.1.

6.2.1 Fourier Analysis

Following the methodology of the previous cylinder case, the unsteady aerodynamic C_L and C_m coefficients obtained with the BDF-DTS approach are analyzed in the frequency domain (Fig. 6.12). This spectrum content provides a guideline to find an educated guess or estimate of the number of harmonics needed with the TSM approach.

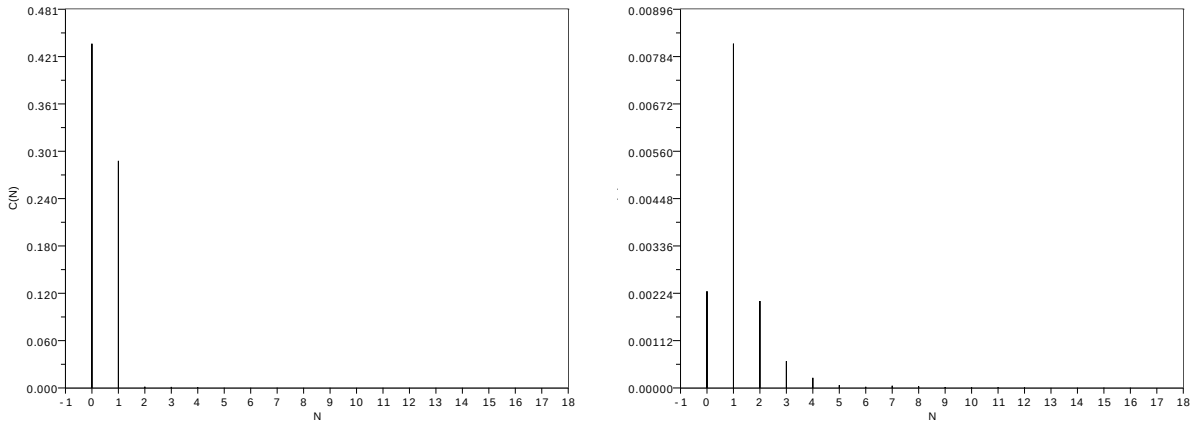

(a) C_L (b) C_m

Figure 6.12: Inviscid CT1. Spectrum of the BDF solution.

It is clear that the lift coefficient contains mainly one harmonic whereas the spectrum of C_m shows significant amplitudes up to the 9^{th} harmonic. One might expect the proper representation of the lift or moment coefficient using TSM(N) will not require the same minimal value of N.

6.2.2 TSM-ALE illustration

In order to illustrate the principles of the TSM-ALE algorithm presented briefly in Sec. 4.1.1, the value $N = 1$ is first retained. Let us recall the TSM time instances are given by:

$$t_n = \frac{n-1}{2N+1} \cdot T, \quad 0 \leq n < 2N+1 \tag{6.11}$$

At each TSM time corresponds a different mesh position as illustrated in Fig. 6.13 where the angle of attack is the angle between the chord and the upstream velocity direction. The angular position of the airfoil is given by

$$\theta(t_n) = \theta_m + \theta_0 \sin(\omega t_n), \quad 0 \leq n < 2N+1 \tag{6.12}$$

where $\theta_m = -\alpha_m$ and $\theta_0 = -\alpha_0$

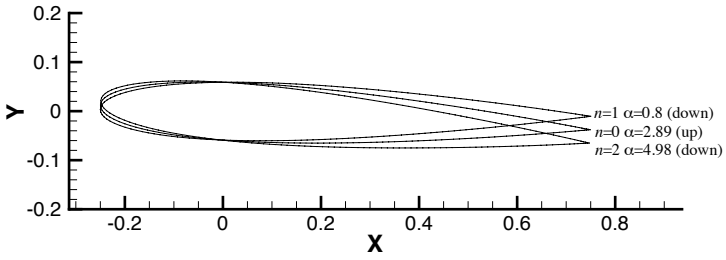

Figure 6.13: (up) increasing angle of attack, (down) decreasing angle of attack

The angular velocity of the aerofoil is computed from the law of motion:

$$\Omega(t_n) = \theta_0 \cos(\omega t_n), \quad 0 \leq n < 2N+1 \tag{6.13}$$

and the grid velocity for each TSM position is calculated as

$$\boldsymbol{s}_n = \boldsymbol{\Omega}_n \wedge (\boldsymbol{x}(t_n - \boldsymbol{x}_c(t_n))$$

where $\boldsymbol{\Omega}$ is the rotational velocity vector and $\boldsymbol{x}_c$ the center of pitching.

6.2.3 TSM simulation

A first TSM simulation is run with the same grid as in the BDF calculation of Section 1.6.1, with the AUSM$^+$ scheme for space discretization, $l_{max} = 16$ for the implicit PJ solver and CFL $= 10^6$ for computing the dual-time.

Global aerodynamic coefficients

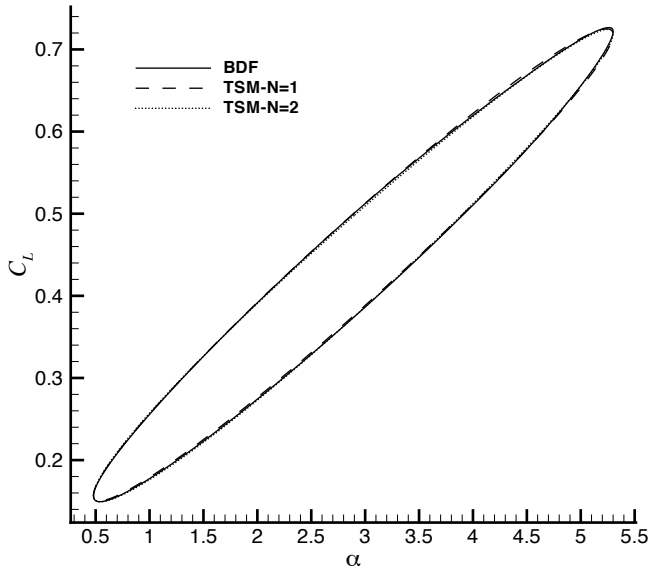

Figure 6.14: Inviscid CT1. Comparison of the C_L coefficient computed using BDF and TSM with $N = 1$ and $N = 2$.

The lift coefficient is plotted in figure 6.14 as a function of angle of attack and compared with the fully periodic BDF result : it is observed that engineering accuracy can be obtained using TSM with only a single harmonic. A similar TSM case is realized by Gopinath & al [27] on an oscillatory pitching airfoil AGARD CT6 and the authors reach the same conclusion.
The Mach number contours obtained with $N = 1$ for the three TSM time instances over the period are displayed in figure 6.15 and compared with the reference BDF calculation: the agreement between BDF and TSM is good for all the instants. On the other hand, the TSM and BDF pitching moment are compared in Figure 6.16 for an increasing number of harmonics. It is obvious that $N = 1$ is not sufficient to retrieve the correct C_m-BDF coefficient. For $N = 8$, the comparison is satisfactory and for $N = 16$, the match is almost perfect. In [76], Woodgate and Badcock studied the same CT1 configuration in a turbulent flow. They find that, in order to be able to reconstruct the pressure correctly with the TSM nearby the shock region, they need to increase the number of modes up to $N = 16$. On the same Figure 6.16, the Fourier series of the BDF solution with a truncated number of harmonic identical to the number used in the TSM calculation (noted Fourier in the legend) is also plotted. This illustrates the non linear effect of the spatial operator $\mathcal{R}$ which is expressed by Eq. (3.18). Indeed, for the same value of N, it can be observed that the Fourier truncated BDF solution is closer to the full BDF solution than the TSM solution.

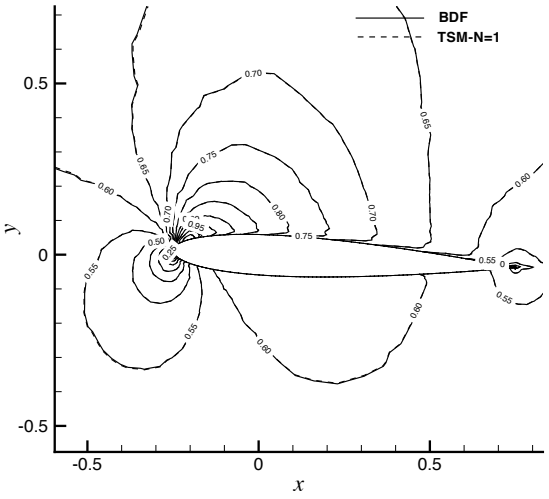

(a) $n = 0$, $t/T = 0$, $\alpha = 2.89°$ (up)

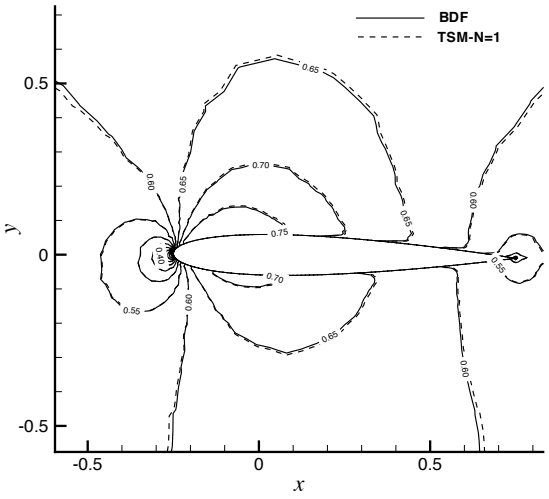

(b) $n = 1$, $t/T = 0.33$, $\alpha = 0.8°$ (down)

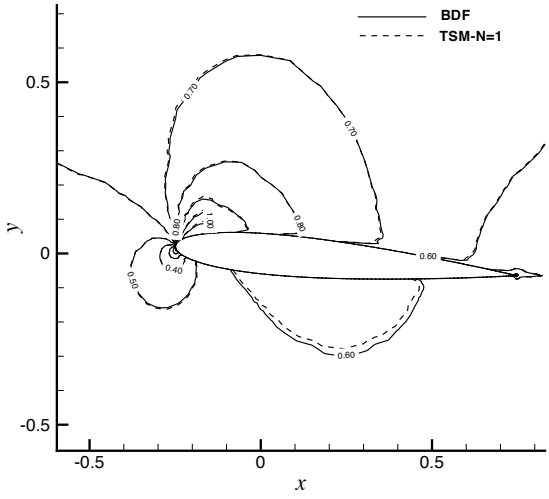

(c) $n = 2$, $t/T = 0.66$, $\alpha = 4.98°$ (down)

Figure 6.15: Inviscid CT1. Mach contours. Comparison of TSM results with $N = 1$ with the reference BDF simulation

In other words, the TSM necessitates more modes than the Fourier decomposition of the solution would indicate. This is why the interest of the initial Fourier decomposition is limited besides the fact that it needs to run an unsteady simulation beforehand. The highest harmonics of small amplitudes which can be neglected with regard to the Fourier decomposition of the solution can actually have significant role in the final solution and cannot be neglected to get an accurate TSM solution. Hence, it will no longer be proceeded to this frequency analysis in the next TSM test cases.

Convergence

The convergence history presented in figure 6.17 shows that between 2000 and 2800 iterations are needed by the fully implicit TSM scheme with diagonal correction to achieve steady-state convergence on dual time. Note the convergence improves with the number of modes increasing : 2800 iterations are needed for $N = 1$ while 2000 iterations are sufficient for $N = 16$.

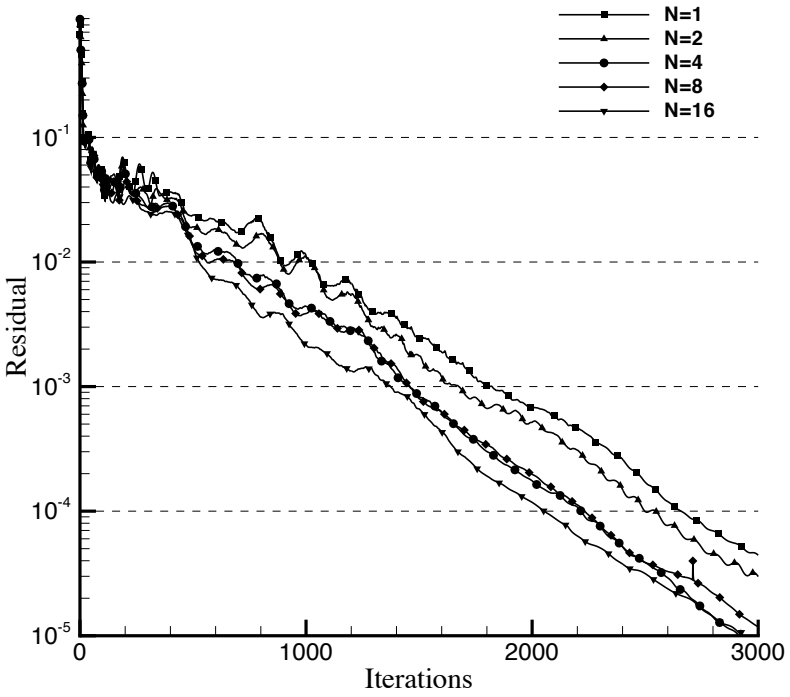

Figure 6.17: Inviscid CT1. Convergence history for the PJ-TSM-ALE method, N ranging from 1 to 16

Efficiency of the TSM approach

All the parameters required for the computation of Φ_1 are summarized in table 6.4. The

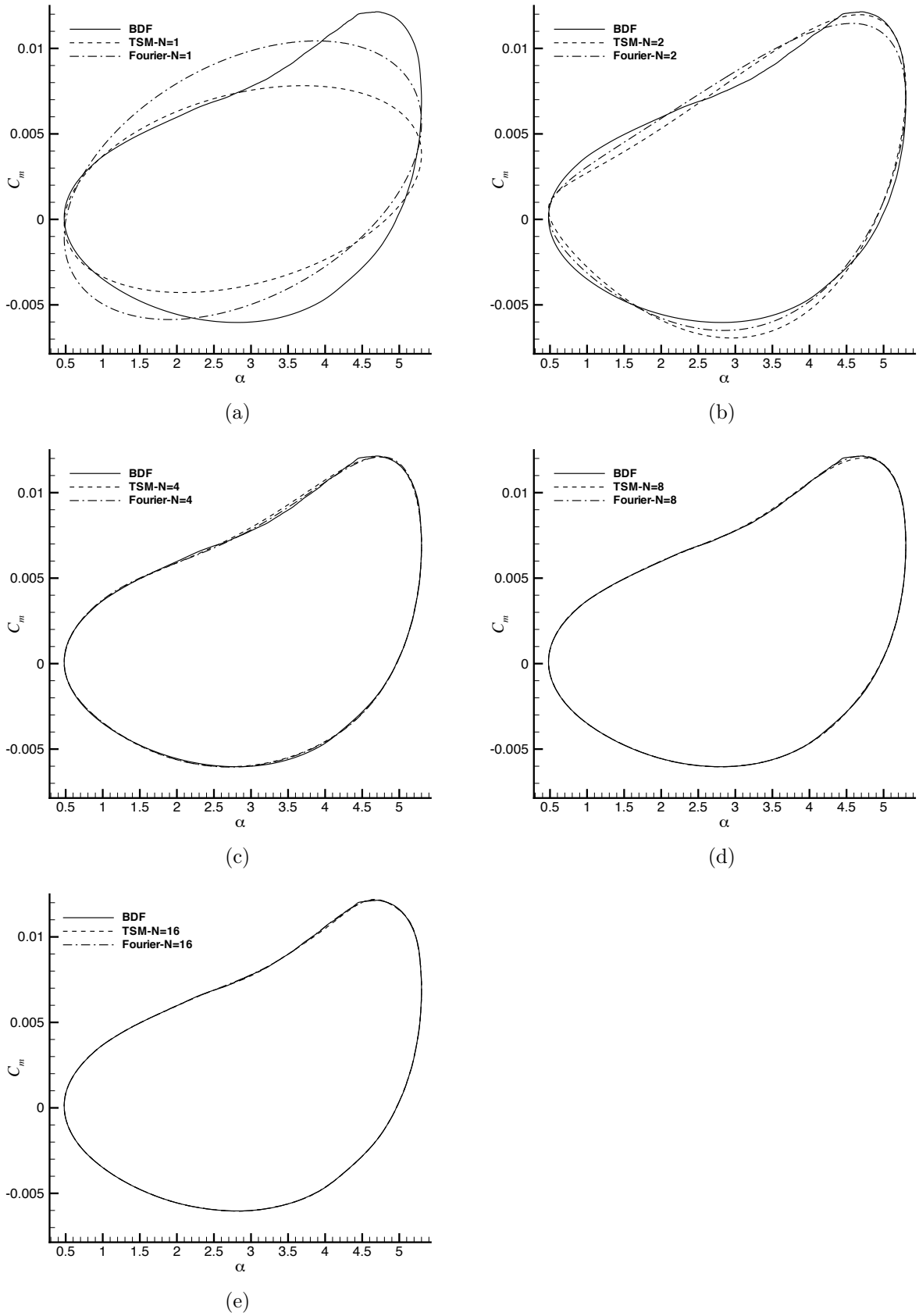

(a) (b) (c) (d) (e)

Figure 6.16: Inviscid CT1. Comparison of the pitching moment coefficient computed using TSM and BDF with an increasing number of harmonics.

Method	m_{max}	$N_{\Delta t}$	N_{cycle}
BDF	100	260	5
TSM	2500		

Table 6.4: Inviscid CT1. Parameters retained for the calculation of cost Φ_1.

global cost ratio between TSM and BDF strategies for the CT1 test-problem is then given by:

$$\eta = \Phi_1(N) \times \Phi_2(N) = (0.01923 \times (2N+1)) \times \Phi_2(N) \tag{6.14}$$

with the linear approximation of Φ_2 given by (4.28).

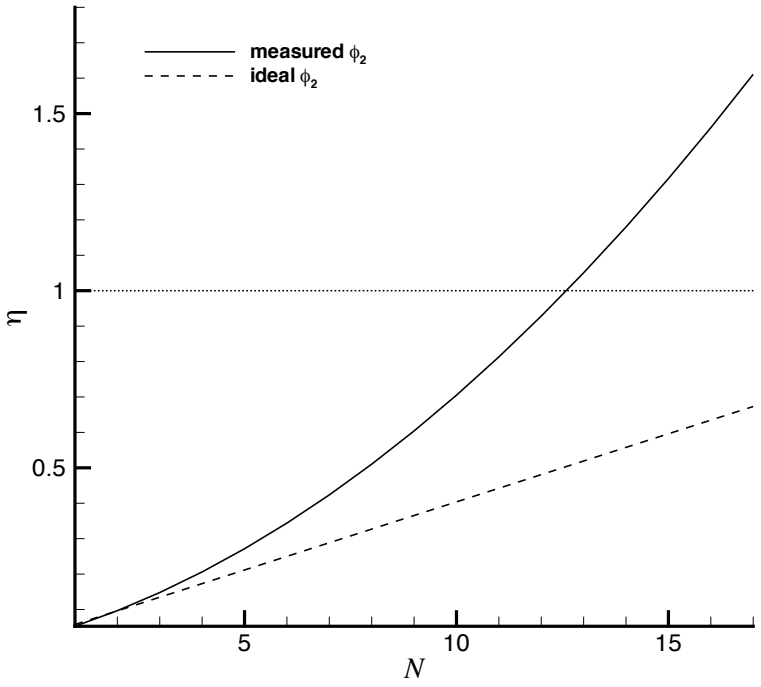

Figure 6.18: Inviscid CT1. Evolution of the global cost ratio between TSM and BDF with an increasing number of harmonics.

For this pitching application, it is concluded from Fig.6.18 the lift coefficient can be obtained using TSM rather than BDF for a cost ratio $\eta = 0.057$ if we consider that $N = 1$ leads to an accurate enough solution. On the other hand, the pitching moment coefficient necessitates more harmonics. The cost reduction for $N = 8$ is only $\eta = 0.51$. Note that using the present implementation of the method (which determines the intrinsic cost ratio contribution Φ_2) the TSM cost would overtake the BDF cost for approximately $N = 13$ harmonics. However, an optimal implementation of the TSM with a unit cost ratio $\Phi_2 \approx 1$ would preserve a net gain $\eta = 0.5$ with $N = 13$ on this test-problem.

Chapter 7

Incompressible flow applications

This last chapter deals with two incompressible laminar flow test cases taken from the recent pitching and heaving airfoil study performed by Kinsey and Dumas [41]. The TSM results on this kind of applications are, to the best of our knowledge, fully original and have been presented in an article submitted to the AIAA Journal and reproduced in Appendix E.

7.1 BDF simulations

7.1.1 Test case description

Among the many pitching and heaving airfoil cases studied by Kinsey & al [41] to analyze the power extraction regime, two configurations were selected, different from each other by their harmonic content response. The first test case, denoted PH from now on, combines pitching and heaving motion with $\theta_0 = 60°$, $H_0 = 1$ and $f^* = 0.18$. The second test case, denoted PP, corresponds to a pure pitching motion with $\theta_0 = 23°$, $H_0 = 0$ and $f^* = 0.12$. In both cases, the Reynolds number based on the freestream conditions and the airfoil chord is equal to $Re = 1100$ hence the flow is assumed laminar. The numerical parameters are the same as in Sec. 2.5.2 (grid, AC parameter, physical time-step, number of dual sub-iterations). The computation is started with a uniform pressure and velocity flow field; 6 (respectively 4) cycles must be computed for PH (resp. PP) before flow periodicity is fully achieved. All the PJ-BDF-ALE-AC results displayed hereafter correspond to the 7^{th} cycle for PH and 5^{th} cycle for PP and will be labelled BDF from now on.

7.1.2 Results

The comparison with the reference results [41] is performed on the force coefficients, more precisely on the C_Y coefficient which is the only one made available by Kinsey and Dumas. The C_X coefficient is also presented for future comparison with the TSM approach. Figure

			Test cases	
			PH	PP
Parameters	Pulsation	ω [rad.s^{-1}]	1.1309	0.7539
	Heaving Amplitude	H_0 [m]	1	0
	Pitching Amplitude	θ_0 [°]	60	23
	Time step	Δt [s]	0.0106	0.0160
	Period	T [s]	5.555	8.333
	Number of time step per period	$N_{\Delta t}$	520	520

Table 7.1: PH and PP test cases. Solver parameters

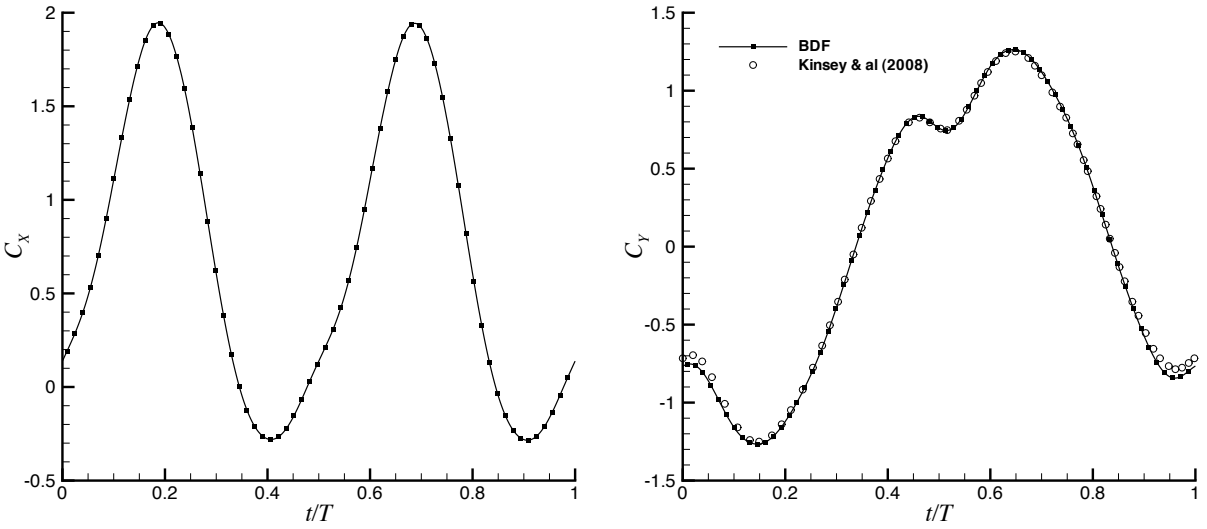

(a) (b)

Figure 7.1: PH testcase. (a): C_X evolution computed using the present BDF method. (b): C_Y evolution computed in [41] and using the present BDF method.

7.1 displays the computed C_X and C_Y coefficients over the normalized time period for the PH test-case; note only 1 out of 8 physical time-steps are plotted for the present BDF computations. Similar results obtained for the PP test-case are plotted in Figure 7.2. The agreement between [41] and the present BDF results is globally very good. A slight difference on the C_Y prediction can be observed in Fig. 7.1 for the PH problem. Further grid and time-refinement did not modify the present BDF results which will consequently be retained as reference data, against which the TSM approach developed in the next section will be compared, both in terms of accuracy and efficiency.

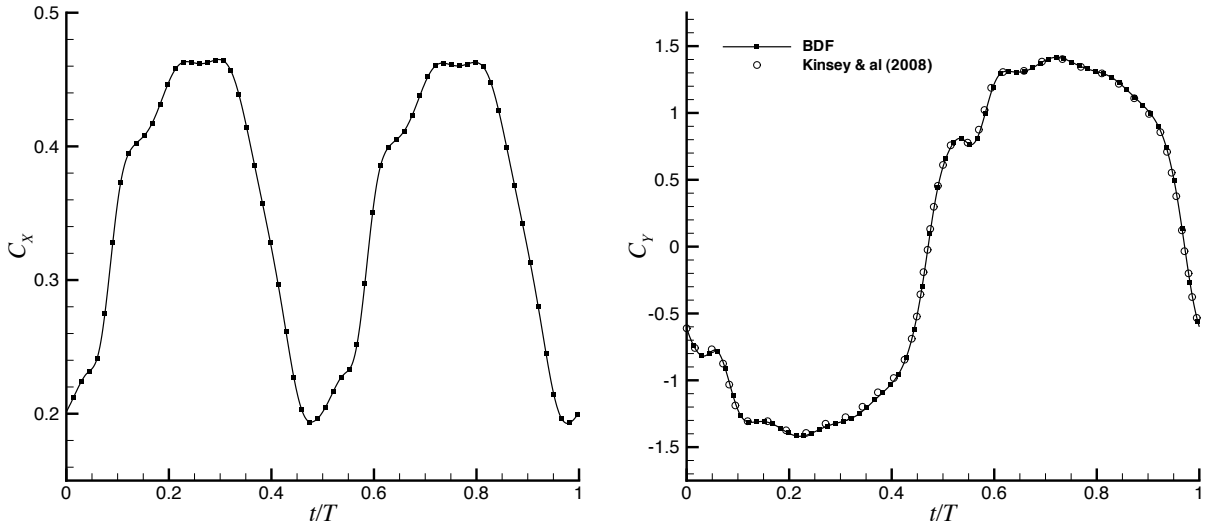

(a) (b)

Figure 7.2: PP testcase. (a): C_X evolution computed using the present BDF method. (b): C_Y evolution computed in [41] and using the present BDF method.

7.2 TSM simulations

The PJ-TSM-ALE-AC method is now applied to the computation of the test-problems PH and PP and its results are compared to those obtained using the PJ-BDF-ALE-AC approach. In the present study, the convergence of TSM to a steady-state will be first analyzed when the number of modes N is varied for accuracy purpose. The reference BDF strategy and the developed TSM approach will then be discussed in terms of accuracy: in particular, the number of modes needed to achieve a sufficient level of accuracy will be investigated for test-problems PH and PP. The potential efficiency gain offered by TSM with respect to BDF will be finally assessed.

7.2.1 Convergence of the TSM approach

All the computations make use of $l_{max} = 16$ for the implicit PJ solver and CFL $= 10^6$ for computing the dual-time step $\Delta\tau_{i,n}^m$ with (4.9). The convergence histories displayed in Fig. 7.3 demonstrate the convergence rate of the TSM solver to a steady-state depends only weakly on the number of modes N: for test-case PH, less than 4000 iterations are needed to achieve a residual decrease by four orders of magnitude while a bit less than 3000 iterations are sufficient for test-case PP, whatever the value of N. The cost of an iteration depends of course on the value of N but this point will be discussed at the end of the section after analyzing the accuracy of the TSM solutions.

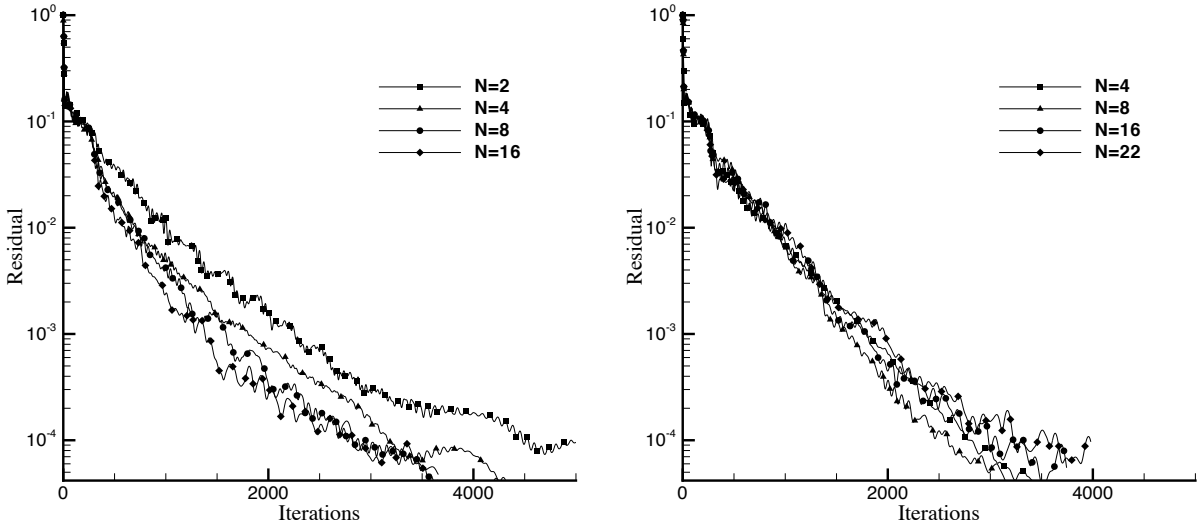

(a) (b)

Figure 7.3: Convergence history for the PJ-TSM-ALE-AC method. (a): PH test problem with increasing number of harmonics (N ranging from 2 to 16). (b): PP test problem with increasing number of harmonics (N ranging from 4 to 22).

7.2.2 Accuracy of the TSM solutions

The accuracy of the TSM solutions will be first assessed in a qualitative way by comparing the steady solutions of the PJ-TSM-ALE-AC system obtained for an increasing number of harmonics with the previously computed BDF solution. This comparison will be performed on the evolution of the global force coefficients C_X, C_Y over a cycle both for the PH and PP test-problems. Next the computed wall pressure distribution over the airfoil and pressure contours at selected instants within the period will also be compared. A more quantitative error analysis between TSM and BDF will be eventually proposed and conclusions regarding the potential efficiency gain offered by TSM with respect to BDF will be drawn.

Global aerodynamic coefficients

Figures 7.4 and 7.5 display the C_X and C_Y coefficients computed using the TSM approach with an increasing number of harmonics for the PH and PP flow problems respectively. These evolutions over a period are plotted along the previously computed BDF results, whose accuracy was checked with respect to [41]. Let us recall the BDF computations use 520 physical times-steps per period and require about 4 (resp. 6) cycles before reaching a periodic solution for the PH (resp. PP) flow problem. The TSM evolutions are reconstructed from the computed $\boldsymbol{w}_n$ fields for any time in the period using the truncated Fourier series representation of the flow solution. For the PH test-problem, the computed evolution using TSM with $N = 2$ and $N = 4$ significantly differs from the reference result;

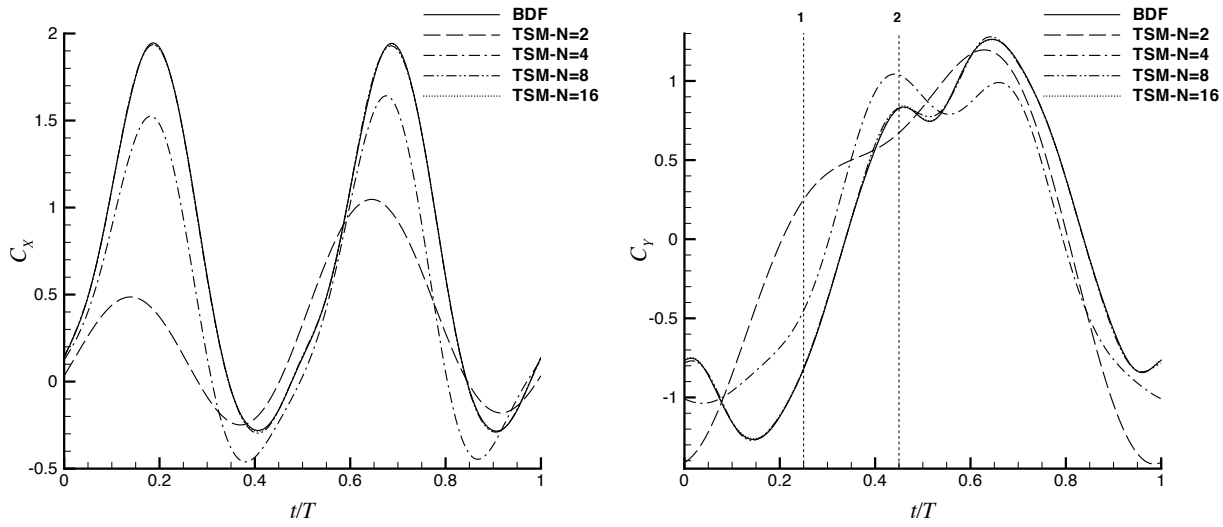

Figure 7.4: PH test-case. Comparison of the C_X (a) and C_Y (b) coefficients computed using BDF and TSM with an increasing number of harmonics.

very small differences between the BDF and TSM evolution remain with $N = 8$ but both evolutions appear superimposed with $N = 16$. For the PP test-problem, the computed evolution of C_X and C_Y using TSM with $N = 4$ and $N = 8$ display significant differences with the reference result; with $N = 16$ there are still some very small discrepancies while with $N = 22$ the BDF and TSM results appear as superimposed.

Wall pressure distributions and pressure fields

Two moments within the period are retained for a closer comparison of the computed flow fields: $t/T = 0.25$ and $t/T = 0.45$. For each of these moments, the wall pressure coefficient distribution obtained by using BDF and TSM(N) is plotted, respectively in Fig. 7.6 and 7.7 for test-problem PH. Let us recall these pressure distributions are reconstructed at each grid point i from the computed $\boldsymbol{w}_{i,n}$ values, applying formula (3.20), (3.21) in each grid cell. For the PH computation, the already very good agreement between BDF and TSM(8) and the almost perfect match between BDF and TSM(16) wall distributions are clearly visible; this similarity is confirmed on the pressure contours displayed in Fig.7.8. For test-problem PP, the wall pressure coefficient distribution obtained by using BDF and TSM(N) is plotted, respectively in Fig. 7.9 and 7.10. The match is already very good with $N = 16$ and almost perfect when $N = 22$; this similarity is confirmed on the pressure contours displayed in Fig.7.11.

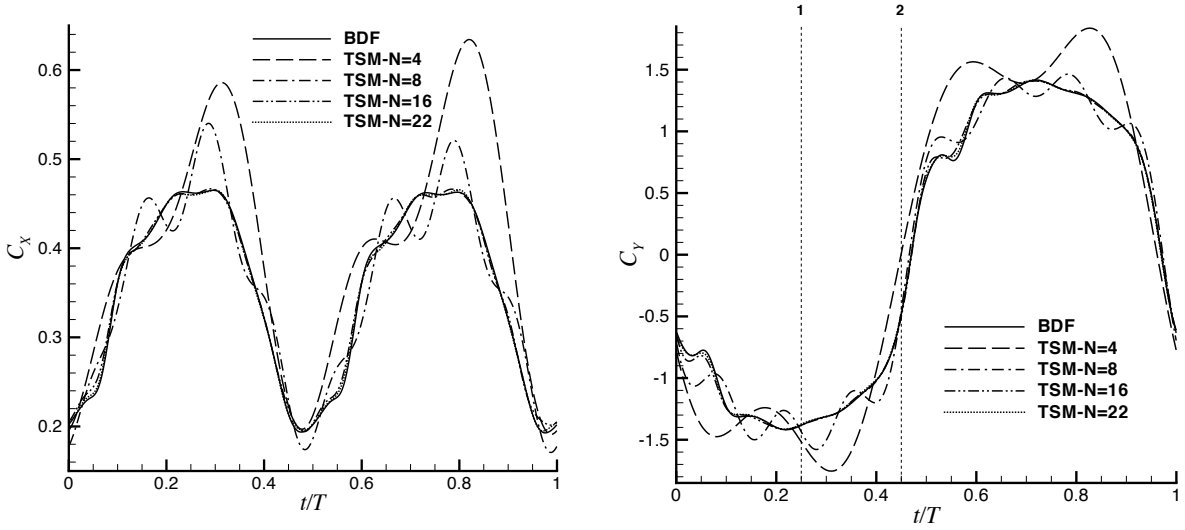

Figure 7.5: PP test-case. Comparison of the C_X (a) and C_Y (b) coefficients computed using BDF and TSM with an increasing number of harmonics.

Quantitative error analysis

The RMS error on the C_X force coefficient is defined as:

$$\epsilon_{RMS}(C_X) = \sqrt{\frac{1}{N_{\Delta t}} \sum_{k=1}^{N_{\Delta t}} \left(\frac{(C_X)_{TSM(N)}(t_k) - (C_X)_{BDF}(t_k)}{(\Delta C_X)_{BDF}} \right)^2}$$

where the values of the C_X coefficients at times t_k in the flow cycle and the amplitude of the C_X variation are readily available for the BDF computation while the values of C_X corresponding to the TSM computation are obtained by reconstruction of the flow solution using a truncation Fourier series with N harmonics. The RMS error on the C_Y force coefficient is similarly defined. These errors are plotted as a function of N in Fig.7.12 to conclude on the best choice of N: the number of harmonics must indeed be taken large enough to ensure the computed TSM solution is sufficiently accurate with respect to the usual BDF solution but not unnecessarily large since the gain expected from the TSM approach with respect to the BDF strategy is a cost reduction rather than an increased accuracy. Consistently with the previous graphical comparisons between BDF and TSM solutions, the error levels achieved on test problem PH for a given number of harmonics are much lower than the errors levels obtained on test problem PP. For test-case PH, the RMS error on C_X and C_Y drops below the 1% level for $N = 8$ while $N = 16$ is needed to fulfill this same criterion for test-case PP.

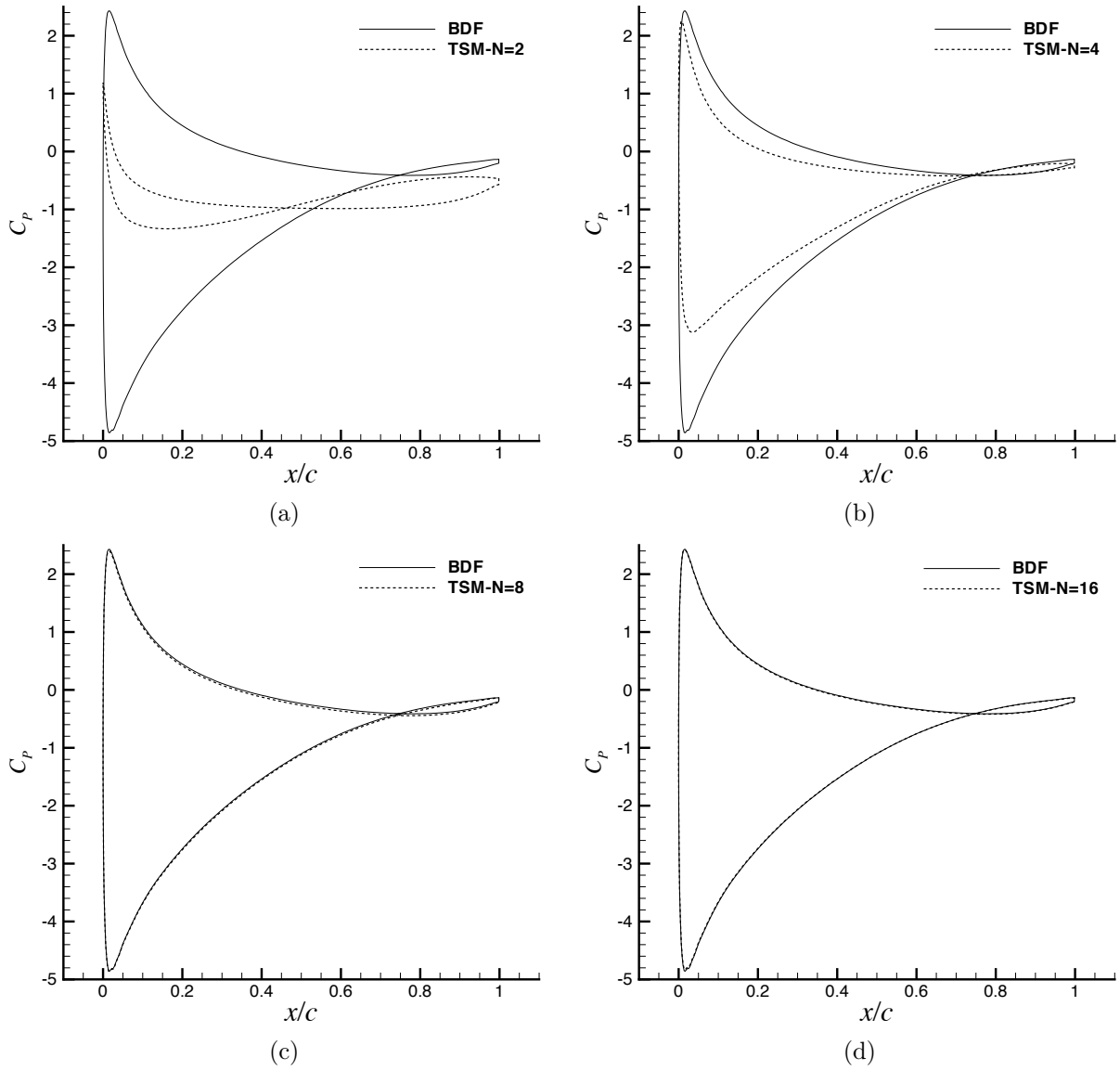

Figure 7.6: Flow problem PH. Reconstructed TSM(N) wall pressure coefficient at time $t/T = 0.25$ for an increasing number N of harmonics. Comparison with the reference BDF distribution.

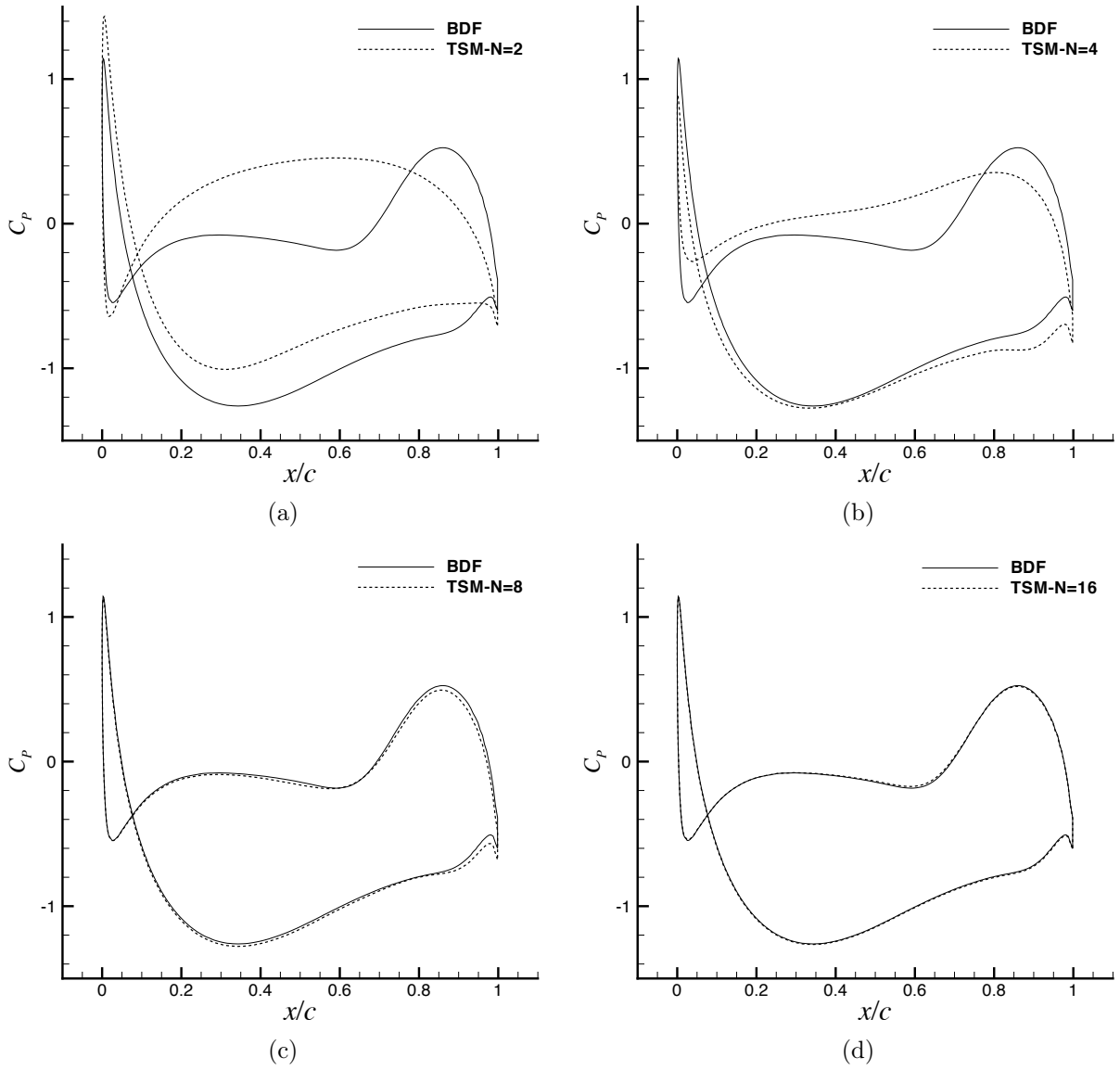

Figure 7.7: Flow problem PH. Reconstructed TSM(N) wall pressure coefficient at time $t/T = 0.45$ for an increasing number N of harmonics. Comparison with the reference BDF distribution.

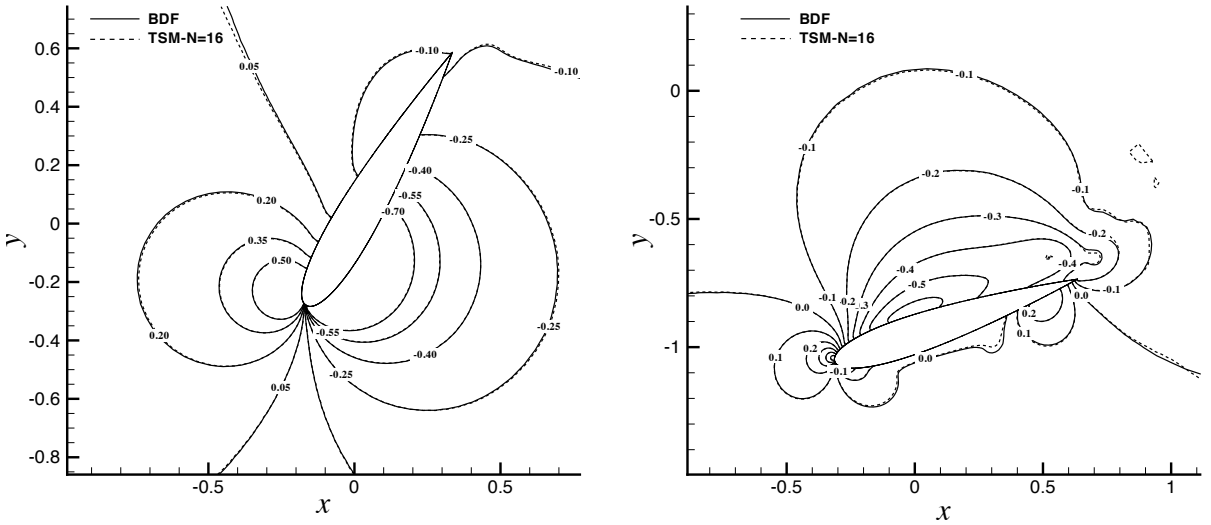

(a) (b)

Figure 7.8: Flow problem PH. Reconstructed TSM pressure field (N=16) at time $t/T = 0.25$ (a) and $t/T = 0.45$ (b).

7.2.3 Efficiency of the TSM approach

In the present study, the same number $N_{\Delta t} = 520$ of physical time-steps per cycle has been used for PH and PP as well as the same number of dual sub-iterations $m_{max}^{BDF} = 100$. As far as global cost is concerned, and regardless of the accuracy issue for the time being, the PH and PP test-cases differ by the number of cycles needed to achieve fully periodic flow ($N_{cycles}^{PH} = 6$ while $N_{cycles}^{PP} = 4$) and the typical number $m_{max}^{TSM(N)}$ of iterations on τ needed to achieve a steady-state for the TSM computations. This number is roughly $m_{max}^{TSM(N)} \approx 3300$ for PH and $m_{max}^{TSM(N)} \approx 2800$ for PP, whatever the number of harmonics N (see Fig. 7.3). All these parameters are summarized in Table 7.2.

Method	m_{max}	$N_{\Delta t}$	N_{cycle}
BDF	100	520	6
TSM	3300		

(a) PH case

Method	m_{max}	$N_{\Delta t}$	N_{cycle}
BDF	100	520	4
TSM	2800		

(b) PP case

Table 7.2: Incompressible TSM simulations. Parameters retained for the calculation of cost Φ_1

Consequently the global cost ratio for TSM and BDF strategies is given, for test-case PH, by

$$\eta^{PH} = \Phi_1^{PH}(N) \times \Phi_2(N) = (0.010577 \times (2N+1)) \times \Phi_2(N) \tag{7.1}$$

and for test-case PP by

$$\eta^{PP} = \Phi_1^{PP}(N) \times \Phi_2(N) = (0.01346 \times (2N+1)) \times \Phi_2(N) \tag{7.2}$$

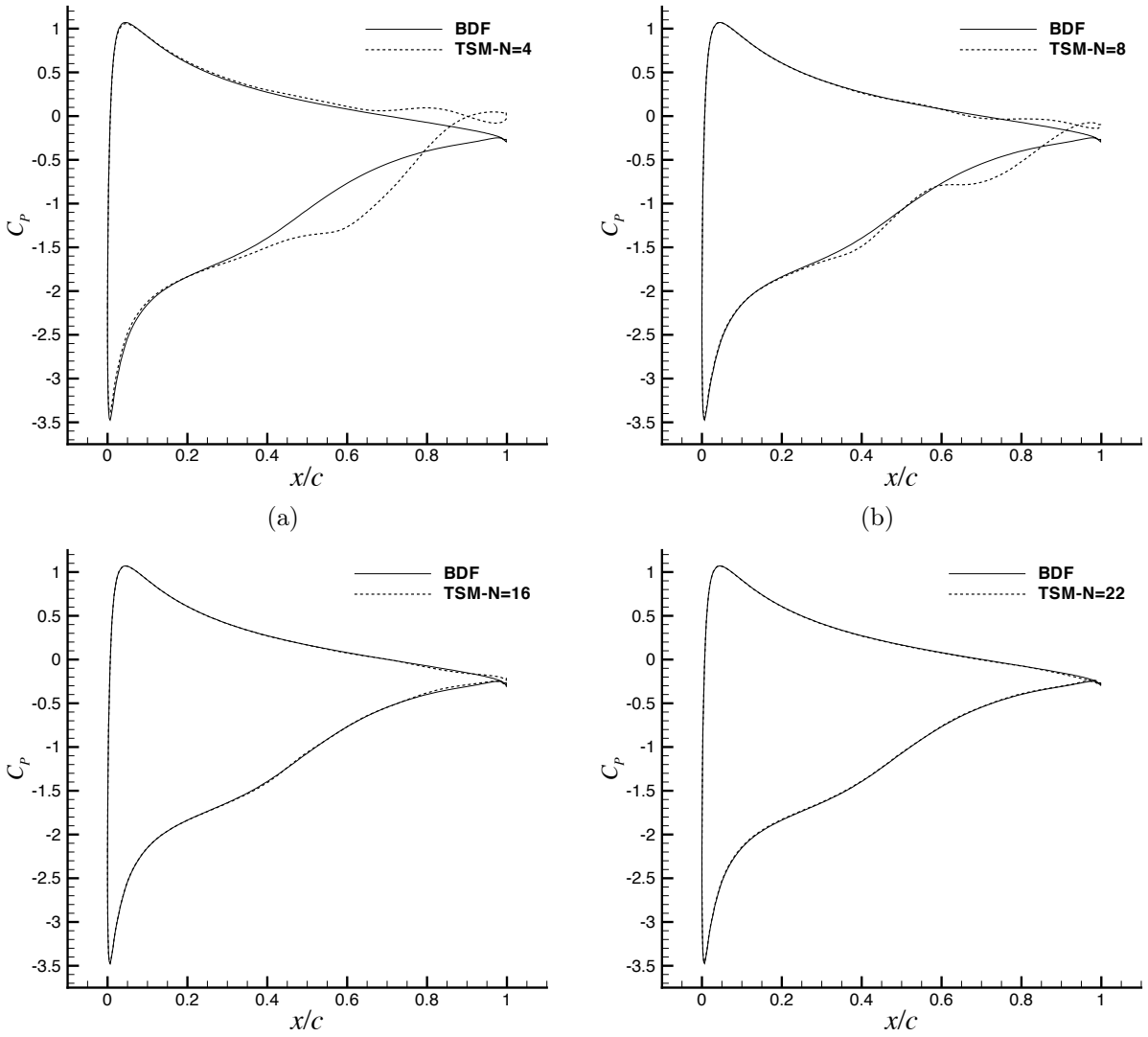

Figure 7.9: Flow problem PP. Reconstructed TSM(N) wall pressure coefficient at time $t/T = 0.25$ for an increasing number N of harmonics. Comparison with the reference BDF distribution.

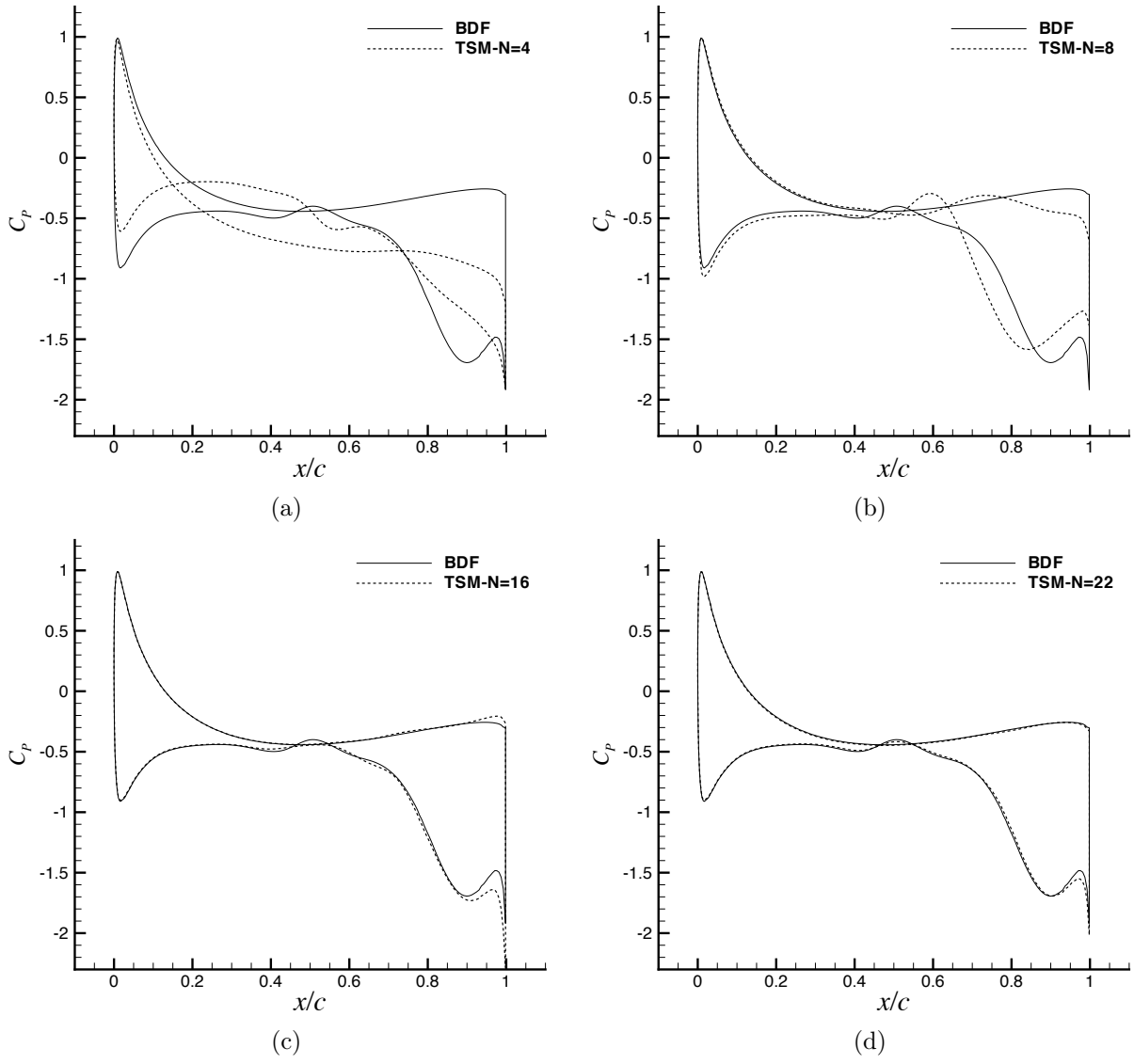

Figure 7.10: Flow problem PP. Reconstructed TSM(N) wall pressure coefficient at time $t/T = 0.45$ for an increasing number N of harmonics. Comparison with the reference BDF distribution.

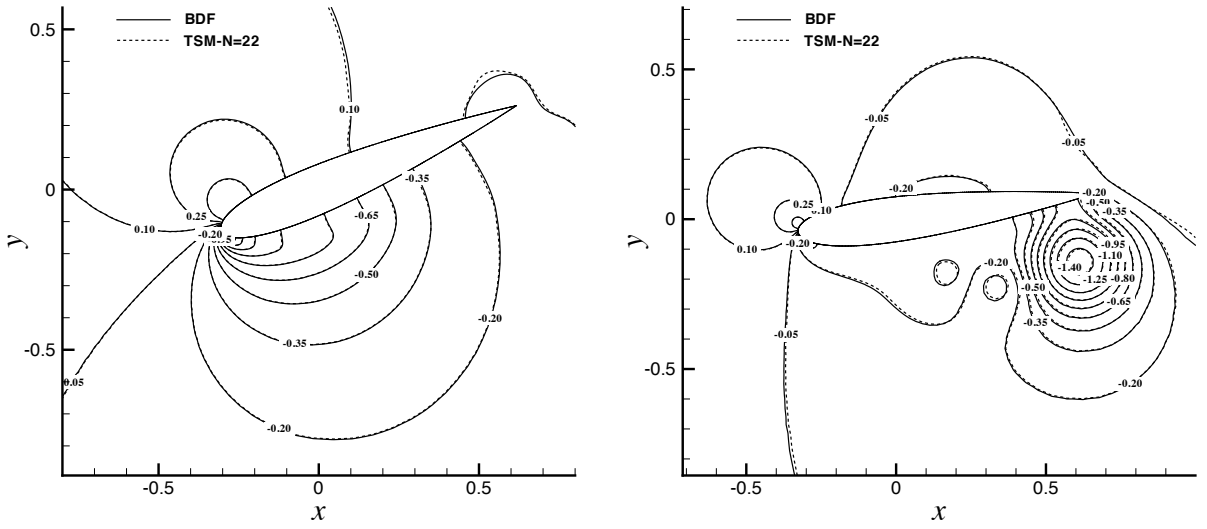

(a) (b)

Figure 7.11: Flow problem PP. Reconstructed TSM pressure field (N=22) at times $t/T = 0.25$ (a) and $t/T = 0.45$ (b)

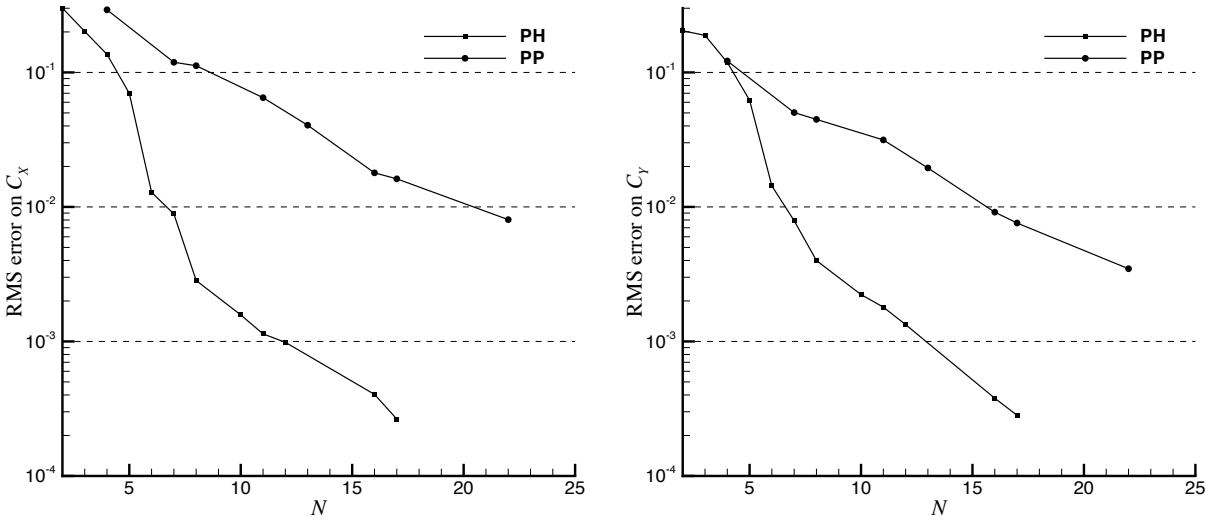

(a) (b)

Figure 7.12: Root mean square error of the normalized difference between the C_X (a) and C_Y (b) coefficients computed using the reference BDF strategy with $N_{\Delta t} = 520$ iterations per cycle and the TSM(N) strategy with increasing N.

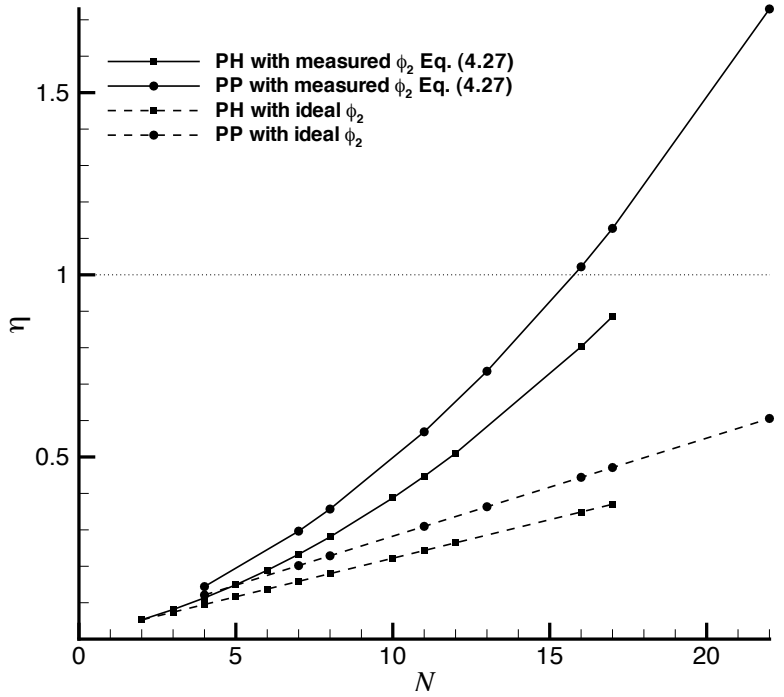

Figure 7.13: Evolution of the global cost ratio $\eta = \mathcal{C}_{TSM(N)}/\mathcal{C}_{BDF}$ between TSM(N) and BDF with an increasing number N of harmonics for TSM(N). Solid lines: measured cost ratio for the PH and PP test-cases. Dashed lines: ideal cost ratio with a TSM(N) implementation of unit cost Φ_2 roughly equal to the unit cost of the BDF approach.

Fig. 7.13 displays the evolution of the global cost ratio for PH and PP, given respectively by (7.1) and (7.2), with the measured unit cost ratio $\Phi_2(N)$ given by (4.28). It can be observed in Fig.7.13 that the measured value of η^{PP} reaches 1 for $N = 16$ while η^{PH} remains below 0.8 for this same number of harmonics. With an improved implementation allowing to reduce the growth of the unit cost Φ_2 with N, the global cost ratio η could remain below 0.5 for $N = 16$.

The key point of the present efficiency analysis is reached when crossing the evolution of $\eta(N)$ given by Fig.7.13 with the accuracy assessment summarized on the RMS-errors for C_X and C_Y plotted in Fig.7.12. The RMS-errors on these aerodynamic coefficients are plotted against the global efficiency ratio η in Fig. 7.14 : the solid lines correspond to the measured evolution of η^{PH} and η^{PP} while the dashed lines correspond to the ideal evolution where the unit cost ratio Φ_2 would remain roughly equal to 1. From the previously performed accuracy analysis, the BDF and reconstructed TSM solutions were found to be almost coincident when the normalized RMS error on C_Y dropped below 1%, corresponding to a number of harmonics $N = 8$ for the PH case and $N = 16$ for the PP case. Retaining this same criterion, it can be observed in Fig.7.14 the TSM approach provides

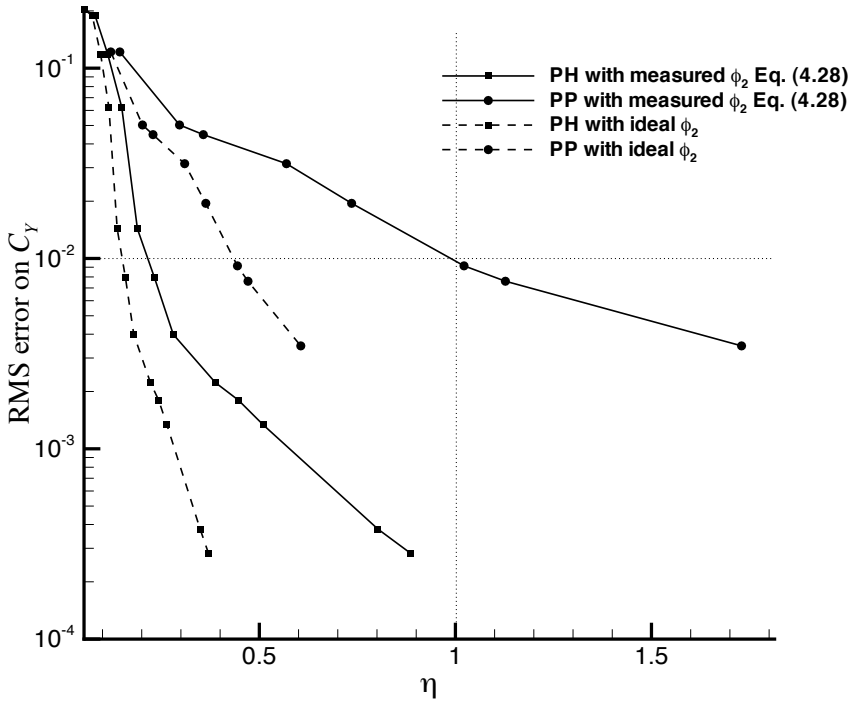

Figure 7.14: Evolution of the root mean square error on C_Y as a function of the global cost ratio $\eta = \dfrac{\mathcal{C}_{TSM(N)}}{\mathcal{C}_{BDF}}$ for test-problems PH and PP. Solid lines: measured cost ratio. Dashed lines: ideal cost ratio with a TSM(N) implementation of unit cost Φ_2 roughly equal to the unit cost of the BDF approach.

a solution as accurate as the conventional BDF strategy for an overall cost divided by 5 when computing the PH case; meanwhile, for the PP case, the larger number of harmonics needed by the TSM approach to provide the same level of accuracy as BDF does not allow to reduce the CPU cost, with $\eta^{PP} \approx 1$ for $N = 16$. An improved implementation of the TSM approach could make the method attractive even for the PP test-case, with an ideal computational cost ratio that could go down to 0.5 for $N = 16$ in that case. The analysis of the TSM efficiency has been focused on the achievable CPU gain using the steady computation of a reduced number of modes within a flow period instead of a full unsteady computation over several cycles. It must be pointed out however the TSM method is also more demanding memory-wise than the BDF strategy since it requires to store $(2N + 1) \times N_{cells}$ unknown states at each step of the steady-state convergence process against N_{cells} unknown states for the BDF method at each step of the time-marching process.

Conclusion and Perspectives

This thesis work is a fundamental contribution to the continuous efficiency improvement of a numerical design process applied to a new concept of Darrieus type sea turbines. The optimal design of sea turbines involves numerous computations of unsteady viscous (turbulent) flows, more precisely of flows displaying a time-periodicity. Up to now these computations are performed using time-accurate solvers which solve the whole transient of the flow prior to the establishment of a periodic flow. Two such solvers have been described in the first part of this report. Starting from a second-order accurate compressible solver based on a BDF physical-time discretization solved by a dual-time-step (DTS) marching implicit procedure, an Arbitrary-Lagrangian-Eulerian (ALE) formulation has been developed to compute unsteady flows over periodically moving bodies. This solver has also been extended to deal with incompressible flows combining the Artificial Compressibility (AC) model with BDF-DTS time-marching and ALE.

A long history of time-periodic flow computations over external (helicopter rotor) and internal (turbomachinery) configurations has led to the development of harmonic methods, either in the frequency or the time domain, which take advantage of the assumed flow periodicity to reduce the computational cost of an established periodic regime by using a Fourier series development of the flow solution. These methods have been briefly reviewed in Chapter 3 of this report and the recently developed Time-Spectral Method (TSM) has been identified as the potentially most appropriate method to reduce the cost of time-periodic incompressible flow computation owing to his moderately complex implementation within the available time-accurate solvers.

The stability issue inherent to the TSM dual-time explicit formulation when the number of harmonics increases and/or the frequency of the periodic phenomenon is high has been highlighted. As pointed out by previous authors [66, 76, 68], the implicit treatment of the large scale TSM system, coupling $(2N + 1)$ systems of conservation laws with N the number of harmonics retained to describe the periodic flows under study, is crucial to ensure the efficiency of the TSM method with respect to a conventional BDF formula.

In the present work, an implicit formulation of the TSM method has been derived from a simple matrix-free treatment previously developed in the context of compressible flows and also extended to the AC system. Special care has been taken to ensure the diagonal dominance property of the TSM implicit stage, with a simple modification of the diagonal contribution which does not significantly affect the convergence of the implicit solver to a steady-state. A basic point-relaxation technique of Jacobi type (PJ standing for Point-Jacobi) has been retained to solve the linear system associated to the implicit TSM scheme for a very low cost per iteration which makes up for the reduced intrinsic efficiency of the method. The proposed TSM implicit treatment has been thoroughly analyzed for a simple linear heat conduction problem and the efficiency gains registered for this model problem using TSM instead of a conventional time-marching technique were sufficient to motivate the implementation of a similar TSM implicit strategy in the initially developed compressible and incompressible flow solvers on unstructured moving grids.

The resulting compressible TSM-ALE-PJ solver has been successfully applied to the computation of the periodic compressible viscous flow over a rotating cylinder and the periodic compressible inviscid flow over a pitching NACA0012 aerofoil. In the cylinder case, $N = 4$ harmonics are required to achieve engineering accuracy for the aerodynamic coefficients of the cylinder whereas a single harmonic is enough to get a correct lift coefficient for the pitching aerofoil case. For this same CT1 test-case, an accurate prediction of the pitching moment requires however to use $N = 8$.
This coarse representation of the flow cycle offered by the spectral formula used for approximating the physical time-derivative combined with an efficient solution of the steady solution for the TSM system coupling the $(2N + 1)$ selected unknown fields within a flow period has allowed a substantial gain of CPU time with respect to conventional time-marching approaches. For the test-problems computed in Chapter 6, the cost reduction offered by TSM with respect to BDF is significant, ranging from more than 94% at best for the CT1 lift to 50% at worst for the CT1 pitching moment.

The computation of a pitching and heaving NACA 0015 airfoil has demonstrated that between $N = 8$ and $N = 16$ harmonics are required by the TSM method to accurately represent such two-dimensional low-Reynolds periodic incompressible flows. A level of accuracy on the flow solution over a period comparable to that offered by a conventional BDF time-integration was achieved using an overall CPU time divided by a factor five. Note however that, for a pure pitching test-case at a lower reduced frequency over the same NACA 0015 geometry, no CPU reduction was observed using TSM(N) instead of BDF because twice more harmonics (16 instead of 8) were needed in that case to achieve an accuracy level similar to that of the BDF approach.

Even though significant CPU cost reductions using TSM appear to depend to a rather

large extent on the computed flow problem, the results obtained in this thesis work can be considered as sufficiently encouraging to motivate the extension of the proposed implicit TSM formulation to three-dimensional turbulent flows. Since the three-dimensional version of the compressible flow solver used as a starting point in this thesis is now available, the steps to take to obtain a 3D turbulent TSM solver are immediately deduced from the present work. Only a bit of development time is needed.

In order to make the TSM approach computationally attractive even when a rather large number of modes is required to achieve a sufficient level of accuracy, ongoing work is devoted on one hand to the optimal implementation of the method so as to reduce as much as possible the growth of the unit cost ratio Φ_2 when N increases and on the other hand to the efficiency improvement of the implicit solver with respect to the PJ method used in the present study. The general minimal residual GMRES solver of Saad and Schultz [63] already used in [68] seems to be an interesting candidate because it does not require diagonal dominance of the implicit matrix for convergence.

A current research axis is also focused on strategies allowing for an automatic determination of the number of harmonics to be used with the TSM approach for ensuring a prescribed accuracy level. This is a difficult task since the harmonic content of the response is generally not *a priori* known. The pitching and heaving airfoil problem of Chapter 7 is a good example of this difficulty since a small change in the motion law parameters significantly impacts the flow behavior. A possible strategy would be to run a calculation with an initial underestimated guess of N and consecutively, another one with $N+1$ with the solution of the previous calculation to initialize the flow. The process would be repeated until the comparison of the two consecutive TSM solutions reaches a prescribed level of convergence. Knowing that the TSM solution tends towards the BDF reference solution when the number of harmonics increases, this should lead automatically to the suitable minimal number N.

Bibliography

[1] Y. Allaneau and A. Jameson. Direct numerical simulations of plunging airfoils. In *48th AIAA Aerospace Sciences Meeting Including the New Horizons Forum and Aerospace Exposition*, AIAA Paper 2010-728, Orlando, Florida, January 2010.

[2] E. Amet, T. Maître, C. Pellone, and J.-L. Achard. 2D numerical simulations of blade-vortex interaction in a darrieus turbine. *Journal of fluids engineering*, November 2009.

[3] S. Antheaume, T. Maître, and J.-L. Achard. Hydraulic darrieus turbines efficiency for free fluid flow conditions versus power farms conditions. *Renewable Energy*, 33:2186–2198, October 2008.

[4] G. N. Barakos and D. Drikakis. Computational study of unsteady turbulent flows around oscillating and ramping aerofoils. *International journal for numerical methods in fluids*, 42(2):163–186, May 2003.

[5] T. J. Barth and D. C. Jespersen. The design and application of upwind schemes on unstructured meshes. In *27th AIAA Aerospace Sciences Meeting*, AIAA Paper 89-0366, January 1989.

[6] J. T. Batina. Unsteady euler algorithm with unstructured dynamic mesh for complex-aircraft aerodynamic analysis. *AIAA Journal*, 29(3):327–333, 1991.

[7] J. A. Benek, J. L. Steger, and F. C. Dougherty. A flexible grid embedding technique with application to the euler equations. *AIAA Paper*, (AIAA Paper 1983-1944), 1983.

[8] M. Bergmann. *Optimisation aérodynamique par réduction de modèle POD et contrôle optimal. Application au sillage laminaire d'un cylindre circulaire*. PhD thesis, Institut National Polytechnique de Lorraine, Décembre 2004.

[9] M. Braza, P. Chassaing, and P. P. Minh. Numerical study and physical analysis of the pressure and velocity fields in the near wake of a circular cylinder. *Journal of fluid mechanics*, 165:79–130, april 1986.

[10] N. Butsuntorn and A. Jameson. Time spectral method for rotorcraft flow. In *46th AIAA Aerospace Sciences Meeting and Exhibit*, AIAA Paper 2008-403, Reno, January 2008.

[11] G. Carte, J. Dusěk, and P. Fraunié. A spectral time discretization for flows with dominant periodicity. *Journal of Computational Physics*, 120:171–183, 1995.

[12] G. Carte, J. Dusěk, and P. Fraunié. Numerical simulation of the mechanisms governing the onset of the bénard-von kármán instability. *International journal for numerical methods in fluids*, 23:753–785, 1996.

[13] T. Chen, P. Vasanthakumar, and L. He. Analysis of unsteady blade row interaction using nonlinear harmonic approach. *Journal of Propulsion and Power*, 17(3):651–658, 2001.

[14] A. J. Chorin. A numerical method for solving incompressible viscous flow problems. *Journal of Computational Physics*, 2:12–26, 1967.

[15] C Corre. Contribution à la simulation et à l'analyse des écoulements compressibles. Technical report, Université Pierre et Marie Curie (Paris VI), Decembre 2004.

[16] C. Corre, K. Khalfallah, and A. Lerat. Line-relaxation methods for a class of centred schemes. *Computational Fluid Dynamics Journal*, 5:213–246, 1996.

[17] D. Darracq, S. Champagneux, and A. Corjon. Computation of unsteady turbulent airfoil flows with an aeroelastic AUSM+ implicit solver. In *16 th Applied Aerodynamics Conference*, AIAA Paper 1998-2411, Albuquerque, June 1998.

[18] M. Delanaye. *Polynomial reconstruction finite volume schemes for the compressible Euler and Navier- Stokes equations on unstructured adaptive grids.* PhD thesis, Université de Liège, 1996.

[19] J. Donea, A. Huerta, J.-Ph. Ponthot, and A. Ferran-Rodriguez. *Encyclopedia of Computational Mechanics*, volume 1 : Fundamentals, chapter 14 - Arbitrary Lagrangian-Eulerian Methods. John Wiley & Sons, 2004.

[20] K. Ekici and K. C. Hall. Nonlinear frequency-domain analysis of unsteady flows in turbomachinery with multiple excitation frequencies. *AIAA Journal*, 46(8):1912–1920, august 2008.

[21] K. Ekici and K.C. Hall. Nonlinear analysis of unsteady flows in multistage turbomachines using harmonic balance. *AIAA Journal*, 45(5):1047–1057, 2007.

[22] D. T. Elsworth and E. F. Toro. Riemann solvers for solving the incompressible navier-stokes equations using the artificial compressibility method. Technical Report 9208, College of Aeronautics report, June 1992.

[23] K.-C. Fang. *Unsteady incompressible flow analysis using C-type grid with a curved branch cut.* PhD thesis, University of Cincinnati, 2000.

[24] J. B. J. Fourier. *Théorie analytique de la chaleur.* Imprimerie de Firmin Didot, imprimeur du roi, 1822.

[25] R. Gilmore and M. B. Steer. Nonlinear circuit analysis using the method of harmonic balance - A review of the art. part I -introductory concepts. *International Journal on Microwave Computer Aided Engineering*, 1(1), 1991.

[26] A. K. Gopinath. *Efficient Fourier-based algorithms for time-periodic unsteady problems.* PhD thesis, Department of Aeronautics and Astronautics, Stanford University, April 2007.

[27] A. K. Gopinath and A. Jameson. Time spectral method for periodic unsteady computations over two-and three-dimensional bodies. *AIAA Paper*, 1220:10–13, 2005.

[28] A. K. Gopinath and A. Jameson. Application of the time spectral method to periodic unsteady vortex shedding. In *44th AIAA Aerospace Sciences Meeting and Exhibit*, AIAA Paper 2006-0449, Reno, USA, January 2006.

[29] K. C. Hall. A linearized euler analysis of unsteady flows in turbomachinery. GTL report 190, Massachusetts Institut of technology, Cambridge (USA), 1987.

[30] K. C. Hall, J. P. Thomas, and W. S. Clark. Computation of unsteady nonlinear flows in cascades using a harmonic balance technique. In *International Symposium on Unsteady Aerodynamics, Aeroacoustics and Aeroelasticity of Turbomachines*, Lyon (France), September 2000.

[31] K. C. Hall, J. P. Thomas, and W. S. Clark. Computation of unsteady nonlinear flows in cascades using a harmonic balance technique. *AIAA Journal*, 40(5):879–886, May 2002.

[32] O. Hassan, K. A. Sorensen, K. Morgan, and N. P. Weatherill. A method for time accurate trubulent compressible fluid flow simulation with moving boundary components employing local remeshing. *International journal for numerical methods in fluids*, 53:1243–1266, 2007.

[33] C. Hirsch. *Numerical computation of internal and external flows*, volume 2. John Wiley, 1988.

[34] A. Jameson. Time-dependent calculations using multigrid with applications to unsteady flows past airfoils and wings. In *10th AIAA Computational Fluid Dynamics Conference*, AIAA Paper 91-1596, June 1991.

[35] A. Jameson. An assessment of dual-time stepping, time spectral and artificial compressibility based numerical algorithms for unsteady flow with applications to flapping wings. In *19th AIAA Computational Fluid Dynamics*, AIAA Paper 2009-4273, San Antonio, Texas, June 2009.

[36] A. Jameson and S. Yoon. Lower-upper implicit schemes with multiple grids for the euler equations. *AIAA Journal*, 25:929–935, 1987.

[37] G. Jin and M. Braza. A nonreflecting outlet boundary condition for incompressible unsteady Navier-Stokes calculations. *Journal of computational physics*, 107(2):239–253, august 1993.

[38] Y. Kallinderis and H.T. Ahn. Incompressible navier-stokes method with general hybrid meshes. *Journal of Computational Physics*, 210:75–108, 2005.

[39] R. Kannan and Z. J. Wang. Overset adaptive cartesian/prism grid method for moving boundary flow problems. *AIAA Journal*, 45(7):1774–1779, 2007.

[40] K. Khalfallah and G. Lacombe. Analysis of implicit treatments for a centred Euler solver. *Computers and Fluids*, 22(2/3):381–406, 1993.

[41] T. Kinsey and G. Dumas. Parametric study of an oscillating airfoil in a power-extraction regime. *AIAA Journal*, 46(6):1318, 2008.

[42] B. Koobus and C. Farhat. Second-order time-accurate and geometrically conservative implicit schemes for flow computations on unstructured dynamic meshes. *Computer Methods in Applied Mechanics and Enginering*, 170:103–129, 1999.

[43] N. Kryloff and N. Boboliuboff. *Introduction to Nonlinear Mechanics*. Princeton University Press, Princeton (USA), 1947.

[44] R. H. Landon. Naca 0012 oscillatory and transient pitching. Technical report, Agard Report No. 702, 1982.

[45] M.-S. Liou. A sequel to AUSM: AUSM$^+$. *Journal of Computational Physics*, 129(0256):364–382, 1996.

[46] M.-S. Liou and C. J. Steffen. A new flux splitting scheme. *Journal of Computational Physics*, 107:23–39, 1993.

[47] H. Luo, J. D. Baum, and R. Lohner. A fast, matrix-free implicit method for compressible flows on unstructured grids. *Journal of Computational Physics*, 146:664–690, 1998.

[48] H. Luo, J. D. Baum, and R. Lohner. An accurate, fast, matrix-free implicit method for computing unsteady flows on unstructured grids. *Computers and Fluids*, 30:137–159, 2001.

[49] H. Luo, J. D. Baum, and R. Löhner. On the computation of multi-material flows using ALE formulation. *Journal of Computational Physics*, 194(1):304 – 328, 2004.

[50] R. C. Maple, P. I. King, P. D. Orkwis, and J. M. Wolff. Adaptative harmonic balance method for nonlinear time-periodic flows. *Journal of Computational Physics*, 193:620–641, 2004.

[51] D. J. Mavriplis. An assessment of linear versus non-linear multigrid methods for unstructured mesh solvers. *Journal of Computational Physics*, 175:302–325, 2002.

[52] M. S. McMullen. *The application of non-linear frequency domain methods to the Euler and Navier-Stokes Equations*. PhD thesis, Department of Aeronautics and Astronautics, Stanford University, March 2003.

[53] M. S. McMullen, A. Jameson, and J. Alonso. Acceleration of convergence to a periodic steady state in turbomachinery flows. In *39th Aerospace Sciences Meeting and Exhibit*, AIAA PAper 2001-0152, Reno (USA), 2001.

[54] M. S. McMullen, A. Jameson, and J. Alonso. Demonstration of nonlinear frequency domain methods. *AIAA Journal*, 44(7), 2006.

[55] K. Nakahashi and G. S. Deiwert. Self adaptative grid method with application to airfoil flow. *AIAA Journal*, 25:513–520, 1987.

[56] O. J. Nastov and J. K. White. Time-mapped harmonic balance. In *36th Design Automation Conference*, New Orleans (USA), juin 1999.

[57] W. Ning and L. He. Computation of unsteady flows around oscillating blades using linear and nonlinear harmonic euler methods. *Journal of Turbomachinery*, 120(3):508–514, July 1998.

[58] W. Noh. Cel: a time-dependant two-space dimensional coupled eulerian-lagrangian code. *Methods in Computational Physics*, 3:117–119, 1964.

[59] R. Peyret. Unsteady evolution of a horizontal jet in a stratified fluid. *Journal of Fluid Mechanics*, 78:49–63, 1976.

[60] R. Peyret and T. Taylor. *Computational methods for fluid flows*. Springer, New-York, 1983.

[61] P. L. Roe. Approximate riemann solvers, parameter vectors, and difference schemes. *Journal of Computational Physics*, 43:357–372, 1981.

[62] S. E. Rogers and D. Kwak. An upwind differencing scheme for the incompressible Navier-Stokes equations. *Applied Numerical Mathematics*, 8:64, 1991.

[63] Y. Saad and M. Schultz. GMRES: A generalized minimal residual algorithm for solving non-symmetric linear systems. *SIAM Journal on Scientific and Statistical Computing*, 7(3), July 1986.

[64] C. E. Shannon. Communication in the presence of noise. In *Proceeding of the Institute of Radio Engineers*, volume 37, pages 10–21, January 1949.

[65] F. Sicot. *Simulation efficace des écoulements instationnaires périodiques en turbomachines*. PhD thesis, Ecole Centrale de Lyon, October 2009.

[66] F. Sicot, G. Puigt, and M. Montagnac. Block-jacobi implicit algorithms for the time spectral method. *AIAA Journal*, 46(12), December 2008.

[67] Sriram, A. K. Gopinath, E. van der Weide, C. Tomlin, and A. Jameson. Aerodynamics and flight control of flapping wing flight vehicles: A preliminary study. In *43rd Aerospace Sciences Meeting and Exhibit*, AIAA Paper 2005-841, Reno (USA), 2005.

[68] X. Su and X. Yuan. Implicit solution of time spectral method for periodic unsteady flows. *International Journal for Numerical Methods in Fluids*, January 2009.

[69] C. H. Tai and Y. Zhao. Parallel unsteady incompressible viscous flow computations using an unstructured multigrid method. *Journal of Computational Physics*, 192:277–311, 2003.

[70] L. K. Taylor and D. L. Whitfield. Unsteady three-dimensional incompressible Euler and Navier-Stokes solver for stationary and dynamic grids. In *22nd AIAA Fluid Dynamics, Plasma Dynamics and Lasers Conference*, June 1991.

[71] T. Trapp. The stringray tidal stream generator: 150 kw demonstrator completes on-site testing. *Energy World*, (304):14–16, 2002.

[72] E van der Weide, A. Gopinath, and A. Jameson. Turbomachinery applications with the time spectral method. In *35th AIAA Fluid Dynamics Conference and Exhibit*, AIAA Paper 2005-4905, June 2005.

[73] J. M. Verdon and J. R. Caspar. A linearized unsteady aerodynamics analysis for transonic cascades. *Journal of Fluid Mechanics*, 149:403–429, December 1984.

[74] G. E. Welch, I. M. Milanovic, and K. B. M. Q. Zaman. Application of harmonic balance technique to synthetic jets in cross-flow. In *43rd Aerospace Sciences Meeting and Exhibit*, AIAA Paper 2005-1111, Reno, Nevada, January 2005.

[75] C. H. K. Williamson. Vortex dynamics in the cylinder wake. *Annual Review of Fluid Mechanics*, 28:477–539, 1996.

[76] M. A. Woodgate and K. J. Badcock. Implicit harmonic balance solver for transonic flow with forced motions. *AIAA Journal*, 47(4):893–901, Jan 2009.

[77] Z. Yang and D. J. Mavriplis. Time spectral method for periodic and quasi-periodic unsteady computations on unstructured meshes. In *40^{th} Fluid Dynamics Conference and Exhibit*, AIAA Paper 2010-5034, July 2010.

[78] J. M. Zanette. *Hydroliennes à flux transverse : mise en œuvre de l'interaction fluide-structure*. PhD thesis, Université de Grenoble, 2010.

[79] M. M. Zdravkovich. *Flow around circular cylinders*, volume 1: Fundamentals. Oxford University Press, 1997.

Part IV

Appendices

Appendix A

Compressible system matrices

A.1 Inviscid Jacobian matrices for primitive variables

As the system of Euler is hyperbolic in time, one can define and study the quantities that propagates along the characteristics. It is essential to identify these directions of disturbance propagation to define consistent numerical fluxes.

In order to investigate the characteristics properties of the Euler equations, we writte the system in quasi linear form for the conservative variables. The convective flux $\boldsymbol{F}^E$ does not depend on the flow gradients and therefore, the system contains only first order derivative.

$$\frac{\partial \boldsymbol{w}}{\partial t} + \boldsymbol{J} \cdot \nabla \boldsymbol{w} = \boldsymbol{S} \tag{A.1}$$

$\boldsymbol{A} = \dfrac{\partial \boldsymbol{F}^E}{\partial \boldsymbol{w}}$ is the jacobian matrix of the inviscid flux in conservative variable form. To find the eigenvalues of $\boldsymbol{A}$, it is easier to work with the local formulation in primitive variables.

$$\begin{aligned} \frac{\partial \rho}{\partial t} + (\boldsymbol{v}_p \cdot \boldsymbol{\nabla})\rho + \rho(\boldsymbol{\nabla} \cdot \boldsymbol{v}_p) = 0 \\ \frac{\partial \boldsymbol{v}_p}{\partial t} + (\boldsymbol{v}_p \cdot \boldsymbol{\nabla})\boldsymbol{v}_p + \frac{1}{\rho}\boldsymbol{\nabla} p = 0 \\ \frac{\partial p}{\partial p} + (\boldsymbol{v}_p \cdot \boldsymbol{\nabla})p + \rho c^2(\boldsymbol{\nabla} \cdot \boldsymbol{v}_p) = 0 \end{aligned} \tag{A.2}$$

Then, if $\boldsymbol{v}_p$ is the vector of primitive variables :

$$\boldsymbol{v}_p = \begin{pmatrix} \rho \\ u \\ v \\ p \end{pmatrix}$$

one can rewrite system (A.1) as :

$$\frac{\partial \boldsymbol{v}_p}{\partial t} + \boldsymbol{J}_p^E \cdot \nabla \boldsymbol{v}_p = 0 \tag{A.3}$$

We are interested in the direction of propagation normal to a face oriented by the vector $\boldsymbol{n} = (n_x, n_y)$.

$$\frac{\partial \boldsymbol{v}_p}{\partial t} + \boldsymbol{A}_p^E n_x \frac{\partial \boldsymbol{v}_p}{\partial x} + \boldsymbol{B}_p^E n_y \frac{\partial \boldsymbol{v}_p}{\partial y} = 0 \tag{A.4}$$

with

$$\boldsymbol{A}_p^E = \begin{pmatrix} u - s_x & \rho & 0 & 0 \\ 0 & u - s_x & 0 & 0 \\ 0 & 0 & u - s_x & 0 \\ 0 & \rho c^2 & 0 & u - s_x \end{pmatrix}$$

$$\boldsymbol{B}_p^E = \begin{pmatrix} v - s_y & 0 & \rho & 0 \\ 0 & v - s_y & 0 & 0 \\ 0 & 0 & v - s_y & 0 \\ 0 & 0 & \rho c^2 & v - s_y \end{pmatrix}$$

The eigenvalues of the system are solution of equation :

$$\det|\boldsymbol{J}_{p\perp}^E - \lambda \boldsymbol{I_d}| = 0 \tag{A.5}$$

where $\boldsymbol{J}_{p\perp}^E = \boldsymbol{J}_p^E \cdot \boldsymbol{n} = \boldsymbol{A}_p\ n_x + \boldsymbol{B}_p\ n_y$ and $\boldsymbol{I_d}$ is the 4×4 identity matrix.
Explicitely,

$$\det \begin{vmatrix} V_n - s_n - \lambda & \rho n_x & \rho n_y & 0 \\ 0 & V_n - s_n - \lambda & 0 & n_x/\rho \\ 0 & 0 & V_n - s_n - \lambda & n_y/\rho \\ 0 & \rho c^2 n_x & \rho c^2 n_y & V_n - s_n - \lambda \end{vmatrix} = 0$$

where $V_n = u\ n_x + v\ n_y$ and $s_n = s_x n_x + s_y n_y$ is the normal grid velocity . The solutions are :

$$\begin{aligned} \lambda_1 = \lambda_2 &= V_n - s_n \\ \lambda_3 &= V_n - s_n + c \\ \lambda_4 &= V_n - s_n - c \end{aligned} \tag{A.6}$$

The transformation matrices $\boldsymbol{L}, \boldsymbol{L}^{-1}$and diagonal matrix $\boldsymbol{\Lambda}^E$ which satisfy the relation $\boldsymbol{J}_{p\perp}^E = \boldsymbol{L}\boldsymbol{\Lambda}_p^E\boldsymbol{L}^{-1}$ are given by :

$$\boldsymbol{L} = \begin{pmatrix} 1 & 0 & \rho/2c & \rho/2c \\ 0 & n_y & n_x/2 & -n_x/2 \\ 0 & -n_x & n_y/2 & -n_y/2 \\ 0 & 0 & \rho c/2 & \rho c/2 \end{pmatrix}$$

$$\boldsymbol{L}^{-1} = \begin{pmatrix} 1 & 0 & 0 & -1/c^2 \\ 0 & n_y & -n_x & 0 \\ 0 & n_x & n_y & 1/\rho c \\ 0 & -n_x & -n_y & 1/\rho c \end{pmatrix}$$

$$\boldsymbol{\Lambda}^E = \begin{pmatrix} V_n - s_n & 0 & 0 & 0 \\ 0 & V_n - s_n & 0 & 0 \\ 0 & 0 & V_n - s_n + c & 0 \\ 0 & 0 & 0 & V_n - s_n - c \end{pmatrix}$$

If $\boldsymbol{M}$ is the Jacobian matrix of transformation of conservative variables towards primitive variables, that is

$$\boldsymbol{M} = \frac{\partial \boldsymbol{w}}{\partial \boldsymbol{v}_p} \tag{A.7}$$

then, the relation between the flux jacobian in conservative variable form $\boldsymbol{J}^E$ and the one in primitive variable form $\boldsymbol{J}_p^E$ can be found by rewritting equation (A.1)

$$\boldsymbol{M}\frac{\partial \boldsymbol{v}_p}{\partial t} + \boldsymbol{J}^E \boldsymbol{M} \cdot \nabla \boldsymbol{v}_p = 0 \tag{A.8}$$

and by multiplying on the left by $\boldsymbol{M}^{-1}$:

$$\frac{\partial \boldsymbol{v}_p}{\partial t} + \boldsymbol{M}^{-1} A M \cdot \nabla \boldsymbol{v}_p = 0 \tag{A.9}$$

Identifying equations (A.3) and (A.9) gives

$$\boldsymbol{J}_p^E = \boldsymbol{M}^{-1}\boldsymbol{J}^E\boldsymbol{M} \quad \text{or} \quad \boldsymbol{J}^E = \boldsymbol{M}\boldsymbol{J}_p^E\boldsymbol{M}^{-1} \tag{A.10}$$

From equation (A.10), one can see that matrices $\boldsymbol{J}_\perp^E = \boldsymbol{J}^E \cdot \mathbf{n}$ et $\boldsymbol{J}_{p\perp}^E = \boldsymbol{J}_p^E \cdot \mathbf{n}$ have the same eigenvalues since they are linked by the equation :

$$\boldsymbol{J}_\perp = \boldsymbol{M}^{-1} J_\perp \boldsymbol{M} \tag{A.11}$$

which leads to $\boldsymbol{\Lambda}_p^E = \boldsymbol{\Lambda}^E$.

The ALE formulation appears only as an additional diagonal term $-s_n$ on the Jacobian matrix $\boldsymbol{J}_\perp^E$. Thus, compared to the original fixed mesh formulation, the new system has the same left and right eigenvectors and the new eigenvalues are easily deduced from the original ones.

A.2 Inviscid Jacobian matrices for conservative variables

The Jacobian matrices for the conservative system of Euler equation are neverthelesse useful, especially in order to writte the ROE scheme.

$$\boldsymbol{A}^E = \frac{\partial \boldsymbol{f}^E}{\partial \boldsymbol{w}} = \begin{pmatrix} -s_x & 1 & 0 & 0 \\ \frac{\gamma-3}{2}u^2 + \frac{\gamma-1}{2}v^2 & (3-\gamma)u - s_x & -(\gamma-1)v & \gamma-1 \\ -uv & v & u - s_x & 0 \\ -\gamma u E + (\gamma-1)u(u^2+v^2) & \gamma E - \frac{\gamma-1}{2}(v^2+3u^2) & -(\gamma-1)uv & \gamma u - s_x \end{pmatrix}$$

$$\boldsymbol{B}^E = \frac{\partial \boldsymbol{g}^E}{\partial \boldsymbol{w}} = \begin{pmatrix} -s_y & 0 & 1 & 0 \\ -uv & v - s_y & u & 0 \\ \frac{\gamma-3}{2}v^2 + \frac{\gamma-1}{2}u^2 & -(\gamma-1)u & (3-\gamma)v - s_y & \gamma-1 \\ -\gamma v E + (\gamma-1)v(u^2+v^2) & -(\gamma-1)uv & -\gamma E + \frac{\gamma-1}{2}(u^2+3v^2) & \gamma v - s_y \end{pmatrix}$$

The inviscid Jacobian matrix is decomposed into:

$$\boldsymbol{J}^E_\perp = \boldsymbol{A}^E n_x + \boldsymbol{B}^E n_y = \boldsymbol{T}\boldsymbol{\Lambda}^E\boldsymbol{T}^{-1}$$

with

$$\boldsymbol{T} = \begin{pmatrix} 1 & 0 & \frac{\rho}{2c} & \frac{\rho}{2c} \\ u & \rho n_y & \frac{\rho}{2c}(u + c n_x) & \frac{\rho}{2c}(u - c n_x) \\ v & -\rho n_x & \frac{\rho}{2c}(v + c n_y) & \frac{\rho}{2c}(v - c n_y) \\ \frac{u^2+v^2}{2} & \rho(u n_y + v n_x) & \frac{\rho}{2c}(H + c V_n) & \frac{\rho}{2c}(H - c V_n) \end{pmatrix}$$

$$\boldsymbol{T}^{-1} = \begin{pmatrix} 1 - \frac{\gamma-1}{2}M^2 & (\gamma-1)\frac{u}{c^2} & (\gamma-1)\frac{v}{c^2} & -\frac{\gamma-1}{c^2} \\ \frac{1}{\rho}(v n_x - u n_y) & \frac{n_y}{\rho} & -\frac{n_x}{\rho} & 0 \\ \frac{c}{\rho}(\frac{\gamma-1}{2}M^2 - \frac{V_n}{c}) & \frac{1}{\rho}(n_x - (\gamma-1)\frac{u}{c}) & \frac{1}{\rho}(n_y - (\gamma-1)\frac{v}{c}) & \frac{\gamma-1}{\rho c} \\ \frac{c}{\rho}(\frac{\gamma-1}{2}M^2 - \frac{V_n}{c} & \frac{1}{\rho}(n_x - (\gamma-1)\frac{u}{c}) & \frac{1}{\rho}(n_y - (\gamma-1)\frac{v}{c}) & \frac{\gamma-1}{\rho c} \end{pmatrix}$$

$$\boldsymbol{\Lambda} = \begin{pmatrix} V_n - s_n & 0 & 0 & 0 \\ 0 & V_n - s_n & 0 & 0 \\ 0 & 0 & V_n - s_n + c & 0 \\ 0 & 0 & 0 & V_n - s_n - c \end{pmatrix}$$

A.3 Viscous Jacobian matrices

In order to ensure the diagonal dominance of the implicit upwind scheme, we neglected the contribution of the tangential Jacobians in the implicit operator (see Sec. 1.4.1). More precisely, we only retained the Jacobian $\boldsymbol{A}_1^V$ in the x direction while we only retained $\boldsymbol{B}_2^V$ in the y direction. These Jacobians matrices reads

$$\boldsymbol{A}_1^V = \frac{\partial \boldsymbol{f}^V}{\partial \boldsymbol{w}_x} = \frac{\mu}{Re\ \rho} \begin{pmatrix} 0 & 0 & 0 & 0 \\ -\frac{4}{3}u & \frac{4}{3} & 0 & 0 \\ -v & 0 & 1 & 0 \\ -\alpha u^2 - \beta v^2 - \frac{\gamma}{Pr}E & \alpha u & \beta v & \frac{\gamma}{Pr} \end{pmatrix} \tag{A.12}$$

$$\boldsymbol{B}_2^V == \frac{\partial \boldsymbol{g}^V}{\partial \boldsymbol{w}_y} = \frac{\mu}{Re\ \rho} \begin{pmatrix} 0 & 0 & 0 & 0 \\ -u & 1 & 0 & 0 \\ -\frac{4}{3}v & 0 & \frac{4}{3} & 0 \\ -\alpha v^2 - \beta u^2 - \frac{\gamma}{Pr}E & \beta u & \alpha v & \frac{\gamma}{Pr} \end{pmatrix} \tag{A.13}$$

with $\alpha = \dfrac{4}{3} - \dfrac{\gamma}{Pr}$ and $\beta = 1 - \dfrac{\gamma}{Pr}$

Since $\boldsymbol{A}_1^V$ and $\boldsymbol{B}_2^V$ are lower triangular matrices, their spectral radius can be computed straightforwardly. Moreover, they share the same diagonal terms, involving that their respective spectral radius are equal.

$$\rho(\boldsymbol{A}_1^V) = \rho(\boldsymbol{B}_2^V) = \frac{\mu}{Re\ \rho} \cdot \max\left[\frac{\gamma}{Pr}, \frac{4}{3}\right] \tag{A.14}$$

For the air at moderate temperature, we then have $\max\left[\frac{\gamma}{Pr}, \frac{4}{3}\right] = \frac{\gamma}{Pr}$, so finally, the spectral radius of $\boldsymbol{J}_\perp^V$ is :

$$\rho\left(\boldsymbol{J}_\perp^V\right) = \rho\left(\boldsymbol{A}_1^V\ n_x^2 + \boldsymbol{B}_2^V n_y^2\right) = \frac{\mu}{Re\ \rho}\frac{\gamma}{Pr} \tag{A.15}$$

Appendix B

Artificial Compressibility

B.1 Inviscid Jacobian matrices

The Jacobian matrices for the artificial compressibility system are simple in comparison with the compressible system. Indeed, naturally, we work with the primitive variables.

$$\boldsymbol{A}^E = \frac{\partial \boldsymbol{f}^E}{\partial \boldsymbol{w}} = \begin{pmatrix} 0 & \beta & 0 \\ 1 & 2u - s_x & 0 \\ 0 & V & u - s_x \end{pmatrix} \tag{B.1}$$

$$\boldsymbol{B}^E = \frac{\partial \boldsymbol{g}^E}{\partial \boldsymbol{w}} = \begin{pmatrix} 0 & 0 & \beta \\ 0 & v - s_y & u \\ 1 & 0 & 2v - s_y \end{pmatrix} \tag{B.2}$$

$$\boldsymbol{J}_\perp^E = \begin{pmatrix} 0 & \beta n_x & \beta n_y \\ n_x & u_n - s_n + u n_x & u n_y \\ n_y & v n_x & u_n - s_n + v n_y \end{pmatrix} \tag{B.3}$$

However, on can notice that the contribution of the ALE flux to the Jacobian matrix is not just an additional term on the diagonal. Therefore the transformation matrices $\boldsymbol{T}$ and $\boldsymbol{T}^{-1}$ in $\boldsymbol{J}_\perp^E = \boldsymbol{A}^E n_x + \boldsymbol{B}^E n_y = \boldsymbol{T}\boldsymbol{\Lambda}^E\boldsymbol{T}^{-1}$ are not identical to the static mesh transformation matrices. They are

$$\boldsymbol{T} = \begin{pmatrix} 0 & -A & B \\ -n_y & n_y V_t + n_x(c - \frac{s_n}{2}) & -n_y V_t + n_x(c + \frac{s_n}{2}) \\ n_x & -n_x V_t + n_y(c - \frac{s_n}{2}) & n_x V_t + n_y(c + \frac{s_n}{2}) \end{pmatrix} \tag{B.4}$$

$A = (c - \frac{s_n}{2})^2 + V_n(c - \frac{s_n}{2})$
$B = (c + \frac{s_n}{2})^2 - V_n(c + \frac{s_n}{2})$

with $c = \sqrt{(V_n - \frac{s_n}{2})^2 + \beta}$ and

$$\boldsymbol{T}^{-1} = \frac{1}{2c(c+\frac{s_n}{2})(c-\frac{s_n}{2})} \begin{pmatrix} -2cV_t & T_{1,2}^{-1} & T_{1,3}^{-1} \\ -(c+\frac{s_n}{2}) & B\ n_x & B\ n_y \\ c-\frac{s_n}{2} & A\ n_x & A\ n_y \end{pmatrix} \tag{B.5}$$

with

$$\begin{aligned} T_{1,2}^{-1} &= -(A+B)c\ n_y - (A-B)(n_y\frac{s_n}{2} + n_x V_t) \\ T_{1,3}^{-1} &= (A+B)c\ n_x + (A-B)(n_x\frac{s_n}{2} - n_y V_t) \\ \det(T) &= -2c(c+\frac{s_n}{2})(c-\frac{s_n}{2}) \end{aligned}$$

and

$$\boldsymbol{\Lambda}^E = \begin{pmatrix} u_n - s_n & 0 & 0 \\ 0 & u_n - \frac{s_n}{2} - c & 0 \\ 0 & 0 & u_n - \frac{s_n}{2} + c \end{pmatrix} \tag{B.6}$$

Obvisously, one can check that imposing $s_n = 0$ into the matrices $\boldsymbol{T}, \boldsymbol{T}^1, \boldsymbol{\Lambda}^E$ leads to the formulation without ALE flux.

B.2 Viscous Jacobian matrices

The viscous Jacobian matrices needed for the computation of the implicit stage are given by

$$\boldsymbol{A}_1^V = \frac{\partial \boldsymbol{f}^V}{\partial \boldsymbol{w}_x} = \frac{1}{Re} \begin{pmatrix} 0 & 0 & 0 \\ 0 & 2 & 0 \\ 0 & 0 & 1 \end{pmatrix} \tag{B.7}$$

$$\boldsymbol{B}_2^V = \frac{\partial \boldsymbol{g}^V}{\partial \boldsymbol{w}_y} = \frac{1}{Re} \begin{pmatrix} 0 & 0 & 0 \\ 0 & 1 & 0 \\ 0 & 0 & 2 \end{pmatrix} \tag{B.8}$$

$$\boldsymbol{J}_\perp^V = \boldsymbol{A}_1^V n_x^2 + \boldsymbol{B}_2^V n_y^2 = \frac{1}{Re} \begin{pmatrix} 0 & 0 & 0 \\ 0 & 2n_x^2 + n_y^2 & 0 \\ 0 & 0 & 2n_y^2 + n_x^2 \end{pmatrix} \tag{B.9}$$

The spectral radius of $\boldsymbol{J}_\perp^V$ is then

$$\rho\left(\boldsymbol{J}_\perp^V\right) = \frac{1}{Re}\max(|2n_x^2 + n_y^2|, |2n_y^2 + n_x^2|) = \frac{1}{Re}\max(n_x^2 + 1, n_y^2 + 1) \tag{B.10}$$

B.3 ROE average state for AC

In this section, a Roe average state that satisfies the Roe matrix conditions for the AC system is sought.The methodology presented in [22] is followed and applied to the the static AC system.
First, we decompose the data difference in terms of the right engenvectors $\widetilde{\boldsymbol{R}_k}$ and the wave strenghts $\widetilde{\alpha_k}$ as:

$$\Delta \boldsymbol{w} = \sum_{k=1}^{3} \widetilde{\alpha_k} \widetilde{\boldsymbol{R}_k} \tag{B.11}$$

where the over tilde denotes the unknown average state. The columns of T being the right eigenvectors of the system, we have :

$$\Delta p = -\widetilde{\alpha_2}(\widetilde{c}(\widetilde{V_n} + \widetilde{c})) + \widetilde{\alpha_3}(-\widetilde{c}(\widetilde{V_n} - \widetilde{c})) \tag{B.12a}$$
$$\Delta u = -\widetilde{\alpha_1} n_y + \widetilde{\alpha_2}(n_y \widetilde{V_t} + \widetilde{c}) + \widetilde{\alpha_3}(-n_y \widetilde{V_t} + n_x \widetilde{c}) \tag{B.12b}$$
$$\Delta v = \widetilde{\alpha_1} n_x + \widetilde{\alpha_2}(-n_x \widetilde{V_t} + n_y \widetilde{c}) + \widetilde{\alpha_3}(n_x \widetilde{V_t} + n_y \widetilde{c}) \tag{B.12c}$$

(B.12b) $\cdot n_x$ + (B.12c) $\cdot n_y$
and (B.12b) $\cdot n_y$ - (B.12c) $\cdot n_x$ leads to :

$$\Delta V_n = \widetilde{\alpha_2}\widetilde{c} + \widetilde{\alpha_3}\widetilde{c} \tag{B.13a}$$
$$\Delta V_t = \widetilde{\alpha_1} + (\widetilde{\alpha_2} + \widetilde{\alpha_3})\widetilde{V_t} \tag{B.13b}$$

The system of (B.13a) and (B.12a) allow to find α_2 and α_3 and then (B.13b) is used to find α_1 Eventually, one has:

$$\widetilde{\alpha_1} = \Delta V_t - \Delta V_n \frac{\widetilde{V_t}}{\widetilde{c}} \tag{B.14a}$$
$$\widetilde{\alpha_2} = \frac{-\Delta p - \Delta V_n(\widetilde{V_n} - \widetilde{c})}{2\ \widetilde{c}^2} \tag{B.14b}$$
$$\widetilde{\alpha_3} = \frac{\Delta p + \Delta V_n(\widetilde{V_n} + \widetilde{c})}{2\ \widetilde{c}^2} \tag{B.14c}$$

The Roe matrix conservativity condition states that:

$$\Delta \boldsymbol{F}^E = \boldsymbol{J}_\perp^E \delta w = \sum_{k=1}^{3} \widetilde{\alpha_k} \widetilde{\lambda_k} \widetilde{\boldsymbol{R}_k} \tag{B.15}$$

$$\beta(\Delta u\ n_x + \Delta v\ n_y) = -\widetilde{\alpha_2}(\widetilde{c}(\widetilde{V_n} + \widetilde{c}))(\widetilde{V_n} - \widetilde{c})) + \widetilde{\alpha_3}(-\widetilde{c}(\widetilde{V_n} - \widetilde{c}))(\widetilde{V_n} + \widetilde{c}) \tag{B.16a}$$

$$\Delta p\ n_x + (2u\ n_x + v\ n_y)\Delta u + (u\ n_y)\Delta v = -\widetilde{\alpha_1} n_y \widetilde{V_n} + \widetilde{\alpha_2}(n_y \widetilde{V_t} + n_x \widetilde{c})(\widetilde{V_n} - \widetilde{c}) + \widetilde{\alpha_3}(-n_y \widetilde{V_t} + n_x \widetilde{c})(\widetilde{V_n} + \widetilde{c}) \tag{B.16b}$$

$$\Delta p\ n_y + (v\ n_x)\Delta u + (u\ n_x + 2v\ n_y)\Delta v = \widetilde{\alpha_1} n_x \widetilde{V_n} + \widetilde{\alpha_2}(-n_x \widetilde{V_t} + n_y \widetilde{c})(\widetilde{V_n} - \widetilde{c}) + \widetilde{\alpha_3}(n_x \widetilde{V_t} + n_y \widetilde{c})(\widetilde{V_n} + \widetilde{c}) \tag{B.16c}$$

(B.16a) is identical to (B.12a) so it doesn't give us any information.
Doing the operation (B.16b)$\cdot n_x$ + (B.16c) $\cdot n_y$ and substituing the expression of α_2 (B.14b) and α_3 (B.14c) into the resulting equation gives :

$$\Delta V_n^2 = 2\ \widetilde{Vn}\ \Delta V_n \tag{B.17}$$

and since:

$$\Delta V_n^2 = (V_n^R)^2 - (V_n^L)^2 \tag{B.18}$$

$$\Delta V_n = V_n^R - V_n^L \tag{B.19}$$

we obtain :

$$\widetilde{V_n} = \frac{1}{2}(V_n^R + V_n^L) \tag{B.20}$$

Doing the operation (B.16b)$\cdot n_y$ - (B.16c) $\cdot n_x$ and substituing the expression of $\alpha_1, \alpha_2, \alpha_3$ into the resulting equation gives :

$$\Delta(V_n V_t) = \Delta V_t \widetilde{V_n} + \Delta V_n \widetilde{V_t} \tag{B.21}$$

and since

$$\Delta(V_n V_t) = V_n^R\ V_t^R - V_n^L\ V_t^L \tag{B.22}$$

$$\Delta V_t = V_t^R - V_t^L \tag{B.23}$$

and using equation (B.20)
one finds :

$$\widetilde{V_t} = \frac{1}{2}(V_t^R + V_t^L) \quad \text{and} \quad \widetilde{c} = \sqrt{\widetilde{V_n}^2 + \beta} \tag{B.24}$$

Appendix C

Compatibility equations

C.1 Compatibility equations

The compatibility equations are the expression of the system of equations in the eigenvectors basis. It has been seen in Appendix A that a matrix $\boldsymbol{L}^{-1}$ can be defined that will diagonalize the matrix $\boldsymbol{J}_p^E$. Introducing the decomposition of $\boldsymbol{J}_p = \boldsymbol{L}\boldsymbol{\Lambda}^E\boldsymbol{L}^{-1}$, the system of Euler equations reads :

$$\frac{\partial \boldsymbol{v}_p}{\partial t} + (\boldsymbol{L}\boldsymbol{\Lambda}\boldsymbol{L}^{-1} \cdot \nabla)\boldsymbol{v}_p = 0 \tag{C.1}$$

and multiplying equation (C.1) by $\boldsymbol{L}^{-1}$, one obtains the system of decoupled compatibility equations :

$$\frac{\partial \boldsymbol{L}^{-1}\boldsymbol{v}_p}{\partial t} + (\boldsymbol{\Lambda} \cdot \nabla)\boldsymbol{L}^{-1}\boldsymbol{v}_p = 0 \tag{C.2}$$

The vector $\boldsymbol{h} = \boldsymbol{L}^{-1}\boldsymbol{v}_p$ is the vector of the characteristic variables. Each of the compatibility equation can be written

$$\frac{\partial h_i}{\partial t} + (\lambda_i \cdot \nabla)h_i = 0 \tag{C.3}$$

Because the right hand side of equation is zero, the characteristic variables h_i are stricly conserved during their propagation along the characteristics C_i defined by

$$\frac{dx_n}{dt} = \lambda_i \tag{C.4}$$

The characteristic variables are also called Riemmann variables and Riemann invariants when they remain constant. This condition reads

$$\delta h_i = 0$$

Sometimes, the Riemann variables can be integrated and leads to simple implementation of the boundary condition (see Sec. 1.5.1). In other cases, the compatibility equations are linearized to be able to find the variables at the boundary (see Sec. 2.4.1).

Appendix D

Non-rotating cylinder

In this section, the mesh is kept fixed and the velocity at the cylinder wall is zero. The previous mesh used with the rotating cylinder is tested with this configuration but it turns out to be not fine enough in the wake to enable the instability.

Hence, a new grid of 32106 cells represented in Fig. D.1 is used. Note that the gris in reference [69] is made of 48103 cells

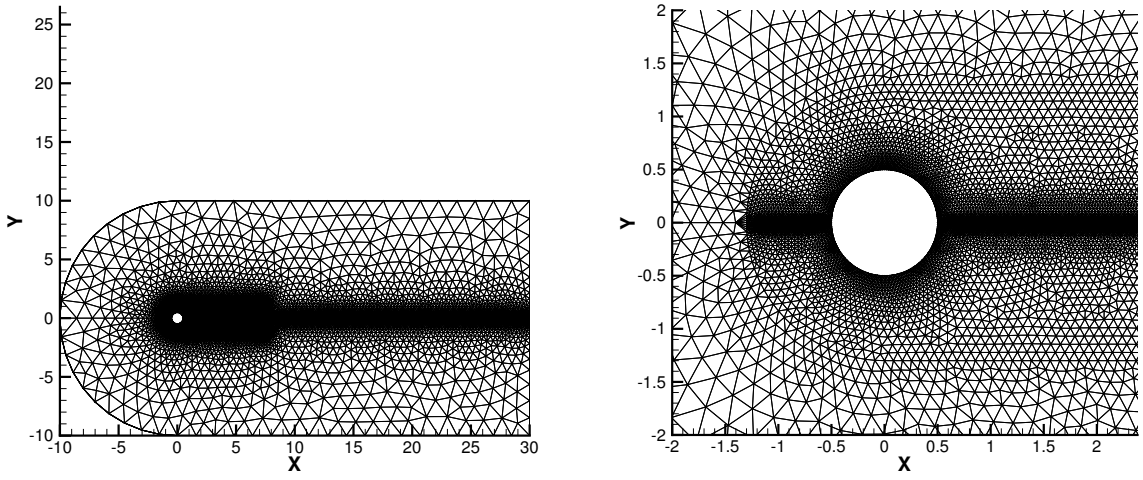

Figure D.1: Non-rotating cylinder. (a): global view of the computational grid (b): close up on the cylinder region.

BDF Results

From reference [69], we know that the Strouhal number is approximately $S_t = 0.195$ which leads to a period $T = 1/f = 5.12s$. The time step is $\Delta t = 0.1$s which gives 50 discretization points per cycle.

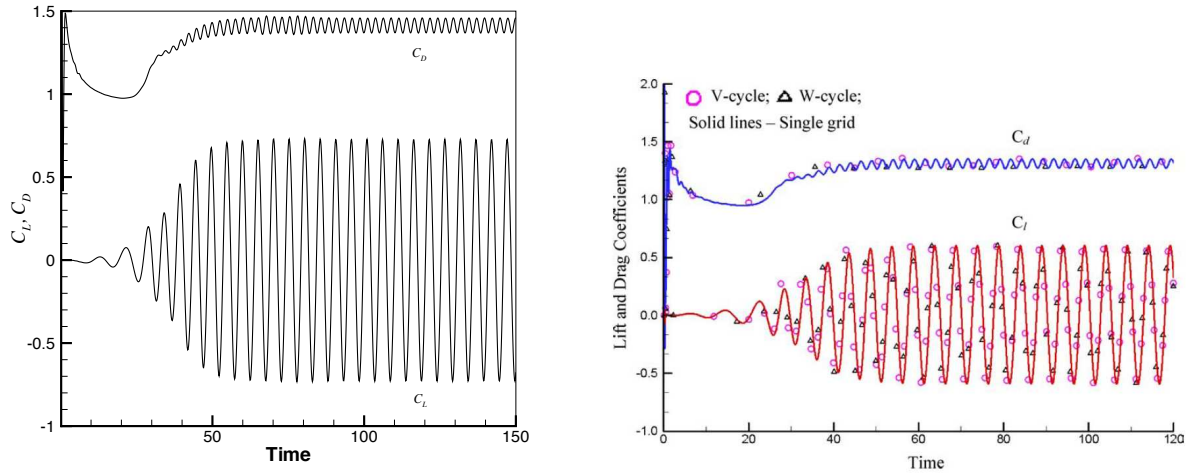

Figure D.2: Non-rotating cylinder. Global aerodynamic coefficients comparison between the PJ-BDF-C solver (a) and reference [69] (b)

Reference	C_L	C_D	Strouhal
HIFUN	$\pm$ 0.73	1.41 $\pm$ 0.044	0.195
Tai & Zhao [69]	$\pm$ 0.64	1.31 $\pm$ 0.041	0.195
Bergmann [8]	$\pm$ 0.69	1.39 $\pm$ 0.045	0.195

Table D.1: Non-rotating cylinder. Comparison of aerodynamic coefficients results, $Re = 200$, $M = 0.2$

Table D.1 shows the results of the BDF approach simulation. They are in good agreement with references [69] and [8]. The Strouhal number is identical.

TSM simulation

So far, the TSM has been used for the prediction of periodic unsteady flows where the period is known a priori. The frequency content of the flow field is a consequence of the time variation of the boundary conditions of the problem. In the present still cylinder case, the flow is indeed periodic but the frequency of unsteadiness is not known a priori. This raises two issues:

- Because the TSM times t_n share the same wall boundary condition, if we initialize the $2N + 1$ problems with the same freestream field, there is no coupling of the equations. All $\boldsymbol{w}_n^0$ are identical, corresponding to the eigenvector of zero eigenvalue for the TSM time operator (see section 3.2.1).

- Because, the time period is not known a priori, one cannot compute exactly the spectral operator. Hence, for different guesses of the time period, the residuals will converge to different levels of accuracy. Only for the exact time period, will the residual go to machine zero to solve exactly $\mathcal{R}_n^t(\boldsymbol{w}) = 0$.

To adress the first issue, the initialization of the flow fields is realized with the results of a TSM simulation with an approximate guess of the period and a non-zero amplitude for the cylinder velocity. Thus, one can hope to obtain initial solutions not too far from the expected final solutions.
To adress the second issue, an optimisation method based on the residual gradient is proposed by Gopinath & al [28] to converge towards the exact time period. This "Gradient Based Variable Time Period" (GBVTP) consists in solving the new problem $\mathcal{R}_n^t(\boldsymbol{w}, T) = 0$ where the period is now part of the solution. We remind that the residual is :

$$\mathcal{R}_n^t(\boldsymbol{w}) = D_t(\boldsymbol{w}_n) = \sum_{p=-N}^{N} d_p \boldsymbol{w}_{n+p} + \mathcal{R}(\boldsymbol{w}_n)$$

The gradient of the square of $\mathcal{R}_n^t$ with respect to the period T is:

$$\frac{\partial \mathcal{R}_n^{t^2}}{\partial T} = 2 \times \mathcal{R}_n^t \times \frac{-1}{T} \sum_{p=-N}^{N} d_p \boldsymbol{w}_{n+p} \tag{D.1}$$

The average of all the gradients over the TSM time instances and cells is used to update the time period for the next dual time iteration

$$T^{m+1} = T^m - \Delta T \frac{\partial \mathcal{R}_n^{t^2}}{\partial T} \tag{D.2}$$

with ΔT a suitable increment to ensure convergence. At every dual time iteration, a new period is computed with (D.2), resulting in a new spectral operator.
Attempts of TSM computation following the presented methodology did not succeed.

Appendix E

Implicit incompressible TSM article

Implicit Time Spectral Method for Periodic Incompressible Flows

S. Antheaume[1] and C. Corre [2]
Laboratoire des Ecoulements Geophysiques et Industriels,

Domaine Universitaire, BP 53, 38041 Grenoble Cedex 9 France

The Time Spectral Method converts a time-periodic flow computation into the solution of $2N+1$ coupled steady computations where N denotes the number of harmonics retained in the Fourier analysis of the flow. The efficiency of the method has been previously demonstrated by several authors for compressible flow applications on structured grids using implicit solution of the large-scale steady system introduced by the coupling. In this paper, the Time Spectral Method is extended to periodic incompressible viscous flows using a finite-volume formulation of the Artificial Compressibility system on general moving unstructured grids. Numerical simulations of low-Reynolds flows over an airfoil show the Time Spectral Method can afford, though not systematically, a reduction by a factor up to 5 of the computational cost with respect to a conventional unsteady technique which computes the whole transient flow behavior.

---

[1] Ph.D candidate
[2] Professor

Nomenclature

$\boldsymbol{A}, \boldsymbol{B}, \boldsymbol{J}$ = flux Jacobian matrices

C_X, C_Y = force coefficients

C_p = pressure coefficient

c = airfoil chord

$\boldsymbol{F}$ = physical flux

f^* = nondimensional frequency, fc/U_∞

H_0 = heaving amplitude

$\mathcal{H}$ = numerical flux

N = number of harmonics

Re = Reynolds number

$\mathcal{R}$ = residual vector discretizing the flux balance

$\boldsymbol{s}$ = grid velocity vector

t, τ = physical and dual time

$\boldsymbol{w}$ = conservative variable vector

$\boldsymbol{x}$ = grid position vector

β = artificial compressibility parameter

η = global cost ratio

θ, θ_0 = angular position and pitching amplitude

ω = angular velocity

Subscripts

i = cell index

∞ = freestream value

n = TSM n^{th} time instant

Superscripts

l = Jacobi iteration counter

m = dual time counter

n = physical time counter

I. Introduction

The design of aerodynamic or hydrodynamic devices often requires the study of unsteady flow configurations. When this design process is performed with numerical tools, the so-called dual-time approach represents a well-established way to efficiently compute unsteady flows. In this approach the unsteady field at each step of the physical time marching procedure is obtained as a steady solution with respect to a dual-time step [1] [2]. This dual-time step (DTS) strategy can also be viewed as finding the solution of the steady (with respect to the dual time) governing equations of the flow augmented by a source term corresponding to the discretization of the physical time derivative using typically a second-order Backward Difference Formula (BDF). The numerical methods previously available for steady flows can be readily extended to handle unsteady flows by simply taking into account this source term. Among the many industrial flow applications requiring unsteady flow analysis, a large set of problems involve time periodicity such as helicopter rotors, wind turbines, flapping-wing propulsion mechanisms as far as external aerodynamics is concerned but also internal flows within rotor-stator combinations in the context of turbomachinery applications. A drawback of the BDF-DTS method for such flows is that it requires to compute, typically from an initial rest configuration, the whole transient of the flow before the periodic flow of interest becomes established. This flaw of the conventional dual-time strategy motivated the development of numerical methods looking directly for the periodic solution of the flow. Taking advantage of the development of the periodic flow solution into a Fourier series, Hall & al [3] introduced an efficient method dedicated to time periodic flows for turbomachinery applications. Following a similar line of thought, Gopinath and Jameson proposed the Time Spectral Method (TSM) for external aerodynamics applications [4]. The TSM method transforms the original system of $(2 + d)$ unsteady equations describing the d-dimensional compressible flow field at each time moment (2 scalar equations expressing mass and energy conservation and d scalar equations expressing the conservation of the d momentum components) into an extended set of $(2N + 1) \times (d + 2)$ equations corresponding to the flow solution at $(2N + 1)$ time moments in the flow period, selected so as to ensure spectral accuracy for the physical time-derivative. To make the method truly attractive, it is of course crucial to efficiently compute the steady-state of this extended system of

conservation laws. Since, as pointed out by [5], the explicit time-integration of the TSM system displays severe stability limits when the number of harmonics N increases, several authors [6–8] have put forward implicit solution strategies. These allow the use of both large CFL numbers ensuring faster convergence to a steady-state and a high number of harmonics N that might be needed to accurately described complex unsteady flows. Up to now, TSM has been used for a wide range of applications dealing mostly with compressible flows: turbomachinery [9], rotorcraft [10]. The context of the present study is the HARVEST industrial/academic joint project devoted to the development of a cross flow water turbine technology allowing to harness the kinetic energy of rivers and oceans streams [11]. The hydrodynamic design of the turbine is currently performed using both an experimental and numerical strategy. The final objective of the present work is to improve the efficiency of the numerical design by replacing the current BDF computations of turbulent flows over sea turbine configurations [12] with a TSM approach. This supposes to adapt the TSM strategy to an incompressible flow solver. A first attempt in this direction has been recently performed by Jameson [13] using an Artificial Compressibility (AC) method but stability concerns emerged when computing high-frequency pitching airfoils. In the present paper, an implicit TSM strategy is successfully applied to the computation of 2D incompressible laminar flow over oscillating airfoils in pitching and heaving motion recently studied in [14] using a conventional BDF method. Such 2D laminar configurations represent only a first step towards the computation of more realistic 3D turbulent flows over water turbines; they were however retained at this stage because their limited cost allows an in-depth assessment of the TSM approach proposed in the present work to speed up the integration of periodic low-speed flows. This approach relies on the AC method to describe the incompressible flow and an ALE strategy to describe the motion of the unstructured computational grids. It is compared to a conventional BDF approach, also combining AC and ALE, both from the viewpoint of accuracy and efficiency. The paper is organized as follows: section II reviews the main ingredients of the DTS-BDF incompressible flow solver (AC model, ALE formulation, implicit time-integration) and displays validation results obtained for flows over a pitching and heaving NACA0015 airfoil recently computed and analyzed by Kinsey and Dumas [14]; section III details the application of TSM to the AC method and section IV describes the adaptation of an implicit

treatment developed in [15] to the TSM system; in section V, the implicit TSM approach is applied to the flow computation of a pitching and heaving NACA0015 airfoil for an increasing number of harmonics N in order to determine the best trade-off between accuracy and cost (both increasing functions of N) and check whether TSM can outperform BDF. Conclusions and perspectives are drawn in the last section.

II. Incompressible flow solver

A. Governing equations

The solution of the incompressible Navier-Stokes equations is typically obtained using either a pressure-based method where pressure and velocity are solved in an iterative fashion through a pressure-correction equation, or a density-based method, such as the artificial compressibility (AC) approach of Chorin [16]. The latter AC strategy has been favored in this work to take advantage of efficient implicit methods previously developed for solving hyperbolic problems [15] and easy to adapt to the AC system. Let us recall the AC method provides a time-accurate solution of the 1D Euler equations by finding the steady-state of the following hyperbolic system of conservation laws with respect to the dual or fictitious time τ

$$\frac{\partial}{\partial \tau} \underbrace{\begin{pmatrix} p \\ u \end{pmatrix}}_{=\boldsymbol{w}} + \underbrace{\begin{pmatrix} 0 & 0 \\ 0 & 1 \end{pmatrix}}_{=\boldsymbol{K}} \cdot \frac{\partial}{\partial t} \begin{pmatrix} p \\ u \end{pmatrix} + \frac{\partial}{\partial x} \underbrace{\begin{pmatrix} \beta u \\ u^2 + p \end{pmatrix}}_{=\boldsymbol{f}(\boldsymbol{w};\beta)} = 0 \tag{1}$$

with x the space variable, t the physical time, p, u the pressure and velocity, β the constant artificial compressibility parameter. At steady-state on τ, the solution $u(x,t)$ of (1) satisfies the zero-divergence condition while both fields $u(x,t)$ and $p(x,t)$ satisfy the unsteady (with respect to t) momentum equation. Rewriting (1) in the compact form of a 1D hyperbolic system with a source term

$$\frac{\partial \boldsymbol{w}}{\partial \tau} + \frac{\partial}{\partial x} \boldsymbol{f}(\boldsymbol{w};\beta) = \boldsymbol{S} = -\boldsymbol{K} \frac{\partial \boldsymbol{w}}{\partial t}$$

makes clear the AC system can be efficiently driven to an accurate steady-solution by making use of tools initially developed in the context of compressible flow solutions: second-order upwind discretization for the flux derivative, second-order BDF discretization for the physical time-derivative

and first-order implicit stage for fast convergence on the dual-time. Note the choice of value for the AC parameter β affects the overall convergence rate as well as the accuracy of the physical solution through the numerical dissipation of the space discretization; however, as long as the steady-state on τ is correctly achieved, the AC system remains consistent with the incompressible flow equations whatever the value of β. Let us now turn to the AC system extended to the case of 2D incompressible viscous flows computed on moving grids. Let $\Omega(t) \subset \Re^2$ be an arbitrary control surface bounded by a smooth closed contour $\partial\Omega(t)$ which moves independently from the flow with a velocity $\boldsymbol{s}(\boldsymbol{x},t) = s_x(t)\ \boldsymbol{i} + s_y(t)\ \boldsymbol{j}$, where $\boldsymbol{x} = x\ \boldsymbol{i} + y\ \boldsymbol{j}$ denotes the vector of Cartesian coordinates in the absolute frame of reference. In the Arbitrary Lagrangian Eulerian (ALE) framework, the 2D Navier-Stokes equations for incompressible unsteady flows, modified to account for the AC method, can be expressed in the following integral form:

$$\frac{\partial}{\partial\tau}\int_{\Omega(t)} \boldsymbol{w}\ d\Omega(t)\ +\ \boldsymbol{K}\frac{\partial}{\partial t}\int_{\Omega(t)} \boldsymbol{w}\ d\Omega(t)\ +\ \int_{\partial\Omega(t)} (\boldsymbol{F}^E - \boldsymbol{F}^V)\cdot\boldsymbol{n}\ d\gamma(t)\ =\ 0\ , \tag{2}$$

where $\boldsymbol{n}$ is the outward unit normal vector and γ the curvilinear abscissa of $\partial\Omega$. The vector of conservative variables $\boldsymbol{w}$, the singular matrix $\boldsymbol{K}$, the inviscid fluxes $\boldsymbol{F}^E = (\boldsymbol{f}^E, \boldsymbol{g}^E)$ and the viscous fluxes $\boldsymbol{F}^V = (\boldsymbol{f}^V, \boldsymbol{g}^V)$ are defined by

$$\boldsymbol{w} = \begin{pmatrix} p \\ u \\ v \end{pmatrix}, \quad \boldsymbol{K} = \begin{pmatrix} 0 & 0 & 0 \\ 0 & 1 & 0 \\ 0 & 0 & 1 \end{pmatrix}, \quad \boldsymbol{f}^E(\boldsymbol{w}) = \begin{pmatrix} \beta(u - s_x) \\ u(u - s_x) + p \\ v(u - s_x) \end{pmatrix}, \quad \boldsymbol{g}^E(\boldsymbol{w}) = \begin{pmatrix} \beta(v - s_y) \\ u(v - s_y) \\ v(v - s_y) + p \end{pmatrix}$$

$$\boldsymbol{f}^V(\frac{\partial\boldsymbol{w}}{\partial x}, \frac{\partial\boldsymbol{w}}{\partial y}) = \frac{1}{Re}\begin{pmatrix} 0 \\ 2\dfrac{\partial u}{\partial x} \\ \dfrac{\partial u}{\partial y} + \dfrac{\partial v}{\partial x} \end{pmatrix}, \quad \boldsymbol{g}^V(\frac{\partial\boldsymbol{w}}{\partial x}, \frac{\partial\boldsymbol{w}}{\partial y}) = \frac{1}{Re}\begin{pmatrix} 0 \\ \dfrac{\partial u}{\partial y} + \dfrac{\partial v}{\partial x} \\ 2\dfrac{\partial v}{\partial y} \end{pmatrix}$$

The pressure p and the components (u, v) of the fluid velocity in the absolute frame of reference are normalized respectively by $\rho_\infty U_\infty^2$ and U_∞, with ρ_∞ and U_∞ the freestream density and velocity magnitude. For the following airfoil flow computations, the Reynolds number $Re = \rho_\infty U_\infty c/\mu_\infty$ is based on the airfoil chord c. The next subsection describes the finite-volume upwind scheme and implicit time-discretization used in this work to solve the so-called ALE-AC system (2).

B. Numerical Methods

1. Spatial discretization

System (2) is solved on general unstructured grids using a finite volume approach. Applying (2) on a given cell Ω_i, introducing the average value $\overline{\boldsymbol{w}}$ of $\boldsymbol{w}$ over the cell and decomposing the flux balance as the sum of fluxes through each face $\Gamma_{i,k}$ of cell Ω_i leads to

$$\frac{\partial}{\partial \tau}(\overline{\boldsymbol{w_i}}|\Omega_i|) + \boldsymbol{K}\frac{\partial}{\partial t}(\overline{\boldsymbol{w_i}}|\Omega_i|) + \sum_k \int_{\Gamma_{i,k}} (\boldsymbol{F}^E - \boldsymbol{F}^V)\cdot \boldsymbol{n}\; d\gamma \;=\; 0 \tag{3}$$

where $|\Omega_i|$ is the surface of the i-th grid cell Ω_i. The normal physical flux vector $(\boldsymbol{F}^E - \boldsymbol{F}^V)\cdot\boldsymbol{n}$ through the face $\Gamma_{i,k}$ of length $|\Gamma_{i,k}|$ is approximated by the numerical flux vector $\mathcal{H} = \mathcal{H}^E - \mathcal{H}^V$ computed at the center i,k of the face $\Gamma_{i,k}$

$$\int_{\Gamma_{i,k}} (\boldsymbol{F}^E - \boldsymbol{F}^V)\cdot \boldsymbol{n}\; d\gamma \;= \left(\mathcal{H}^E_{i,k} - \mathcal{H}^V_{i,k}\right)|\Gamma_{i,k}| + O(h^p)$$

where h denotes a typical grid length. The space accuracy order p will depend on the choice of polynomial reconstruction used for the conservative variable inside each grid cell; a linear reconstruction will be systematically used in this work leading to second-order accuracy in space. For this reason and without loss of accuracy, the average state in cell i is replaced by the state at cell center, denoted $\boldsymbol{w}_i$ from now on. The Roe approximate Riemann solver initially developed to solve the compressible Euler equations [17] is adapted to the hyperbolic ALE-AC system (2) and combined with a MUSCL variable reconstruction approach [18] [19] in order to derive the inviscid numerical flux formula $\mathcal{H}^E_{i,k}$

$$\mathcal{H}^E_{i,k} = \frac{1}{2}(\boldsymbol{F}^E(w^L_k)\cdot\boldsymbol{n}_{i,k} + \boldsymbol{F}^E(w^R_k)\cdot\boldsymbol{n}_{i,k}) + \frac{1}{2}\boldsymbol{Q}^E_{i,k}(\boldsymbol{w}^L_k - \boldsymbol{w}^R_k) \tag{4}$$

where $\boldsymbol{w}^{L/R}$ are the reconstructed states, respectively, on the left and right side of the k^{th} interface $\Gamma_{i,k}$ of cell Ω_i, $\boldsymbol{Q}^E$ is the Roe numerical dissipation matrix. The states at face center i,k are linearly reconstructed from the cell center values in the cells i and $o(i,k)$ sharing the face $\Gamma_{i,k}$ and the cell gradients $\boldsymbol{\nabla w}$ in each of these cells

$$\begin{cases} \boldsymbol{w}^L_k = \boldsymbol{w}_i + \boldsymbol{\nabla w}_i\cdot\boldsymbol{r}_{i,k} \\ \boldsymbol{w}^R_k = \boldsymbol{w}_{o(i,k)} + \boldsymbol{\nabla w}_{o(i,k)}\cdot\boldsymbol{r}_{o(i,k)} \end{cases} \tag{5}$$

where $\boldsymbol{r}_{i,k}$ (resp. $\boldsymbol{r}_{o(i,k)}$) denotes the vector extending from the cell center i (resp. $o(i,k)$) to the center of the interface $\Gamma_{i,k}$. The gradient $\boldsymbol{\nabla w}_i$ is computed at each cell center i using a least-square

formula applied on a fixed spatial support including the neighboring cells sharing at least a node with cell i [19]. The Roe numerical dissipation matrix $\boldsymbol{Q}^E$ is given by:

$$\boldsymbol{Q}^E = |\boldsymbol{A}^E n_x + \boldsymbol{B}^E n_y| = |\boldsymbol{J}_\perp^E|$$

where $\boldsymbol{n} = (n_x, n_y)$ and $\boldsymbol{A}^E$, $\boldsymbol{B}^E$ are the inviscid flux Jacobian matrices: $\boldsymbol{A}^E = d\boldsymbol{f}^E/d\boldsymbol{w}, \boldsymbol{B}^E = d\boldsymbol{g}^E/d\boldsymbol{w}$. An immediate calculation for system (2) yields:

$$\boldsymbol{J}_\perp^E = \begin{pmatrix} 0 & \beta n_x & \beta n_y \\ n_x & V_\perp - s_\perp + u\ n_x & u\ n_y \\ n_y & v\ n_x & V_\perp - s_\perp + v\ n_y \end{pmatrix}$$

where $V_\perp = u\ n_x + v\ n_y$, $s_\perp = s_x n_x + s_y n_y$. This Jacobian matrix can be also expressed as $\boldsymbol{J}_\perp^E = \boldsymbol{T}|\boldsymbol{\Lambda}^E|\boldsymbol{T}^{-1}$ with $\boldsymbol{\Lambda}^E$ the diagonal matrix containing the real eigenvalues of the hyperbolic system (2). The Roe dissipation matrix is eventually computed as

$$\boldsymbol{Q}_{i,k}^E = \boldsymbol{T}_{i,k}|\boldsymbol{\Lambda}_{i,k}^E|\boldsymbol{T}_{i,k}^{-1}$$

with the state $\boldsymbol{w}_{i,k}$ taken as the arithmetic average of $\boldsymbol{w}_{i,k}^L$, $\boldsymbol{w}_{i,k}^R$ following Taylor and Whitfield [20]. The viscous fluxes are approximated using a linearly exact extension of the diamond method of Noh [21], not detailed here. Let us point out the steady-state of (2) depends on the AC parameter β through the numerical dissipation matrix $\boldsymbol{Q}^E$. The numerical inviscid flux balance or residual will be denoted from now on

$$\mathcal{R}_i^E(\boldsymbol{w}, \boldsymbol{x}, \boldsymbol{s}) = \frac{1}{|\Omega_i|} \sum_k \mathcal{H}_{i,k}^E\ |\Gamma_{i,k}| \tag{6}$$

where, in the context of the ALE formulation, the dependence of this flux balance on the mesh position $\boldsymbol{x}$ and speed $\boldsymbol{s}$ has been made explicit. Similarly, the viscous flux balance or residual will be denoted

$$\mathcal{R}_i^V(\boldsymbol{w}, \boldsymbol{x}) = \frac{1}{|\Omega_i|} \sum_k \mathcal{H}_{i,k}^V\ |\Gamma_{i,k}| \tag{7}$$

with an explicit dependence on the grid position $\boldsymbol{x}$. Since only rigid body motion is considered for the moving grid computation performed in the present work, the cell surface $|\Omega_i|$ will remain constant over time and can be removed from the dual and physical time derivatives in (3) to be

inserted into the inviscid and viscous residual (6) and (7). The semi-discrete form (3) of the ALE-AC system can also be expressed as

$$\frac{\partial \boldsymbol{w}_i}{\partial \tau_i} + \boldsymbol{K}\frac{\partial \boldsymbol{w}_i}{\partial t} + \mathcal{R}_i^E(\boldsymbol{w}, \boldsymbol{x}, \boldsymbol{s}) = \mathcal{R}_i^V(\boldsymbol{w}, \boldsymbol{x}) \tag{8}$$

2. Time-discretization including ALE treatment

When dealing with moving airfoils in the ALE reference frame, two main approaches can be considered for taking into account the grid motion. The first approach is the rigid body technique in which all grid points have the same motion as the airfoil. The initial quality of the mesh is preserved but unsteady boundary conditions must be implemented that include the grid velocities. A drawback of this approach is that, for high frequency pitching movements, relative velocity of in cells away from the center of rotation may become very large leading to excessive numerical dissipation. The second approach deforms the inner cells of the grid to conform to the instantaneous position of the airfoil while the outer boundaries are kept fixed. Deformation can be performed using methods based on spring analogy, which involve either the solution of a large system of equations for the displacements of nodes [22, 23] and/or a local remeshing at each physical time step of the calculation [24, 25]. In all these methods, a geometric conservation law must also be satisfied to avoid volume discretization errors [26]. The Chimera technique is yet another alternative for dealing with moving bodies that makes use of independently meshed overlapping zones, typically a grid zone attached to the body and a grid zone for the background domain [27, 28]. While the deforming grid approach is required for aeroelastic studies or problems involving moving bodies within fixed multi-block geometries, it can be avoided for the simple heaving and pitching airfoils cases treated in this study. Consequently, a simple rigid body approach is retained with the mesh position $\boldsymbol{x}$ directly derived from the law of motion and the grid velocity $\boldsymbol{s}$ computed using the simple analytical relationship

$$\boldsymbol{s}(t) = \boldsymbol{\Omega}(t) \wedge (\boldsymbol{x}(t) - \boldsymbol{x}_c(t)) + \boldsymbol{t} \tag{9}$$

where $\boldsymbol{\Omega}$ is the rotational velocity vector, $\boldsymbol{x}_c$ the center of rotation and $\boldsymbol{t}$ the translation velocity vector.

For the sake of clarity and without loss of generality, the dual time step resolution is left aside in this section. Using a second-order backward difference formula (BDF) for the physical time-derivative in (8) yields the following second-order discretization of the ALE-AC system:

$$\boldsymbol{K}\frac{\left(\frac{3}{2}\boldsymbol{w}_i^{n+1}-2\boldsymbol{w}_i^{n}+\frac{1}{2}\boldsymbol{w}_i^{n-1}\right)}{\Delta t}+\mathcal{R}_i^E\left(\boldsymbol{w}^{n+1},\boldsymbol{x}^{n+1},\boldsymbol{s}^{n+1}\right)=\mathcal{R}_i^V\left(\boldsymbol{w}^{n+1},\boldsymbol{x}^{n+1}\right) \tag{10}$$

3. Implicit Time integration

The fully discrete ALE-AC system (10) can also be expressed as

$$\boldsymbol{K}\frac{\left(\frac{3}{2}\boldsymbol{w}_i^{n+1}-2\boldsymbol{w}_i^{n}+\frac{1}{2}\boldsymbol{w}_i^{n-1}\right)}{\Delta t}+\mathcal{R}_i\left(\boldsymbol{w}^{n+1}\right)=0 \tag{11}$$

with the full residual $\mathcal{R}$ defined by $\mathcal{R}_i\left(\boldsymbol{w}^{n+1}\right)=\mathcal{R}_i^E\left(\boldsymbol{w}^{n+1}\right)-\mathcal{R}_i^V\left(\boldsymbol{w}^{n+1}\right)$, where the dependence on the grid position and velocity has been omitted for the sake of simplicity. The non-linear system (11) is solved using a DTS approach, that is the new state $\boldsymbol{w}^{n+1}$ is iteratively obtained as the steady-solution with respect to the dual-time τ of the augmented system

$$\frac{\boldsymbol{w}_i^{n,m+1}-\boldsymbol{w}_i^{n,m}}{\Delta\tau_i^{n,m}}+\boldsymbol{K}\frac{\left(\frac{3}{2}\boldsymbol{w}_i^{n,m}-2\boldsymbol{w}_i^{n}+\frac{1}{2}\boldsymbol{w}_i^{n-1}\right)}{\Delta t}+\mathcal{R}_i\left(\boldsymbol{w}^{n,m}\right)=0 \tag{12}$$

where $\boldsymbol{w}^{n,m}$ is the fictitious state at the m^{th} subiteration on τ performed between the n^{th} and $(n+1)^{th}$ physical time-levels. The initial fictitious state at each physical time-level is chosen as $\boldsymbol{w}^{n,0}=\boldsymbol{w}^{n}$ and the new physical state is defined as $\boldsymbol{w}^{n+1}=\boldsymbol{w}^{n,m_{max}}$ with m_{max} the number of sub-iterations on τ needed to achieve steady-state convergence of (12). The efficiency of the method is ensured by making use of an implicit dual-time integration

$$\frac{\Delta\boldsymbol{w}_i^{n,m}}{\Delta\tau_i^{n,m}}=-\mathcal{R}_i\left(\boldsymbol{w}^{n,m+1}\right)-\boldsymbol{K}\frac{\left(\frac{3}{2}\boldsymbol{w}_i^{n,m+1}-2\boldsymbol{w}_i^{n}+\frac{1}{2}\boldsymbol{w}_i^{n-1}\right)}{\Delta t}=-\mathcal{R}_i^t\left(\boldsymbol{w}^{n,m+1}\right) \tag{13}$$

with $\boldsymbol{w}^{n,m+1}=\boldsymbol{w}^{n,m}+\Delta\boldsymbol{w}^{n,m}$. Since the solution accuracy (on t and x) does not depend on the dual-time increment $\Delta\boldsymbol{w}^{n,m}$ which goes to zero at steady-state on τ, the full residual $\mathcal{R}_i^t\left(\boldsymbol{w}^{n,m+1}\right)$ can be expanded as

$$\mathcal{R}_i^t\left(\boldsymbol{w}^{n,m+1}\right)=\mathcal{R}_i^t\left(\boldsymbol{w}^{n,m}\right)+\boldsymbol{K}\frac{3}{2}\frac{\Delta\boldsymbol{w}_i^{n,m}}{\Delta t}+\frac{1}{|\Omega_i|}\sum_k\left(\Delta\mathcal{H}_{i,k}^{(i)}\right)^{n,m}\ |\Gamma_{i,k}| \tag{14}$$

where $(\Delta\mathcal{H}_{i,k}^{(i)})^{n,m}=\mathcal{H}^{(i)^{n,m+1}}-\mathcal{H}^{(i)^{n,m}}$ and $\mathcal{H}^{(i)}=\mathcal{H}^{E(i)}-\mathcal{H}^{V(i)}$ denotes the numerical flux formula retained in the implicit stage. Since the implicit stage vanishes at steady-state this numerical

flux formula does not impact the overall accuracy and its design is solely guided by stability and efficiency requirements. Following [29], [30], [24] the inviscid numerical flux $\mathcal{H}^{E(i)}$ appearing in the implicit stage is simply computed using the first-order Rusanov numerical flux:

$$\mathcal{H}_{i,k}^{E(i)} = \frac{1}{2}(\boldsymbol{F}_i^E \cdot \boldsymbol{n}_{i,k} + \boldsymbol{F}_{o(i,k)}^E \cdot \boldsymbol{n}_{i,k}) + \frac{1}{2}\rho(\boldsymbol{J}_\perp^E)_{i,k}(\boldsymbol{w}_i - \boldsymbol{w}_{o(i,k)}) \tag{15}$$

where $\rho(\boldsymbol{J}_\perp^E)_{i,k}$ is the spectral radius of the inviscid Jacobian matrix $\boldsymbol{J}_\perp^E$ computed at the center of face $\Gamma_{i,k}$. The implicit numerical viscous flux takes the following simplified form

$$\mathcal{H}_{i,k}^{V(i)} = \frac{\rho(\boldsymbol{J}_\perp^V)_{i,k}}{||\boldsymbol{r}_{i,k}|| + ||\boldsymbol{r}_{o(i,k)}||}(\boldsymbol{w}_{o(i,k)} - \boldsymbol{w}_i) = \widetilde{\rho(\boldsymbol{J}_\perp^V)}_{i,k}(\boldsymbol{w}_{o(i,k)} - \boldsymbol{w}_i) \tag{16}$$

where $\rho(\boldsymbol{J}_\perp^V)_{i,k}$ is the spectral radius of the viscous Jacobian matrix. More details on the derivation of the implicit viscous flux can be found in [15]. Inserting the expressions (15) (16) of the implicit numerical fluxes into the expansion of the residual (14) and rearranging (13) yields the following implicit solution for the ALE-AC system (10):

$$\boldsymbol{D}_i^{n,m}\Delta\boldsymbol{w}_i^{n,m} + \frac{1}{2|\Omega_i|}\sum_k \left(\Delta\boldsymbol{F}_{o(i,k)}^E\right)^{n,m} \cdot \boldsymbol{n}_{i,k}\ |\Gamma_{i,k}| - \sum_k C_{i,k}^{n,m}\Delta\boldsymbol{w}_{o(i,k)}^{n,m} = -\mathcal{R}_i^t(\boldsymbol{w}^{n,m}) \tag{17}$$

The coefficients $\boldsymbol{D}_i^{n,m}$, $C_{i,k}^{n,m}$ are defined by:

$$\boldsymbol{D}_i^{n,m} = \left(\frac{\boldsymbol{I}}{\Delta\tau_i^{n,m}} + \frac{3}{2}\frac{\boldsymbol{K}}{\Delta t} + \sum_k C_{i,k}^{n,m}\boldsymbol{I}\right) \quad , \quad C_{i,k}^{n,m} = \frac{1}{|\Omega_i|}\left(\frac{1}{2}\rho(\boldsymbol{J}_\perp^E) + \widetilde{\rho(\boldsymbol{J}_\perp^V)}\right)_{i,k}^{n,m}|\Gamma_{i,k}| \tag{18}$$

with $\boldsymbol{I}$ the identity matrix; note the implicit stage is in fact matrix-free with a scalar diagonal coefficient D for $\Delta p_i^{n,m}$ deprived from the $\frac{3}{2\Delta t}$ contribution in the mass conservation equation and including this term in the momentum conservation equations which involve $\Delta u_i^{n,m}$ and $\Delta v_i^{n,m}$. Equation (17) can be solved at a very low cost per iteration using a simple point-Jacobi relaxation method. Denoting l the iteration counter associated with this method when (17) is iteratively solved to obtain $\boldsymbol{w}^{n,m+1}$ from the known $\boldsymbol{w}^{n,m}$ and introducing $\Delta\phi^{(l)} = \phi^{(l)} - \phi^{n,m}$, the PJ-BDF-ALE-AC

procedure reads:

$$
\begin{aligned}
&\Delta \boldsymbol{w}_i^{(0)} = 0 \\
&\begin{cases} l = 0,\ l_{max} - 1 \\ \Delta \boldsymbol{w}_i^{(l+1)} = (\boldsymbol{D}_i^{n,m})^{-1} \left(-\mathcal{R}_i^t(\boldsymbol{w}^{n,m}, \boldsymbol{x}^{n+1}, \boldsymbol{s}^{n+1}) - \dfrac{1}{2|\Omega_i|} \displaystyle\sum_k \left(\Delta \boldsymbol{F}^E_{o(i,k)} \right)^{(l)} \cdot \boldsymbol{n}_{i,k}\ |\Gamma_{i,k}| + \sum_k C_{i,k}^{n,m} \Delta \boldsymbol{w}_{o(i,k)}^{(l)} \right) \end{cases} \\
&\boldsymbol{w}_i^{n,m+1} = \boldsymbol{w}_i^{n,m} + \Delta \boldsymbol{w}_i^{(l_{max})}
\end{aligned}
\tag{19}
$$

C. Solver Validation

The solver presented in the previous section is validated by computing incompressible unsteady laminar flows over pitching and heaving airfoils which were recently studied by Kinsey and Dumas [14]. The airfoil flow computations presented in [14] were performed using a conventional pressure-based solver implemented in a commercial solver on very fine grids and with a very small time-step to ensure time and grid convergence and allow a fine analysis of the flowfield. These computations will therefore be retained as first reference data and the ability of the proposed PJ-BDF-ALE-AC to provide similar results will be established in the present section.

1. Test-cases description

The geometry under study is a NACA0015 airfoil submitted to a pitching motion and/or a heaving motion. These prescribed motions are defined by the following laws of evolution for the pitching angle $\theta(t)$, around an axis located at one-third of the airfoil chord, and the vertical position $y(t)$

$$
\begin{cases} \theta(t) = \theta_0 \sin(\omega t) \\ y(t) = H_0 \sin(\omega t + \frac{\pi}{2}) \end{cases}
\tag{20}
$$

where θ_0 and H_0 are respectively the pitching and heaving amplitudes, ω is the angular velocity. The reduced frequency f^* is defined as $f^* = \frac{fc}{U_\infty}$, where U_∞ is the freestream velocity. The first test case, denoted PH from now on, combines pitching and heaving motion with $\theta_0 = 60°$, $H_0 = 1$ and $f^* = 0.18$. The second test case, denoted PP, corresponds to a pure pitching motion with $\theta_0 = 23°$, $H_0 = 0$ and $f^* = 0.12$. In both cases, the Reynolds number based on the freestream conditions and the airfoil chord is equal to $Re = 1100$ hence the flow is assumed laminar.

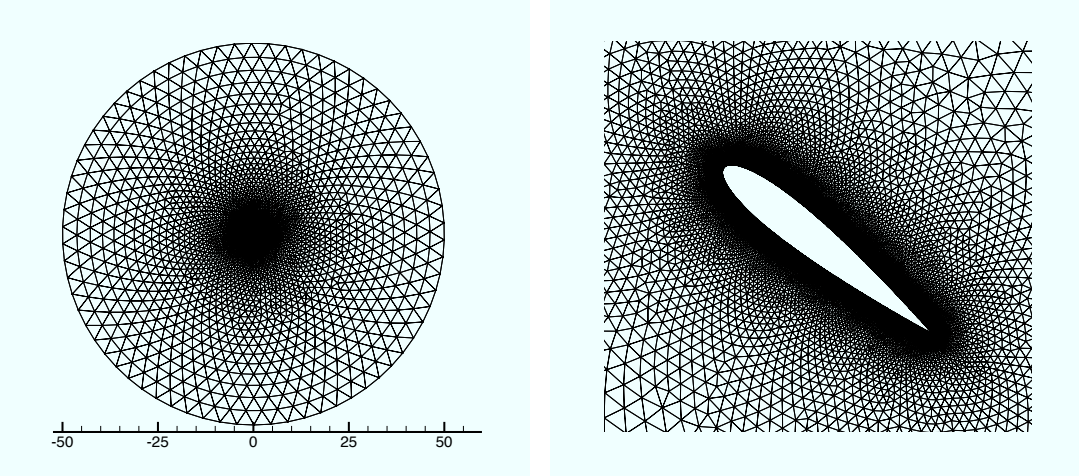

(a) (b)

Fig. 1 (a): global view of the computational grid. (b): close-up on the airfoil region.

2. Numerical parameters

The computational mesh displayed in Fig.1 was generated so as to be similar to the grid used in [14] since both the proposed PJ-BDF-ALE-AC solver and the commercial solver used by Kinsey and Dumas are second-order methods on unstructured triangular grids. This mesh counts 32000 cells, with 360 points set on the airfoil and a near body resolution tailored to satisfy the criterion $y_p^2 \frac{U_\infty}{\nu_\infty \Delta} \sim 1$, where y_p is the distance from the wall to the first adjacent cell centroid and Δ is the minimal edge length on the airfoil. The enforcement of this criterion combines a low cell-Reynolds number and a moderate cell aspect-ratio near the airfoil surface to ensure solution accuracy. The AC parameter β is constant and equal to 5; this value was retained as offering a good trade-off between accuracy and efficiency after a careful assessment of the flow solver on several incompressible reference flows (this study is not reproduced for the sake of conciseness and because the focus of the present work is on the TSM approach applied to the AC solver, not on the AC solver itself).

For each case, 520 physical time steps per period or cycle are used corresponding to a fixed non-dimensional value of $\Delta t \approx 1.06^{-2}$ and $\Delta t \approx 1.16^{-2}$ for the PH an PP test cases respectively. The local dual time step is computed as $\Delta\tau_i^{n,m} = \text{CFL} \max(\frac{h_i}{(\rho^E)_i^{n,m}}, \frac{h_i^2}{(2\rho^V)_i^{n,m}})$ with h_i a characteristic length of the cell Ω_i, ρ^E and ρ^V the spectral radii of the inviscid and viscous Jacobian matrices and CFL the multiplication factor of the characteristic time-step chosen as large as possible, $\text{CFL} = 10^6$,

to ensure fast convergence to the dual steady-state through the use of very large values for $\Delta\tau_i^{n,m}$. At each physical time step, 100 dual time iterations are performed with 16 iterations of the PJ method to solve (19). The residual drops by 3 to 4 orders of magnitude for all the time instants of a cycle; it has been checked that this criterion is sufficient to obtain converged results (global aerodynamic coefficients, wall distribution, fields).

The computation is started with a uniform pressure and velocity flow field; 6 (respectively 4) cycles must be computed for PH (resp. PP) before flow periodicity is fully achieved. A variation of the mean aerodynamic coefficient inferior to 0.2% between two consecutive cycles is the criterion typically used to ensure a fully periodic flow is obtained. All the PJ-BDF-ALE-AC results displayed hereafter correspond to the 7^{th} cycle for PH and 5^{th} cycle for PP and will be labelled BDF from now on.

3. Results

The comparison with the reference results [14] is performed on the force coefficients, more precisely on the C_Y coefficient which is the only one made available by Kinsey and Dumas. The C_X coefficient is also presented for future comparison with the TSM approach. Figure 2 presents the computed C_X and C_Y coefficients over the normalized time period for the PH test-case; note only 1 out of 8 physical time-steps are plotted for the present BDF computations. Similar results obtained for the PP test-case are plotted in Figure 3. The agreement between [14] and the present BDF results is globally very good. A slight difference on the C_Y prediction can be observed in Fig. 2 for the PH problem. Further grid and time-refinement did not modify the present BDF results which will consequently be retained as reference data, against which the TSM approach developed in the next section will be compared, both in terms of accuracy and efficiency.

III. Artificial Compressibility and Time Spectral Method

The present section explains how the time-spectral method, essentially used up to now in the context of compressible flows for structured grid computations, can be combined with the unstructured AC solver described in the previous section. The straightforward application of the TSM for the ALE-AC system is first explained; next, the method of resolution of the AC-ALE TSM discretization is

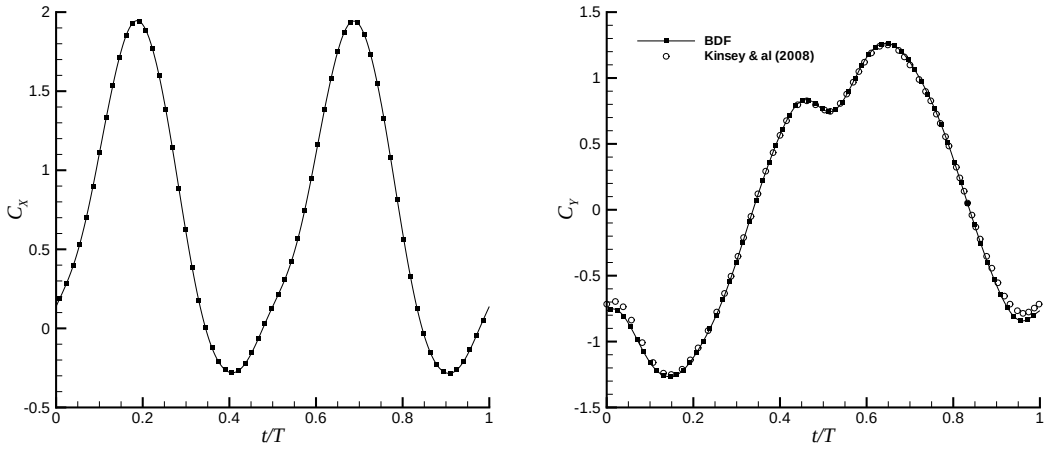

(a) (b)

Fig. 2 PH test case. (a): C_X evolution computed using the present BDF method. (b): C_Y evolution computed in [14] and using the present BDF method.

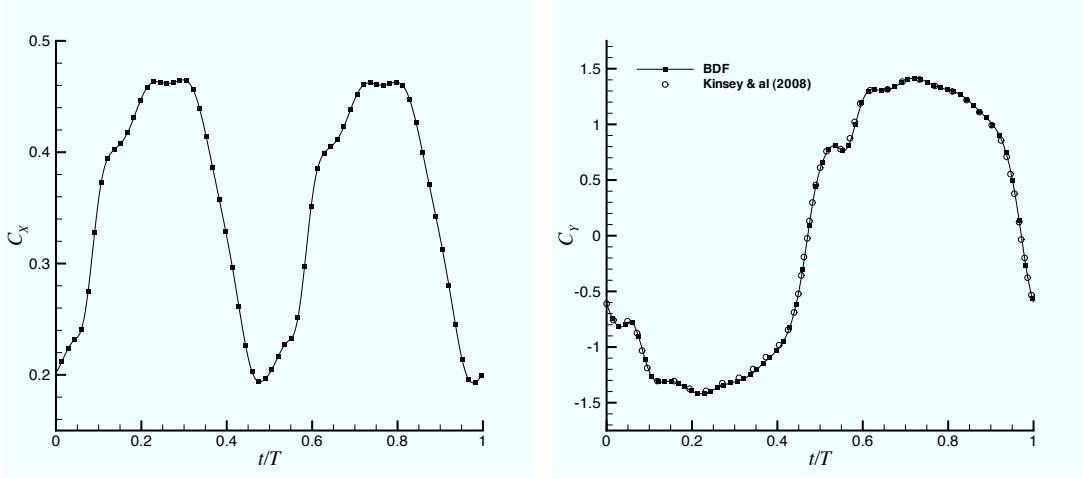

(a) (b)

Fig. 3 PP test case. (a): C_X evolution computed using the present BDF method. (b): C_Y evolution computed in [14] and using the present BDF method.

described and the necessary modifications to perform on the implicit treatment are detailed.

A. TSM discretization of the ALE-AC system

Taking advantage of the time periodicity of $\boldsymbol{w}$, the solution vector can be decomposed into a Fourier series

$$\boldsymbol{w} = \sum_{k=-\infty}^{+\infty} \widehat{\boldsymbol{w}_k}(x) e^{\underline{i}k\omega t} \tag{21}$$

where ω is the pulsation of the periodic phenomenon related to the period T by $\omega = 2\pi/T$. The complex number $\underline{i}$ is underlined to avoid confusion with the cell index i. In practice, the solution is represented with a finite number of harmonics N

$$\boldsymbol{w} = \sum_{k=-N}^{N} \widehat{\boldsymbol{w}_k}(x) e^{\underline{i}k\omega t} \tag{22}$$

The Nyquist-Shannon theorem [31] states that the k^{th} Fourier coefficient $\widehat{\boldsymbol{w}_k}$ with $-N \leq k \leq N$ can be accurately computed with $2N+1$ time instances evenly distributed over the time period

$$\widehat{\boldsymbol{w}_k}(x) = \frac{1}{2N+1} \sum_{n=0}^{2N} \boldsymbol{w}_n e^{-\underline{i}k\omega n \Delta t} \tag{23}$$

with $\boldsymbol{w}_n \equiv \boldsymbol{w}(t_n = n\Delta t)$ and $\Delta t = T/(2N+1)$. The main idea of the TSM [4] is then to look for these solutions $\boldsymbol{w}_n$ in order to retrieve the solution at any time t in the period using (22). The space-discretized ALE-AC system at time instance t_n reads :

$$\boldsymbol{K} \frac{\partial \boldsymbol{w}_n}{\partial t} + \mathcal{R}(\boldsymbol{w}_n, \boldsymbol{x}_n, \boldsymbol{s}_n) = 0 \tag{24}$$

where $\boldsymbol{w} = \{\boldsymbol{w}_i\}$ is the set of solution values in all the grid cells and $\mathcal{R} = \{\mathcal{R}_i\}$ is the set of residual values computed in all the grid cells, which depends non-linearly on $\boldsymbol{w}$. From now on, $\boldsymbol{w}_{i,n}$ will denote the solution at the grid point i and the n^{th} time instance t_n in the period. Using the Fourier decomposition (22) of $\boldsymbol{w}_n$ into equation (24) leads to $2N+1$ equations (one for each wavenumber) in the frequency domain

$$\boldsymbol{K} \sum_{k=-N}^{N} \underline{i}k\omega \widehat{\boldsymbol{w}_k} e^{\underline{i}k\omega n \Delta t} + \widehat{\mathcal{R}}(\widehat{\boldsymbol{w}_k}, \widehat{\boldsymbol{x}_k}, \widehat{\boldsymbol{s}_k}) = 0 \tag{25}$$

The operator $\widehat{\mathcal{R}}$ could be directly computed from $\widehat{\boldsymbol{w}_k}$ but, because of its non-linearity, this would involve complex series of convolution becoming massively time consuming [3]. Using equation (23) allows to cast system (25) back into the time domain and to retrieve the original residual vector $\mathcal{R}$

because of the bijective property of the Fourier transform

$$\boldsymbol{K} D_t(\boldsymbol{w}_n) + \mathcal{R}(\boldsymbol{w}_n, \boldsymbol{x}_n, \boldsymbol{s}_n) = 0 \tag{26}$$

where $D_t(\boldsymbol{w}_n)$ is the spectral derivative with respect to time which couples the time instances.The spectral time operator expressed in the time domain becomes

$$D_t(\boldsymbol{w}_n) = \sum_{p=-N}^{N} d_p \boldsymbol{w}_{n+p} \tag{27}$$

In equation (27) the subscript $n+p$ must be understood as expressed modulo $2N+1$ to get the corresponding positive subscript. For instance $\boldsymbol{w}_{-N} = \boldsymbol{w}_{N+1}$. The d_p coefficients are given by

$$d_p = \begin{cases} \frac{\pi}{T}(-1)^{(p+1)} \csc\left(\frac{\pi p}{2N+1}\right) & \text{if } p \neq 0 \\ \\ 0 & \text{if } p = 0 \end{cases} \tag{28}$$

Since the spectral time-derivative depends on the whole set of solutions $\boldsymbol{w}_{n+p}$ with p ranging from $-N$ to N, system (26) must be written for each time instance in the period

$$\boldsymbol{K} D_t(\boldsymbol{w}_n) + \mathcal{R}(\boldsymbol{w}_n, \boldsymbol{x}_n, \boldsymbol{s}_n) = 0, \quad 0 \leq n < 2N+1 \tag{29}$$

B. Resolution of the TSM-ALE-AC system

The non-linear system of equations (29) is iteratively solved through a dual time-marching strategy, that is looking for the steady-state with respect to τ of the following system

$$\frac{\partial \boldsymbol{w}_n}{\partial \tau} = -\mathcal{R}_n^t(\boldsymbol{w}, \boldsymbol{x}_n, \boldsymbol{s}_n), \quad 0 \leq n < 2N+1 \tag{30}$$

where the total residual is defined as $\mathcal{R}_n^t(\boldsymbol{w}) = K D_t(\boldsymbol{w}_n) + \mathcal{R}(\boldsymbol{w}_n, \boldsymbol{x}_n, \boldsymbol{s}_n)$ for the TSM approach. The $2N+1$ steady values $\boldsymbol{w}_n$ are coupled through the spectral approximation $D_t(\boldsymbol{w}_n)$ of the physical time derivative. Let us denote $\boldsymbol{w}_n^m$ the intermediate value of $\boldsymbol{w}_n$ at the m^{th} iteration of the dual-time evolution to a steady-state. Using a simple first-order Euler explicit discretization for the dual-time derivative, the steady-state is reached by iteratively solving

$$\frac{\Delta \boldsymbol{w}_n^m}{\Delta \tau_{i,n}^m} = -\mathcal{R}_n^t(\boldsymbol{w}^m, \boldsymbol{x}_n, \boldsymbol{s}_n), \quad 0 \leq n < 2N+1 \tag{31}$$

where $\Delta \boldsymbol{w}_n^m = \boldsymbol{w}_n^{m+1} - \boldsymbol{w}_n^m$ and $\Delta \tau_{i,n}^m$ is the local (dual) time-step in cell i of the grid associated with the time instance t_n within the period. Note that, in the present study, the $2N+1$ grid positions

and velocities are *a priori* known from the prescribed grid motion. In particular, the velocity $\boldsymbol{s}_n$ is calculated with equation (9) at time t_n. Adapting to the present AC system the stability analysis conducted in [5] for TSM compressible flow computations using an explicit formulation similar to (31) leads to the following CFL-like stability condition for the choice of $\Delta\tau_{i,n}^m$:

$$\Delta\tau_{i,n}^m = \mathrm{CFL}\frac{h_i}{||\lambda||_{i,n}^m + N\omega h_i} \tag{32}$$

with h_i a characteristic length of the cell i in the computational grid, $||\lambda||_{i,n}^m$ the spectral radius of the Jacobian matrix associated with the inviscid AC system at time instance t_n and CFL ≤ 1. Looking for the solution of a steady incompressible flow, the matrix K would be equal to zero and the above condition would not include the $N\omega h_i$ contribution. When the explicit TSM scheme is applied to obtain the solution of a periodic incompressible flow with either a high frequency ($\omega >> 1$) and/or a high number N of harmonics, condition (32) can become particularly restrictive. Using an Euler implicit dual-time integration for integrating (30) in each grid cell i at each time instance t_n allows the use of large dual-time steps, hence fast convergence to a steady-state independently of ω or N, but the following implicit non-linear TSM-ALE-AC problem must be solved:

$$\frac{\Delta\boldsymbol{w}_{i,n}^m}{\Delta\tau_{i,n}^m} = -\mathcal{R}_{i,n}^t(\boldsymbol{w}^{m+1}, \boldsymbol{x}_n, \boldsymbol{s}_n), \quad 0 \leq n < 2N+1 \tag{33}$$

C. Implicit time spectral method: PJ-TSM-ALE-AC system

The full TSM residual is defined by $\mathcal{R}^t(\boldsymbol{w}) = \boldsymbol{K}D_t(\boldsymbol{w}) + \mathcal{R}(\boldsymbol{w})$ with the spectral difference operator D_t linear and the spatial discretization operator $\mathcal{R}$ formally unchanged with respect to the BDF approach. Following a line of work similar to that described for the BDF approach, the TSM residual at dual time-level $m+1$ can be approximated as follows

$$\mathcal{R}_{i,n}^t\left(\boldsymbol{w}^{m+1}\right) = \mathcal{R}_{i,n}^t\left(\boldsymbol{w}^m\right) + \boldsymbol{K}D_t(\Delta\boldsymbol{w}_{i,n}^m) + \frac{1}{|\Omega_i|}\sum_k \left(\Delta\mathcal{H}_{(i,k),n}^{(i)}\right)^m \ |\Gamma_{i,k}| \tag{34}$$

where the flux increment balance $\Delta\mathcal{H}^{(i)}$ is computed using the formulae (15) and (16) previously introduced when deriving the BDF implicit stage but now applied with the variable increment $\Delta\boldsymbol{w}_{i,n}^m$ instead of $\Delta\boldsymbol{w}_i^{n,m}$. Expanding this flux increment balance and the spectral approximation of the physical time derivative with (27) (28) leads to the following implicit relationship, where the terms

depending on $\Delta \boldsymbol{w}_{i,n}^m$ have been gathered in the Left Hand Side (LHS)

$$\left(\frac{1}{\Delta\tau_{i,n}^m}+\sum_k C_{(i,k),n}^m\right)\Delta\boldsymbol{w}_{i,n}^m \;=\; -\mathcal{R}_{i,n}^t(\boldsymbol{w}^m)-\frac{1}{2|\,\Omega_{i,n}|}\sum_k\left(\Delta\boldsymbol{F}_{o(i,k),n}^E\right)^m\cdot\boldsymbol{n}_{(i,k),n}\;|\Gamma_{(i,k),n}| \\ +\sum_k C_{(i,k),n}^m\Delta\boldsymbol{w}_{(o(i,k)),n}^m-\boldsymbol{K}\sum_{p=-N}^{N}d_p\Delta\boldsymbol{w}_{i,n+p}^m \tag{35}$$

with the scalar coefficients $C_{(i,k),n}^m$ defined by:

$$C_{(i,k)n}^m=\frac{1}{|\Omega_{i,n}|}\left(\frac{1}{2}\rho(\boldsymbol{J}_\perp^E)+\rho(\widetilde{\boldsymbol{J}_\perp^V})\right)_{(i,k),n}^m|\Gamma_{(i,k),n}| \tag{36}$$

and $d_0=0$ in the spectral time-derivative so that there is no contribution of this term to the above LHS. Following the strategy adopted to solve the BDF-ALE-AC system, a Point-Jacobi strategy could be applied to obtain an iterative solution of the above TSM-ALE-AC system. However, a significant difference arises when going from the BDF to the TSM system: while the BDF formula strengthens the diagonal dominance of the linear system associated with the implicit stage, the TSM formula introduces only off-diagonal terms which lead to a loss of diagonal dominance. This issue was pointed out by Su and Yuan in [8] and the problem was then fixed by using the GMRES solver of Saad and Schultz [32] to solve the implicit TSM system. Woodgate and Badcock [7] also highlight the performance reduction of their Krylov linear solver due to the loss of diagonal dominance for the matrix of the implicit system. In the present work, a simple fix is adopted: the LHS coefficient of $\Delta\boldsymbol{w}_{i,n}^m$ in (35) is modified to include the contribution $\boldsymbol{K}\sum_{p=-N}^{p=N}|d_p|$, which is sufficient to ensure the diagonal dominance of the implicit stage with only a limited impact on its efficiency. System (35) is then iteratively solved using a simple PJ relaxation technique, yielding the following PJ-TSM-ALE-AC system:

$$\begin{cases}\Delta\boldsymbol{w}_{i,n}^{(0)}=0\\ \\ \left\{\begin{array}{l} l=0,\;l_{max}-1\\ \\ \Delta\boldsymbol{w}_{i,n}^{(l+1)}=\left(\boldsymbol{D}_{i,n}^m\right)^{-1}\\ \left(-\mathcal{R}_{i,n}^t(\boldsymbol{w}^m)-\dfrac{1}{2|\,\Omega_{i,n}|}\displaystyle\sum_k\left(\Delta\boldsymbol{F}_{o(i,k),n}^E\right)^{(l)}\cdot\boldsymbol{n}_{(i,k),n}\;|\Gamma_{(i,k),n}|+\sum_k C_{(i,k),n}^m\Delta\boldsymbol{w}_{(o(i,k)),n}^{(l)}-\boldsymbol{K}\sum_{p=-N}^{N}d_p\Delta\boldsymbol{w}_{i,n+p}^{(l)}\right)\end{array}\right.\\ \\ \boldsymbol{w}_{i,n}^{m+1}=\boldsymbol{w}_{i,n}^m+\Delta\boldsymbol{w}_{i,n}^{(l_{max})}\end{cases} \tag{37}$$

with the modified diagonal coefficient $\boldsymbol{D}_{i,n}^m = \dfrac{1}{\Delta\tau_{i,n}^m} + \sum_k C_{(i,k),n}^m + \boldsymbol{K} \sum_{p=-N}^{N} |d_p|$.

IV. Assessment of TSM against BDF

The above PJ-TSM-ALE-AC method is now applied to the computation of the test-problems PH and PP and its results are compared to those obtained using the PJ-BDF-ALE-AC approach. To the best of our knowledge, the only previous application of TSM to the AC system for incompressible laminar periodic flow has been performed by Jameson [13], but with a limited success since stability concerns were encountered for high frequency and/or large number of harmonics. In the present study, the convergence of TSM to a steady-state will be first analyzed when the number of harmonics N is varied for accuracy purpose. The reference BDF strategy and the newly developed TSM approach will then be discussed in terms of accuracy: in particular, the number of modes needed to achieve a sufficient level of accuracy will be investigated for test-problems PH and PP. The potential efficiency gain offered by TSM with respect to BDF will be finally assessed.

A. Convergence of the TSM approach

The convergence of (37) to a steady-state is monitored by plotting the pressure residual defined as the root mean square of the residual operator $\mathcal{R}^t(\boldsymbol{w})$ first component, computed in all the grid cells and averaged by the number of time instances over the period:

$$res_{av}^m = \frac{1}{2N+1} \sum_{n=0}^{2N} \sqrt{\frac{1}{N_{cell}} \sum_{i=1}^{N_{cell}} \frac{\Delta p_{i,n}^{m\ 2}}{\Delta \tau_{i,n}^{m\ 2}}}$$

This quantity is normalized by its value at the first iteration to facilitate the comparison between calculations performed with different values for the number of harmonics N. All the computations make use of $l_{max} = 16$ for the implicit PJ solver and CFL $= 10^6$ for computing the dual-time step $\Delta\tau_{i,n}^m$ with (32). The AC parameter β is the same as in the previous BDF calculations ($\beta = 5$).

The convergence histories displayed in Fig. 4 demonstrate the convergence rate of the TSM solver to a steady-state depends only weakly on the number of harmonics N: for test-case PH, less than 4000 iterations are needed to achieve a residual decrease by four orders of magnitude while a bit less than 3000 iterations are sufficient for test-case PP, whatever the value of N. The cost of an

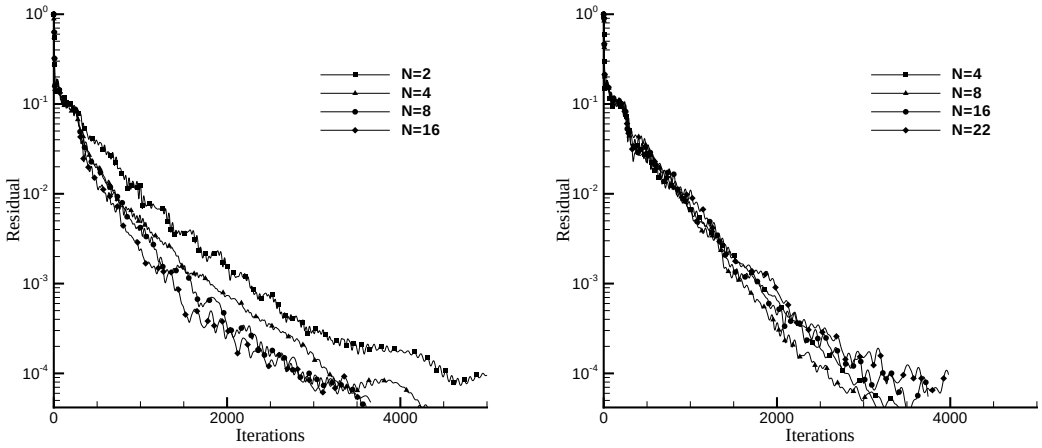

(a) (b)

Fig. 4 Convergence history for the PJ-TSM-ALE-AC method. (a): PH test problem with increasing number of harmonics (N ranging from 2 to 16). (b): PP test problem with increasing number of harmonics (N ranging from 4 to 22).

iteration depends of course on the value of N but this point will be discussed at the end of the section after analyzing the accuracy of the TSM solutions.

B. Accuracy of the TSM solutions

The accuracy of the TSM solutions will be first assessed in a qualitative way by comparing the steady solutions of the PJ-TSM-ALE-AC system obtained for an increasing number of harmonics with the previously computed BDF solution. This comparison will be performed on the evolution of the global force coefficients C_X, C_Y over a cycle both for the PH and PP test-problems. Next the computed wall pressure distribution over the airfoil and pressure contours at selected instants within the period will also be compared. A more quantitative error analysis between TSM and BDF will be eventually proposed and conclusions regarding the potential efficiency gain offered by TSM with respect to BDF will be drawn.

1. Global aerodynamic coefficients

Figures 5 and 6 display the C_X and C_Y coefficients computed using the TSM approach with an increasing number of harmonics for the PH and PP flow problems respectively. These evolutions

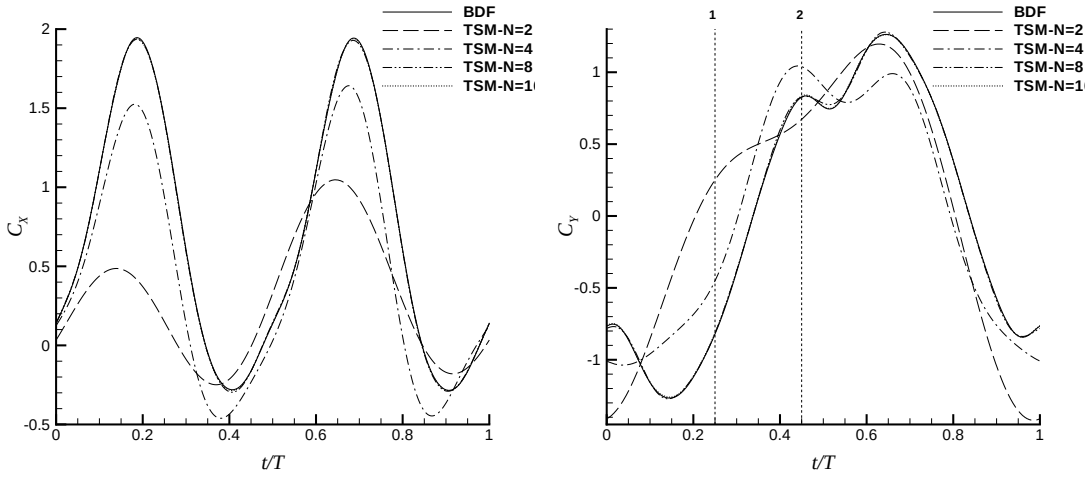

(a) (b)

Fig. 5 PH test-case. Comparison of the C_X (a) and C_Y (b) coefficients computed using BDF and TSM with an increasing number of harmonics.

over a period are plotted along the previously computed BDF results, whose accuracy was checked with respect to [14]. Let us recall the BDF computations use 520 physical times-steps per period and require about 4 (resp. 6) cycles before reaching a periodic solution for the PH (resp. PP) flow problem. The TSM evolutions are reconstructed from the computed $\boldsymbol{w}_n$ fields for any time in the period using the truncated Fourier series representation of the flow solution. For the PH test-problem, the computed evolution using TSM with $N = 2$ and $N = 4$ significantly differs from the reference result; very small differences between the BDF and TSM evolution remain with $N = 8$ but both evolutions appear superimposed with $N = 16$. For the PP test-problem, the computed evolution of C_X and C_Y using TSM with $N = 4$ and $N = 8$ display significant differences with the reference result; with $N = 16$ there are still some very small discrepancies while with $N = 22$ the BDF and TSM results appear as superimposed.

2. Wall pressure distributions and pressure fields

Two moments within the period are retained for a closer comparison of the computed flow fields: $t/T = 0.25$ and $t/T = 0.45$. For each of these moments, the wall pressure coefficient distribution obtained by using BDF and TSM(N) is plotted, respectively in Fig. 7 and 9 for test-problem PH. Let us recall these pressure distributions are reconstructed at each grid point i from the computed

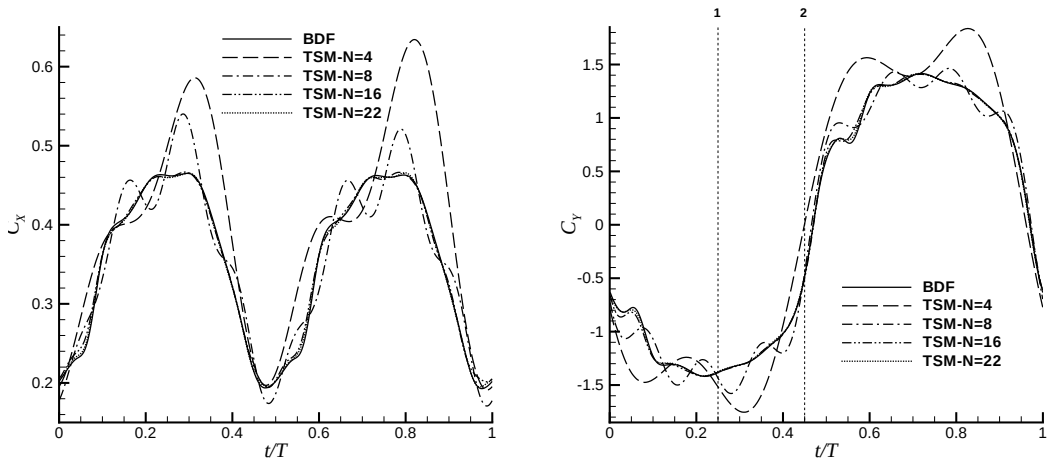

(a) (b)

Fig. 6 PP test-case. Comparison of the C_X (a) and C_Y (b) coefficients computed using BDF and TSM with an increasing number of harmonics.

$\boldsymbol{w}_{i,n}$ values, applying formulae (22) and (23) in each grid cell. For the PH computation, the already very good agreement between BDF and TSM(8) and the almost perfect match between BDF and TSM(16) wall distributions are clearly visible; this similarity is confirmed on the pressure contours displayed in Fig. 11. For test-problem PP, the wall pressure coefficient distribution obtained by using BDF and TSM(N) is plotted, respectively in Fig. 8 and 10. The match is already very good with $N = 16$ and almost perfect when $N = 22$; this similarity is confirmed on the pressure contours displayed in Fig. 12.

3. Quantitative error analysis

The RMS error on the C_X force coefficient is defined as:

$$\epsilon_{RMS}(C_X) = \sqrt{\frac{1}{N_{\Delta t}} \sum_{k=1}^{N_{\Delta t}} \left(\frac{(C_X)_{TSM(N)}(t_k) - (C_X)_{BDF}(t_k)}{(\Delta C_X)_{BDF}} \right)^2}$$

where the values of the C_X coefficients at times t_k in the flow cycle and the amplitude ΔC_X of the C_X variation are readily available for the BDF computation while the values of C_X corresponding to the TSM computation are obtained by reconstruction of the flow solution using a truncation Fourier series with N harmonics. The RMS error on the C_Y force coefficient is similarly defined. These errors are plotted as a function of N in Fig. 13 to conclude on the best choice of N: the

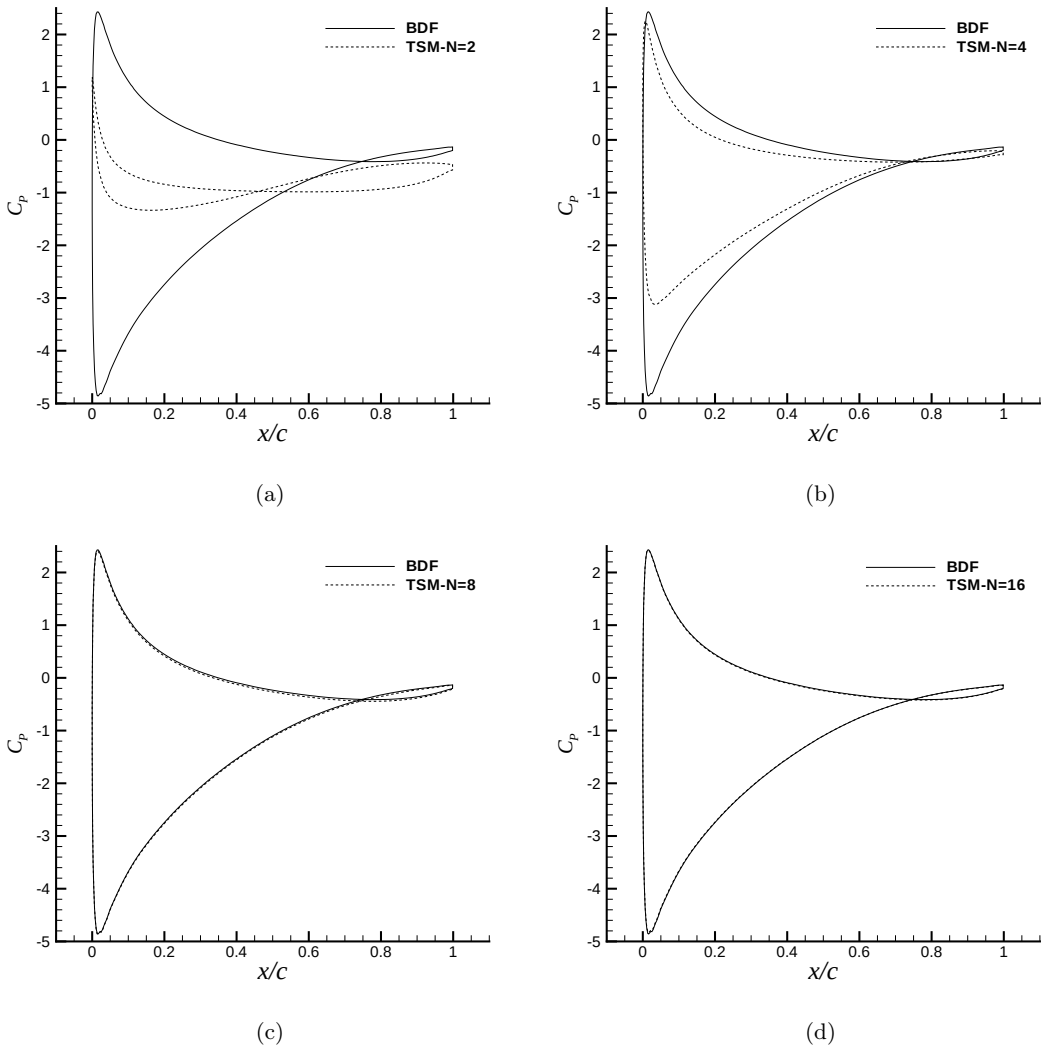

Fig. 7 Flow problem PH. Reconstructed TSM(N) wall pressure coefficient at time $t/T = 0.25$ for an increasing number N of harmonics. Comparison with the reference BDF distribution.

number of harmonics must indeed be taken large enough to ensure the computed TSM solution is sufficiently accurate with respect to the usual BDF solution but not unnecessarily large since the gain expected from the TSM approach with respect to the BDF strategy is a cost reduction rather than an increased accuracy. Consistently with the previous graphical comparisons between BDF and TSM solutions, the error levels achieved on test problem PH for a given number of harmonics are much lower than the errors levels obtained on test problem PP. For test-case PH, the RMS error on C_X and C_Y drops below the 1% level for $N = 8$ while $N = 16$ is needed to fulfill this same criterion for test-case PP.

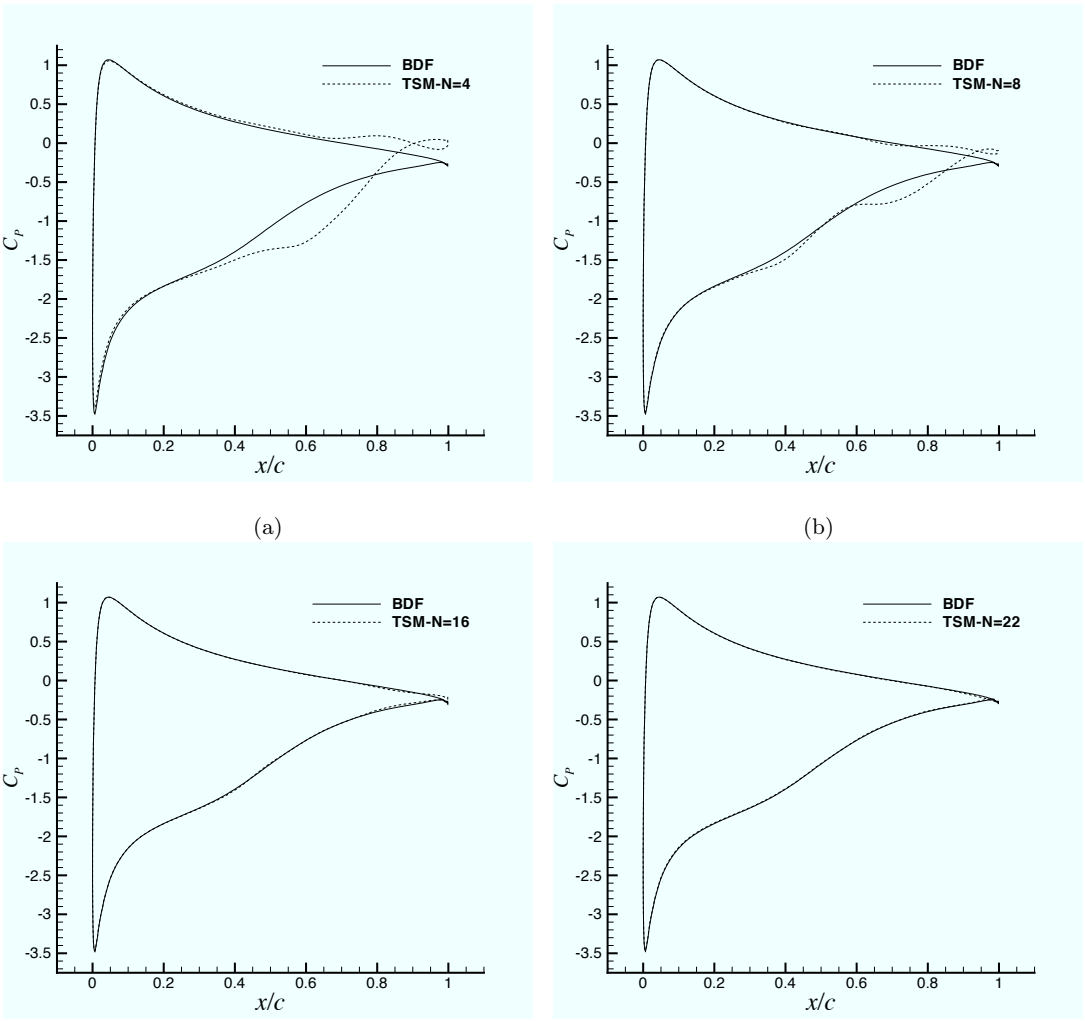

(a) (b)

(c) (d)

Fig. 8 Flow problem PP. Reconstructed TSM(N) wall pressure coefficient at time $t/T = 0.25$ for an increasing number N of harmonics. Comparison with the reference BDF distribution.

C. Efficiency of the TSM approach

The global computational cost of the usual BDF approach can be expressed as:

$$\mathcal{C}_{BDF} = N_{\Delta t} \times N_{cycles} \times m_{max}^{BDF} \times l_{max} \times N_{cells} \times c_u^{BDF}$$

where $N_{\Delta t}$ is the number of physical time-steps used to describe a flow period or cycle, N_{cycles} is the number of cycles to be computed before a periodic solution is actually reached, m_{max}^{BDF} is the number of dual sub-iterations used at each physical time-step to reach the dual steady-state, l_{max} is the number of iterations used with the PJ relaxation method, N_{cells} is the grid size and c_u^{BDF} is

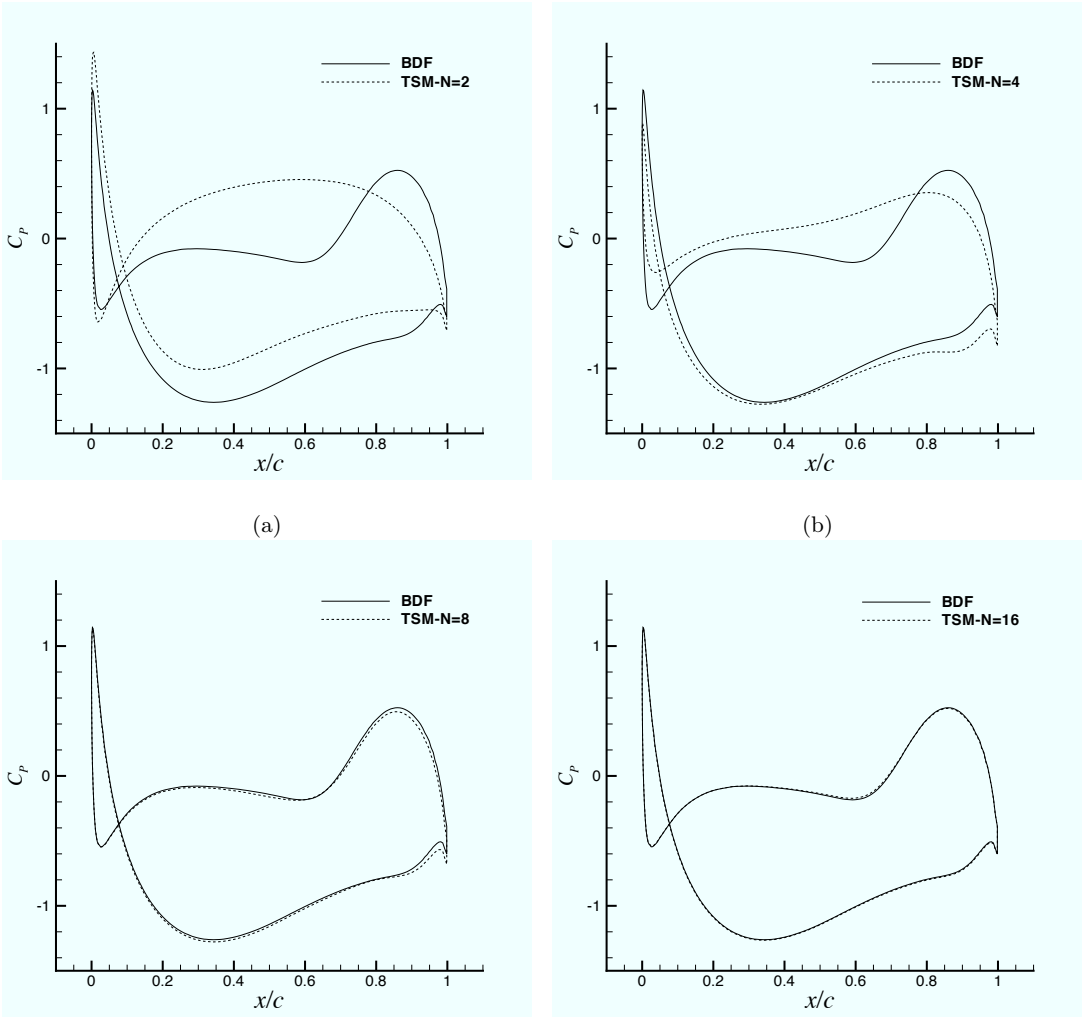

Fig. 9 Flow problem PH. Reconstructed TSM(N) wall pressure coefficient at time $t/T = 0.45$ for an increasing number N of harmonics. Comparison with the reference BDF distribution.

the unit cost (per point and per iteration) of the PJ-BDF-ALE-AC method.

Meanwhile, the global computational cost of the newly proposed TSM approach is expressed as:

$$\mathcal{C}_{TSM(N)} = (2N+1) \times m_{max}^{TSM(N)} \times l_{max} \times N_{cells} \times c_u^{TSM}(N)$$

where $(2N+1)$ is the number of time-instances retained to describe the flow period, m_{max}^{TSM} is the number of iterations on the dual time needed to drive the PJ-TSM-ALE-AC system to a steady-state , l_{max} is the number of iterations used with the PJ relaxation method, N_{cells} is the grid size and $c_u^{TSM(N)}$ is the unit cost (per point and per iteration) of this PJ-TSM-ALE-AC method.

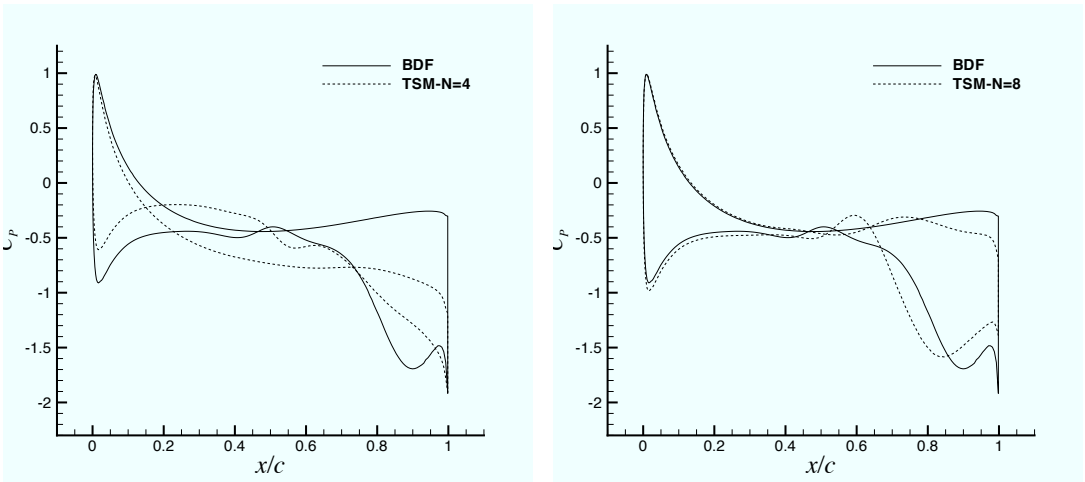

(a) (b)

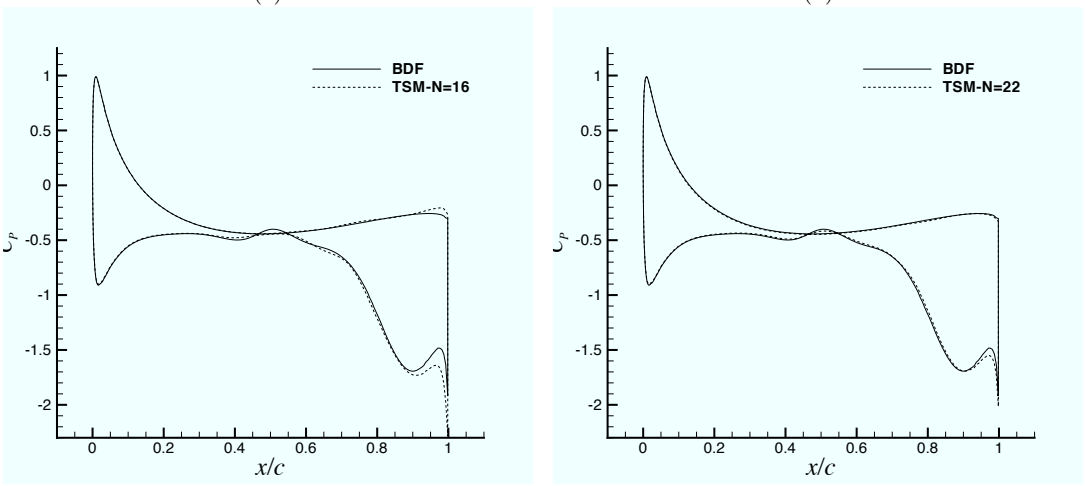

(c) (d)

Fig. 10 Flow problem PP. Reconstructed TSM(N) wall pressure coefficient at time $t/T = 0.45$ for an increasing number N of harmonics. Comparison with the reference BDF distribution.

Since l_{max} is the same for BDF and TSM, the cost ratio between TSM(N) and BDF used with the same computational grid reads:

$$\eta = \frac{\mathcal{C}_{TSM(N)}}{\mathcal{C}_{BDF}} = \underbrace{\frac{(2N+1)}{N_{\Delta t} \times N_{cycles}} \times \frac{m_{max}^{TSM(N)}}{m_{max}^{BDF}}}_{\Phi_1} \times \underbrace{\frac{c_u^{TSM(N)}}{c_u^{BDF}}}_{\Phi_2}$$

where, for the given flow solver described and used in this work, the contribution Φ_1 depends on the flow problem only while the contribution Φ_2, ratio of the unit costs associated with the TSM(N) and BDF methods, depends on the numerical implementation of these methods into the computer code in use. In the present study, the same number $N_{\Delta t} = 520$ of physical time-steps per cycle has

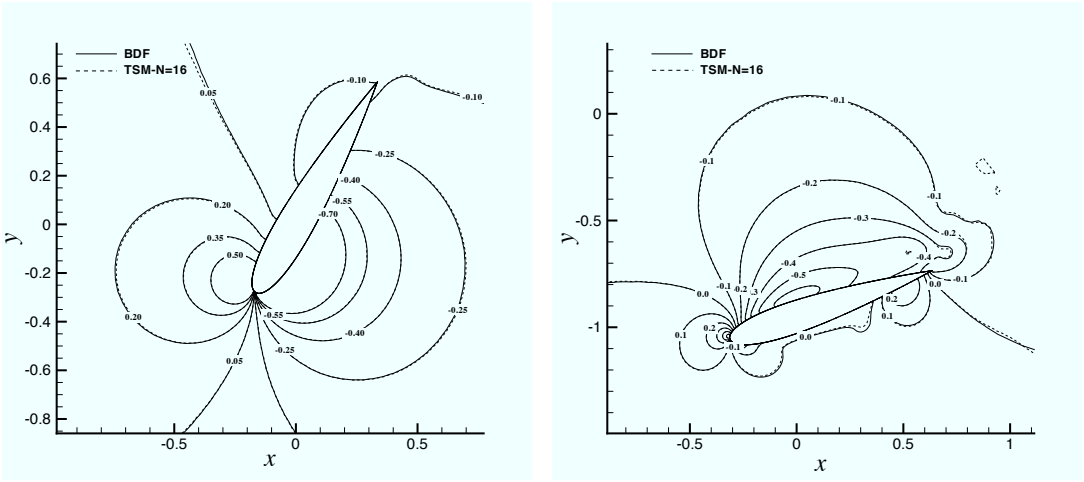

(a) (b)

Fig. 11 Flow problem PH. Reconstructed TSM pressure field ($N = 16$) at time $t/T = 0.25$ (a) and $t/T = 0.45$ (b).

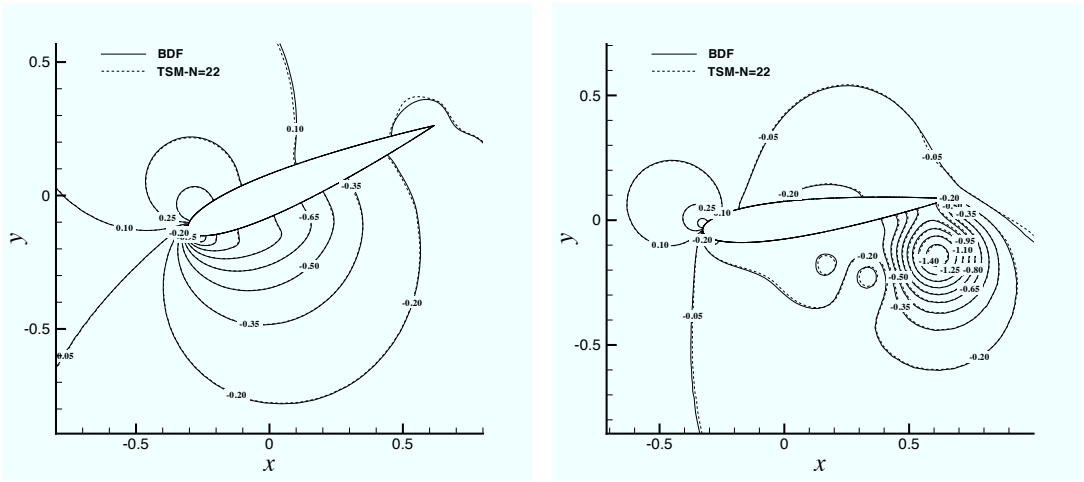

(a) (b)

Fig. 12 Flow problem PP. Reconstructed TSM pressure field ($N = 22$) at times $t/T = 0.25$ (a) and $t/T = 0.45$ (b).

been used for PH and PP as well as the same number of dual sub-iterations $m_{max}^{BDF} = 100$. As far as global cost is concerned, and regardless of the accuracy issue for the time being, the PH and PP test-cases differ by the number of cycles needed to achieve fully periodic flow ($N_{cycles}^{PH} = 6$ while $N_{cycles}^{PP} = 4$) and the typical number $m_{max}^{TSM(N)}$ of iterations on τ needed to achieve a steady-state for the TSM computations. This number is roughly $m_{max}^{TSM(N)} \approx 3300$ for PH and $m_{max}^{TSM(N)} \approx 2800$

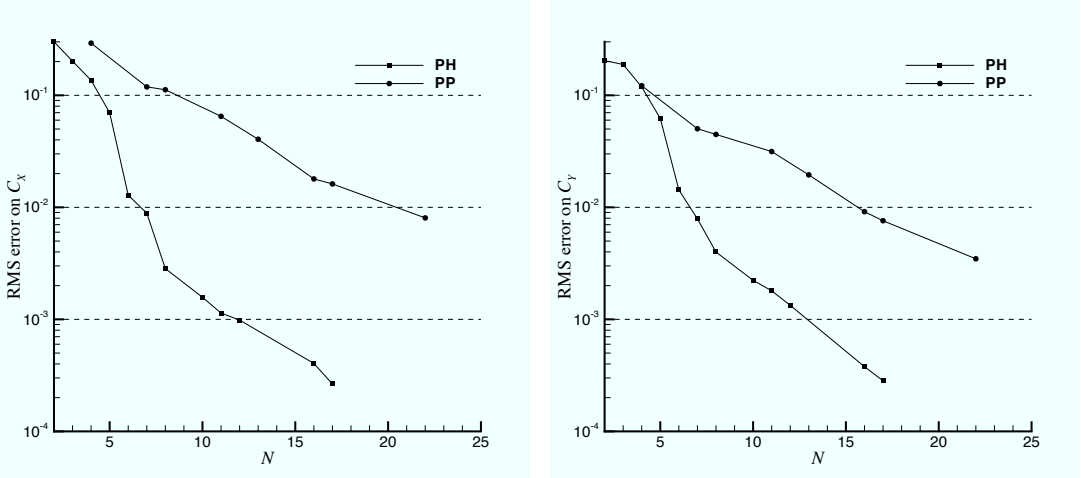

(a) (b)

Fig. 13 Root mean square error of the normalized difference between the C_X (a) and C_Y (b) coefficients computed using the reference BDF strategy with $N_{\Delta t} = 520$ iterations per cycle and the TSM(N) strategy with increasing N.

for PP, whatever the number of harmonics N (see Fig. 4). Consequently, the global cost ratio for TSM and BDF strategies is given, for test-case PH, by

$$\eta^{PH} = \Phi_1^{PH}(N) \times \Phi_2(N) = (0.010577 \times (2N+1)) \times \Phi_2(N) \tag{38}$$

and for test-case PP by

$$\eta^{PP} = \Phi_1^{PP}(N) \times \Phi_2(N) = (0.01346 \times (2N+1)) \times \Phi_2(N) \tag{39}$$

The unit cost ratio between the TSM approach and the BDF method should display a weak dependency only on the number N of harmonics, on one hand through the extra terms introduced by the spectral time approximation and on the other hand through the extra-cost that might be induced by the memory access associated with the large-scale TSM systems which couple $2N+1$ systems of conservation laws. Ideally, with no memory issues, one would expect $\Phi_2(N)$ to remain close to unity whatever the value of N. In practice, the ratio of the TSM(N) and BDF unit costs has been numerically estimated as a linear function of N (which is implementation-dependent)

$$\Phi_2(N) \approx 0.8208 + 0.0925 \times N \tag{40}$$

Fig. 14 displays the evolution of the global cost ratio for PH and PP, given respectively by (38)

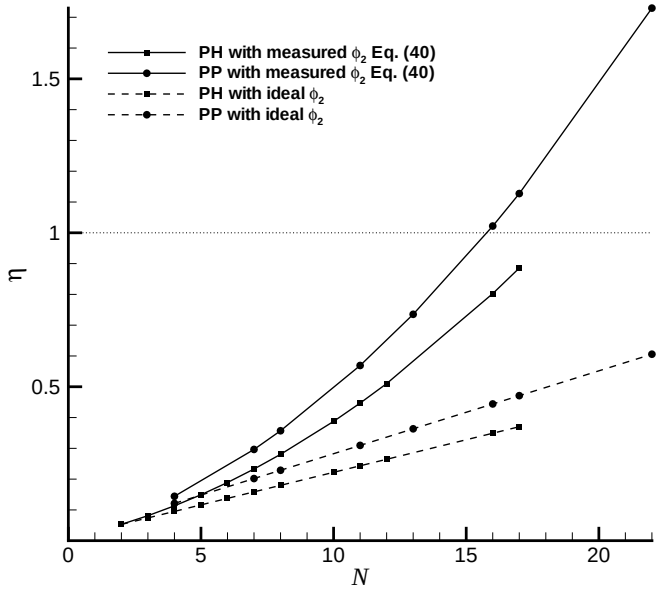

Fig. 14 Evolution of the global cost ratio $\eta = \mathcal{C}_{TSM(N)}/\mathcal{C}_{BDF}$ between TSM(N) and BDF with an increasing number N of harmonics for TSM(N). Solid lines: measured cost ratio for the PH and PP test-cases. Dashed lines: ideal cost ratio with a TSM(N) implementation of unit cost Φ_2 roughly equal to the unit cost of the BDF approach.

and (39), with the measured unit cost ratio $\Phi_2(N)$ given by (40), in which case η^{PH} and η^{PP} vary quadratically with N, or with an ideal unit cost ratio roughly equal to 1, in which case the variation of η^{PH} and η^{PP} remains linear with respect to N. Though ideal, this latter case provides an upper limit for the number of harmonics N that might be used by the TSM approach before its computational cost exceeds that of the BDF approach. It can be observed in Fig. 14 that the measured value of η^{PP} reaches 1 for $N = 16$ while η^{PH} remains below 0.8 for this same number of harmonics. With an improved implementation allowing to reduce the growth of the unit cost ratio Φ_2 with N, the global cost ratio η could remain below 0.5 for $N = 16$.

The key point of the present efficiency analysis is reached when crossing the evolution of $\eta(N)$ given by Fig. 14 with the accuracy assessment summarized on the RMS-errors for C_X and C_Y plotted in Fig. 13. The RMS-errors on these aerodynamic coefficients are plotted against the global efficiency ratio η in Fig. 15: the solid lines correspond to the measured evolution of η^{PH} and η^{PP} while the dashed lines correspond to the ideal evolution where the unit cost ratio Φ_2 would remain roughly

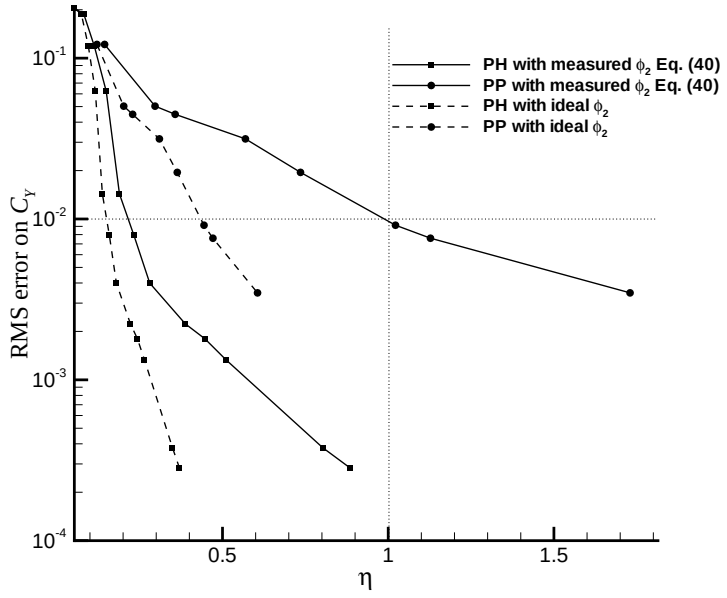

Fig. 15 Evolution of the root mean square error on C_Y as a function of the global cost ratio $\eta = \frac{\mathcal{C}_{TSM(N)}}{\mathcal{C}_{BDF}}$ for test-problems PH and PP. Solid lines: measured cost ratio. Dashed lines: ideal cost ratio with a TSM(N) implementation of unit cost Φ_2 roughly equal to the unit cost of the BDF approach.

equal to 1. From the previously performed accuracy analysis, the BDF and reconstructed TSM solutions were found to be almost coincident when the normalized RMS error on C_Y dropped below 1%, corresponding to a number of harmonics $N = 8$ for the PH case and $N = 16$ for the PP case. Retaining this same criterion, it can be observed in Fig. 15 the TSM approach provides a solution as accurate as the conventional BDF strategy for an overall cost divided by 5 when computing the PH case; meanwhile, for the PP case, the larger number of harmonics needed by the TSM approach to provide the same level of accuracy as BDF does not allow to reduce the CPU cost, with $\eta^{PP} \approx 1$ for $N = 16$. An improved implementation of the TSM approach could make the method attractive even for the PP test-case, with an ideal computational cost ratio that could go down to 0.5 for $N = 16$ in that case. The analysis of the TSM efficiency has been focused on the achievable CPU gain using the steady computation of a reduced number of modes within a flow period instead of a full unsteady computation over several cycles. It must be pointed out however the TSM method is also more demanding memory-wise than the BDF strategy since it requires to store $(2N+1) \times N_{cells}$

unknown states at each step of the steady-state convergence process against N_{cells} unknown states for the BDF method at each step of the time-marching process.

V. Conclusion

The TSM method has been successfully applied to the computation of periodic incompressible flows over airfoils using an artificial compressibility formulation within an ALE framework on general unstructured grids. As pointed out by previous authors [6–8], the implicit treatment of the large scale TSM system, coupling $(2N+1)$ systems of conservation laws with N the number of harmonics retained to describe the periodic flows under study, is crucial to ensure the efficiency of the TSM method with respect to a conventional BDF formula. In the present work, an implicit formulation of the TSM method has been derived from a simple matrix-free treatment previously developed in the context of compressible flows and readily applicable to the AC system. Special care has been taken to ensure the diagonal dominance property of the TSM implicit stage, with a simple modification of the diagonal contribution which does not significantly affect the convergence of the implicit solver to a steady-state. A basic point-relaxation technique has been retained to solve the linear system associated implicit TSM scheme for a very low cost per iteration which makes up for the reduced intrinsic efficiency of the method (a few thousand inexpensive iterations are needed to achieve steady-state). The computation of low-Reynolds periodic flow over a pitching and heaving NACA0015 airfoil has demonstrated that between $N = 8$ and $N = 16$ harmonics are required by the TSM method to accurately represent these two-dimensional unsteady flows. This coarse representation of the flow cycle offered by the spectral formula used for discretizing the physical time-derivative combined with an efficient solution of the steady solution for the TSM system coupling the $(2N+1)$ selected unknown fields within a flow period has allowed a substantial gain of CPU time for the computed pitching and heaving test-case over a NACA0015 airfoil: a level of accuracy on the flow solution over a period comparable to that offered by a conventional BDF time-integration was achieved using an overall CPU time divided by a factor five. Note however no reduction was observed using TSM(N) for the pure pitching test-case at a lower reduced frequency because twice as many harmonics (16 instead of 8) were needed in that case to achieve an accuracy

level similar to that of the BDF approach. In order to make the TSM approach computationally attractive even when a rather large number of modes are required to achieve a sufficient level of accuracy, ongoing work is devoted on one hand to the optimal implementation of the method so as to reduce as much as possible the growth of the unit cost ratio Φ_2 when N increases and on the other hand to the efficiency improvement of the implicit solver with respect to the PJ method used in the present study in order to potentially reduce both Φ_1 and Φ_2. Efficient relaxation strategies proposed for instance in [33] will be investigated in this perspective. Our current research is also focused on strategies allowing an automatic determination of the number of harmonics to be used with the TSM approach for ensuring a prescribed accuracy level.

References

[1] Peyret, R., and Taylor, T. D., *Computational Methods in Fluid Flow*, 2nd ed., Springer-Verlag, New York, 1983.

[2] Jameson, A., "Time-Dependent Calculations using Multigrid with Applications to Unsteady Flows Past Airfoils and Wings," *10th AIAA Computational Fluid Dynamics Conference*, AIAA Paper 91-1596, Jun. 1991.

[3] Hall, K. C., Thomas, J. P., and Clark, W. S., "Computation of Unsteady Nonlinear Flows in Cascades using a Harmonic Balance Technique," *AIAA Journal*, Vol. 40, No. 5, 2002, pp. 87–886.

[4] Gopinath, A., and Jameson, A.,"Time Spectral Method for Periodic Unsteady Computations Over Two-and Three-Dimensional Bodies," *43rd AIAA Aerospace Sciences Meeting and Exhibit*, AIAA Paper 2005-1220, Jan. 2005.

[5] van der Weide, E., Gopinath, A., and Jameson, A., "Turbomachinery Applications with the Time Spectral Method," *35th AIAA Fluid Dynamics Conference and Exhibit*, AIAA Paper 2005-4905, June 2005.

[6] Sicot, F., Puigt, G., and Montagnac, M., "Block-Jacobi Implicit Algorithms for the Time Spectral Method," *AIAA Journal*, Vol. 46, No. 12, 2008, pp. 3080–3089.

[7] Woodgate, M. A., and Badcock, K. J., "Implicit Harmonic Balance Solver for Transonic Flow with Forced Motions," *AIAA Journal*, Vol. 47, No. 4, 2009, pp. 893–901.

[8] Su, X., and Yuan, X., "Implicit Solution of Time Spectral Method for Periodic Unsteady Flows," *International Journal for Numerical Methods in Fluids*, Jan 2009. doi: 10.1002/fld.2111

[9] Ekici, K., and Hall, K. C., "Nonlinear Analysis of Unsteady Flows in Multistage Turbomachines Using Harmonic Balance," *AIAA Journal*, Vol. 45, No. 5, 2007, pp. 1047, 1057.

[10] Butsuntorn, N., and Jameson, A., "Time Spectral Method for Rotorcraft Flow," *46th AIAA Aerospace Sciences Meeting and Exhibit*, AIAA Paper 2008-403, Jan. 2008.

[11] Antheaume, S., Maître, T., and Achard, J.-L., "Hydraulic Darrieus Turbines Efficiency for Free Fluid Flow Conditions Versus Power Farms Conditions," *Renewable Energy*, Vol. 33, 2008, pp. 2186–2198.

[12] Amet, E., Maître, T., Pellone, C., and Achard, J.-L., "2D Numerical Simulations of Blade-Vortex Interaction in a Darrieus Turbine," *Journal of fluids engineering*, Vol. 131, 2009.

[13] Jameson, A., "An Assessment of Dual-Time Stepping, Time Spectral and Artificial Compressibility Based Numerical Algorithms for Unsteady Flow with Applications to Flapping Wings," *19th AIAA Computational Fluid Dynamics*, AIAA Paper 2009-4273, Jun. 2009.

[14] Kinsey, T., and Dumas., G., "Parametric Study of an Oscillating Airfoil in a Power-Extraction Regime," *AIAA Journal*, Vol. 46, No. 6, 2008, pp. 1318–1330.

[15] Kloczko, T., Corre, C., and Beccantini, A., "Low-Cost Implicit Schemes for All-Speed Flows on Unstructured Meshes," *International Journal for Numerical Methods in Fluids*, 2008. doi: 10.1002/fld.1730

[16] Chorin, A. J., "A Numerical Method for Solving Incompressible Viscous Flow Problems," *Journal of Computational Physics*, Vol. 2, 1967, pp. 12–26.

[17] Roe, P. L., "Approximate Riemann Solvers, Parameter Vectors, and Difference Schemes," *Journal of Computational Physics*, Vol. 43, 1981, pp. 357–372.

[18] Barth, T. J., and Jespersen, D. C., "The Design and Application of Upwind Schemes on Unstructured Meshes," *27th AIAA Aerospace Sciences Meeting*, AIAA Paper 89-0366, Jan. 1989.

[19] Delanaye, M., "Polynomial Reconstruction Finite Volume Schemes for the Compressible Euler and Navier-Stokes Equations on Unstructured Adaptive Grids," PhD thesis, 1996, Université de Liège.

[20] Taylor, L. K., and Whitfield, D. L., "Unsteady Three-Dimensional Incompressible Euler and Navier-Stokes Solver for Stationary and Dynamic Grids," *22nd AIAA Fluid Dynamics, Plasma Dynamics and Lasers Conference*, June 1991.

[21] Noh, W., "Cel: A Time-Dependant Two-Space Dimensional Coupled Eulerian-Lagrangian Code," *Methods in Computational Physics*, Vol. 3, 1964, pp. 117–119.

[22] Nakahashi, K., and Deiwert, G. S., "Self Adaptive Grid Method with Application to Airfoil Flow," *AIAA Journal*, Vol. 25, Issue 4, 1987, pp. 513–520.

[23] Batina, J. T., "Unsteady Euler Algorithm with Unstructured Dynamic Mesh for Complex-Aircraft Aerodynamic Analysis," *AIAA Journal*, Vol. 29, No. 3, 1991, pp. 327–333.

[24] Luo, H., Baum, J. D., and Lohner, R., "An Accurate, Fast, Matrix-Free Implicit Method for Computing Unsteady Flows on Unstructured Grids," *Computers and Fluids*, Vol. 30, 2001, pp. 137–159.

[25] Hassan, O., Sørensen, K. A., Morgan, K., and Weatherill, N. P., "A Method for Time Accurate Turbulent Compressible Fluid Flow Simulation with Moving Boundary Components Employing Local Remeshing," *International Journal for Numerical Methods in Fluids*, Vol. 53, Issue 8, 2007, pp. 1243–1266.

[26] Koobus, B., and Farhat, C., "Second-Order Time-Accurate and Geometrically Conservative Implicit Schemes for Flow Computations on Unstructured Dynamic Meshes," *Computer Methods in Applied Mechanics and Enginering*, Vol. 170, 1999, pp.103–129.

[27] Benek, J. A., Steger, J. L., and Dougherty, F. C., "A Flexible Grid Embedding Technique with Application to the Euler Equations," AIAA Paper 1983-1944, 1983.

[28] Kannan, R., and Wang, Z. J., "Overset Adaptive Cartesian/Prism Grid Method for Moving Boundary Flow Problems," *AIAA Journal*, Vol. 45, No. 7, 2007, pp. 1774–1779.

[29] Jameson, A., and Yoon, S., "Lower-Upper Implicit Schemes With Multiple Grids for the Euler Equations," *AIAA Journal*, Vol. 25, 1987, pp. 929–935.

[30] Luo, H., Baum, J. D., and Lohner, R., "A fast, Matrix-Free Implicit Method for Compressible Flows on Unstructured Grids," *Journal of Computational Physics*, Vol. 146, 1998, pp. 664–690.

[31] Shannon, C. E., "Communication in the Presence of Noise," *Proceeding of the Institute of Radio Engineers*, Vol. 37, pp. 10–21, Jan. 1949.

[32] Saad, Y., and Schultz, M., "GMRES: A Generalized Minimal Residual Algorithm for Solving Non-Symmetric Linear Systems," *SIAM Journal on Scientific and Statistical Computing*, Vol. 7, No. 3, July 1986.

[33] Liang, C., Kannan, R., and Wang, Z.J., "A p-multigrid spectral difference method with explicit and implicit smoothers on unstructured triangular grids", *Computers and Fluids*, Vol. 38, 2009, pp. 254–265.

Appendix F

Article AIAA en français

Méthode de décomposition spectrale temporelle implicite pour le calcul d'écoulements incompressibles périodiques en temps

S. Antheaume[1] and C. Corre [2]
Laboratoire des Ecoulements Geophysiques et Industriels,

Domaine Universitaire, BP 53, 38041 Grenoble Cedex 9 France

La méthode TSM (Time Spectral Method) consiste à remplacer le calcul instationnaire d'une solution périodique en temps en le calcul de $2N + 1$ problèmes stationnaires couplés où N est le nombre d'harmoniques retenus dans la série de Fourier tronquée du système Navier-Stokes. L'efficacité de la méthode a dores et déjà été démontrée par plusieurs auteurs pour des applications d'écoulements compressibles dans le contexte de maillages structurés en utilisant une formulation implicite pour résoudre le système augmenté par le couplage des équations. Dans ce papier, la TSM est étendue aux écoulements périodiques incompressibles visqueux en utilisant une formulation Volumes Finis de la méthode de compressibilité artificielle sur des maillages non-structurés en mouvement. Des simulations numériques d'écoulements à bas Reynolds autour de profils en mouvement de battement et d'oscillation montrent que la TSM permet d'atteindre des réductions de coût de facteur 5 dans le meilleur des cas en comparaison avec une méthode de calcul instationnaire classique.

---

[1] Ph.D candidate
[2] Professor

Nomenclature

$\boldsymbol{A}, \boldsymbol{B}, \boldsymbol{J}$ = Matrices Jacobiennes des flux

C_X, C_Y = Coefficients d'efforts

C_p = Coefficient de pression

c = Corde du profil

$\boldsymbol{F}$ = Flux physique

f^* = Fréquence adimensionnelle, fc/U_∞

H_0 = Amplitude de battement

$\mathcal{H}$ = Flux numériques

N = Nombre d'harmoniques

Re = Nombre de Reynolds

$\mathcal{R}$ = Vecteur des résidus spatiaux

$\boldsymbol{s}$ = Vecteur vitesse de grille

t, τ = Temps physique et fictif

$\boldsymbol{w}$ = Vecteur des variables conservatives

$\boldsymbol{x}$ = Vecteur de la position de grille

β = Paramètre de compressibilité artificielle

η = Rapport global des coûts TSM et BDF

θ, θ_0 = Position angulaire et amplitude d'oscillation

ω = Vitesse angulaire

Indices

i = Indice de cellule

∞ = Valeur à l'infini amont

n = n^{ime} instant TSM

Exposants

l = Compteur des itérations Jacobi

m = Compteur de la boucle en temps fictif

n = Compteur de la boucle en temps physique

I. Introduction

La conception de machines aérodynamiques ou hydrodynamique nécessite souvent le calcul d'écoulements instationnaires. Quand cette étape de conception est réalisée avec des outils numériques, l'approche dite "en temps fictif" est une méthode classique pour calculer ces écoulements instationnaires. Dans cette approche, le champ instationnaire à chaque pas de temps physique est obtenu comme solution stationnaire d'un problème en temps fictif ou dual [1] [2]. Cette stratégie en temps dual, Dual Time Step ou DTS peut aussi être interprétée comme la recherche d'une solution (par rapport au temps dual) des équations stationnaires de l'écoulement augmentées d'un terme source correspondant à la discrétisation de la dérivée en temps physique réalisée typiquement avec un schéma précis au second ordre, Backward Difference Formula (BDF). Les méthodes numériques disponibles pour les écoulements stationnaires peuvent alors être très facilement adaptées pour traiter ces écoulements instationnaires en prenant simplement en compte ce terme source. Parmi les nombreuses applications industrielles qui nécessitent une analyse instationnaire de l'écoulement, beaucoup présentent une périodicité temporelle comme par exemple les rotors d'hélicoptères, les éoliennes pour ce qui concerne l'aérodynamique externe et les turbomachines pour l'aérodynamique interne. Un inconvénient de la méthode BDF-DTS est qu'elle requière de calculer, typiquement depuis un état initial correspondant au repos, toute la période transitoire avant que l'écoulement périodique s'établisse. Ce défaut des méthodes classiques en temps dual a motivé le développement de méthodes numériques s'intéressant uniquement à trouver l'état périodique établi. Profitant du développement de la solution périodique en série de Fourier, Hall & al [3] ont introduit une méthode efficace dédiée aux écoulements périodiques en temps pour les applications turbomachines. En reprenant la même idée, Gopinath et Jameson proposent la Time Spectral Method ou TSM pour traiter de problèmes aérodynamiques externes [4]. La TSM transforme le système original de $(2+d)$ équations instationnaires décrivant l'écoulement compressible de dimension d pour chaque instant (2 correspondant aux équations de conservation de masse et d'énergie et d le nombre d'équations scalaires exprimant la conservation des d composantes de la quantité de mouvement) en un système étendu de $(2N+1)\times(d+2)$ équations correspondant à la solution de l'écoulement à $(2N+1)$ instants dans la période, choisis de façon à assurer la précision spectrale de la dérivée en temps physique. Pour

rendre la méthode vraiment attractive, il est bien entendu très important de calculer efficacement l'état stationnaire de ce système étendu de lois de conservations. Comme l'on fait remarquer van der Weide & al dans [5], l'intégration en temps explicite du système TSM montre une limite de stabilité très sévère si le nombre d'harmoniques N augmente ou si la fréquence du phénomène périodique calculé est importante. Plusieurs auteurs [6–8] ont donc mis en place des stratégies d'intégration en temps implicite. Cela permet l'utilisation de grands CFL qui assurent une convergence plus rapide vers l'état stationnaire et la possibilité d'utiliser un grand nombre d'harmoniques N comme la description précise d'écoulements périodiques de spectre riches peut l'exiger. Jusqu'à présent, la TSM a été utilisée pour un grand nombre d'applications qui traitent essentiellement d'écoulements compressibles : turbomachines [9], rotors d'hélicoptères [10]. Le contexte de la présente étude est le projet HARVEST qui s'attache à développer une technologie de turbine hydrolienne permettant la conversion de l'énergie cinétique des courants de marées et/ou de rivières en énergie électrique [11]. La conception hydrodynamique de cette turbine est actuellement réalisée en utilisant des stratégies expérimentales et numériques. L'objectif final de ce travail est d'améliorer l'efficacité de la partie numérique en remplaçant les calculs BDF actuels d'écoulements turbulents 3D autour de la turbine [12] par une approche TSM. Cela suppose d'adapter la stratégie TSM dans un solveur incompressible. Une première tentative en ce sens a été récemment proposée par Jameson [13] en utilisant une méthode de Compressibilité Artificielle (AC) mais des problèmes de stabilité sont très vite apparus dès lors qu'il a calculé des profils oscillants avec une fréquence élevée. Dans ce papier, une formulation TSM implicite est proposée et appliquée avec succès au calcul d'écoulements incompressibles laminaires autour de profils en mouvement de battement et d'oscillation récemment étudiés par Kinsey et Dumas [14] avec une approche BDF classique. Les calculs de telles configurations 2D stationnaires représentent un premier pas vers le calcul plus compliqué d'écoulements turbulents 3D sur des turbines hydroliennes. Ils restent néanmoins intéressants, à cette étape de développement, car leur faible coût permet une évaluation rigoureuse de la capacité de la TSM a accélérer le calcul d'écoulements périodiques en temps à bas Reynolds. Cette approche utilise la méthode AC pour décrire l'écoulement incompressible et une stratégie ALE pour décrire le mouvement de maillages non-structurés. Elle est comparée avec une approche BDF classique qui combine aussi AC et ALE

du point de vue de la précision et de l'efficacité. Le papier est organisé comme suit : la partie II rappelle les principaux ingrédients du solveur incompressible DTS-BDF (modèle AC, formulation ALE, intégration en temps implicite) et montre des résultats de validation obtenus pour les cas de profils NACA0015 en mouvement de battement et oscillation récemment analysés par Kinsey et Dumas [14]; la partie III détaille l'application de la TSM à la méthode AC et la section IV décrit l'adaptation à un traitement implicite développé dans [15] pour le système TSM; dans la section V, la méthode TSM implicite est appliquée au calcul d'écoulement autour d'un profil NACA0015 en mouvement de battement et oscillation pour un nombre croissant d'harmoniques N dans le but de déterminer le meilleur compromis entre précision et coût (tous les deux fonctions croissantes de N) et de savoir si la TSM peut surpasser la BDF. Des conclusions et perspectives sont tirées dans la dernière partie.

II. Solveur Incompressible

A. Equations

La solution des équations Navier-Stokes incompressibles est typiquement obtenue en utilisant soit, une méthode à équation de pression où pression et vitesse sont résolues de façon itérative à travers une équation de correction pour la pression soit, une méthode basé sur la masse volumique comme la méthode de compressibilité artificielle (AC) de Chorin [16]. Cette dernière stratégie est celle retenue dans cette étude afin de pouvoir bénéficier des méthodes implicites efficaces précédemment développées pour traiter des problèmes hyperboliques [15] et facilement adaptables au système AC. Rappelons que la méthode AC permet d'obtenir la solution instationnnaire des équation d'Euler 1D en recherchant l'état stationnaire du système hyperbolique de lois de conservations suivant par rapport à un temps fictif ou dual τ

$$\underbrace{\frac{\partial}{\partial \tau}\begin{pmatrix} p \\ u \end{pmatrix}}_{=\boldsymbol{w}} + \underbrace{\begin{pmatrix} 0 & 0 \\ 0 & 1 \end{pmatrix}}_{=\boldsymbol{K}} \cdot \frac{\partial}{\partial t}\begin{pmatrix} p \\ u \end{pmatrix} + \frac{\partial}{\partial x}\underbrace{\begin{pmatrix} \beta u \\ u^2 + p \end{pmatrix}}_{=\boldsymbol{f}(\boldsymbol{w};\beta)} = 0 \tag{1}$$

avec x la variable d'espace, t le temps physique, p, u la pression et vitesse, β, le paramètre constant de compressibilité artificielle. A l'état stationnaire sur τ, la solution $u(x,t)$ de (1) satisfait la condition de divergence nulle tandis que les deux champs $u(x,t)$ et $p(x,t)$ satisfont les équations de

quantités de mouvement instationnaires (par rapport à t). Si l'on réécrit (1) sous forme compacte d'un système hyperbolique 1D avec terme source, l'on obtient

$$\frac{\partial \boldsymbol{w}}{\partial \tau} + \frac{\partial}{\partial x}\boldsymbol{f}(\boldsymbol{w};\beta) = \boldsymbol{S} = -\boldsymbol{K}\frac{\partial \boldsymbol{w}}{\partial t}$$

et il devient clair que le système AC peut être efficacement conduit vers une solution stationnaire précise en utilisant des outils initialement développé dans le contexte des écoulement compressibles : discrétisation amont au deuxième ordre des gradients des flux, discrétisation BDF au deuxième ordre de la dérivée en temps physique et premier ordre implicite pour une convergence rapide en temps dual. Notons que le choix de la valeur du paramètre β affecte la convergence générale ainsi que la précision de la solution physique à travers la dissipation numérique de la discrétisation en espace. Cependant, tant que l'état stationnaire par rapport à τ est correctement atteint, le système AC reste consistent avec les équations incompressibles quel que soit la valeur de β. Tournons nous maintenant vers le système AC étendu au cas d'écoulements incompressibles 2D visqueux pour des maillages en mouvement. Supposons que $\Omega(t) \subset \Re^2$ est une surface de contrôle arbitraire délimité par un contour continu fermé $\partial\Omega(t)$ qui se déplace indépendamment du fluide à la vitesse $\boldsymbol{s}(\boldsymbol{x},t) = s_x(t)\ \boldsymbol{i} + s_y(t)\ \boldsymbol{j}$, où $\boldsymbol{x} = x\ \boldsymbol{i} + y\ \boldsymbol{j}$ est le vecteur des coordonnées cartésiennes dans le référentiel absolu. Dans ce référentiel ALE, les équations 2D Navier-Stokes pour les écoulements instationnaires incompressibles, modifiées pour prendre en compte la méthode AC, peuvent s'exprimer sous la forme intégrale :

$$\frac{\partial}{\partial \tau}\int_{\Omega(t)} \boldsymbol{w}\ d\Omega(t)\ +\ \boldsymbol{K}\frac{\partial}{\partial t}\int_{\Omega(t)} \boldsymbol{w}\ d\Omega(t)\ +\ \int_{\partial\Omega(t)} (\boldsymbol{F}^E - \boldsymbol{F}^V)\cdot \boldsymbol{n}\ d\gamma(t)\ =\ 0\ , \tag{2}$$

où $\boldsymbol{n}$ est le vecteur unitaire normal sortant et γ l'abscisse curviligne du contour $\partial\Omega$. Le vecteur des variables conservatives $\boldsymbol{w}$, la matrice singulière $\boldsymbol{K}$, les flux convectifs $\boldsymbol{F}^E = (\boldsymbol{f}^E, \boldsymbol{g}^E)$ et visqueux $\boldsymbol{F}^V = (\boldsymbol{f}^V, \boldsymbol{g}^V)$ sont définis par

$$\boldsymbol{w} = \begin{pmatrix} p \\ u \\ v \end{pmatrix}, \quad \boldsymbol{K} = \begin{pmatrix} 0 & 0 & 0 \\ 0 & 1 & 0 \\ 0 & 0 & 1 \end{pmatrix}, \quad \boldsymbol{f}^E(\boldsymbol{w}) = \begin{pmatrix} \beta(u - s_x) \\ u(u - s_x) + p \\ v(u - s_x) \end{pmatrix}, \quad \boldsymbol{g}^E(\boldsymbol{w}) = \begin{pmatrix} \beta(v - s_y) \\ u(v - s_y) \\ v(v - s_y) + p \end{pmatrix}$$

$$\boldsymbol{f}^V(\frac{\partial \boldsymbol{w}}{\partial x}, \frac{\partial \boldsymbol{w}}{\partial y}) = \frac{1}{Re} \begin{pmatrix} 0 \\ 2\dfrac{\partial u}{\partial x} \\ \dfrac{\partial u}{\partial y} + \dfrac{\partial v}{\partial x} \end{pmatrix}, \quad \boldsymbol{g}^V(\frac{\partial \boldsymbol{w}}{\partial x}, \frac{\partial \boldsymbol{w}}{\partial y}) = \frac{1}{Re} \begin{pmatrix} 0 \\ \dfrac{\partial u}{\partial y} + \dfrac{\partial v}{\partial x} \\ 2\dfrac{\partial v}{\partial y} \end{pmatrix}$$

La pression p et les composantes (u, v) de la vitesse du fluide dans le référentiel absolu sont normalisés respectivement par $\rho_\infty U_\infty^2$ et U_∞, avec ρ_∞ et U_∞ les magnitudes de la masse volumique et vitesse à l'infini amont. Pour les calculs d'écoulements autour de profils qui vont suivre, le nombre de Reynolds $Re = \rho_\infty U_\infty c/\mu_\infty$ est basé sur la corde du profil c. La prochaine sous-partie décrit les approches volumes-finis, schéma upwind et intégration en temps implicite utilisées dans ce travail pour résoudre le système ALE-AC (2).

B. Méthodes numériques

1. Discrétisation spatiale

Le système (2) est intégré sur des maillages non structurés en utilisant une approche Volume Finis. En appliquant (2) sur une cellule donnée Ω_i, en introduisant la valeur moyenne $\overline{\boldsymbol{w}}$ de $\boldsymbol{w}$ sur la cellule et en décomposant la balance des flux comme la somme des flux à travers chaque face $\Gamma_{i,k}$ de la cellule Ω_i, on obtient

$$\frac{\partial}{\partial \tau}(\overline{\boldsymbol{w}_i}|\Omega_i|) + \boldsymbol{K}\frac{\partial}{\partial t}(\overline{\boldsymbol{w}_i}|\Omega_i|) + \sum_k \int_{\Gamma_{i,k}} (\boldsymbol{F}^E - \boldsymbol{F}^V) \cdot \boldsymbol{n} \; d\gamma \;=\; 0 \tag{3}$$

où $|\Omega_i|$ est la surface de la i-ème cellule Ω_i. Le vecteur des flux physiques normal $(\boldsymbol{F}^E - \boldsymbol{F}^V) \cdot \boldsymbol{n}$ à travers la face $\Gamma_{i,k}$ de longueur $|\Gamma_{i,k}|$ est approchée par le flux physique numérique $\mathcal{H} = \mathcal{H}^E - \mathcal{H}^V$ calculé au centre i, k de la face $\Gamma_{i,k}$

$$\int_{\Gamma_{i,k}} (\boldsymbol{F}^E - \boldsymbol{F}^V) \cdot \boldsymbol{n} \; d\gamma \;= \left(\mathcal{H}^E_{i,k} - \mathcal{H}^V_{i,k}\right) |\Gamma_{i,k}| + O(h^p)$$

où h est une longueur de grille typique. La précision en espace p dépend du choix de la reconstruction polynomiale utilisée pour la variable conservative à l'intérieur de chaque cellule; une reconstruction

linéaire est systématiquement utilisée dans cette étude conduisant à une précision au second ordre en espace. Pour cette raison et, ce, sans perte de précision, l'état moyenné dans la cellule i est remplacé par l'état au centre de la cellule, noté $\boldsymbol{w}_i$ à partir de maintenant. Le solveur approché de Roe initialement développé pour les équations d'Euler compressibles [17] est adapté au système hyperbolique ALE-AC (2) et combiné avec une approche MUSCL pour la reconstruction [18] [19] pour obtenir la formule du flux physique numérique $\mathcal{H}_{i,k}^E$

$$\mathcal{H}_{i,k}^E = \frac{1}{2}(\boldsymbol{F}^E(w_k^L)\cdot\boldsymbol{n}_{i,k} + \boldsymbol{F}^E(w_k^R)\cdot\boldsymbol{n}_{i,k}) + \frac{1}{2}\boldsymbol{Q}_{i,k}^E(\boldsymbol{w}_k^L - \boldsymbol{w}_k^R) \tag{4}$$

où $\boldsymbol{w}^{L/R}$ sont les états reconstruits, respectivement, à gauche et à droite de la k^{ieme} interface $\Gamma_{i,k}$ de la cellule Ω_i, $\boldsymbol{Q}^E$ est la matrice de dissipation de Roe. Les valeurs des états au centre de la face i,k sont linéairement reconstruit depuis les valeurs des états aux centres des cellules i et $o(i,k)$ partageant la face $\Gamma_{i,k}$ et leurs gradients $\boldsymbol{\nabla w}$ dans chacune de ces cellules.

$$\begin{cases} \boldsymbol{w}_k^L = \boldsymbol{w}_i + \boldsymbol{\nabla w}_i \cdot \boldsymbol{r}_{i,k} \\ \boldsymbol{w}_k^R = \boldsymbol{w}_{o(i,k)} + \boldsymbol{\nabla w}_{o(i,k)} \cdot \boldsymbol{r}_{o(i,k)} \end{cases} \tag{5}$$

où $\boldsymbol{r}_{i,k}$ (resp. $\boldsymbol{r}_{o(i,k)}$) désigne le vecteur s'étendant du centre de la cellule i (resp. $o(i,k)$) au centre de l'interface $\Gamma_{i,k}$. Le gradient $\boldsymbol{\nabla w}_i$ est calculé à chaque centre de cellule i en utilisant une formule aux moindres carrés appliquée sur un support fixé incluant les cellules voisines partageant au moins un nœud avec la cellule i [19]. La matrice de dissipation de Roe $\boldsymbol{Q}^E$ est donnée par :

$$\boldsymbol{Q}^E = |\boldsymbol{A}^E n_x + \boldsymbol{B}^E n_y| = |\boldsymbol{J}_\perp^E|$$

où $\boldsymbol{n} = (n_x, n_y)$ et $\boldsymbol{A}^E$, $\boldsymbol{B}^E$ sont les matrices Jacobiennes des flux numériques convectifs : $\boldsymbol{A}^E = d\boldsymbol{f}^E/d\boldsymbol{w}, \boldsymbol{B}^E = d\boldsymbol{g}^E/d\boldsymbol{w}$. Le calcul immédiat pour le système (2) donne :

$$\boldsymbol{J}_\perp^E = \begin{pmatrix} 0 & \beta n_x & \beta n_y \\ n_x & V_\perp - s_\perp + u\, n_x & u\, n_y \\ n_y & v\, n_x & V_\perp - s_\perp + v\, n_y \end{pmatrix}$$

où $V_\perp = u\, n_x + v\, n_y$, $s_\perp = s_x n_x + s_y n_y$. Cette matrice Jacobienne peut aussi être exprimée comme $\boldsymbol{J}_\perp^E = \boldsymbol{T}|\boldsymbol{\Lambda}^E|\boldsymbol{T}^{-1}$ avec $\boldsymbol{\Lambda}^E$ la matrice diagonale qui contient les valeurs propres réelles du système hyperbolique (2). La matrice de dissipation de Roe peut finalement être calculée comme :

$$\boldsymbol{Q}_{i,k}^E = \boldsymbol{T}_{i,k}|\boldsymbol{\Lambda}_{i,k}^E|\boldsymbol{T}_{i,k}^{-1}$$

avec l'état $\boldsymbol{w}_{i,k}$ pris comme la moyenne arithmétique de $\boldsymbol{w}_{i,k}^L$ et $\boldsymbol{w}_{i,k}^R$ en suivant Taylor and Whitfield [20]. Les flux visqueux sont approchés en utilisant une extension linéaire exacte de la méthode "diamant" de Noh [21] qui n'est pas détaillée ici.

Précisons que l'état stationnaire de (2) dépend du paramètre AC β à travers la matrice de dissipation $\boldsymbol{Q}^E$. La balance des flux numériques convectifs ou résidu sera notée à partir de maintenant

$$\mathcal{R}_i^E(\boldsymbol{w}, \boldsymbol{x}, \boldsymbol{s}) = \frac{1}{|\Omega_i|} \sum_k \mathcal{H}_{i,k}^E \ |\Gamma_{i,k}| \tag{6}$$

où, dans le contexte de la formulation ALE, la dépendance de cette balance des flux par rapport à la position de maillage $\boldsymbol{x}$ et sa vitesse $\boldsymbol{s}$ a été rendue explicite. De façon similaire, la balance des flux visqueux ou résidu sera noté

$$\mathcal{R}_i^V(\boldsymbol{w}, \boldsymbol{x}) = \frac{1}{|\Omega_i|} \sum_k \mathcal{H}_{i,k}^V \ |\Gamma_{i,k}| \tag{7}$$

avec une dépendance explicite vis à vis de la position de grille $\boldsymbol{x}$. Comme, seul le mouvement de corps rigide sera considéré dans ce travail, la surface de cellule $|\Omega_i|$ reste constante au cours du temps et peut être retirée des dérivées en temps physique et dual dans (3) pour être insérée dans les résidus spatiaux convectifs et visqueux (6) et (7). La forme semi-discrète (3) du système ALE-AC peut aussi être exprimée comme

$$\frac{\partial \boldsymbol{w}_i}{\partial \tau_i} + \boldsymbol{K} \frac{\partial \boldsymbol{w}_i}{\partial t} + \mathcal{R}_i^E(\boldsymbol{w}, \boldsymbol{x}, \boldsymbol{s}) = \ \mathcal{R}_i^V(\boldsymbol{w}, \boldsymbol{x}) \tag{8}$$

2. Discrétisation en temps incluant le traitement ALE

Quand on traite de profils en mouvement dans le repère ALE de référence, deux principales approches peuvent être considérée pour prendre en compte le mouvement de maillage. La première approche est la technique de corps rigide où tous les points de grille sont animés du même mouvement que le profil. La qualité initiale du maillage est préservée mais des conditions limites instationnaires doivent être implémentées qui incluent les vitesses de grille. Un inconvénient de cette méthode

est que, pour des profils dont la fréquence d'oscillation est importante, la vitesse relative dans les cellules loin du centre de rotation peut devenir très importante conduisant à une dissipation numérique trop importante. La seconde approche consiste à déformer les cellules intérieures pour se conformer à la position instantanée du profil tandis que les frontières extérieures sont fixes. La déformation peut être réalisée avec des méthodes basées sur l'analogie de ressort, qui implique soit, de trouver la solution d'un grand système d'équations pour le déplacement des nœuds [22, 23] et/ou un remaillage local à chaque pas de temps physique du calcul [24, 25]. Dans les deux cas de la dernière approche, une loi de conservation géométrique doit aussi être introduite et par conséquent satisfaite pour éviter les erreurs de discrétisation sur les surfaces (2D) et volumes (3D) [26]. La technique Chimère offre encore une autre alternative pour traiter des corps en mouvement en utilisant des zones indépendamment maillées qui se superposent, typiquement, une zone de grille attachée au corps et une autre en arrière plan [27, 28]. Alors que l'approche maillage déformable est nécessaire pour des études aéroélastiques ou des problèmes qui impliquent des corps en mouvement dans une géométrie multi-blocs, elle peut être évitée pour les cas de simples profils en mouvement de battement et d'oscillation considérés dans cette étude. En conséquence, une simple approche de corps rigide est retenue avec la position de maillage $\boldsymbol{x}$ directement dérivée de la loi du mouvement et une vitesse de grille $\boldsymbol{s}$ calculée en utilisant la simple relation analytique :

$$\boldsymbol{s}(t) = \boldsymbol{\Omega}(t) \wedge (\boldsymbol{x}(t) - \boldsymbol{x}_c(t)) + \boldsymbol{t} \tag{9}$$

où $\boldsymbol{\Omega}$ est la vitesse angulaire de rotation, $\boldsymbol{x}_c$ est le centre de rotation et $\boldsymbol{t}$ est la vitesse de translation. Par souci de simplicité et sans perte de généralité, la résolution en temps dual est mise de coté dans cette partie. En utilisant une discrétisation au second ordre Backward Difference Formula (BDF) pour la dérivée en temps physique dans (8), on obtient le système ALE-AC suivant discrétisé au second-ordre

$$\boldsymbol{K}\frac{\left(\frac{3}{2}\boldsymbol{w}_i^{n+1} - 2\boldsymbol{w}_i^{n} + \frac{1}{2}\boldsymbol{w}_i^{n-1}\right)}{\Delta t} + \mathcal{R}_i^E\left(\boldsymbol{w}^{n+1}, \boldsymbol{x}^{n+1}, \boldsymbol{s}^{n+1}\right) = \mathcal{R}_i^V\left(\boldsymbol{w}^{n+1}, \boldsymbol{x}^{n+1}\right) \tag{10}$$

3. Intégration en temps implicite

Le système ALE-AC complet discrétisé (10) peut aussi être exprimé comme

$$\boldsymbol{K}\frac{\left(\frac{3}{2}\boldsymbol{w}_i^{n+1}-2\boldsymbol{w}_i^{n}+\frac{1}{2}\boldsymbol{w}_i^{n-1}\right)}{\Delta t}+\mathcal{R}_i\left(\boldsymbol{w}^{n+1}\right)=0 \tag{11}$$

avec le résidu complet $\mathcal{R}$ défini par $\mathcal{R}_i\left(\boldsymbol{w}^{n+1}\right)=\mathcal{R}_i^E\left(\boldsymbol{w}^{n+1}\right)-\mathcal{R}_i^V\left(\boldsymbol{w}^{n+1}\right)$ où la dépendance vis à vis de la position et de la vitesse de grille a cette fois été omise par souci de simplicité. Le système non-linéaire (11) est simplement résolu avec une méthode DTS, c'est à dire que le nouvel état $\boldsymbol{w}^{n+1}$ est obtenu de façon itérative comme solution stationnaire en temps dual τ du système augmenté

$$\frac{\boldsymbol{w}_i^{n,m+1}-\boldsymbol{w}_i^{n,m}}{\Delta\tau_i^{n,m}}+\boldsymbol{K}\frac{\left(\frac{3}{2}\boldsymbol{w}_i^{n,m}-2\boldsymbol{w}_i^{n}+\frac{1}{2}\boldsymbol{w}_i^{n-1}\right)}{\Delta t}+\mathcal{R}_i\left(\boldsymbol{w}^{n,m}\right)=0 \tag{12}$$

où $\boldsymbol{w}^{n,m}$ est l'état fictif à la m^{ieme} sous itération sur τ entre la n^{ieme} et $(n+1)^{\text{ieme}}$ boucle en temps physique. L'état fictif initial à chaque pas de temps physique est choisi comme $\boldsymbol{w}^{n,0}=\boldsymbol{w}^{n}$ et le nouvel état physique est défini comme $\boldsymbol{w}^{n+1}=\boldsymbol{w}^{n,m_{max}}$ avec m_{max} le nombre de sous itérations sur τ nécessaires pour atteindre l'état stationnaire de convergence de (12). L'efficacité de la méthode est assurée par le fait d'utiliser une intégration implicite en temps dual

$$\frac{\Delta\boldsymbol{w}_i^{n,m}}{\Delta\tau_i^{n,m}}=-\mathcal{R}_i\left(\boldsymbol{w}^{n,m+1}\right)-\boldsymbol{K}\frac{\left(\frac{3}{2}\boldsymbol{w}_i^{n,m+1}-2\boldsymbol{w}_i^{n}+\frac{1}{2}\boldsymbol{w}_i^{n-1}\right)}{\Delta t}=-\mathcal{R}_i^t\left(\boldsymbol{w}^{n,m+1}\right) \tag{13}$$

avec $\boldsymbol{w}^{n,m+1}=\boldsymbol{w}^{n,m}+\Delta\boldsymbol{w}^{n,m}$. Comme la précision de la solution (en t et x) ne dépend pas de l'incrément en temps dual $\Delta\boldsymbol{w}^{n,m}$ qui tend vers zéro à l'état stationnaire sur τ, le résidu complet $\mathcal{R}_i^t\left(\boldsymbol{w}^{n,m+1}\right)$ peut être développé comme

$$\mathcal{R}_i^t\left(\boldsymbol{w}^{n,m+1}\right)=\mathcal{R}_i^t\left(\boldsymbol{w}^{n,m}\right)+\boldsymbol{K}\frac{3}{2}\frac{\Delta\boldsymbol{w}_i^{n,m}}{\Delta t}+\frac{1}{|\Omega_i|}\sum_k\left(\Delta\mathcal{H}_{i,k}^{(i)}\right)^{n,m}\ |\Gamma_{i,k}| \tag{14}$$

avec $(\Delta\mathcal{H}_{i,k}^{(i)})^{n,m}=\mathcal{H}^{(i)^{n,m+1}}-\mathcal{H}^{(i)^{n,m}}$ et $\mathcal{H}^{(i)}=\mathcal{H}^{E(i)}-\mathcal{H}^{V(i)}$ la notation pour le flux numérique retenu dans la phase implicite. Comme l'incrément implicite disparaît à l'état stationnaire, la formule du flux numérique implicite n'impacte pas la précision globale et son choix est simplement guidé par des considérations de stabilité et efficacité. En suivant [29], [30], [24], le flux numérique convectif $\mathcal{H}^{E(i)}$ qui apparaît dans la phase implicite est simplement calculé en utilisant le flux

numérique de Rusanov précis au premier-ordre :

$$\mathcal{H}_{i,k}^{E(i)} = \frac{1}{2}(\boldsymbol{F}_i^E \cdot \boldsymbol{n}_{i,k} + \boldsymbol{F}_{o(i,k)}^E \cdot \boldsymbol{n}_{i,k}) + \frac{1}{2}\rho(\boldsymbol{J}_\perp^E)_{i,k}(\boldsymbol{w}_i - \boldsymbol{w}_{o(i,k)}) \tag{15}$$

où $\rho(\boldsymbol{J}_\perp^E)_{i,k}$ est le rayon spectral de la matrice Jacobienne des flux $\boldsymbol{J}_\perp^E$ calculé au centre de la face $\Gamma_{i,k}$. Le flux numérique implicite visqueux prend simplement la forme simplifiée

$$\mathcal{H}_{i,k}^{V(i)} = \frac{\rho(\boldsymbol{J}_\perp^V)_{i,k}}{||\boldsymbol{r}_{i,k}|| + ||\boldsymbol{r}_{o(i,k)}||}(\boldsymbol{w}_{o(i,k)} - \boldsymbol{w}_i) = \widetilde{\rho(\boldsymbol{J}_\perp^V)}_{i,k}(\boldsymbol{w}_{o(i,k)} - \boldsymbol{w}_i) \tag{16}$$

où $\rho(\boldsymbol{J}_\perp^V)_{i,k}$ est le rayon spectral de la matrice Jacobienne visqueuse. Plus de détails sur la dérivation de ce flux implicite visqueux peuvent être trouvés dans la référence [15]. En insérant les expressions (15) (16) des flux numériques implicites dans le développement du résidu (14) et en réarrangeant (13), on obtient la forme implicite suivante pour le système ALE-AC (10) :

$$\boldsymbol{D}_i^{n,m}\Delta\boldsymbol{w}_i^{n,m} + \frac{1}{2|\Omega_i|}\sum_k \left(\Delta\boldsymbol{F}_{o(i,k)}^E\right)^{n,m} \cdot \boldsymbol{n}_{i,k}\ |\Gamma_{i,k}| - \sum_k C_{i,k}^{n,m}\Delta\boldsymbol{w}_{o(i,k)}^{n,m} = -\mathcal{R}_i^t(\boldsymbol{w}^{n,m}) \tag{17}$$

Les coefficients $\boldsymbol{D}_i^{n,m}$, $C_{i,k}^{n,m}$ sont définis par :

$$\boldsymbol{D}_i^{n,m} = \left(\frac{\boldsymbol{I}}{\Delta\tau_i^{n,m}} + \frac{3}{2}\frac{\boldsymbol{K}}{\Delta t} + \sum_k C_{i,k}^{n,m}\boldsymbol{I}\right) \quad , \quad C_{i,k}^{n,m} = \frac{1}{|\Omega_i|}\left(\frac{1}{2}\rho(\boldsymbol{J}_\perp^E) + \widetilde{\rho(\boldsymbol{J}_\perp^V)}\right)_{i,k}^{n,m}|\Gamma_{i,k}| \tag{18}$$

avec $\boldsymbol{I}$ la matrice identité; notons que la phase implicite est en fait "sans-matrice" avec un coefficient diagonal D pour $\Delta p_i^{n,m}$ privé de la contribution $\frac{3}{2\Delta t}$ dans l'équation de conservation de la masse en en incluant ce terme dans les équations de conservation de quantité de mouvement qui implique $\Delta u_i^{n,m}$ and $\Delta v_i^{n,m}$. L'equation (17) peut être résolue pour un coût par point et par itération extrêmement faible en utilisant une méthode de relaxation Jacobi par point. Si on note l, le compteur des itérations associé à cette méthode quand (17) est résolue de manière itérative pour obtenir $\boldsymbol{w}^{n,m+1}$ depuis l'état connu $\boldsymbol{w}^{n,m}$ et si on introduit la notation $\Delta\phi^{(l)} = \phi^{(l)} - \phi^{n,m}$, la procédure PJ-BDF-ALE-AC se résume à :

$$\Delta\boldsymbol{w}_i^{(0)} = 0$$

$$\begin{cases} l = 0,\ l_{max} - 1 \\ \Delta\boldsymbol{w}_i^{(l+1)} = (\boldsymbol{D}_i^{n,m})^{-1}\left(-\mathcal{R}_i^t(\boldsymbol{w}^{n,m}, \boldsymbol{x}^{n+1}, \boldsymbol{s}^{n+1}) - \frac{1}{2|\Omega_i|}\sum_k \left(\Delta\boldsymbol{F}_{o(i,k)}^E\right)^{(l)} \cdot \boldsymbol{n}_{i,k}\ |\Gamma_{i,k}| + \sum_k C_{i,k}^{n,m}\Delta\boldsymbol{w}_{o(i,k)}^{(l)}\right) \end{cases}$$

$$\boldsymbol{w}_i^{n,m+1} = \boldsymbol{w}_i^{n,m} + \Delta\boldsymbol{w}_i^{(l_{max})} \tag{19}$$

C. Validation du solveur

Le solver présenté dans la partie précédente est validé en calculant des écoulements incompressibles laminaires autour de profils en battement et oscillation qui ont été récemment étudié par Kinsey and Dumas [14]. Les calculs de profils présentés dans [14] ont été réalisés en utilisant une méthode incompressible conventionnelle à équation de pression implémentée dans un solver commercial sur des maillages très fins et en utilisant des pas de temps très petits pour s'assurer de la convergence de grille et permettre une analyse fine de l'écoulement. En conséquence, ces calculs sont retenus comme référence et la capacité du code PJ-BDF-ALE-AC à fournir des résultats équivalents va être établie dans cette même partie.

1. Description des cas-tests

La géométrie étudiée est un profil NACA0015 soumis à un mouvement d'oscillation et/ou de battement. Ces mouvements sont définis par les lois d'évolution suivantes pour l'angle d'oscillation $\theta(t)$, autour d'un axe situé à un tiers de la corde, et la position verticale $y(t)$

$$\begin{cases} \theta(t) = \theta_0 \sin(\omega t) \\ y(t) = H_0 \sin(\omega t + \frac{\pi}{2}) \end{cases} \tag{20}$$

où θ_0 et H_0 sont respectivement les amplitudes d'oscillation et de battement et ω la vitesse angulaire. La fréquence réduite f^* est définie par $f^* = \frac{fc}{U_\infty}$, où U_∞ est la vitesse à l'infini amont. Le premier cas test, noté PH à partir de maintenant, combine oscillation et battement avec $\theta_0 = 60°$, $H_0 = 1$ et $f^* = 0.18$. Le second cas test, noté PP, correspond à un mouvement de pure oscillation avec $\theta_0 = 23°$, $H_0 = 0$ et $f^* = 0.12$. Dans les deux cas, le nombre de Reynolds basé sur les conditions amont au loin et la corde du profil est égal à $Re = 1100$ et donc l'écoulement peut être considéré comme laminaire.

2. Paramètre numériques

Le maillage reproduit dans la Fig. 1 a été généré de façon à être très proche de celui utilisé dans [14] puisque les deux méthodes, solveur PJ-BDF-ALE-AC et solveur commercial FLUENT utilisé par Kinsey and Dumas sont précises au deuxième ordre et utilisent des maillages non-structurés triangulaires. Le maillage compte 32000 cellules, avec 360 points sur le profil et une résolution

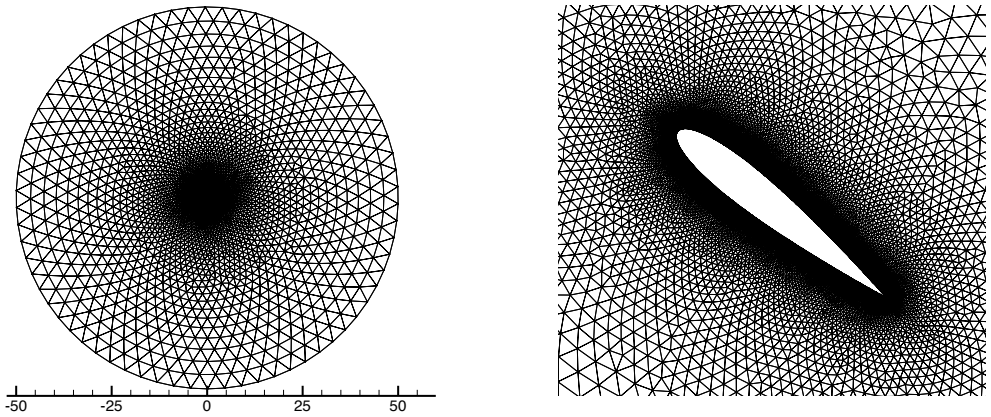

(a) (b)

Fig. 1 (a) : Vue générale du maillage (b) : zoom sur la région du profil.

proche paroi taillée de façon à satisfaire le critère $y_p^2 \frac{U_\infty}{\nu_\infty \Delta} \sim 1$, où y_p est la distance depuis la paroi jusqu'au centre de la première cellule et Δ est la plus petite taille de face sur le profil. L'application de ce critère combine un petit Reynolds de maille et un rapport d'aspect modéré près de la surface pour s'assurer de la précision de la solution. Le paramètre AC β est constant et égal à 5; cette valeur a été retenue comme offrant un bon compromis entre précision et efficacité après une évaluation rigoureuse du solveur sur plusieurs cas incompressibles de référence (cette étude n'est pas reproduite ici par souci de concision et parce que le point de focale de ce travail est l'approche TSM appliquée au solveur AC et non le solveur AC en lui-même.

Pour chaque cas, 520 pas de temps par période ou cycle sont utilisés correspondant à une valeur adimensionelle fixe de $\Delta t \approx 1.06^{-2}$ et $\Delta t \approx 1.16^{-2}$ pour les cas PH et PP respectivement. Le pas de temps dual local est calculé comme suit $\Delta\tau_i^{n,m} = \text{CFL} \max(\frac{h_i}{(\rho^E)_i^{n,m}}, \frac{h_i^2}{(2\rho^V)_i^{n,m}})$ avec h_i une distance caractéristique de la cellule Ω_i, ρ^E et ρ^V les rayons spectraux des matrices Jacobiennes des flux convectifs et visqueux et CFL, le facteur de multiplication du pas de temps dual caractéristique choisi aussi grand que possible, CFL $= 10^6$, pour s'assurer de la convergence rapide vers l'état stationnaire en temps dual à travers l'utilisation de très grandes valeurs pour $\Delta\tau_i^{n,m}$. A chaque pas de temps physique, 100 itérations en temps dual sont réalisées avec 16 itérations Point Jacobi pour résoudre (19). Le résidu décroit alors de 3 ou 4 ordres en magnitude pour tous les instants

du cycle. Il a été vérifié que ce critère est suffisant pour obtenir des résultats convergés (coefficients aérodynamiques globaux, distribution de pression à la paroi, champs). Le calcul est démarré avec un champ de pression et vitesse uniforme; 6 (respectivement 4) cycles doivent être calculés pour PH (resp. PP) avant que la périodicité soit complètement atteinte. Une variation de la moyenne du coefficient aérodynamique inférieure à 0.2% entre deux cycles consécutifs est typiquement retenu pour justifier d'un écoulement véritablement périodique. En suivant ce critère, tous les résultats du solveur PJ-BDF-ALE-AC présentés ensuite correspondent donc au 7^{ieme} cycle pour PH et 5^{ieme} cycle pour PP et seront "étiquettés" BDF à partir de maintenant.

3. Résultats

La comparaison avec les résultats de référence [14] est effectuée sur les coefficients d'efforts, plus précisément sur le coefficient C_Y qui est le seul rendu disponible par Kinsey et Dumas. Le coefficient C_X est aussi présenté pour comparaison ultérieure avec l'approche TSM.

La figure 2 présente les coefficients calculés C_X et C_Y en fonction de la période normalisée pour le cas PH; notez que seulement 1 pas de temps sur les 8 est représenté pour les calculs BDF pour la clarté du dessin. Des résultats semblables sont obtenus pour le cas PP et sont montrés dans la figure 3. L'accord entre [14] et nos résultats BDF est globalement très bon. Une légère différence sur le C_Y peut être observée sur la figure 2 pour le cas PH. Un raffinement du maillage et du pas de temps n'ont pas modifié les résultats et, par conséquent, ceci sont retenus comme résultats de référence et serviront de base de comparaison avec les résultats TSM sur les aspects précision et temps de calcul.

III. Compressibilité Artificielle et TSM

Cette partie explique comment la TSM, essentiellement utilisée jusqu'à présent dans le contexte d' écoulements compressibles et de maillages structurés peut être couplée avec le solveur AC non structuré décrit dans la partie précédente. L'application directe de la TSM pour le système ALE-AC est tout d'abord expliquée; ensuite, la méthode de résolution du système discrétisé AC-ALE TSM est décrite et les modifications nécessaires pour le traitement implicite sont détaillées.

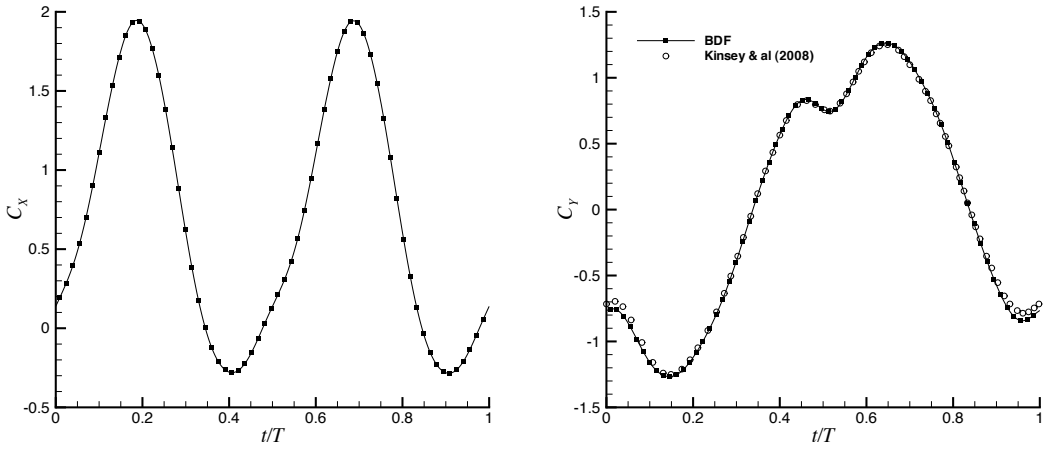

(a) (b)

Fig. 2 Cas test PH. (a): Evolution du C_X en utilisant notre approche BDF. (b): Evolution du C_Y calculé dans [14] et avec notre approche BDF

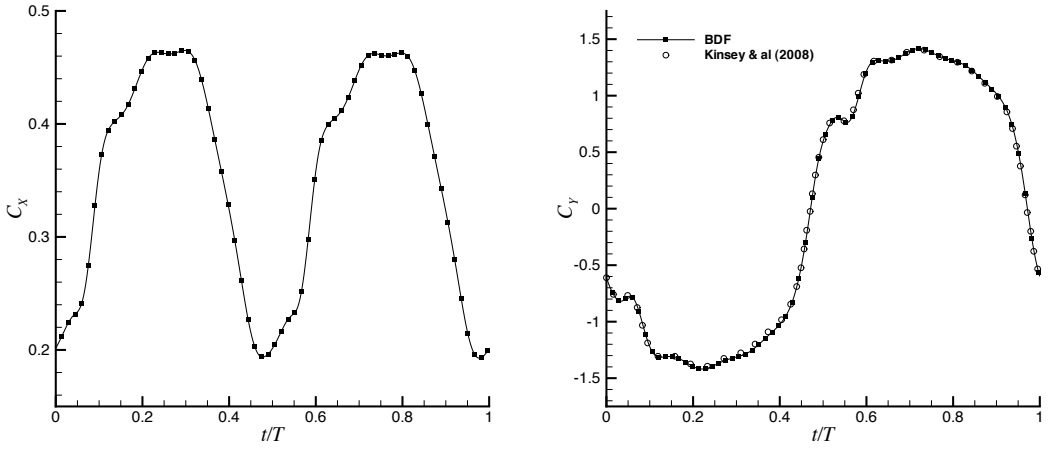

(a) (b)

Fig. 3 Cas test PP. (a): Evolution du C_X evolution en utilisant notre approche BDF. (b): Evolution du C_Y calculé dans [14] et avec notre approche BDF

A. Discrétisation TSM du système ALE-CA

Profitant de la périodicité temporelle de $\boldsymbol{w}$, le vecteur solution peut être décomposé en série de Fourier

$$\boldsymbol{w} = \sum_{k=-\infty}^{+\infty} \widehat{\boldsymbol{w}_k}(x) e^{\overline{ik\omega t}} \tag{21}$$

où ω est la pulsation du phénomène périodique, reliée à la période T par $\omega = 2\pi/T$. Le nombre complexe imagniaire pur $\underline{i}$ est souligné pour éviter toute confusion avec l'indice de cellule i. En pratique la solution est représentée avec un nombre fini d'harmoniques$N$

$$\boldsymbol{w} = \sum_{k=-N}^{N} \widehat{\boldsymbol{w}_k}(x) e^{\underline{i} k\omega t} \tag{22}$$

Le théorème de Nyquist-Shannon [31] spécifie que les k^{ieme} coefficients de Fourier, $\widehat{\boldsymbol{w}_k}$ with $-N \leq k \leq N$ peuvent être exactement calculés avec $2N+1$ instants répartis uniformément sur la période

$$\widehat{\boldsymbol{w}_k}(x) = \frac{1}{2N+1} \sum_{n=0}^{2N} \boldsymbol{w}_n e^{-\underline{i} k\omega n \Delta t} \tag{23}$$

avec $\boldsymbol{w}_n \equiv \boldsymbol{w}(t_n = n\Delta t)$ et $\Delta t = T/(2N+1)$. La principale idée de la TSM [4] sonsiste alors à rechercher ces $2N+1$ solutions $\boldsymbol{w}_n$ afin de retrouver la solution à n'importe quel temps dans la période en utilisant (22). La système ALE-AC discrétisé spatialement au temps t_n est alors :

$$\boldsymbol{K} \frac{\partial \boldsymbol{w}_n}{\partial t} + \mathcal{R}(\boldsymbol{w}_n, \boldsymbol{x}_n, \boldsymbol{s}_n) = 0 \tag{24}$$

où $\boldsymbol{w} = \{\boldsymbol{w}_i\}$ représente en fait l'ensembel des solutions dans toutes les cellules et $\mathcal{R} = \{\mathcal{R}_i\}$ est l'ensemble des valeurs de résidu calculés dans toutes les cellules et qui dépend de façon non linéaire de $\boldsymbol{w}$. A partir de maintenant $\boldsymbol{w}_{i,n}$ désignera la solution au point de maillage i et aun^{ieme} instant t_n dans la période. En utilisant la décomposition en série de Fourier (22) de $\boldsymbol{w}_n$ dans l'équation (24), cela conduit à $2N+1$ equations (une pour chaque longueur d'onde) dans le domaine fréquentiel

$$\boldsymbol{K} \sum_{k=-N}^{N} \underline{i} k\omega \widehat{\boldsymbol{w}_k} e^{\underline{i} k\omega n \Delta t} + \widehat{\mathcal{R}}(\widehat{\boldsymbol{w}_k}, \widehat{\boldsymbol{x}_k}, \widehat{\boldsymbol{s}_k}) = 0 \tag{25}$$

L'opérateur $\widehat{\mathcal{R}}$ pourrait être directement calculé à partir de $\widehat{\boldsymbol{w}_k}$, mais, à cause de sa non-linéarité, cela impliquerait des séries de convolutions complexes qui deviendraient rapidement exhorbitantes à calculer [3]. Le fait d'utiliser l'équation (23) permet de revenir dans le domaine temporel et de retrouver l'opérateur résidu spatial originel $\mathcal{R}$ grace à la propriété de bijection de la transformée de Fourier

$$\boldsymbol{K} D_t(\boldsymbol{w}_n) + \mathcal{R}(\boldsymbol{w}_n, \boldsymbol{x}_n, \boldsymbol{s}_n) = 0 \tag{26}$$

où $D_t(\boldsymbol{w}_n)$ est le nouvel opérateur spectral de dérivée par rapport au temps qui couple tous les instants. Cet opérateur spectral, exprimé dans le domaine temporel s'écrit :

$$D_t(\boldsymbol{w}_n) = \sum_{p=-N}^{N} d_p \boldsymbol{w}_{n+p} \tag{27}$$

Dans l'équation (27), l'indice $n+p$ doit être interprété comme exprimé modulo $2N+1$ pour obtenir l'indice positif correspondant. Par exemple $\boldsymbol{w}_{-N} = \boldsymbol{w}_{N+1}$. Les coefficients d_p sont donnés par

$$d_p = \begin{cases} \frac{\pi}{T}(-1)^{(p+1)} \csc\left(\frac{\pi p}{2N+1}\right) & \text{if } p \neq 0 \\ 0 & \text{if } p = 0 \end{cases} \tag{28}$$

Comme la dérivée spectrale en temps dépend de l'ensemble des solutions $\boldsymbol{w}_{n+p}$ avec p allant de $-N$ à N, le système (26) doit être écrit de manière couplée pour chaque instants dans la période

$$\boldsymbol{K} D_t(\boldsymbol{w}_n) + \mathcal{R}(\boldsymbol{w}_n, \boldsymbol{x}_n, \boldsymbol{s}_n) = 0, \quad 0 \leq n < 2N+1 \tag{29}$$

B. Resolution du système TSM-ALE-AC

Le système non-linéaire d'équations (29) est résolu de manière itérative à travers une stratégie de pas de temps dual, autrement dit en recherchant l'état stationnaire par rapport à τ du système suivant

$$\frac{\partial \boldsymbol{w}_n}{\partial \tau} = -\mathcal{R}_n^t(\boldsymbol{w}, \boldsymbol{x}_n, \boldsymbol{s}_n), \quad 0 \leq n < 2N+1 \tag{30}$$

où le résidu total est défini par $\mathcal{R}_n^t(\boldsymbol{w}) = K D_t(\boldsymbol{w}_n) + \mathcal{R}(\boldsymbol{w}_n, \boldsymbol{x}_n, \boldsymbol{s}_n)$ pour l'approche TSM. Les $2N+1$ valeurs stationnaires$\boldsymbol{w}_n$ sont couplées à travers l'approche spectrale $D_t(\boldsymbol{w}_n)$ de la dérivée en temps physique. Notons maintenant $\boldsymbol{w}_n^m$, la valeur intermédiaire de $\boldsymbol{w}_n$ à l'itération m vers l'état stationnaire en temps dual. En utilisant une simple discrétisation Euler du premier ordre pour la dérivée en temps dual, l'état stationnaires est atteint en résolvant de façon itérative

$$\frac{\Delta \boldsymbol{w}_n^m}{\Delta \tau_{i,n}^m} = -\mathcal{R}_n^t(\boldsymbol{w}^m, \boldsymbol{x}_n, \boldsymbol{s}_n), \quad 0 \leq n < 2N+1 \tag{31}$$

où $\Delta \boldsymbol{w}_n^m = \boldsymbol{w}_n^{m+1} - \boldsymbol{w}_n^m$ et $\Delta\tau_{i,n}^m$ est le pas de temps dual (local) dans la cellule i du maillage associé à l'instant t_n de la période. Notez que dans cette étude, les $2N+1$ positions et vitesses de grille sont *a priori* connues de par les lois de mouvements imposées. En particulier, la vitesse $\boldsymbol{s}_n$ est calculée avec l'équation (9) au temps t_n. Adapter au système TSM-AC l'analyse de stabilité conduite par van der Weide dans [5] pour le système TSM compressible qui utilise une formulation explicite identique à (31), conduit à la condition de stabilité suivante pour le choix du CFL

$$\Delta\tau_{i,n}^m = \mathrm{CFL}\frac{h_i}{||\lambda||_{i,n}^m + N\omega h_i} \tag{32}$$

avec h_i une longueur caractéristique de la cellule i dans la grille, $||\lambda||_{i,n}^m$ le rayon spectral de la matrice Jacobienne associée au système Euler AC au temps t_n et CFL ≤ 1. Si on recherche la solution stationnaire de l'écoulement incompressible, la matrice k est réduite à la matrice nulle et la condition précédente n'inclurait pas la contribution $N\omega h_i$. Quand une formulation TSM explicite est utilisée avec une haute fréquence ($\omega >> 1$) et/ou un nombre d'harmoniques importants N, la condition (32) peut devenir particulièrement restrictive. Le fait d'utiliser une formulation Euler implicite en temps dual pour intégrer (30) dans chaque cellule i à chaque instant t_n permet d'utiliser des grands pas de temps dual, et donc d'avoir une convergence efficace en temps dual vers l'état stationnaire indépendant de ω ou N, mais le problème non linéaire TSM-ALE-AC implicite non linéaire doit être résolu :

$$\frac{\Delta \boldsymbol{w}_{i,n}^m}{\Delta\tau_{i,n}^m} = -\mathcal{R}_{i,n}^t(\boldsymbol{w}^{m+1}, \boldsymbol{x}_n, \boldsymbol{s}_n), \quad 0 \leq n < 2N+1 \tag{33}$$

C. TSM implicite : système PJ-TSM-ALE-AC

Le résidu complet TSM est défini par $\mathcal{R}^t(\boldsymbol{w}) = \boldsymbol{K}D_t(\boldsymbol{w}) + \mathcal{R}(\boldsymbol{w})$ avec l'opérateur de dérivée spectrale D_t linéaire et l'opérateur résidu spatial $\mathcal{R}$ formellement inchangé par rapport à l'approche BDF. En suivant la ligne de conduite décrite pour l'approche BDF, le résidu TSM au niveau de temps dual $m+1$ peut être approché de la manière suivante

$$\mathcal{R}_{i,n}^t\left(\boldsymbol{w}^{m+1}\right) = \mathcal{R}_{i,n}^t\left(\boldsymbol{w}^m\right) + \boldsymbol{K}D_t(\Delta \boldsymbol{w}_{i,n}^m) + \frac{1}{|\Omega_i|}\sum_k \left(\Delta\mathcal{H}_{(i,k),n}^{(i)}\right)^m \ |\Gamma_{i,k}| \tag{34}$$

où l'incrément de balance de flux $\Delta\mathcal{H}^{(i)}$ est calculé en utilisant les formules (15) et (16) précédemment introduites pour dériver la phase implicite BDF et appliquées maintenant avec l'incrément de variable $\Delta\boldsymbol{w}_{i,n}^{m}$ au lieu de $\Delta\boldsymbol{w}_{i}^{n,m}$. Développer cet incrément de balance de flux et l'approche spectrale de la dérivée en temps physique avec (27) (28) conduit à la relation implicite suivante, où les termes dépendants de $\Delta\boldsymbol{w}_{i,n}^{m}$ ont été rassemblés dans le membre de gauche Left Hand Side (LHS).

$$\begin{aligned}\left(\frac{1}{\Delta\tau_{i,n}^{m}}+\sum_{k}C_{(i,k),n}^{m}\right)\Delta\boldsymbol{w}_{i,n}^{m} \;=\; & -\mathcal{R}_{i,n}^{t}(\boldsymbol{w}^{m})-\frac{1}{2|\;\Omega_{i,n}|}\sum_{k}\left(\Delta\boldsymbol{F}_{o(i,k),n}^{E}\right)^{m}\cdot\boldsymbol{n}_{(i,k),n}\;|\Gamma_{(i,k),n}| \\ & +\sum_{k}C_{(i,k),n}^{m}\Delta\boldsymbol{w}_{(o(i,k)),n}^{m}-\boldsymbol{K}\sum_{p=-N}^{N}d_{p}\Delta\boldsymbol{w}_{i,n+p}^{m}\end{aligned} \tag{35}$$

avec les coefficients scalaires $C_{(i,k),n}^{m}$ définis par

$$C_{(i,k)n}^{m}=\frac{1}{|\Omega_{i,n}|}\left(\frac{1}{2}\rho(\boldsymbol{J}_{\perp}^{E})+\rho(\widetilde{\boldsymbol{J}_{\perp}^{V}})\right)_{(i,k),n}^{m}|\Gamma_{(i,k),n}| \tag{36}$$

et $d_0 = 0$ dans l'opérateur de dérivée spectrale de sorte qu'il n'y a pas de contribution de ce terme dans le membre de gauche ci-dessus. En suivant la stratégie adoptée pour résoudre le système BDF-ALE-AC, une stratégie Point Jacobi pourrait être appliquée pour obtenir une solution itérative du système TSM-ALE-AC ci-dessus. Cependant, une différence fondamentale apparaît quand on passe du système BDF au système TSM : tandis que la formule BDF renforce la dominance diagonale du système linéaire associé à la phase implicite, la formule TSM introduit des termes hors-diagonaux qui conduisent à une perte de dominance diagonale. Ce problème a été souligné par Su et Yuan dans [8] a a été ensuite résolu en utilisant le solveur GMRES de Saad et Schultz [32] pour résoudre le système TSM implicite. Woodgate and Badcock [7] ont aussi fait remarquer une réduction de la performance de leur solveur de Krylov à cause de la perte de dominance diagonale de la matrice du système implicite. Dans ce travail, un simple correctif est utilisé : le LHS de $\Delta\boldsymbol{w}_{i,n}^{m}$ dans (35) est modifié pour inclure la contribution $\boldsymbol{K}\sum_{p=-N}^{p=N}|d_p|$, ce qui est suffisant pour s'assurer de la dominance diagonale de la phase implicite avec un impact limité sur son efficacité. Le système (35) est ensuite résolu en utilisant une simple technique de relaxation PJ, conduisant ainsi au système PJ-TSM-ALE-AC suivant :

$$
\begin{aligned}
&\Delta \boldsymbol{w}_{i,n}^{(0)} = 0 \\
&\begin{cases}
l = 0,\ l_{max} - 1 \\
\Delta \boldsymbol{w}_{i,n}^{(l+1)} = \left(\boldsymbol{D}_{i,n}^{m}\right)^{-1} \\
\left(-\mathcal{R}_{i,n}^{t}(\boldsymbol{w}^{m}) - \dfrac{1}{2|\ \Omega_{i,n}|} \sum_{k} \left(\Delta \boldsymbol{F}_{o(i,k),n}^{E} \right)^{(l)} \cdot \boldsymbol{n}_{(i,k),n}\ |\Gamma_{(i,k),n}| + \sum_{k} C_{(i,k),n}^{m} \Delta \boldsymbol{w}_{(o(i,k)),n}^{(l)} - \boldsymbol{K} \sum_{p=-N}^{N} d_p \Delta \boldsymbol{w}_{i,n+p}^{(l)} \right)
\end{cases} \\
&\boldsymbol{w}_{i,n}^{m+1} = \boldsymbol{w}_{i,n}^{m} + \Delta \boldsymbol{w}_{i,n}^{(l_{max})}
\end{aligned}
\tag{37}
$$

avec le coefficient diagonal modifié $\boldsymbol{D}_{i,n}^{m} = \dfrac{1}{\Delta \tau_{i,n}^{m}} + \sum_{k} C_{(i,k),n}^{m} + \boldsymbol{K} \sum_{p=-N}^{N} |d_p|$

IV. Evaluation de la TSM par rapport au BDF

Le solveur PJ-TSM-ALE-AC présenté ci-avant est maintenant appliqué au calcul des cas tests PH et PP et ces résultats sont comparés avec ceux obtenus en utilisant l'approche PJ-BDF-ALE-AC. A notre connaissance, l'unique tentative de couplage de la TSM et du système AC pour les écoulements incompressibles laminaires a été réalisée par Jameson [13], avec un succès limité puisque des limites de stabilités sont apparus pour des hautes fréquences et/ou un grand nombre d'harmoniques. Dans cette étude, la convergence de la TSM vers un état stationnaire va être tout d'abord analysée quand le nombre d'harmoniques N est augmenté pour des raisons de précision. La stratégie de référence BDF et la nouvelle approche TSM seront ensuite comparées en termes de précision : en particulier, le nombre de modes nécessaires pour atteindre un niveau suffisant de précision sera étudié pour les cas test PH et PP. Le gain potentiel en efficacité offert par la TSM par rapport au BDF sera finalement évalué.

A. Convergence de l'approche TSM

La convergence de (37) vers un état stationnaire est surveillée en traçant le résidu de pression défini comme la racine carrée de la moyenne, Root Mean Square (RMS) de la première composante de l'opérateur résidu $\mathcal{R}^{t}(\boldsymbol{w})$, calculé dans toutes les cellules et moyenné par le nombre d'instants dans

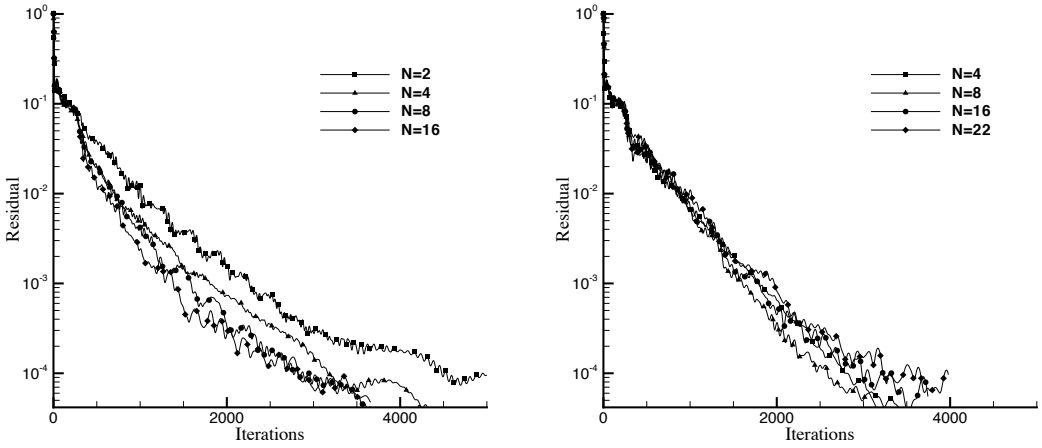

(a) (b)

Fig. 4 Historiques de convergence de la méthode PJ-TSM-ALE-AC. (a) : cas test PH pour un nombre croissant d'harmoniques (N allant de 2 à 16). (b) cas test PP pour un nombre croissant d'harmoniques (N allant de 4 à 22).

la période

$$res_{av}^{m} = \frac{1}{2N+1} \sum_{n=0}^{2N} \sqrt{\frac{1}{N_{cell}} \sum_{i=1}^{N_{cell}} \frac{\Delta p_{i,n}^{m\ 2}}{\Delta \tau_{i,n}^{m\ 2}}}$$

Cette quantité est normalisée par sa valeur à la première itération pour faciliter la comparaison entre les calculs réalisés avec différentes valeurs du nombre d'harmoniques N. Tous les calculs utilisent $l_{max} = 16$ itérations pour le solveur implicite PJ et un CFL $= 10^6$ pour calculer le pas de temps dual $\Delta\tau_{i,n}^{m}$ avec (32). Le paramètre AC β est identique à celui utilisé pour les calculs BDF précédents ($\beta = 5$).

Les historiques de convergence montrés dans la Fig. 4 démontrent que la vitesse de convergence du solveur TSM vers l'état stationnaire ne dépend que faiblement du nombre d'harmoniques N : pour le cas test PH moins de 4000 itérations sont nécessaires pour atteindre une baisse du résidu de 4 ordres en magnitude quand un peu moins de 3000 sont suffisantes pour le cas test PP, quel que soit la valeur de N. Le coût d'une itération dépend bien sur de la valeur de N mais ce point va être discuté à la fin de cette partie après avoir analysé la précision des solutions TSM.

B. Précision des solutions TSM

La précision des solutions TSM va tout d'abord être évaluée de façon qualitative en comparant les solutions stationnaires du système PJ-TSM-ALE-AC obtenues pour un nombre croissant d'harmoniques avec la solution BDF précédente. Cette comparaison sera effectuée sur l'évolution des coefficients d'effort globaux C_X, C_Y sur un cycle pour les cas test PH et PP. Ensuite, les distributions de pression autour du profil pour 2 instants sélectionnes dans la période seront aussi comparées. Une analyse plus quantitative de l'erreur sera finalement proposée et des conclusions concernant le gain d'efficacité potentiel offert par la TSM vis à vis du BDF seront tirées.

1. Coefficients aérodynamiques globaux

Les figures 5 et 6 montrent les coefficients C_X et C_Y calculés avec l'approche TSM et un nombre croissant d'harmoniques pour les problèmes d'écoulements PH et PP respectivement. Ces évolutions sur une période sont tracées avec les résultats BDF précédemment calculés et dont la précision a été auparavant vérifiée en comparaison de [14]. Rappelons que les calculs BDF utilisent 520 pas de te temps physique par période et nécessitent 4 (resp. 6) cycles avant d'atteindre l'état périodique établi pour le cas PH (resp. PP). Les évolutions TSM sont reconstruites à partir des champs $\boldsymbol{w}_n$ pour n'importe quel temps dans la période grâce à la série de Fourier tronquée de la solution. Pour le cas test PH, l'évolution calculée avec la TSM pour $N = 2$ et $N = 4$ diffère considérablement des résultats de référence; de petites différences entre BDF et TSM restent pour $N = 8$ et les 2 évolutions apparaissent superposées pour $N = 16$. Pour le cas test PP, les évolutions des C_X et C_Y calculées avec la TSM pour $N = 4$ et $N = 8$ montrent des différences importantes avec les résultats de référence; avec $N = 16$, il y a toujours quelques petites imperfections tandis que pour $N = 22$, les solutions BDF et TSM apparaissent superposées.

2. Distributions de coefficient de pression à la paroi et champs de pression

Deux instants dans la période sont retenus pour une comparaison plus précise des champs calculés : $t/T = 0.25$ et $t/T = 0.45$. Pour chacun de ces instants, la distribution du coefficient de pression à la paroi obtenue en utilisant BDF et TSM(N) est tracée, respectivement dans la figure 7 et 9 pour le cas test PH. Rappelons que ces distributions de pression sont reconstruites à chaque point de grille

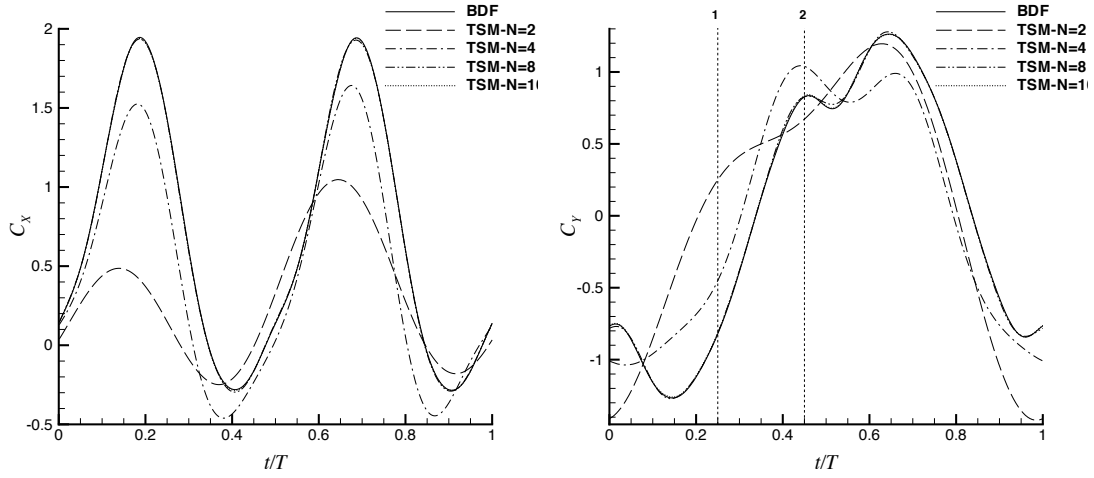

(a) (b)

Fig. 5 Cas test PH. Comparaison des coefficients C_X (a) et C_Y (b) pour un nombre croissant d'harmoniques.

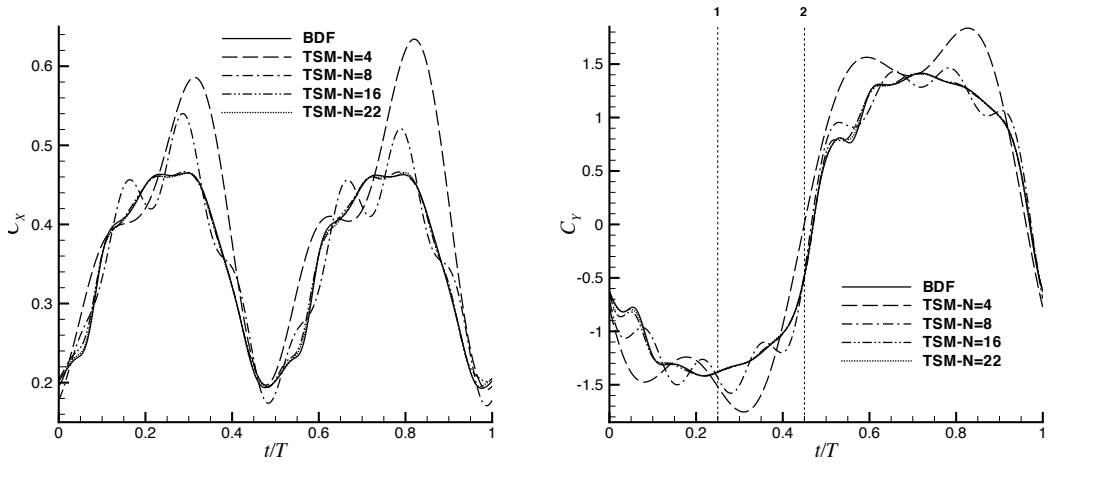

(a) (b)

Fig. 6 Cas test PP. Comparaison des coefficients C_X (a) et C_Y (b) pour un nombre croissant d'harmoniques.

i à partir des valeurs $\boldsymbol{w}_{i,n}$ calculées et en appliquant les formules (22) and (23) dans chaque cellule. Pour le calcul de PH, le très bon accord entre BDF et TSM(8) et l'accord presque parfait entre BDF et TSM(16) sont clairement visibles; ceci est confirmé par les contours de pression reproduits dans la Fig. 11. Pour le cas PP, la distribution du coefficient de pression obtenu avec BDF et TSM(N) est représentée, respectivement dans la Fig. 8 et 10. L'accord est déjà très bon pour $N = 16$ et

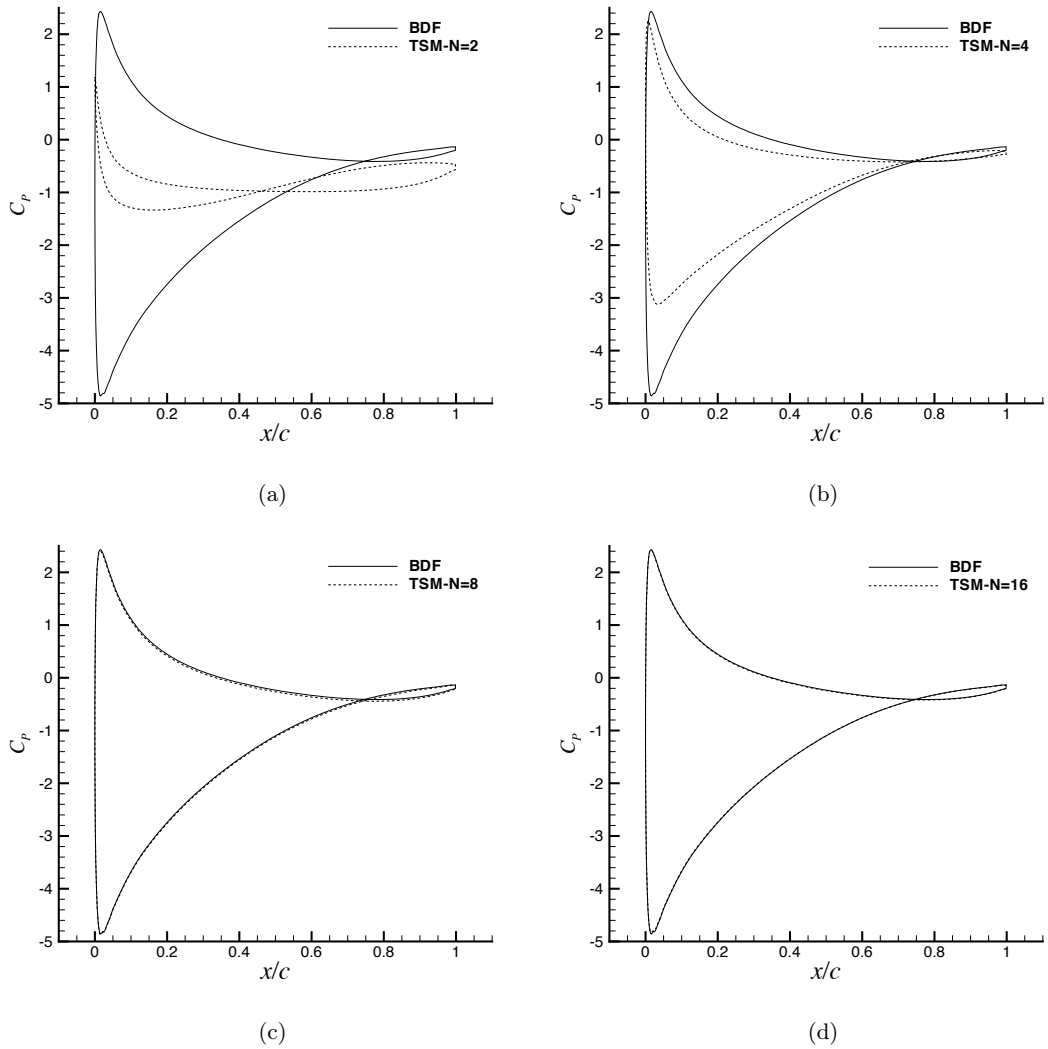

(a) (b)

(c) (d)

Fig. 7 Cas test PH. Distribution (reconstruite) du coefficient de pression à la paroi pour la TSM(N) au temps $t/T = 0.25$ pour un nombre croissant d'harmoniques. Comparaison avec les distributions de référence BDF.

presque parfait pour $N = 22$. Cette similarité est confirmée par les champs de pression de la figure 12.

3. Analyse quantitative de l'erreur

L'erreur RMS sur le coefficient d'effort C_X est défini par :

$$\epsilon_{RMS}(C_X) = \sqrt{\frac{1}{N_{\Delta t}} \sum_{k=1}^{N_{\Delta t}} \left(\frac{(C_X)_{TSM(N)}(t_k) - (C_X)_{BDF}(t_k)}{(\Delta C_X)_{BDF}} \right)^2}$$

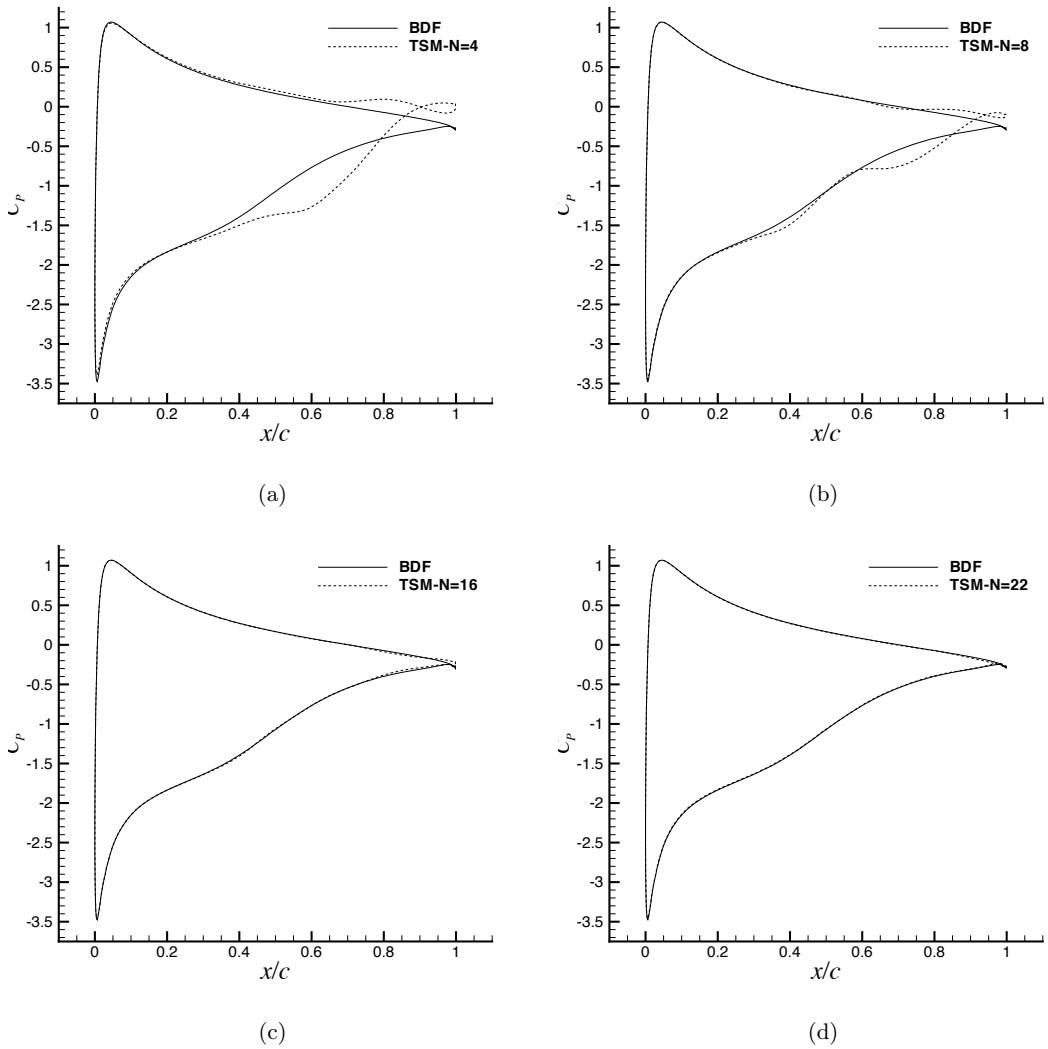

Fig. 8 Cas test PP. Distribution (reconstruite) du coefficient de pression à la paroi pour la TSM(N) au temps $t/T = 0.25$ pour un nombre croissant d'harmoniques. Comparaison avec les distributions de référence BDF.

où les valeurs des coefficients C_X aux temps t_k dans le cycle de l'écoulement et l'amplitude ΔC_X de la variation de C_X sont directement disponibles pour les calculs BDF tandis que les valeurs de C_X correspondantes au calcul TSM sont obtenues par reconstruction de la solution de l'écoulement en utilisant la série de Fourier tronquée avec N harmoniques. L'erreur RMS sur le coefficient de force C_Y est définie de façon identique. Ces erreurs sont tracées en fonction de N dans la Fig. 13 pour déterminer le meilleur choix de N : le nombre d'harmoniques doit en effet être pris suffisamment grand pour s'assurer que la solution TSM calculée est suffisamment précise en comparaison du

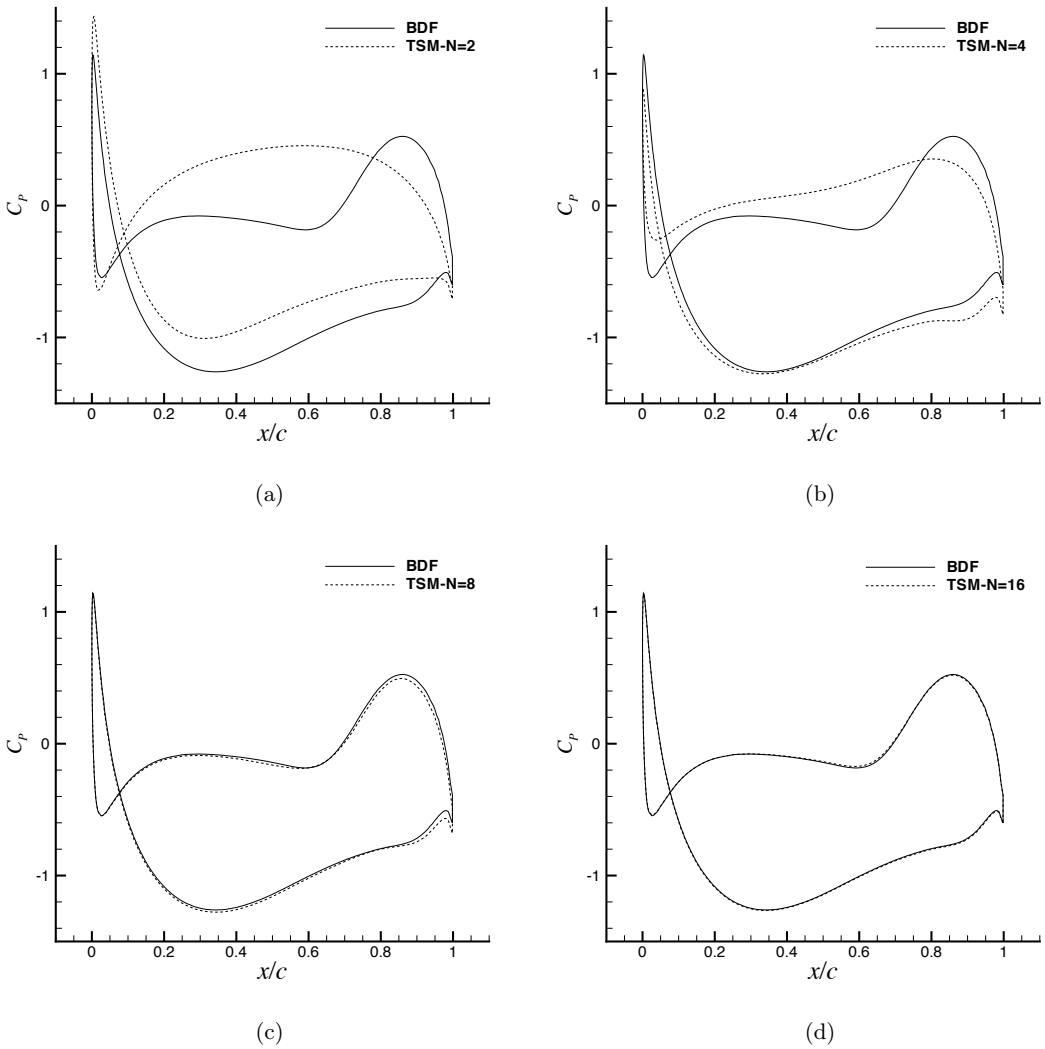

Fig. 9 Cas test PH. Distribution (reconstruite) du coefficient de pression à la paroi pour la TSM(N) au temps $t/T = 0.45$ pour un nombre croissant d'harmoniques. Comparaison avec les distributions de référence BDF.

calcul usuel BDF mais pas trop grand non plus dans le sens ou le gain espéré avec l'approche TSM par rapport à l'approche BDF est un gain en temps de calcul plus qu'un gain en précision. De façon cohérente avec les représentations graphiques des comparaisons BDF et TSM précédentes, les niveaux d'erreur atteints pour le cas PH pour un nombre donné d'harmoniques sont bien plus bas que pour le cas PP. Pour le cas PH, les erreur RMS sur le C_X et C_Y descendent sous la barre de 1% pour $N = 8$ tandis que $N = 16$ harmoniques sont nécessaires pour satisfaire le même critère pour le cas PP.

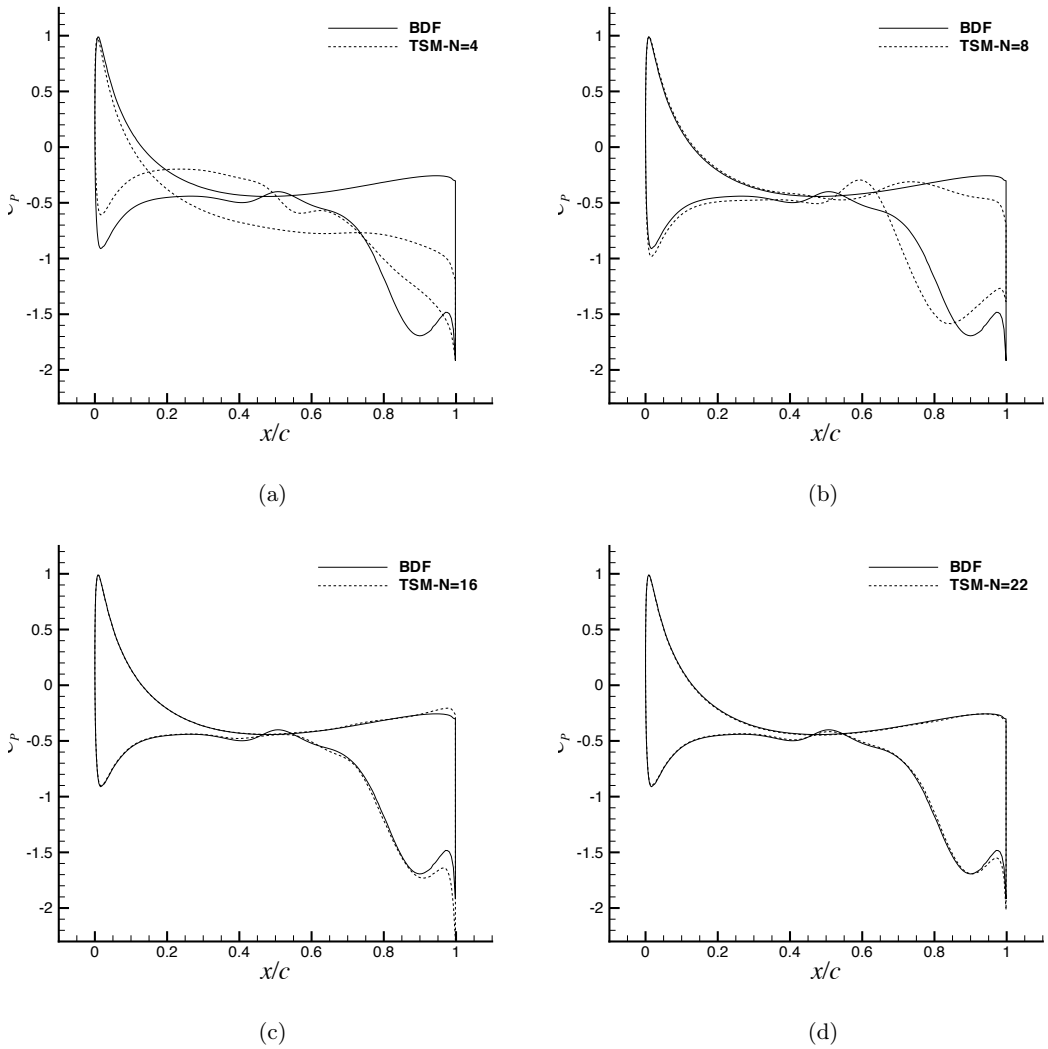

(a) (b)

(c) (d)

Fig. 10 Cas test PP. Distribution (reconstruite) du coefficient de pression à la paroi pour la TSM(N) au temps $t/T = 0.45$ pour un nombre croissant d'harmoniques. Comparaison avec les distributions de référence BDF.

C. Efficacité de l'approche TSM

Le coût global de l'approche BDF usuelle peut être exprimée comme :

$$\mathcal{C}_{BDF} = N_{\Delta t} \times N_{cycles} \times m_{max}^{BDF} \times l_{max} \times N_{cells} \times c_u^{BDF}$$

où $N_{\Delta t}$ est le nombre de pas de temps utilisé pour décrire une période ou un cycle, N_{cycles} est le nombre de cycles nécessaires avant d'atteindre l'état périodique établi, m_{max}^{BDF} est le nombre de sous-itérations en temps dual utilisées à chaque pas de temps physique pour atteindre l'état

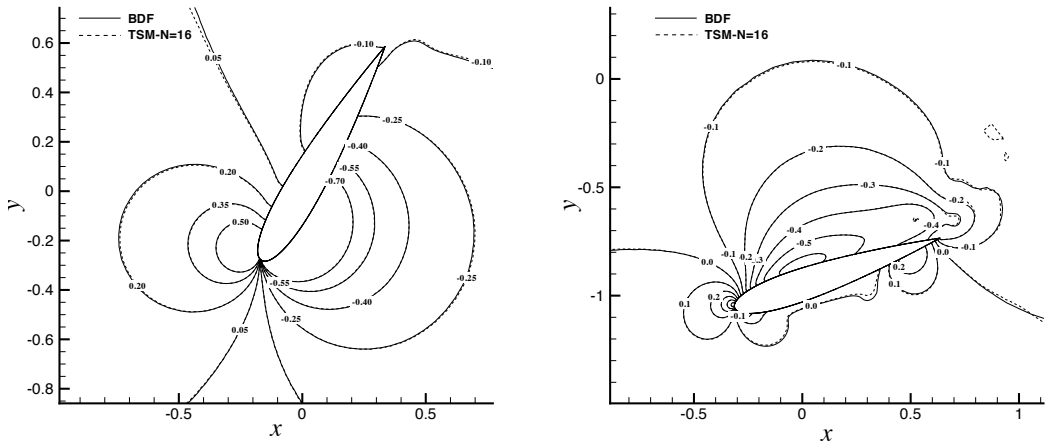

(a) (b)

Fig. 11 Cas test PH. Champ de pression TSM reconstruit ($N = 16$) au temps $t/T = 0.25$ (a) et $t/T = 0.45$ (b).

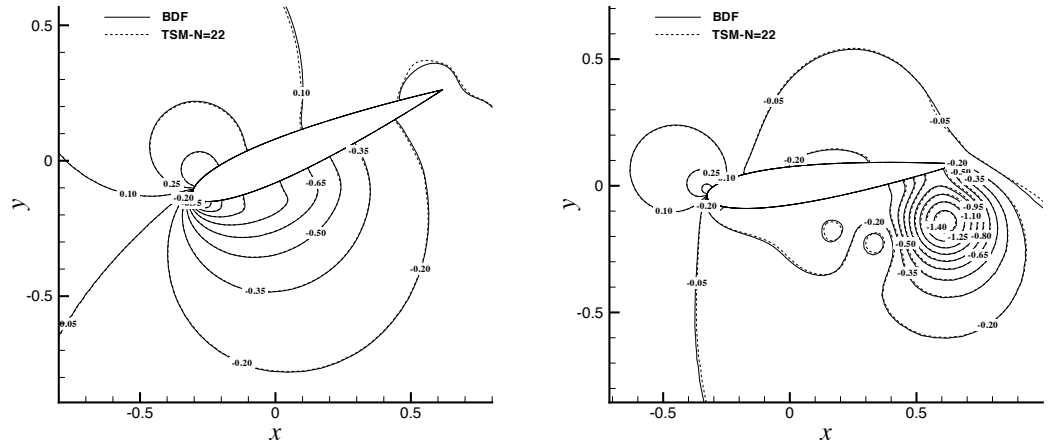

(a) (b)

Fig. 12 Cas test PP. Champ de pression TSM reconstruit ($N = 22$) au temps $t/T = 0.25$ (a) et $t/T = 0.45$ (b).

stationnaire dual, l_{max} est le nombre d'itérations utilisées avec la méthode de résolution de relaxation PJ, N_{cells} est la taille de grille et c_u^{BDF} est le coût unitaire (par point et par itération) de la méthode PJ-BDF-ALE-AC.

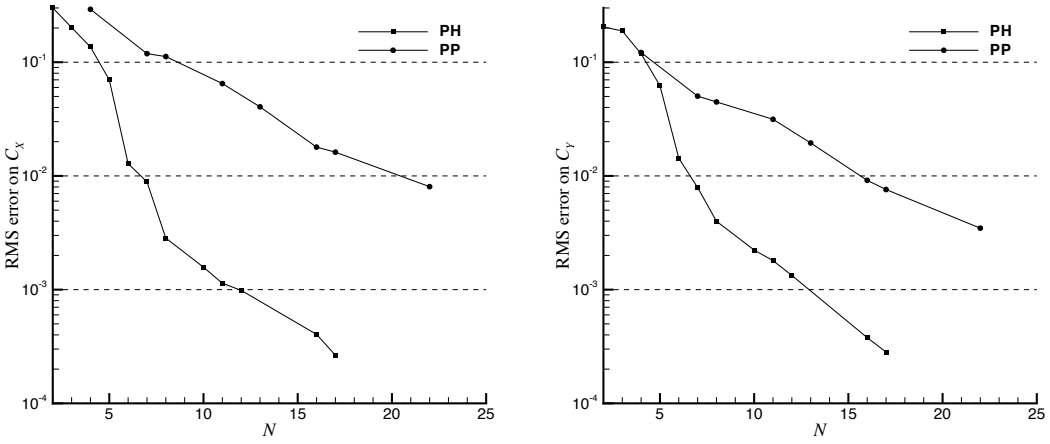

Fig. 13 Erreur RMS de la différence normalisée entre les coefficients C_X (a) et C_Y (b) calculés avec la stratégie BDF de référence avec $N_{\Delta t} = 520$ itérations par cycle et la stratégie TSM(N) avec un nombre croissant N.

Par ailleurs, le coût global de la nouvelle approche TSM proposée peut être exprimé comme :

$$\mathcal{C}_{TSM(N)} = (2N+1) \times m_{max}^{TSM(N)} \times l_{max} \times N_{cells} \times c_u^{TSM}(N)$$

où $(2N + 1)$ est le nombre d'instants retenus pour décrire la période, m_{max}^{TSM} est le nombre d'itérations sur le temps dual nécessaires pour conduire le système TSM-ALE-AC vers l'état stationnaire, l_{max} est le nombre d'itérations utilisées par la méthode de relaxation PJ, N_{cells} est la taille de grille et $c_u^{TSM(N)}$ est le coût unitaire par point et par itération de cette méthode PJ-TSM-ALE-AC.

Comme l_{max} est le même pour BDF et TSM, le rapport de coût entre TSM(N) et BDF utilisés sur le même maillage revient à :

$$\eta = \frac{\mathcal{C}_{TSM(N)}}{\mathcal{C}_{BDF}} = \underbrace{\frac{(2N+1)}{N_{\Delta t} \times N_{cycles}} \times \frac{m_{max}^{TSM(N)}}{m_{max}^{BDF}}}_{\Phi_1} \times \underbrace{\frac{c_u^{TSM(N)}}{c_u^{BDF}}}_{\Phi_2}$$

où, pour le solveur donné et décrit dans ce travail, la contribution Φ_1 dépend du problème considéré seulement tandis que la contribution Φ_2, rapport des coûts unitaires associés aux méthodes TSM(N) et BDF, dépend de l'implémentation numérique de ces méthodes dans le code utilisé. Dans cette

étude, le même nombre $N_{\Delta t} = 520$ de pas de temps physiques par cycle a été utilisé pour les cas PH et PP et il en va de même pour le nombre de sous-itérations en temps dual $m_{max}^{BDF} = 100$. En ce qui concerne le coût global et indépendamment de la problématique de la précision pour le moment, les cas PH et PP diffèrent de par le nombre de cycles nécessaires pour atteindre l'état périodique établi ($N_{cycles}^{PH} = 6$ tandis que $N_{cycles}^{PP} = 4$) et de par le nombre typique $m_{max}^{TSM(N)}$ d'itérations sur τ pour atteindre l'état stationnaire pour les calculs TSM. Ce nombre vaut grossièrement $m_{max}^{TSM(N)} \approx 3300$ pour PH et $m_{max}^{TSM(N)} \approx 2800$ pour PP, quel que soit le nombre d'harmoniques N (voir Fig. 4). Par conséquent, le rapport de coût entre les stratégies TSM et BDF est donné, pour le cas test PH, par

$$\eta^{PH} = \Phi_1^{PH}(N) \times \Phi_2(N) = (0.010577 \times (2N + 1)) \times \Phi_2(N) \tag{38}$$

et pour le cas test PP par

$$\eta^{PP} = \Phi_1^{PP}(N) \times \Phi_2(N) = (0.01346 \times (2N + 1)) \times \Phi_2(N) \tag{39}$$

Le rapport de coût unitaire entre les approches TSM et BDF devrait montrer une faible dépendance uniquement vis à vis du nombre d'harmoniques, d'un coté à cause des termes supplémentaires introduit par l'approximation spectrale de la dérivée et d'un autre coté à travers le coût supplémentaire dû au temps d'accès mémoire associé au grand système TSM qui couple les $2N + 1$ systèmes de lois de conservation. Idéalement, sans problèmes de mémoire, on devrait s'attendre à un rapport $\Phi_2(N)$ qui reste proche de l'unité quel que soit la valeur de N. En pratique, ce rapport a été numériquement estimé comme une fonction linéaire de N (qui est dépendant de l'implémentation)

$$\Phi_2(N) \approx 0.8208 + 0.0925 \times N \tag{40}$$

La Fig. 14 montre l'évolution du rapport de coût global pour les cas PH et PP, donnés respectivement par (38) et (39), avec un rapport de coût unitaire mesuré $\Phi_2(N)$ donné par (40), auquel cas η^{PH} et η^{PP} varient de façon quadratique avec N, ou avec un rapport de coût unitaire idéal égal à 1, auquel cas la variation de η^{PH} et η^{PP} reste linéaire par rapport à N. Bien qu'idéal, ce dernier cas fournit une limite haute du nombre d'harmoniques N qui pourraient être utilisés avant que le

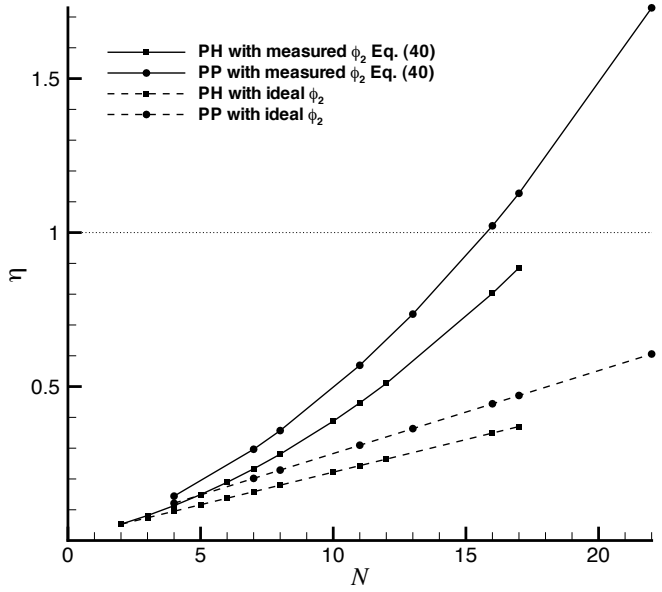

Fig. 14 Evolution du rapport de coût global $\eta = \mathcal{C}_{TSM(N)}/\mathcal{C}_{BDF}$ entre la TSM(N) et la BDF pour un nombre croissant d'harmoniques N. Lignes pleines : rapport de coût mesuré pour PH et PP. Lignes pointillées : rapport de coût idéal $\Phi_2 = 1$.

coût de l'approche TSM dépasse le coût de l'approche BDF. On peut observer dans la Fig. 14 que la valeur mesurée de η^{PP} atteint 1 pour $N = 16$ tandis que η^{PH} reste en dessous de 0.8 pour le même nombre d'harmoniques. Avec une meilleure implémentation qui permettrait de réduire l'augmentation du rapport de coût unitaire Φ_2 avec N, ce rapport de coût global pourrait rester en dessous de 0.5 pour $N = 16$.

Le point clé de cette analyse d'efficacité est atteint quand on croise l'évolution de $\eta(N)$ donné par la Fig. 14 avec les résultats d'erreurs pour C_X et C_Y représentés dans la Fig. 13. Les erreurs RMS sur ces coefficients aérodynamiques sont représentés en fonction du rapport de coût global dans la Fig. 15 : les lignes pleines correspondent à l'évolution mesurée de η^{PH} et η^{PP} tandis que les lignes pointillées correspondent à l'évolution idéale où le rapport de coût unitaire Φ_2 reste grossomodo égal à 1. D'après l'analyse précédente concernant la précision, les solutions BDF et TSM reconstruites ont été jugées coïncidentes quand l'erreur RMS normalisée descend en dessous de 1%, ce qui correspond à $N = 8$ pour le cas PH et $N = 16$ pour le cas PP. Si on retient ce même critère, on peut observer dans la Fig. 15 que l'approche TSM fournit une solution aussi précise que l'approche

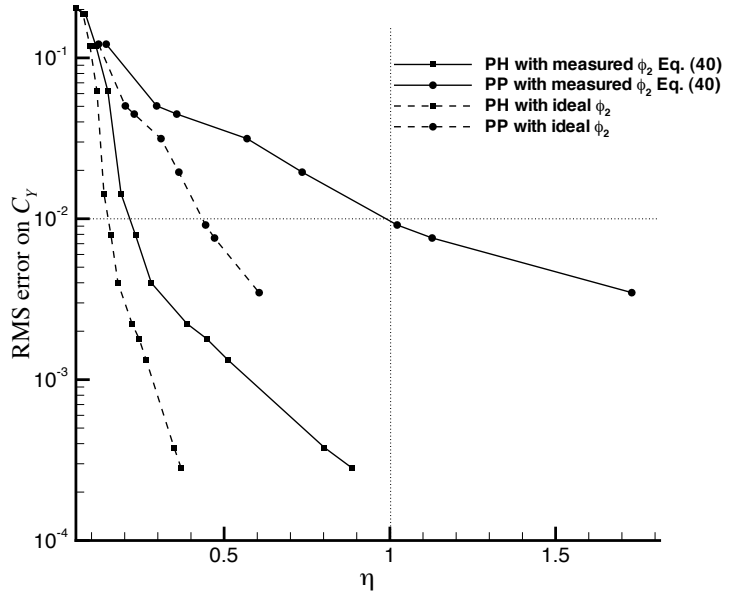

Fig. 15 Evolution de l'erreur RMS sur le C_Y en fonction du rapport de coût global $\eta = \frac{\mathcal{C}_{TSM(N)}}{\mathcal{C}_{BDF}}$ pour les cas PH et PP. Lignes pleines : rapport de coût mesuré pour PH et PP. Lignes pointillées : rapport de coût idéal $\Phi_2 = 1$.

BDF conventionnelle pour un coût total divisé d'un facteur 5 pour le cas PH; en procédant de la même manière, pour le cas PP, le nombre d'harmoniques nécessaire à la TSM pour produire le même niveau de précision que la BDF ne permet pas de réduire le coût CPU, puisque $\eta^{PP} \approx 1$ for $N = 16$. Une meilleure implémentation de l'approche TSM pourrait rendre l'approche attractive, même pour le cas PP, avec un rapport de coût global idéal qui descendrait alors à 0.5 pour $N = 16$ dans ce cas. L'analyse de l'efficacité de la TSM s'est concentrée sur le gain CPU atteignable en utilisant le calcul stationnaire d'un nombre limité de modes dans une période au lieu d'une solution instationnaire complète sur plusieurs cycles. Il est important de souligner cependant que la TSM est aussi plus consommatrice d'espace mémoire que la stratégie BDF puisqu'elle requière de stocker $(2N + 1) \times N_{cells}$ inconnues à chaque étape du calcul vers l'état stationnaire à comparer aux N_{cells} inconnues de la méthode BDF à chaque étape de la procédure de marche en temps classique.

V. Conclusion

La méthode TSM a été appliquée avec succès au calcul d'écoulements périodiques incompressibles autour de profils en utilisant une méthode de compressibilité artificielle dans le cadre d'une formulation ALE sur maillages non-structurés. Comme l'ont souligné nombre d'auteurs avant nous [6–8], le traitement implicite du grand système TSM, qui couple les $2N+1$ systèmes de lois de conservation avec N, le nombre d'harmoniques retenus pour décrire l'écoulement périodique qui nous intéresse, est crucial pour s'assurer de l'efficacité de la méthode TSM par rapport à une formule BDF conventionnelle. Dans ce travail, une formulation implicite de la TSM a été dérivée à partir du simple traitement sans-matrice développé précédemment dans le contexte des écoulements compressibles et applicable directement au système AC. Une attention spéciale a été portée pour s'assurer de la propriété de dominance diagonale de la phase implicite, avec une simple modification de la contribution diagonale qui n'affecte pas trop la convergence du solveur implicite vers l'état stationnaire. Une technique de relaxation par point a été retenue pour résoudre le système linéaire implicite TSM pour un coût par itération très bas qui contrebalance la réduction d'efficacité intrinsèque à la méthode (quelques milliers d'itérations de moindre coût sont nécessaires pour obtenir l'état stationnaire). Le calcul de l'écoulement périodique incompressible à bas-Reynolds autour d'un profil NACA0015 en battement et oscillation a démontré qu'entre $N = 8$ et $N = 16$ harmoniques sont requis par la TSM pour représenter de façon précise ces écoulements instationnaires bi-dimensionnels. Cette discrétisation grossière de la période sur le cycle "autorisée" par la formule spectrale utilisée pour la dérivée en temps physique couplée à une méthode de résolution efficace du système TSM couplant les $2N+1$ instants choisis dans la période nous a permis d'observer un gain CPU substantiel pour le cas test d'un profil NACA0015 en battement et oscillation considéré. Un niveau de précision comparable à celui offert par une méthode BDF conventionnelle d'intégration en temps a été atteint pour un coût total CPU divisé d'un facteur cinq. Cependant, pour le cas du profil en mouvement d'oscillation pure, nous n'avons pas observé de réduction de temps de calcul en utilisant TSM principalement parce qu'il est nécessaire d'utiliser deux fois plus d'harmoniques (16 au lieu de 8) pour ce cas, pour atteindre un niveau de précision identique à celui de la méthode BDF.

Afin de rendre l'approche TSM intéressante d'un point de vue temps de calcul quand un grand

nombre de modes sont requis pour une bonne précision, le travail en cours s'attache d'une part à améliorer l'implémentation de la méthode de façon à réduire le plus possible l'accroissement du rapport de coût unitaire Φ_2 quand N augmente et d'un autre coté, à l'amélioration de l'efficacité du solveur implicite par rapport à la méthode PJ utilisée dans cette étude pour réduire potentiellement à la fois les rapports Φ_1 and Φ_2. Des stratégies de relaxation efficaces proposées par exemple dans [33] vont être étudiées dans cette perspective. Notre recherche actuelle se consacre aussi aux stratégies permettant de déterminer automatiquement et a priori le nombre d'harmoniques à utiliser avec l'approche TSM pour s'assurer d'un niveau de précision donné.

References

[1] Peyret, R., and Taylor, T. D., *Computational Methods in Fluid Flow*, 2nd ed., Springer-Verlag, New York, 1983.

[2] Jameson, A., "Time-Dependent Calculations using Multigrid with Applications to Unsteady Flows Past Airfoils and Wings," *10th AIAA Computational Fluid Dynamics Conference*, AIAA Paper 91-1596, Jun. 1991.

[3] Hall, K. C., Thomas, J. P., and Clark, W. S., "Computation of Unsteady Nonlinear Flows in Cascades using a Harmonic Balance Technique," *AIAA Journal*, Vol. 40, No. 5, 2002, pp. 87–886.

[4] Gopinath, A., and Jameson, A.,"Time Spectral Method for Periodic Unsteady Computations Over Two-and Three-Dimensional Bodies," *43rd AIAA Aerospace Sciences Meeting and Exhibit*, AIAA Paper 2005-1220, Jan. 2005.

[5] van der Weide, E., Gopinath, A., and Jameson, A., "Turbomachinery Applications with the Time Spectral Method," *35th AIAA Fluid Dynamics Conference and Exhibit*, AIAA Paper 2005-4905, June 2005.

[6] Sicot, F., Puigt, G., and Montagnac, M., "Block-Jacobi Implicit Algorithms for the Time Spectral Method," *AIAA Journal*, Vol. 46, No. 12, 2008, pp. 3080–3089.

[7] Woodgate, M. A., and Badcock, K. J., "Implicit Harmonic Balance Solver for Transonic Flow with Forced Motions," *AIAA Journal*, Vol. 47, No. 4, 2009, pp. 893–901.

[8] Su, X., and Yuan, X., "Implicit Solution of Time Spectral Method for Periodic Unsteady Flows," *International Journal for Numerical Methods in Fluids*, Jan 2009. doi: 10.1002/fld.2111

[9] Ekici, K., and Hall, K. C., "Nonlinear Analysis of Unsteady Flows in Multistage Turbomachines Using Harmonic Balance," *AIAA Journal*, Vol. 45, No. 5, 2007, pp. 1047, 1057.

[10] Butsuntorn, N., and Jameson, A., "Time Spectral Method for Rotorcraft Flow," *46th AIAA Aerospace Sciences Meeting and Exhibit*, AIAA Paper 2008-403, Jan. 2008.

[11] Antheaume, S., Maître, T., and Achard, J.-L., "Hydraulic Darrieus Turbines Efficiency for Free Fluid Flow Conditions Versus Power Farms Conditions," *Renewable Energy*, Vol. 33, 2008, pp. 2186–2198.

[12] Amet, E., Maître, T., Pellone, C., and Achard, J.-L., "2D Numerical Simulations of Blade-Vortex Interaction in a Darrieus Turbine," *Journal of fluids engineering*, Vol. 131, 2009.

[13] Jameson, A., "An Assessment of Dual-Time Stepping, Time Spectral and Artificial Compressibility Based Numerical Algorithms for Unsteady Flow with Applications to Flapping Wings," *19th AIAA Computational Fluid Dynamics*, AIAA Paper 2009-4273, Jun. 2009.

[14] Kinsey, T., and Dumas., G., "Parametric Study of an Oscillating Airfoil in a Power-Extraction Regime," *AIAA Journal*, Vol. 46, No. 6, 2008, pp. 1318–1330.

[15] Kloczko, T., Corre, C., and Beccantini, A., "Low-Cost Implicit Schemes for All-Speed Flows on Unstructured Meshes," *International Journal for Numerical Methods in Fluids*, 2008. doi: 10.1002/fld.1730

[16] Chorin, A. J., "A Numerical Method for Solving Incompressible Viscous Flow Problems," *Journal of Computational Physics*, Vol. 2, 1967, pp. 12–26.

[17] Roe, P. L., "Approximate Riemann Solvers, Parameter Vectors, and Difference Schemes," *Journal of Computational Physics*, Vol. 43, 1981, pp. 357–372.

[18] Barth, T. J., and Jespersen, D. C., "The Design and Application of Upwind Schemes on Unstructured Meshes," *27th AIAA Aerospace Sciences Meeting*, AIAA Paper 89-0366, Jan. 1989.

[19] Delanaye, M., "Polynomial Reconstruction Finite Volume Schemes for the Compressible Euler and Navier-Stokes Equations on Unstructured Adaptive Grids," PhD thesis, 1996, Université de Liège.

[20] Taylor, L. K., and Whitfield, D. L., "Unsteady Three-Dimensional Incompressible Euler and Navier-Stokes Solver for Stationary and Dynamic Grids," *22nd AIAA Fluid Dynamics, Plasma Dynamics and Lasers Conference*, June 1991.

[21] Noh, W., "Cel: A Time-Dependant Two-Space Dimensional Coupled Eulerian-Lagrangian Code," *Methods in Computational Physics*, Vol. 3, 1964, pp. 117–119.

[22] Nakahashi, K., and Deiwert, G. S., "Self Adaptive Grid Method with Application to Airfoil Flow," *AIAA Journal*, Vol. 25, Issue 4, 1987, pp. 513–520.

[23] Batina, J. T., "Unsteady Euler Algorithm with Unstructured Dynamic Mesh for Complex-Aircraft Aerodynamic Analysis," *AIAA Journal*, Vol. 29, No. 3, 1991, pp. 327–333.

[24] Luo, H., Baum, J. D., and Lohner, R., "An Accurate, Fast, Matrix-Free Implicit Method for Computing Unsteady Flows on Unstructured Grids," *Computers and Fluids*, Vol. 30, 2001, pp. 137–159.

[25] Hassan, O., Sørensen, K. A., Morgan, K., and Weatherill, N. P., "A Method for Time Accurate Turbulent Compressible Fluid Flow Simulation with Moving Boundary Components Employing Local Remeshing," *International Journal for Numerical Methods in Fluids*, Vol. 53, Issue 8, 2007, pp. 1243–1266.

[26] Koobus, B., and Farhat, C., "Second-Order Time-Accurate and Geometrically Conservative Implicit Schemes for Flow Computations on Unstructured Dynamic Meshes," *Computer Methods in Applied Mechanics and Enginering*, Vol. 170, 1999, pp.103–129.

[27] Benek, J. A., Steger, J. L., and Dougherty, F. C., "A Flexible Grid Embedding Technique with Application to the Euler Equations," AIAA Paper 1983-1944, 1983.

[28] Kannan, R., and Wang, Z. J., "Overset Adaptive Cartesian/Prism Grid Method for Moving Boundary Flow Problems," *AIAA Journal*, Vol. 45, No. 7, 2007, pp. 1774–1779.

[29] Jameson, A., and Yoon, S., "Lower-Upper Implicit Schemes With Multiple Grids for the Euler Equations," *AIAA Journal*, Vol. 25, 1987, pp. 929–935.

[30] Luo, H., Baum, J. D., and Lohner, R., "A fast, Matrix-Free Implicit Method for Compressible Flows on Unstructured Grids," *Journal of Computational Physics*, Vol. 146, 1998, pp. 664–690.

[31] Shannon, C. E., "Communication in the Presence of Noise," *Proceeding of the Institute of Radio Engineers*, Vol. 37, pp. 10–21, Jan. 1949.

[32] Saad, Y., and Schultz, M., "GMRES: A Generalized Minimal Residual Algorithm for Solving Non-Symmetric Linear Systems," *SIAM Journal on Scientific and Statistical Computing*, Vol. 7, No. 3, July 1986.

[33] Liang, C., Kannan, R., and Wang, Z.J., "A p-multigrid spectral difference method with explicit and implicit smoothers on unstructured triangular grids", *Computers and Fluids*, Vol. 38, 2009, pp. 254–265.

Titre : Méthode de décomposition spectrale temporelle implicite pour le calcul d'écoulements incompressibles périodiques

Résumé : Ce travail de thèse se consacre au développement et à l'analyse d'une méthode de décomposition spectrale en temps TSM (Time Spectral Method) visant à calculer efficacement des écoulements à périodicité temporelle. L'intérêt principal de cette formulation réside dans la possibilité de s'affranchir du calcul de la solution transitoire pour rechercher directement l'état périodique établi et dans l'utilisation de grands pas de temps grace à la précision spectrale de la discrétisation temporelle TSM. La méthode TSM consiste à remplacer le calcul instationnaire d'une solution périodique en temps en le calcul de $2N + 1$ problèmes stationnaires couplés où N est le nombre d'harmoniques retenus dans la série de Fourier tronquée du système Navier-Stokes. La TSM est implémentée dans un code numérique qui résoud les équations instationnaires de Navier-Stokes dans un contexte de maillages non-structurés mis en mouvement grace à une approche ALE (Arbitary Lagrangian Eulerian). Une formulation implicite est proposée afin de rendre la méthode encore plus attrayante en termes de temps de calcul. Un apport original de cette thèse est l'extension de la TSM au calcul d'écoulements incompressibles laminaires en utilisant une méthode de compressibilité artificelle. Les cas tests de profils en mouvement de battement et d'oscillation permettent d'analyser et d'apprécier l'efficacité de cette nouvelle approche.

Mots-clés : Décomposition spectrale en temps, compressibilité artificielle, ALE, méthode implicite, écoulements incompressibles

Title: Implicit Time Spectral Method for time-periodic incompressible flows

Abstract: This Ph.D work deals with the implementation and analysis of a Time Spectral Method (TSM) dedicated to the efficient calculation of time-periodic flows. The main interest of the formulation lies in the fact that the calculation of the flow transient is not needed anymore and, instead, the final periodic solution can be directly looked for. Besides, the use of large physical time step is made possible by the spectral accuracy of the TSM time derivative operator. The Time Spectral Method converts a time-periodic flow computation into the solution of $2N + 1$ coupled steady computations where N denotes the number of harmonics retained in the Fourier analysis of the flow. The TSM is implemented into a Navier-Stokes solver in the context of general moving unstructured grids using an ALE (Arbitary Lagrangian Eulerian) formulation. An implicit scheme is proposed to make the approach even more attractive in terms of computational cost. An original contribution of this thesis is the extension of the TSM to the computation of laminar incompressible flows using the artificial compressibility method. Numerical simulations of oscillating and heaving airfoils allow a fine analysis of the TSM and show that it can lead to substantial computational cost reduction.

Keywords: Time Spectral Method, artificial compressibility, ALE, implicit method, incompressible flows